TRACE ELEMENT AND ISOTOPIC FINGERPRINTING OF OLIVINE PHENOCRYSTS AS RECORDERS OF MAGMATIC PROCESSES IN THE GOLDEN TROUT VOLCANIC FIELD, KERN PLATEAU, CA

By

Mark Szymanski

A Thesis Presented to

The Faculty of Humboldt State University

In Partial Fulfillment of the Requirements for the Degree

Master of Science in Environmental Systems: Geology

Committee Membership

Dr. Brandon Browne, Committee Chair

Dr. Jasper Oshun, Committee Member

Dr. Melanie Michalak, Committee Member

Dr. Mark Hemphill-Haley, Committee Member

Dr. Margaret Lang, Program Graduate Coordinator

July 2018

ABSTRACT

TRACE ELEMENT AND ISOTOPIC FINGERPRINTING OF OLIVINE PHENOCRYSTS AS RECORDERS OF MAGMATIC PROCESSES IN THE GOLDEN TROUT VOLCANIC FIELD, KERN PLATEAU, CA

Mark Szymanski

Quaternary mafic volcanism in the western Basin and Range and in the southeastern Sierra Nevada is largely controlled by extensional stresses that promote magma generation through decompression melting of the lithospheric and asthenospheric mantle. Where volcanism occurs in the Sierra Nevada, like at the Golden Trout Volcanic Field GTVF), the eruption rate, number of vents, and eruption volume is an order of magnitude less than at neighboring Basin and Range volcanic fields such as the Big Pine Volcanic Field (BPVF). To determine the factors that cause these differences in adjacent and contemporaneous volcanic fields, I sampled rocks from both fields and analyzed major and trace element compositions of olivine phenocrysts via electron microprobe, stable oxygen isotope compositions of olivine via laser fluorination, and whole-rock radiogenic isotope compositions via HR MC-ICP-MS. Major and trace element compositions between the GTVF and BPVF are overlapping with Fo values ranging from 67.61 to 88.77 and 77.72 to 88.13, respectively. $\delta^{18}O$ values are higher at GTVF (5.680 to 6.520 ‰) than at BPVF (5.554 to 5.750 ‰). Whole rock $^{87}Sr/^{86}Sr$ and $^{143}Nd/^{144}Nd$ ratios at the GTVF range from 0.705420 to 0.706026 and 0.512492 to 0.512604 and overlap

with values from BPVF and other regional volcanic fields. Similar mantle source compositions between the GTVF and BPVF indicate that differences in eruption rate, number of vents, and eruption volume are resultant from greater amounts of crustal contamination at GTVF. The presence of magmas with similar source compositions in and near the southern Sierra Nevada suggests that the regional extension characteristic of the Basin and Range has affected the southeastern Sierra Nevada block. Unfaulted crust in regionally extensional tectonic settings limits magma ascent, but doesn't seem to inhibit magma genesis at depth.

ACKNOWLEDGEMENTS

I thank Ilya Bindeman, Jim Palandri, David Zakharov, and Michael Hudak for assistance and training for laser fluorination analyses at the University of Oregon. Additionally, thank you to Frank Tepley for training and assistance on electron microprobe analyses at Oregon State University. Thank you to the Northern California Geological Society for their generous award of the Richard Chambers Grant. Additionally, I would like to thank the donors of the Bud Burke Scholarship for selecting me as a recipient. Thank you to my committee members, Jasper Oshun, Melanie Michalak, and Mark Hemphill-Haley, for their valuable input and feedback. I would like to offer a big thanks to my advisor, Brandon Browne, for suggesting a project in the Golden Trout Volcanic Field and all the help, mentorship, and fun that came with it. Finally, I would like to thank my family and friends. Thank you for the love and support.

TABLE OF CONTENTS

ABSTRACT ii

ACKNOWLEDGEMENTS iv

LIST OF TABLES vi

LIST OF FIGURES vii

LIST OF APPENDICES x

INTRODUCTION 1

METHODS 22

RESULTS 25

Olivine Major and Trace Elements 25

Olivine Oxygen Isotopes 32

Whole Rock Radiogenic Isotopes 34

DISCUSSION 36

Olivine Major and Trace Elements 36

Olivine Oxygen Isotopes 38

Whole Rock Radiogenic Isotopes 40

CONCLUSIONS 42

REFERENCES 43

APPENDIX A: RAW Olivine phenocryst core compositions VIA EMPA 50

APPENDIX B: Normalized olivine phenocryst core compositions VIA EMPA 83

APPENDIX C: BSE images and EMP analysis locations 115

LIST OF TABLES

Table 1. Physical characteristics of Quaternary volcanic fields located in eastern California (modified from Browne et al., 2017a). Data sources for CVF: Duffield et al., 1980; Bacon, 1982. BPVF: Omerod et al., 1991; Turrin and Gillespe, 1986; Blondes et al., 2008; Woolford, 2009; Vazquez and Woolford; 2015. GTVF: Webb, 1950; Bacon and Duffield, 1981; du Bray and Dellinger, 1981; Moore and Sisson, 1985; Browne et al., 2017a. 7

LIST OF FIGURES

Figure 1. Regional map of southeastern California showing the locations of the GTVF, BPVF, and CVF (outlined with dashed lines) with active Quaternary faults shown as red lines. 3

Figure 2. Regional map of the southwestern United States showing the locations of Basin and Range volcanic fields (red triangles) and the relative physiographic provinces of the area (SNP = Sierra Nevada Province; GVP = Great Valley Province). The black rectangle outlines the locations of the GTVF, BPVF, and CVF. Locations of volcanic fields are from Putirka et al., 2012b. 5

Figure 3. $^{87}Sr/^{86}Sr$ and $^{143}Nd/^{144}Nd$ ratios showing the corresponding compositions of mantle values: DM refers to depleted mantle, PREMA refers to prevalent mantle reservoir, HIMU refers to mantle with high U/Pb ratio, BSE refers to bulk silicate earth, and EM1 and EM2 refer to enriched mantle compositions with EM1 having low $^{87}Sr/^{86}Sr$ and EM2 high $^{87}Sr/^{86}Sr$ (Adapted from Rollinson, 1993)..... 10

Figure 4. Relative isotopic compositions of different regions of the Earth (Adapted from Rollinson, 1993)..... 11

Figure 5. $\delta^{18}O$ vs SiO_2 wt % for basaltic melt compositions. Normal-$\delta^{18}O$ array determined experimentally for closed system differentiation. High-$\delta^{18}O$ and Low-$\delta^{18}O$ magmas that plot outside of this array require contamination by materials with different $\delta^{18}O$ values from the basaltic melt (adapted from Bindeman, 2008a)..... 13

Figure 6. Sample locations from each of the four mafic vents of the GTVF. LWC samples are solid black squares. SFC samples are solid orange diamonds. TC samples are solid green circles. GC samples are solid red triangles. 18

Figure 7. Sample locations from 3 mafic vents of the BPVF. PC samples are open purple squares. QC samples are open blue circles. AC samples are open light blue triangles. ... 20

Figure 8. Whole rock compositions of samples from the GTVF and BPVF acquired using XRF. GTVF samples are from LWC (filled black squares), SFC (filled orange diamonds), TC (filled green circles), GC (filled red triangles). BPVF samples are from PC (open purple squares), QC (open dark blue circles, and AC (empty light blue triangle). GTVF data are from Browne et al. (2017a). BPVF data are from Blondes et al. (2008) and Vazquez and Woolford (2015). 21

Figure 9. Weight percent major and trace element compositions of olivine phenocrysts of GTVF and BPVF. GTVF samples include LWC (black filled squares), SFC (orange filled

diamonds), TC (green filled circles), and GC (red filled triangles). BPVF samples include PC (open purple squares), QC (open dark blue circles), and AC (open light blue triangles). Previous work by Browne et al. (2017a) are shown with LWC (black crosses), SFC (orange x's with a vertical line), and GC (red x's). Green shaded field on Fo vs NiO plot is indicative of mantle olivine compositions after Takahashi (1985). 27

Figure 10. $\delta^{18}O$ values of olivine versus Fo content of olivine. Light red shaded field represents all values of $\delta^{18}O$ and Fo analyzed at GC although both data sets were not analyzed for all samples. GVFC samples include LWC (black filled squares), SFC (orange filled diamonds), TC (green filled circles), and GC (red filled triangles). BPVF include PC (open purple squares), QC (open dark blue circles), and AC (open light blue triangles). 27

Figure 11. Histograms of Fo and NiO concentrations from samples collected from the GTVF and BPVF. Green rectangle represents mantle olivine concentrations from Takahashi (1985). 28

Figure 12. Olivine phenocryst core compositions from five samples at GC. Light blue unfilled squares are near-vent spatter agglutinate (17GT10), red filled triangles are near-vent lava flow (17GT8), orange filled squares are near-vent lava flow (GCPS0701), yellow filled circles are lava flow terminus (GCPS0710), and purple open circles are near-vent spatter agglutinate (GCPS0703). The three GCPS data are from Browne et al. (2017a). 30

Figure 13. Sample locations from GC from this study and Browne et al. (2017a). Light blue unfilled squares are near-vent spatter agglutinate (17GT10), red filled triangles are near-vent lava flow (17GT8), orange filled squares are near-vent lava flow (GCPS0701), yellow filled circles are lava flow terminus (GCPS0710), and purple open circles are near-vent spatter agglutinate (GCPS0703). The three GCPS data are from Browne et al. (2017a). 31

Figure 14. $\delta^{18}O$ of olivine phenocrysts from BPVF and GTVF plotted against eruption ages. GTVF values are outlined (dashed line). Fields for MORB olivine and Sierra Nevada granodiorite whole rock $\delta^{18}O$ values are shown in green and orange, respectively. GTVF samples include LWC (filled black squares), SFC (filled orange diamonds), TC (filled green circles), GC (filled red triangles), PC (empty purple squares), QC (empty dark blue circles), and AC (empty light blue triangle). Previous $\delta^{18}O$ values of olivine phenocrysts obtained by Vazquez (2009) are also shown: LWC is black "x" with vertical line, TC is green horizontal dash, PC is empty purple diamond, and BP peridotite xenolith is dark red cross. 33

Figure 15. $^{87}Sr/^{86}Sr$ vs $^{143}Nd/^{144}Nd$ for GTVF, BPVF, and other surrounding volcanic fields and Sierran rocks (from Putirka et al., 2012a). LWC (black filled squares), SFC (orange filled diamonds), TC (green filled circles), GC (red filled triangles), BPVF

(purple empty squares), Coso Volcanic Field (red empty triangles). All other fields are denoted by colors and the appropriate labels. BPVF data are from Blondes et al., 2008. CVF data are from Bacon et al., 1984 and Groves, 1996. 35

LIST OF APPENDICES

APPENDIX A: Olivine phenocryst core compositions by EMPA 50

APPENDIX B: Normalized olivine phenocryst core compositions by EMPA 83

APPENDIX C: BSE images and EMPA analysis locations 115

INTRODUCTION

Volcanic activity typically results in the formation of large individual volcanoes that erupt several times over their lifetime or as "volcanic fields", which are characterized as areas with several closely spaced volcanoes. Volcanoes that occur in volcanic fields are often small (<1 km^3) cinder cones with lava flows that were produced through single and relatively short-lived eruptions (i.e., days to a few years) of basalt magma, although some volcanic fields may also contain small rhyolite lava domes. Some volcanic fields contain hundreds of small basaltic and rhyolite volcanoes scattered over ~5,000 km^2 (e.g., San Francisco Volcanic Field, northern Arizona), whereas other volcanic fields are composed of small basaltic and rhyolite volcanoes that are situated along linear chains that follow faults (e.g., the Coso and Big Pine Volcanic Fields, eastern California). Because volcanic fields represent both a valuable natural resource in terms of potential geothermal energy production and a natural hazard in terms of dangerous volcanic activity, investigating volcanic fields is important to furthering our understanding of where and how these systems form and evolve.

One location where volcanic fields are widespread is near the tectonic boundary between the western edge of the Basin and Range Province and the eastern margin of the Sierra Nevada block in eastern California (Duffield et al., 1980; Valentine and Perry, 2007; Blondes et al., 2008; Browne et al., 2017a) (Figure 1). Contemporaneous volcanic fields at this tectonic boundary include the Big Pine Volcanic Field (BPVF), the Coso Volcanic Field (CVF), and the Golden Trout Volcanic Field (GTVF). Geologic mapping

and geochemical analyses of volcanic rocks combined with geophysical and geodetic measurements from both the BPVF and the CVF indicate that these volcanic fields are the product of extensional forces that thin the lithosphere and promote decompression-induced partial melting of the underlying mantle (Duffield et al., 1980; Luedke and Smith, 1981; Bacon, 1982; Bierman et al., 1991; Beard and Glazner, 1995; Dixon et al., 2000; Mordick and Glazner, 2006; Blondes et al., 2008; Slemmons et al., 2008; Phillips and Majkowski, 2011; Gazel et al., 2012; Putirka et al., 2012a). Findings from these studies conclude that magma that forms through decompression melting of the mantle then exploits weaknesses in the crust resultant of regional extensional stress, which allows magma to ascend along faults and erupt at surface.

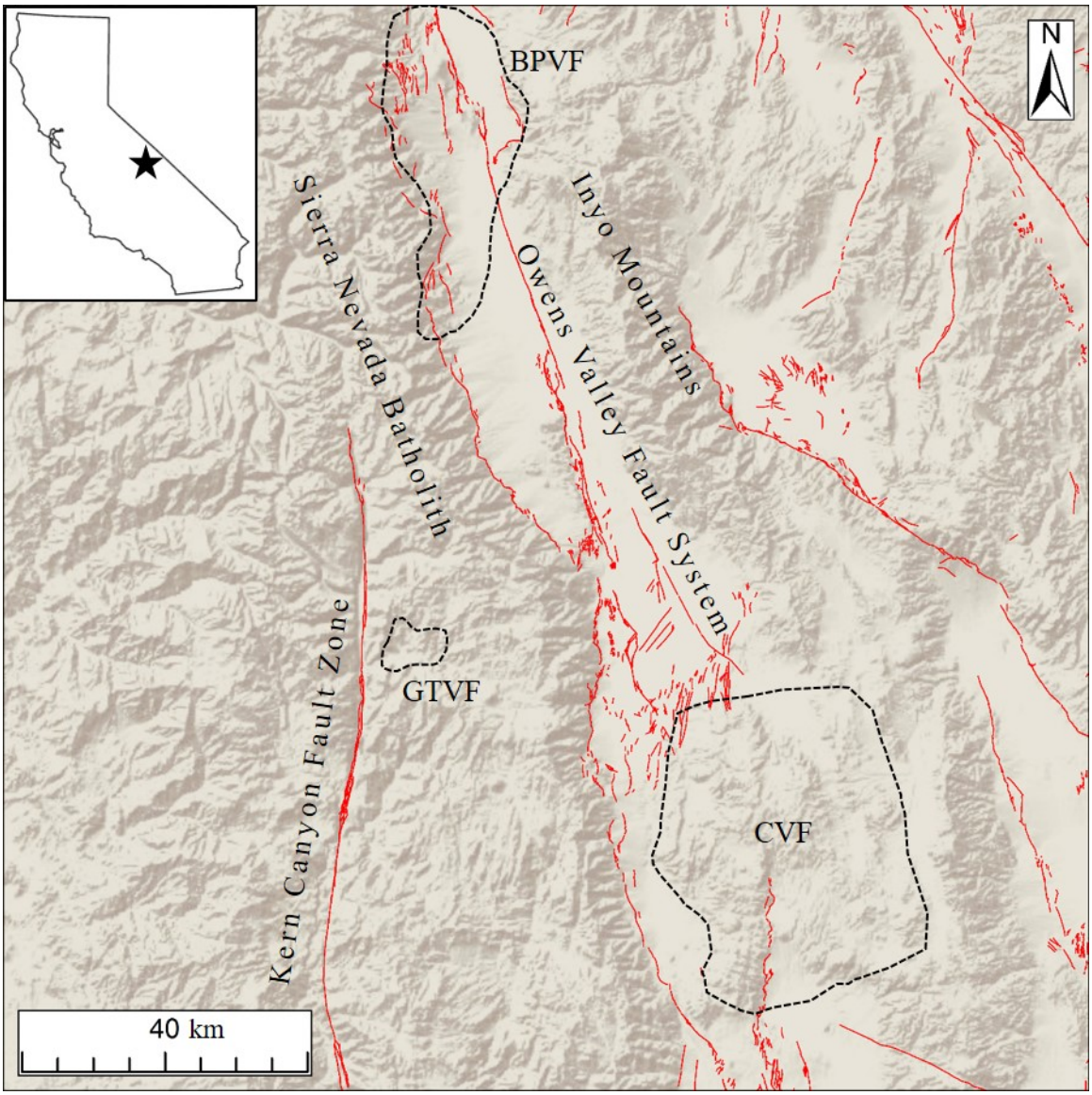

Figure 1. Regional map of southeastern California showing the locations of the GTVF, BPVF, and CVF (outlined with dashed lines) with active Quaternary faults shown as red lines.

The other volcanic field that occurs near the boundary between the western Basin and Range and the eastern Sierra Nevada is the Golden Trout Volcanic Field (GTVF),

which has received less scientific attention than the BPVF and CVF. However, geologic mapping and exploratory geochemical analyses of basaltic volcanic rocks from the GTVF indicate that it differs from the BPVF and CVF in several noteworthy ways. For example, the GTVF is the only recorded location of Quaternary volcanism within the Sierra Nevada block (Lawson, 1904; Knopf, 1918; Webb, 1950; Bacon and Duffield, 1981; Moore and Sisson, 1985), unlike the widespread occurrence of volcanic fields to the east in the Basin and Range (Figure 2). Another difference is that the number of vents, size of the volcanic field, and eruption rate of the GTVF are an order of magnitude lower than the BPVF and CVF (Browne et al., 2017a) (Table 1). Finally, unlike volcanoes in the BPVF and the CVF, volcanoes in the GTVF are not aligned along linear chains nor are they displaced by faulting (Lawson, 1904; Knopf, 1918; Webb, 1950; du Bray and Dellinger, 1981; Moore and Sisson, 1985; Browne et al., 2017a).

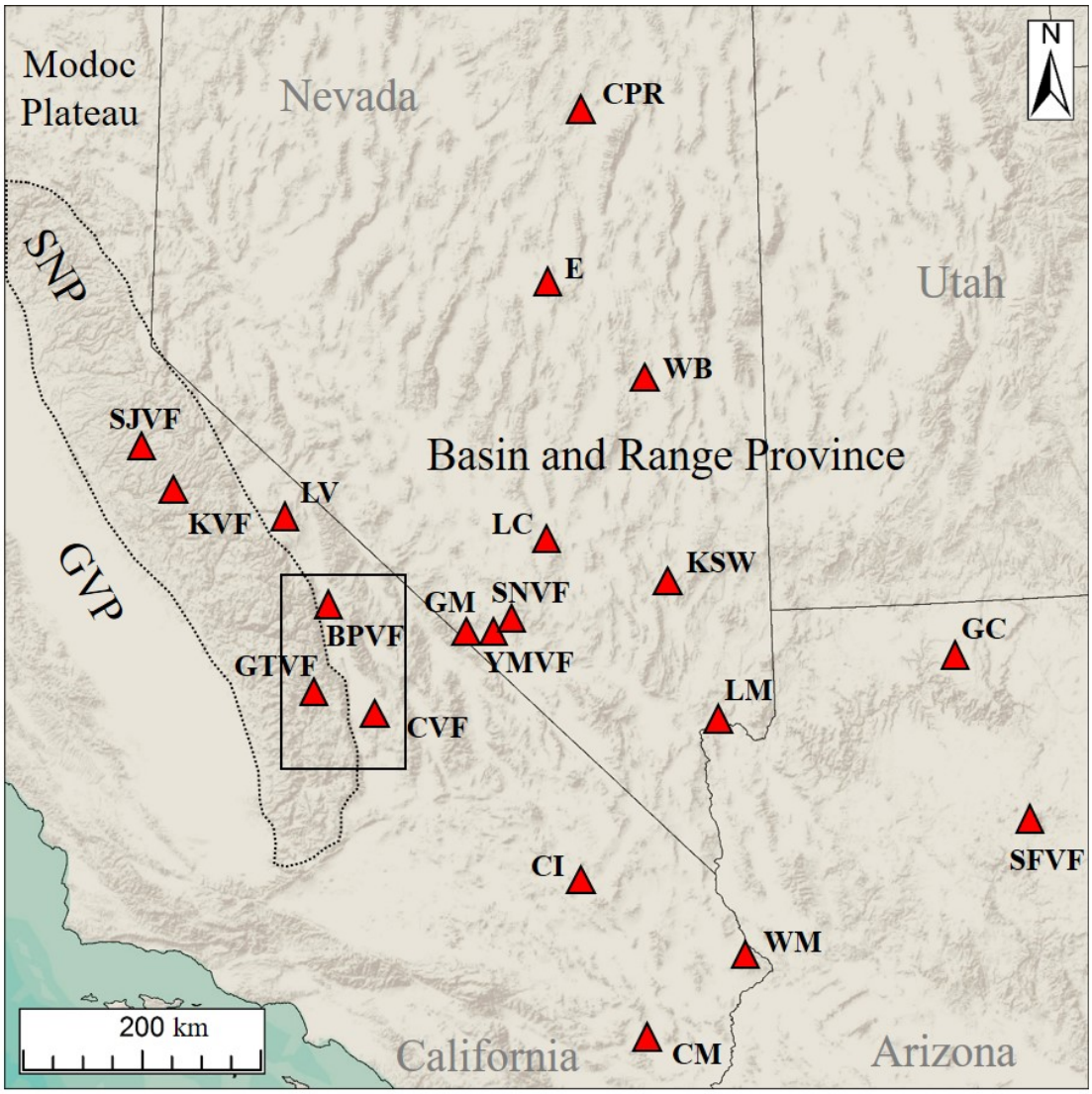

Figure 2. Regional map of the southwestern United States showing the locations of Basin and Range volcanic fields (red triangles) and the relative physiographic provinces of the area (SNP = Sierra Nevada Province; GVP = Great Valley Province). CM – Chocolate Mountains; CPR – Carl Piñon Range; E – Eureka; GC – Grand Canyon Volcanics; GM – Grapevine Mountains; KSW – Kane Springs Wash; LC – Luna Crater; LM – Lake Meade; LV – Long Valley; R-C – Raton-Clayton Volcanic Field; SFVF – San Francisco

Volcanic Field; SNVF – Southern Nevada Volcanic Field; WB – Windous Butte; WM – Whipple Mountains; YMVF – Yucca Mountain Volcanic Field. The black rectangle outlines the locations of the GTVF, BPVF, and CVF. Locations of volcanic fields are from Putirka et al. (2012b).

Table 1. Physical characteristics of Quaternary volcanic fields located in eastern California (modified from Browne et al., 2017a). Data sources for CVF: Duffield et al. (1980) and Bacon (1982). BPVF: Omerod et al. (1991), Turrin and Gillespe (1986), Blondes et al. (2008), Woolford (2009), and Vazquez and Woolford (2015). GTVF: Webb (1950), Bacon and Duffield (1981). du Bray and Dellinger (1981), Moore and Sisson (1985), and Browne et al. (2017a).

Volcanic Field	Mafic Vents	Felsic Vents	Area (km^2)	Age Range (Ma)	Eruption Rate	Vents per Year
CVF	54	38	1,200	2.0 – < 0.01	2.8 km^3/my	3 x 10^{-5}
BPVF	24	1	500	1.2 – 0.01	2.0 km^3/my	2 x 10^{-5}
GTVF	4	4	200	2.4 – < 0.01	0.1 km^3/my	0.5 x 10^{-5}

The goal of this thesis is to advance our understanding of why the eruption rate, which influences the number of vents and volcanic field size, in the GTVF is significantly lower compared to its two closest and contemporaneous volcanic fields – the BPVF and CVF. The following hypotheses will be tested in this thesis:

Hypothesis #1: The eruption rate of the GTVF is significantly lower than its contemporaneous and neighboring volcanic fields because the mantle source from which GTVF magma originates is different than the mantle source that underlies the BPVF and CVF.

Hypothesis #2: The eruption rate of the GTVF is significantly lower than its contemporaneous and neighboring volcanic fields because magmas ascend through thicker crust with fewer pathways (e.g., faults) than magma in the BPVF and CVF. More specifically, thicker and unfaulted crust in the GTVF promote more crustal

contamination, storage, and differentiation while also limiting ascent from a mantle source to the surface.

To test hypothesis #1, I measured radiogenic and stable Sr and Nd isotope concentrations from the most "mafic" (i.e., least contaminated) rock samples of each GTVF vent to precisely fingerprint its mantle source. Rb-Sr and Sm-Nd systems were used because they are reliable indicators widely used to characterize the mantle source of igneous rocks due to relative compatibility between stable isotopes and the radiogenic daughter isotopes produced from each system (e.g., Rollinson, 1993; White, 2013). Moreover, isotope ratios in magmas remain unchanged by subsequent crystallization events because mass differences between isotopes are so small that the isotopes are not fractionated (e.g., Rollinson, 1993). The Rb-Sr system is useful because Rb is more incompatible in the mantle than Sr, which causes continental crust to become enriched in Rb over time as prolonged partial melting of the mantle occurs. Moreover, because radioactive ^{87}Rb decays to ^{87}Sr, the ratio between radiogenic ^{87}Sr and stable ^{86}Sr will be higher for rocks that formed in the continental crust than rocks that formed in the mantle (Figure 3).

The Sm-Nd system is useful because Sm is more compatible than Nd in the mantle, which causes the continental crust to become depleted in Sm over time as prolonged partial melting of the mantle occurs. As a result, radiogenic ^{143}Nd is produced in greater amounts in the mantle than in the crust as ^{147}Sm decays. The ratio between ^{143}Nd and the stable isotope ^{144}Nd is used to compare the composition of the mantle

source from which an igneous melt originated. Figure 3 and Figure 4 show how $^{87}Sr/^{86}Sr$ vs. $^{143}Nd/^{144}Nd$ ratios can be used to relate different mantle sources. Figure 4 utilizes the common εSr and εNd rather than the ratios from Figure 3 to show source differentiation relative to the composition of Bulk Silicate Earth. These notations indicate that the $^{87}Sr/^{86}Sr$ and $^{143}Nd/^{144}Nd$ ratios have been normalized to a standard, conventionally the Chondritic Uniform Reservoir (CHUR) isotopic composition (Equations 1 and 2).

$$(1)\ \varepsilon_{Nd} = \frac{\left(\frac{^{143}Nd}{^{144}Nd}\right) sample - \left(\frac{^{143}Nd}{^{144}Nd}\right) CHUR}{\left(\frac{^{143}Nd}{^{144}Nd}\right) CHUR}\ x\ 10{,}000$$

$$(2)\ \varepsilon_{Sr} = \frac{\left(\frac{^{87}Sr}{^{86}Sr}\right) sample - \left(\frac{^{87}Sr}{^{86}Sr}\right) CHUR}{\left(\frac{^{87}Sr}{^{86}Sr}\right) CHUR}\ x\ 10{,}000$$

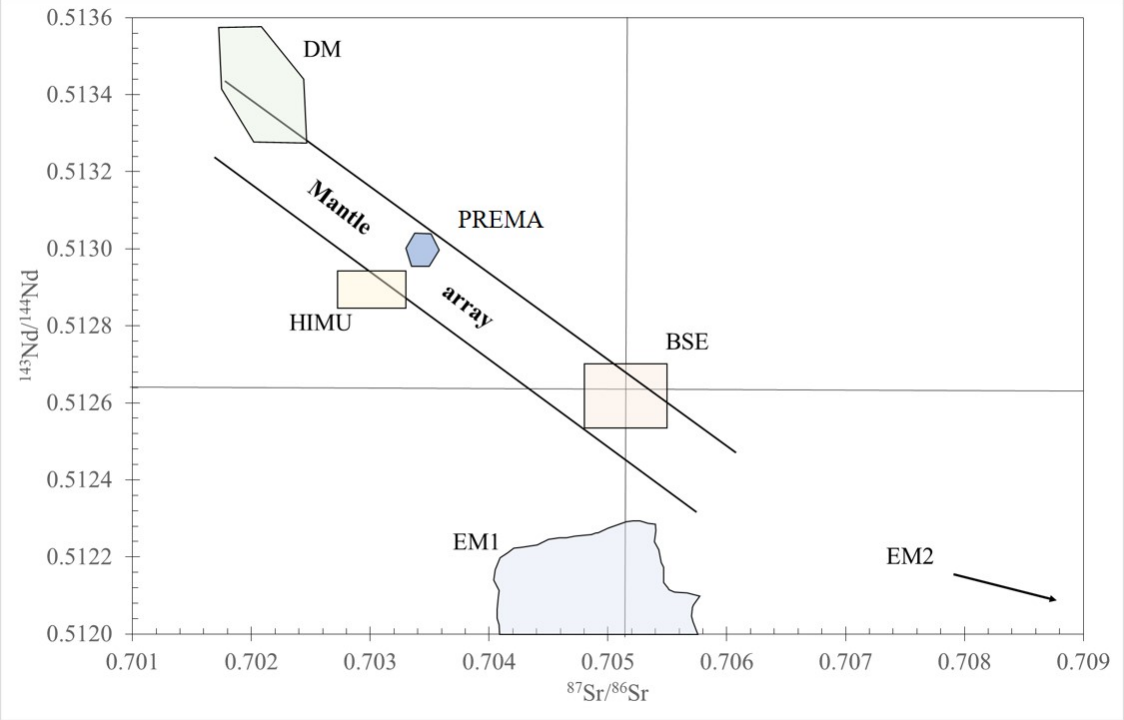

Figure 3. $^{87}Sr/^{86}Sr$ and $^{143}Nd/^{144}Nd$ ratios showing the corresponding compositions of mantle values: DM refers to depleted mantle, PREMA refers to prevalent mantle reservoir, HIMU refers to mantle with high U/Pb ratio, BSE refers to bulk silicate earth, and EM1 and EM2 refer to enriched mantle compositions with EM1 having low $^{87}Sr/^{86}Sr$ and EM2 high $^{87}Sr/^{86}Sr$ (Adapted from Rollinson, 1993).

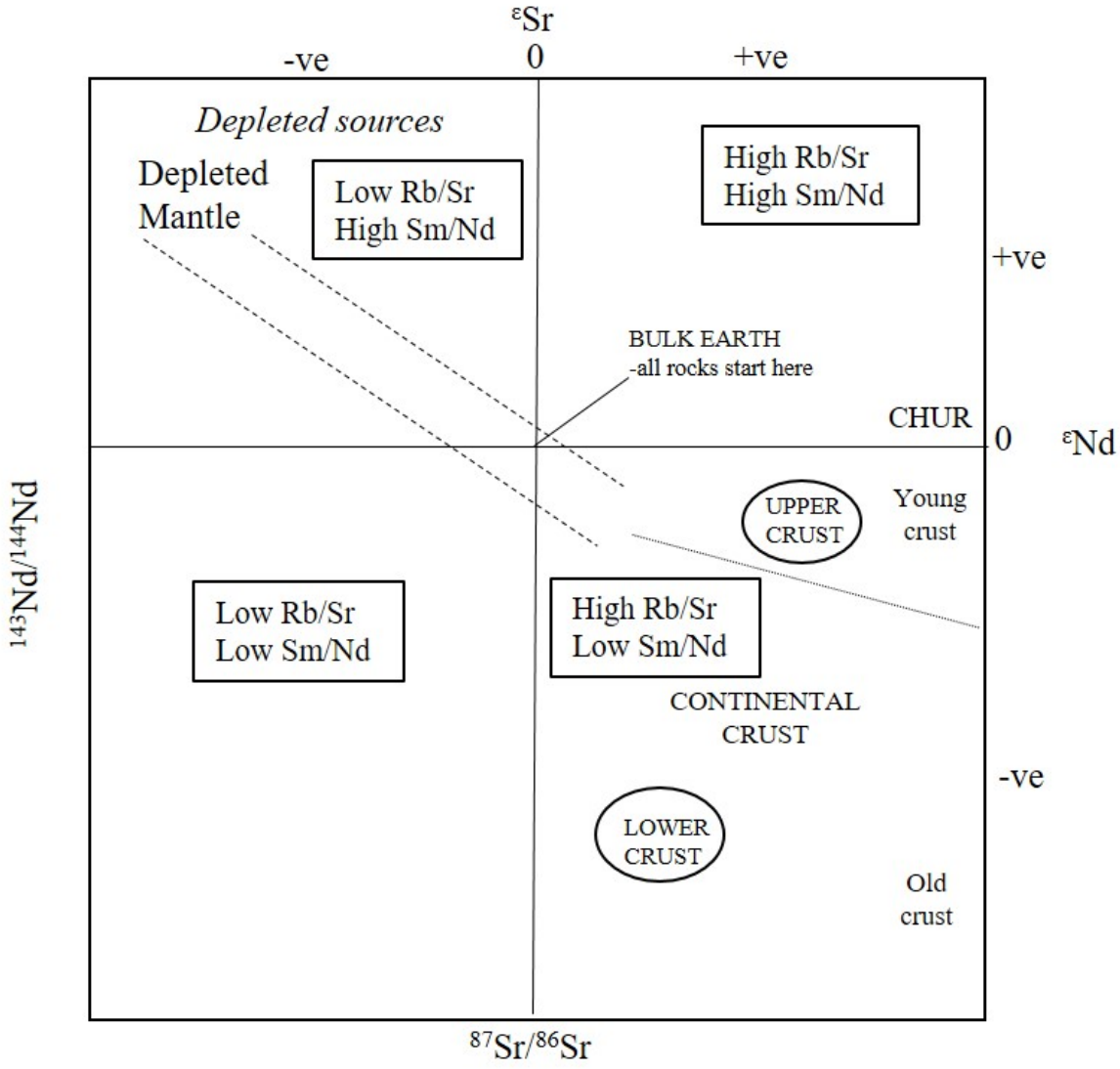

Figure 4. Relative isotopic compositions of different regions of the Earth (Adapted from Rollinson, 1993).

Major and trace element concentrations of olivine phenocrysts – coupled with oxygen isotope concentrations of olivine phenocrysts – from lava flows in the GTVF were analyzed in order to test Hypothesis #2. Major and trace element compositions of

phenocrysts are records of the crystallization conditions (e.g., melt composition, pressure, and temperature) at which they originally nucleated and grew and therefore are used as recorders of mantle source and magmatic differentiation during ascent. Olivine in particular is utilized here because it is the best recorder of the original magma (melt) composition that formed by partial melting of the mantle due to it being one of the very first crystallizing phases. Olivine compositions are also more homogeneous in mantle rocks compared to other mantle minerals, like garnet, spinel, clinopyroxene, and orthopyroxene (De Hoog et al., 2010). Because trace element diffusion in olivine is relatively fast at magmatic temperatures, only compositions of the cores of olivine phenocrysts (not rims) are utilized in this study in order to avoid the effect of changing melt compositions during magma evolution (De Hoog et al., 2010).

Stable oxygen isotope compositions of olivine phenocrysts from each vent are used here to measure crustal contamination between vents and over time in both the GTVF and BPVF. Olivine phenocrysts are used to measure crustal contamination because they are one of the earliest crystallizing phases and the time of disequilibria between olivine-glass will be reflected by elevated $\delta^{18}O$ values (Eiler, 1997 and 2001). The ratio of $^{18}O/^{16}O$ in igneous rocks is commonly normalized to the Standard Mean Ocean Water (SMOW) ratio and expressed as $\delta^{18}O$ (Equation 3).

$$(3)\ \delta^{18}O = \left[\frac{^{18}O/^{16}O\ (sample) - \ ^{18}O/^{16}O\ (standard)}{^{18}O/^{16}O\ (standard)}\right] x\ 1000$$

Oxygen isotopes provide an opportunity to determine whether a magma is still in equilibrium with the mantle from which it was generated or if it assimilated crust during ascent to the surface (Figure 5; Bindeman, 2008a; Bindeman et al., 2008b; Auer et al., 2008;). This is because in general, continental crust is enriched in $\delta^{18}O$ compared to the mantle due to the long interaction of continental crust with the hydrosphere (Rollinson, 1993).

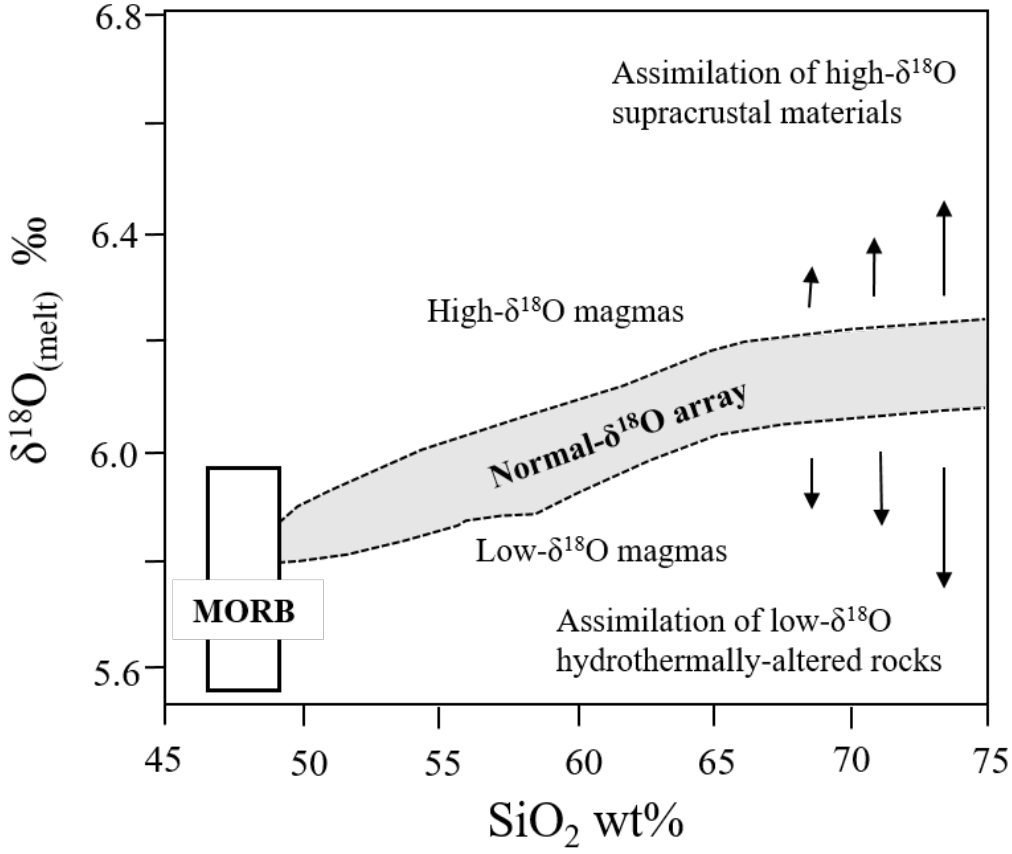

Figure 5. $\delta^{18}O$ vs SiO_2 wt % for basaltic melt compositions. Normal-$\delta^{18}O$ array determined experimentally for closed system differentiation. High-$\delta^{18}O$ and Low-$\delta^{18}O$

magmas that plot outside of this array require contamination by materials with different $\delta^{18}O$ values from the basaltic melt (adapted from Bindeman, 2008a).

The Sierra Nevada province extends from the Modoc Plateau and southern Cascades in northeastern California down to the Mojave Desert in southeastern California (Figure 2). The Sierra Nevada is bound by the Great Valley Province of central California to the west and by the Basin and Range Province to the east. The west side of the Sierra Nevada slopes relatively gently toward the Great Valley. In contrast the east side of the Sierra Nevada drops steeply to the valleys of the western Basin and Range province. At the eastern boundary transtensional faulting in the form of the Eastern California Shear Zone separates the Sierra Nevada from the Basin and Range province (Unruh et al., 2003). The Sierra Nevada batholith formed largely between 130 and 80 Ma (Evernden and Kistler, 1971; Chen and Moore, 1982; Saleeby et al., 1987; Bateman, 1992; Coleman et al., 2004; Paterson et al., 2011) and is characterized by >2,000-m-tall peaks of Mesozoic granitic rocks that have been carved by subsequent glaciation.

Volcanism within the southern Sierra Nevada is scarce relative to physiographic provinces like the Cascades or the Basin and Range, but examples exist in the southern Sierra Nevada in the Kern Volcanic Field (Figure 2; Manley et al., 2000; Putirka and Busby, 2007) and in the GTVF (Browne et al., 2017a). Different mechanisms have been proposed for Cenozoic volcanism in the Sierra Nevada Province. Ducea and Saleeby (1998) and Manley et al. (2000) argue that lithospheric delamination of an eclogitic root beneath the Sierra Nevada occurred between ~3.5 and 7 Ma, which resulted in an

upwelling of asthenospheric mantle that generated primitive and potassium-rich magmas that erupted in the central and southern Sierra Nevada (Moore and Dodge, 1980; Van Kooten, 1980; Van Kooten, 1981). Alternatively, Gazel et al. (2012) and Putirka et al. (2012a) propose that rather than delamination, lithospheric "degradation" caused Quaternary volcanism in the southern Sierra Nevada. This model relates to the opening of a slab window after the passage of the Mendocino Triple Junction approximately 12 Ma. The main cause for lithospheric degradation is the regional extension of the lithosphere throughout the Basin and Range. The presence of degraded lithosphere beneath the GTVF would suggest that regional extension may have affected the Sierra Nevada, despite it being considered a relatively competent block. Thus, an understanding of the source and petrologic evolution of the GTVF provides an opportunity to contribute to the discussion about the mechanism for this Quaternary volcanism in the southern Sierra Nevada.

The Basin and Range province exists through much of the western United States and northern Mexico. It is characterized by 'horst' and 'graben' topography or tilted blocks with these ridge-valley combinations bound by normal and transtensional faults on either side (Figure 2; Stewart, 1971; Eaton, 1982). Quaternary volcanism within the Basin and Range is another result of the extensional tectonics throughout the region (Valentine and Perry, 2007). Multiple volcanic fields produced as a result of these extensional tectonics formed in and near the Owens Valley east of the Sierra Nevada including Big Pine, Coso, and Cima Volcanic Fields (Duffield, 1980; Wilshire et al., 2002; Blondes et al., 2008).

The Eastern California Shear Zone accommodates approximately 25% of the Pacific and North American relative plate motion (McClusky et al., 2001). North of the Garlock Fault this motion is dextral transtensional and distributed over several fault systems including the Owens Valley Fault Zone (OVFZ). The north-northeast-striking OVFZ is located within Owens Valley and displaces the BPVF. It has experienced a minimum average dextral slip-rate of ~2.8 mm/yr during the Late Pleistocene and perhaps as much as 4.5 mm/yr since 55 ka (Kirby et al., 2008). In addition to the dextral-oblique slip of 4.6 ± 0.5 mm/yr, the divergent fault-perpendicular component of movement along the OVFZ is estimated at approximately 2.6 ± 0.6 mm/yr (McClusky et al., 2001). This rate of divergence supports the model for magma production in the BPVF resulting from decompression of the underlying mantle.

The Kern Canyon fault – located about 7 km west of the GTVF – is a 130 km long series of sub-vertical north-striking faults located approximately 30 km west of the Eastern California Shear Zone (Figure 1; Nadin and Saleeby, 2010). It formed in the Cretaceous as a dextral transpressive ductile shear zone that translated up to approximately 12 km of dextral displacement progressively from 80–95 Ma between emplaced plutons (Nadin and Saleeby, 2008). The Kern Canyon fault was then reactivated in the Miocene as a dextral transtensional zone coinciding with southern Sierra extension and volcanism in the KVF (Nadin and Saleeby, 2008). Although seismically quiet, evidence for Quaternary activity along the Kern Canyon fault as an east-side down extensional structure (Nadine and Saleeby, 2010; Brossy et al., 2012) includes a Tioga (~18ka) moraine displaced ~2.8 m at Soda Spring, about 6 km east of

the GTVF (Brossy et al., 2012). No GTVF deposits show evidence of faulting (Bacon and Duffield, 1981; Moore and Sisson, 1985; Browne et al., 2017a).

The GTVF is located on the Kern Plateau approximately 25 km south of Mt. Whitney and 60 km southwest of BPVF in the southern Sierra Nevada at an average elevation of 2,600 m (Figure 1). It contains 8 total vents, 4 of which are mafic scoria cones with associated lava flows and 4 that are felsic lava domes. The felsic vents are not addressed in this study. The 4 mafic vents at GTVF are Little Whitney Cone (LWC), South Fork Cone (SFC), Tunnel Cone (TC), and Groundhog Cone (GC) (Figure 6). Moore and Lamphere (1983) obtained whole rock K-Ar ages for LWC of 743,000 ± 11,000 BP and 176,000 ± 21,000 BP for SFC. There are no radiogenic ages for TC, but Moore and Lamphere (1983) argue it is nearly contemporaneous with SFC based on paleomagnetic measurements. However, results of geochemical analyses show clear differences in some major and trace element compositions of TC and SFC, which call the assumed contemporaneous ages of the vents into question (Browne et al., 2017a). Deposits from GC are unglaciated, which Moore and Sisson (1981) interpreted to reflect a Holocene age, but ^{36}Cl cosmogenic dating of olivine in GC lavas indicate a Pleistocene eruption age ranging between 27 and 59 ka (Browne et al., 2017b). Whole rock compositions of mafic eruptions from GTVF range from olivine basalt to olivine basaltic andesite and exhibit Hawaiian to Violent Strombolian eruption styles (Figure 8; Browne et al., 2017a). No Quaternary faults have been identified in GTVF in contrast to contemporaneous volcanic fields like the BPVF and CVF where vents are often aligned

on north-south striking normal faults and deposits are offset (Duffield et al., 1980; Bacon and Duffield, 1981; Vazquez and Woolford, 2015).

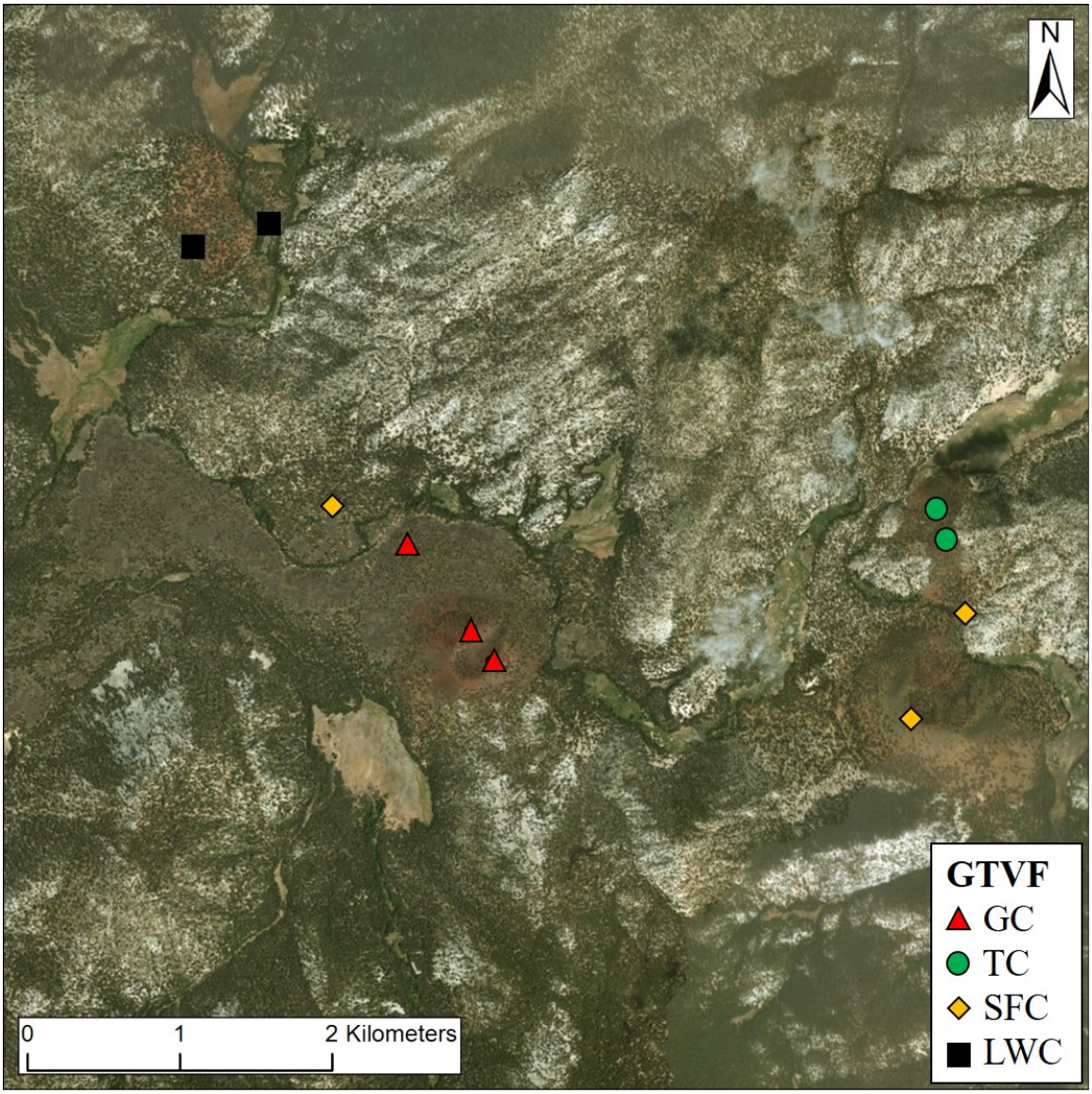

Figure 6. Sample locations from each of the four mafic vents of the GTVF. LWC samples are solid black squares. SFC samples are solid orange diamonds. TC samples are solid green circles. GC samples are solid red triangles.

BPVF is located within the Owens Valley graben at an elevation of about 1200 m. (Figure 1). It has at least 24 mafic vents and 1 felsic rhyolite dome (Blondes et al., 2008). Of these 24 mafic vents, 3 vents were selected for sampling based on their approximate contemporaneous age with vents in the GTVF: Papoose Canyon (PC), Quarry Cone (QC), and Armstrong Canyon (AC) (Figure 7). Blondes et al. (2008) determined $^{40}Ar/^{39}Ar$ ages for PC of 760.8 ± 22.8 ka and for QC of 90.5 ± 17.6 ka. Vazquez and Woolford (2015) acquired a ^{36}Cl age for Armstrong Canyon of 17.1 ± 1.4 ka assuming 1 mm of erosion per 1,000 years. Vents in BPVF are generally aligned along north or northwest striking normal faults where scoria cones and local tephra deposits were emplaced (Duffield et al., 1980; Bacon and Duffield, 1981; Vazquez and Woolford, 2015). Whole rock compositions of the BPVF range from olivine basalt to alkali olivine basalt; many lavas host peridotitic xenoliths (Figure 8; Blondes et al., 2008; Gazel et al., 2012). Compositions of xenoliths suggest a relatively shallow mantle source and the absence of an eclogitic root beneath the field (Gazel et al., 2012).

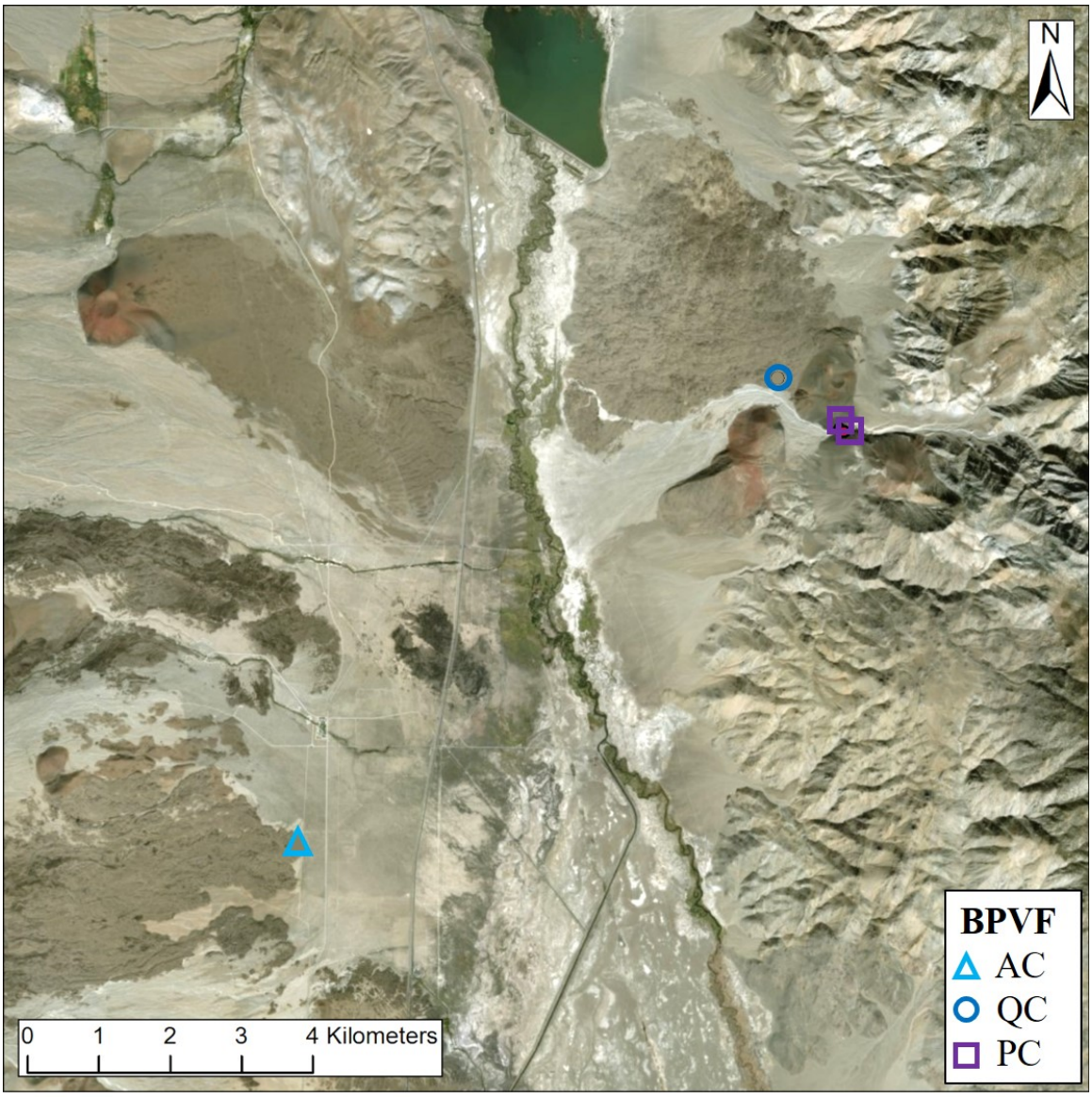

Figure 7. Sample locations from 3 mafic vents of the BPVF. PC samples are open purple squares. QC samples are open blue circles. AC samples are open light blue triangles.

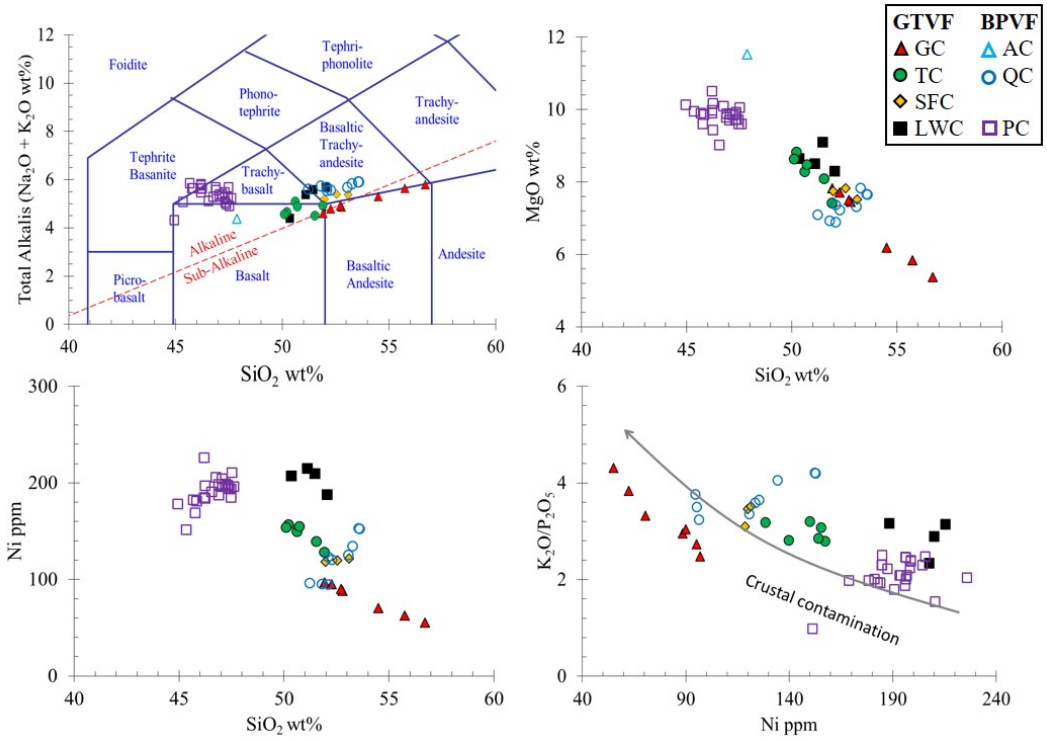

Figure 8. Whole rock compositions of samples from the GTVF and BPVF acquired using XRF. GTVF samples are from LWC (filled black squares), SFC (filled orange diamonds), TC (filled green circles), GC (filled red triangles). BPVF samples are from PC (open purple squares), QC (open dark blue circles, and AC (empty light blue triangle). GTVF data are from Browne et al. (2017a). BPVF data are from Blondes et al. (2008) and Vazquez and Woolford (2015).

METHODS

Fresh rock samples from proximal and distal locations at each of the four mafic GTVF vents were collected in July, 2017. Rock samples from three similarly aged mafic vents at BPVF were also collected during this time. Dense (vesicle-poor) samples of lava flows and spatter agglutinate were selected so as to maximize the concentration of olivine phenocrysts. Polished thin sections were prepared from each of the 14 samples, which were utilized for electron microprobe analyses. Descriptions of sample preparation and analysis of major and trace element mineral compositions, stable oxygen isotope measurements, and Sr and Nd radiogenic isotope measurements are described below.

Thin sections from 8 samples were analyzed for major (Si, Fe, Mg)- and trace- (Ni, Mn, Ca, Cr, Al, P) element compositions of olivine phenocrysts from both GTVF and BPVF. The raw and normalized analyses are available in Appendices A and B, respectively. These analyses were performed on a CAMECA SX 100 electron microprobe equipped with five wave-length-dispersive spectrometers (WDS) in the Electron Microprobe Laboratory at Oregon State University. The five analyzer crystals, paired with detectors, used for analysis are listed in order and were calibrated using the following standards: Spectrometer 1 was a thallium acid phthalate (TAP) crystal calibrated to detect Si with Olivine USNM 2256 and Al with Labradorite USNM 115900. Spectrometer 2 was a large thallium acid phthalate (LTAP) crystal calibrated to detect Mg with Olivine USNM 2256 and P with Fluorapatite USNM 104021. Spectrometer 3 was a large pentaerythritol (LPET) crystal calibrated to detect Cr with Chromite USNM

117075. Spectrometer 4 was a lithium fluoride (LIF) crystal calibrated to detect Mn with Pyroxmangite Engi (Hoos E.T.H., Zurich) reference # 245, Fe with Olivine USNM 2256, and Ni with a Ni-Si Mineral Mount from the University of Maryland made by Astimex Scientific Ltd. Spectrometer 5 was a pentaeythritol (PET) crystal calibrated to detect Ca with Augite USNM 122142 and Cr with Chromite USNM 117075.

Olivine phenocryst cores were analyzed using 15 keV accelerating voltage, 50 μA beam current, and 1 μm beam diameter. Count times varied from 20 to 90 s depending on the element and desired detection limit. For all analyses, zero-time intercept functions were applied to reduce the effects of alkali migration. Back scattered images (BSE) of all analyzed phenocrysts were taken on the same instrument using the CAMECA Peak Site software and are available with analysis point locations in Appendix C.

Samples from each vent at GTVF and BPVF were mechanically crushed with a Bico WD Chipmunk Jaw Crusher in the Mineral Separation Laboratory at Humboldt State University. Samples were then sieved to a 300 micron to 2 mm size fraction. Individual olivine phenocrysts from sieved samples were separated by hand under a specimen microscope. Depending on the size of phenocrysts, 1-20 olivine separates were picked for each sample to achieve a mass of 2-5 mg per sample. Oxygen isotope compositions of olivine separates for each sample were determined via laser fluorination at the Stable Oxygen Isotope Laboratory at the University of Oregon with a 35 W CO_2-laser (e.g., Bindeman 2008). Samples were reacted with BrF_5 reagent to liberate oxygen which was purified by being passed through a series of cryogenic traps and a mercury diffusion pump. The gas was then converted into CO_2 gas using a small platinum-graphite

converter. Oxygen isotope ratios of the gas were measured with a Finnigan MAT 253 mass spectrometer. The Gore Mountain Garnet (GMG, $\delta^{18}O = 5.75\ ^{o}/_{oo}$) and the San Carlos Olivine (SCO, $\delta^{18}O = 5.35\ ^{o}/_{oo}$) were used as standards. Analytical uncertainties for the oxygen isotope analyses are $\leq 0.1\ ^{o}/_{oo}$. Five analyses were run for GC and two analyses each for the other three GTVF vents. Two analyses were run for PC and one analysis each for the other two BPVF vents. Two additional analyses were run, one for TC and one for LWC, to check an anomalously high value at TC and for added constraint on the $\delta^{18}O$ of LWC.

One 100 mg sample of fresh rock chips from each of the four GTVF vents were powdered and dissolved into a mixture of double-distilled concentrate HNO_3 and HF and then dried on a hot plate at 80°C in the Radiogenic Isotope Laboratory at the University of Queensland. Once fluoride had been converted to nitrate, the dried residue was dissolved with 3 ml of 2N HNO_3 and 1.5 ml was loaded onto a stack of Sr-spec, Thru-spec, and LN-spec resin columns to separate Sr, Nd, and Hf from matrix. $^{87}Sr/^{86}Sr$ and $^{143}Nd/^{144}Nd$ ratios were measured in static mode on a Nu Plasma High Resolution Multi Collector Inductively Coupled Plasma Mass Spectrometer (HR MC-ICP-MS) using a modified CETAC ASX-110FR auto-sampler and a DSN-100 desolvating nebulizing system. Mass fractionation of the $^{87}Sr/^{86}Sr$ and $^{143}Nd/^{144}Nd$ ratios was corrected for by normalizing to $^{86}Sr/^{88}Sr = 0.1194$ and $^{146}Nd/^{144}Nd = 0.7219$, respectively. Instrumental drift was monitored and calibrated with SRM-987 Sr and a laboratory Nd-metal as standards.

RESULTS

Olivine Major and Trace Elements

Major and trace element compositions of olivine phenocryst cores from GTVF and BPVF are plotted on multi-element Harker diagrams in Figure 9 and Figure 10 and as histograms in Figure 11. Olivine from LWC are the most primitive of all samples in this study from the GTVF and BPVF in terms of both Fo (Fo = 100 * (Mg/(Mg+Fe)); 85.05 to 88.77) and NiO (0.149 to 0.474 wt%) concentrations. Olivine from both TC and SFC are intermediate in composition between LWC and GC with Fo values ranging from 80.90 to 88.43 and 76.19 to 87.47, respectively. NiO concentrations from TC and SFC are also intermediate, ranging from 0.102 to 0.295 wt% and 0.096 to 0.239 wt%, respectively. Olivine from spatter agglutinate (sample 17GT10) erupted from GC are characterized by Fo values of 78.72 to 87.75 and NiO values of 0.133 to 0.227 wt%. In contrast, olivine from the GC lava flow (sample 17GT8) have Fo values that range from 67.61 to 78.55 and NiO concentrations of 0.080 to 0.113 wt%. The range of olivine compositions at GC is shown in Figure 11. Major and trace element compositions of olivine phenocrysts from each of the three sampled vents at BPVF overlap with the compositions of olivine from GTVF vents.

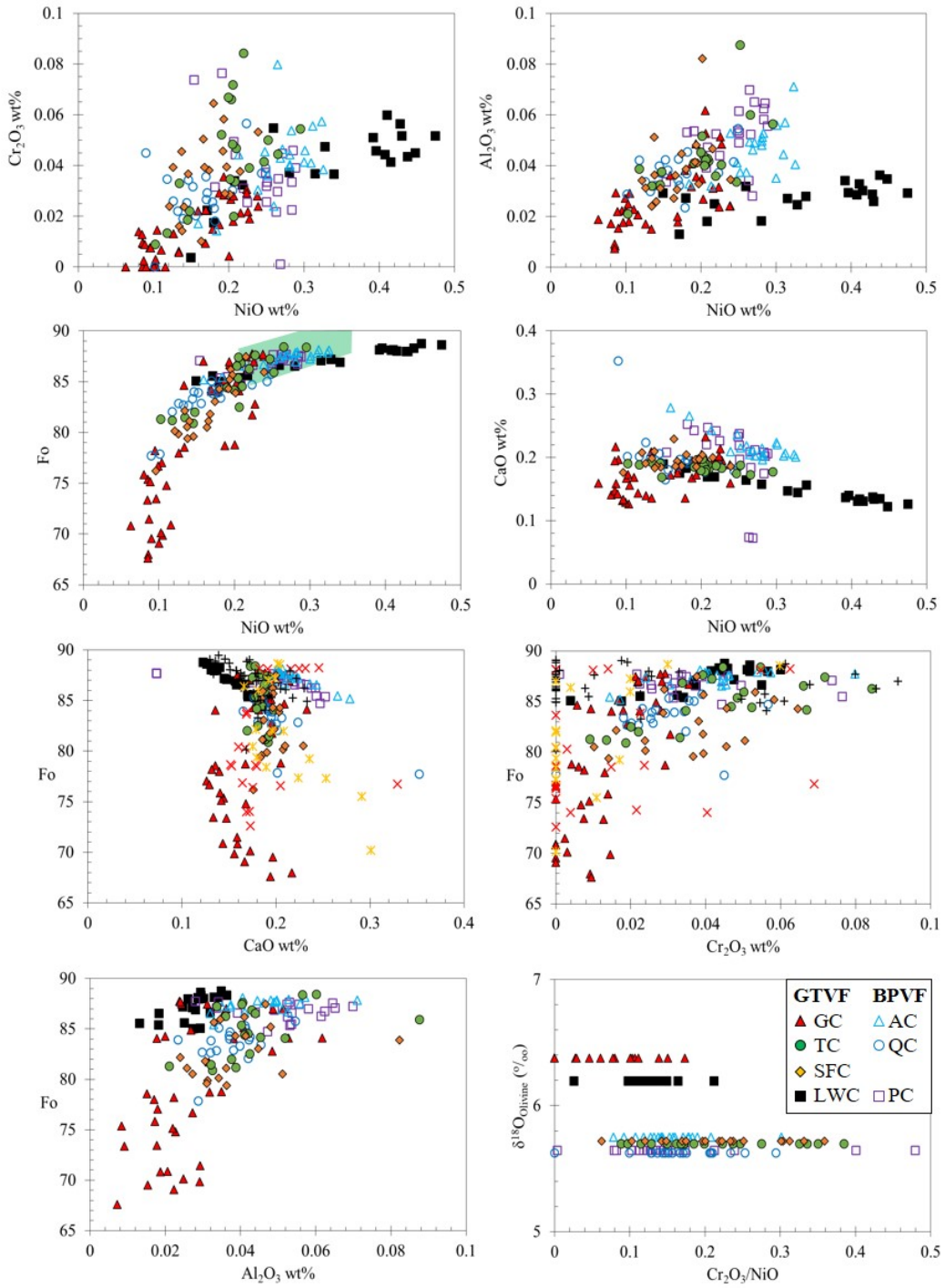
Cr2O3 wt%
NiO wt%
Al2O3 wt%
NiO wt%
Fo
NiO wt%
CaO wt%
NiO wt%
Fo
CaO wt%
Fo
Cr2O3 wt%
Fo
Al2O3 wt%
δ18OOlivine (‰)
Cr2O3/NiO
GTVF
BPVF
GC
AC
TC
QC
SFC
LWC
PC

Figure 9. Weight percent major and trace element compositions of olivine phenocrysts of GTVF and BPVF. GTVF samples include LWC (black filled squares), SFC (orange filled diamonds), TC (green filled circles), and GC (red filled triangles). BPVF samples include PC (open purple squares), QC (open dark blue circles), and AC (open light blue triangles). Previous work by Browne et al. (2017a) are shown with LWC (black crosses), SFC (orange x's with a vertical line), and GC (red x's). Green shaded field on Fo vs NiO plot is indicative of mantle olivine compositions after Takahashi (1985).

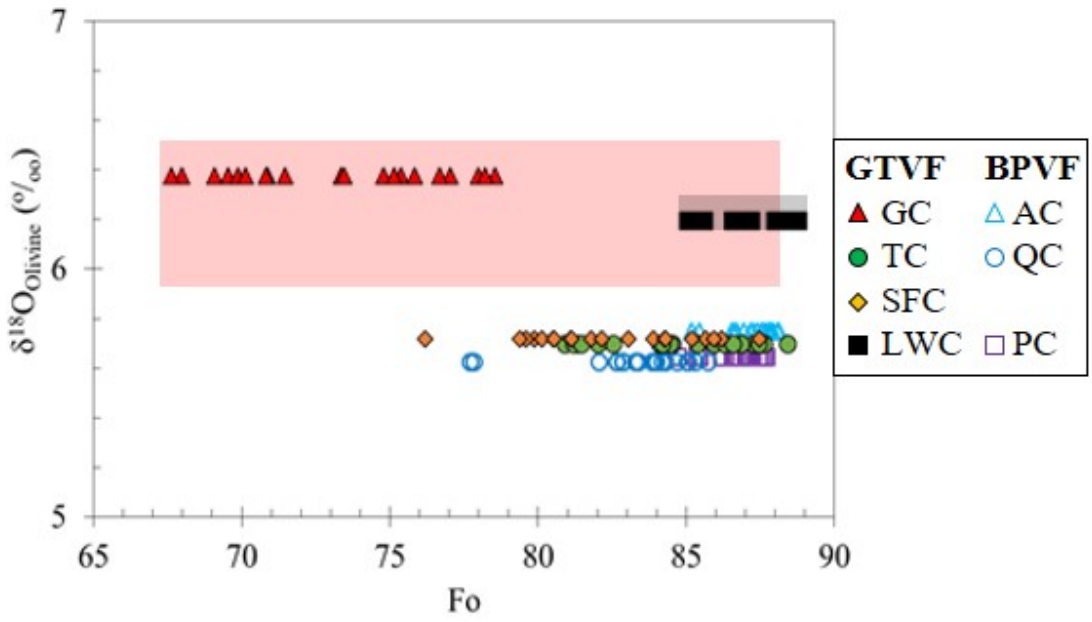

Figure 10. $\delta^{18}O$ values of olivine versus Fo content of olivine. Light red shaded field represents all values of $\delta^{18}O$ and Fo analyzed at GC although both data sets were not analyzed for all samples. GVFC samples include LWC (black filled squares), SFC (orange filled diamonds), TC (green filled circles), and GC (red filled triangles). BPVF

include PC (open purple squares), QC (open dark blue circles), and AC (open light blue triangles).

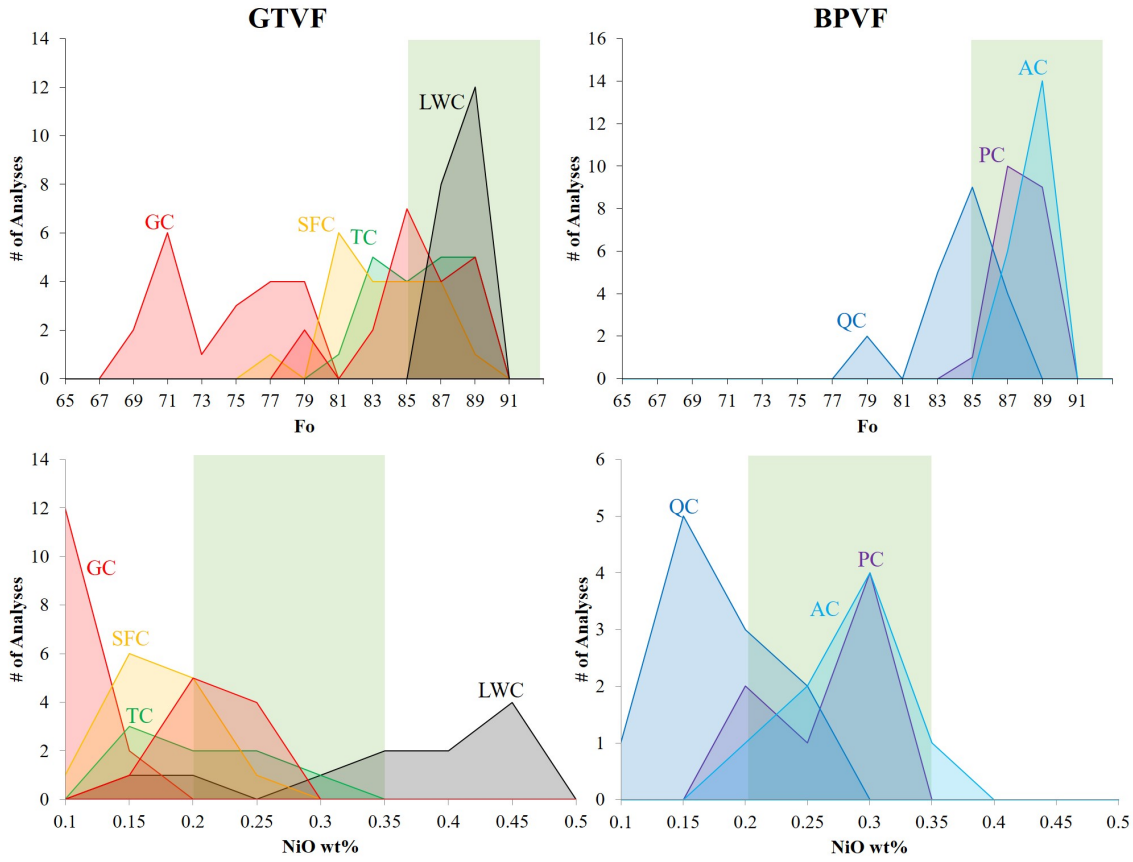

Figure 11. Histograms of Fo and NiO concentrations from samples collected from the GTVF and BPVF. Green rectangle represents mantle olivine concentrations from Takahashi (1985).

The significant range of olivine compositions at GC is compared with the values of three samples obtained by Browne et al. (2017a) in Figure 12. These data also share

the range of compositions presented in this study with olivine from a lava flow (GCPS0701) of a different lobe than 17GT8 overlapping with the spatter agglutinate of 17GT10. Additionally, olivine from a lava flow (GCPS0710) at the flow terminus and from a spatter agglutinate (GCPS0703) at the vent overlap with the most compositionally evolved lava flow of 17GT8 (Figure 13). In terms of Fo, olivine from GC lava flows range from 67.61 to 88.21 and olivine from GC spatter agglutinate range from 74.26 to 87.75.

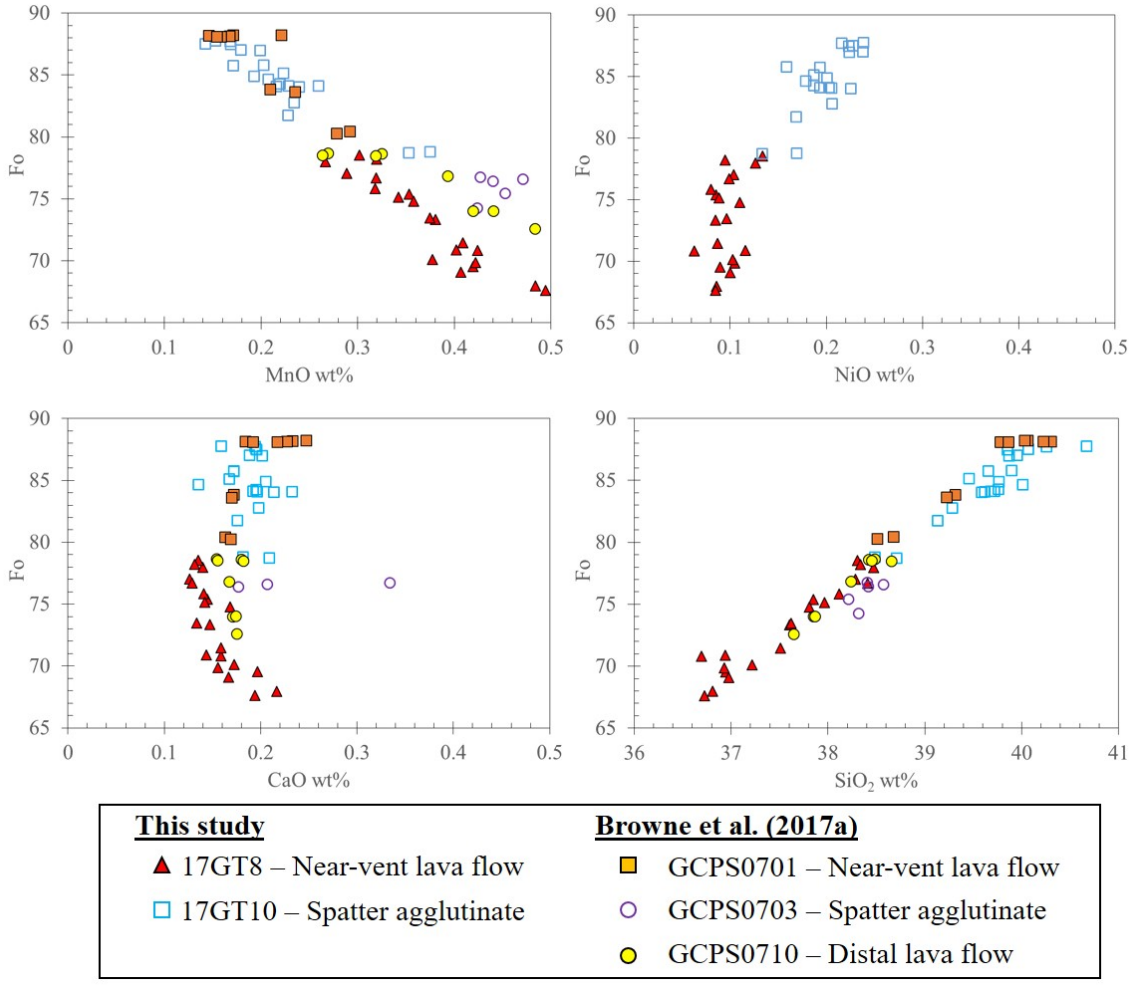

Figure 12. Olivine phenocryst core compositions from five samples at GC. Light blue unfilled squares are near-vent spatter agglutinate (17GT10), red filled triangles are near-vent lava flow (17GT8), orange filled squares are near-vent lava flow (GCPS0701), yellow filled circles are lava flow terminus (GCPS0710), and purple open circles are near-vent spatter agglutinate (GCPS0703). The three GCPS data are from Browne et al. (2017a).

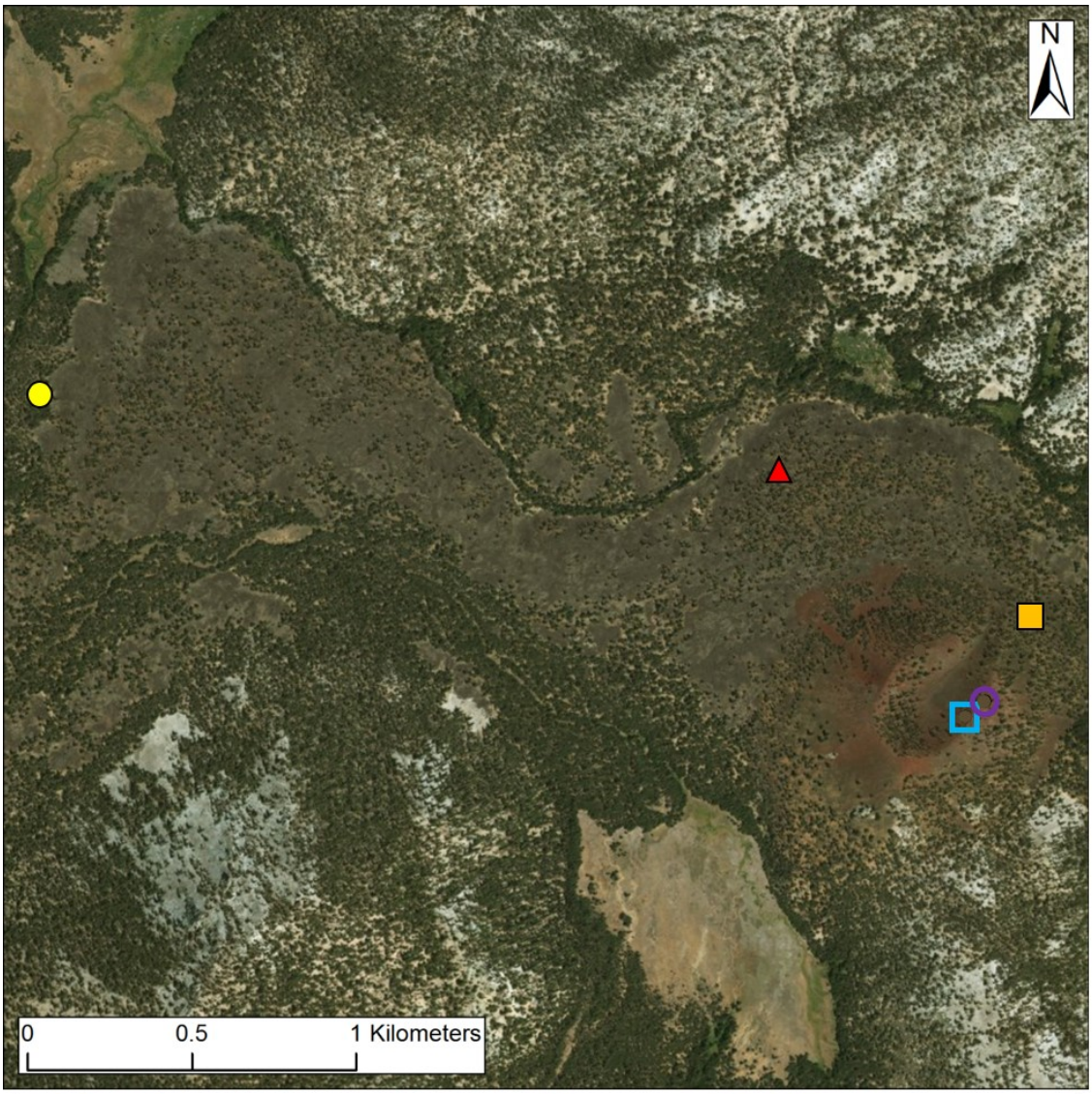

Figure 13. Sample locations from GC from this study and Browne et al. (2017a). Light blue unfilled squares are near-vent spatter agglutinate (17GT10), red filled triangles are near-vent lava flow (17GT8), orange filled squares are near-vent lava flow (GCPS0701),

yellow filled circles are lava flow terminus (GCPS0710), and purple open circles are near-vent spatter agglutinate (GCPS0703). The three GCPS data are from Browne et al. (2017a).

Olivine Oxygen Isotopes

The $\delta^{18}O$ values of olivine phenocrysts from GTVF and BPVF are shown in Figure 14. Almost all $\delta^{18}O$ values for olivine from the GTVF and BPVF plot between mantle values and values for the Paradise Granodiorite (from Lackey, 2008), which is the country rock underlying the GTVF volcanoes (Moore and Sisson, 1985). Measurements of $\delta^{18}O$ in olivine from LWC deposits range from 6.195 to 6.280 ‰. Olivine in SFC and TC deposits have the lowest $\delta^{18}O$ values of the GTVF ranging from 5.719 to 5.734 ‰ and 5.680 to 5.697 ‰, respectively. Olivine in GC deposits have the most variable and highest $\delta^{18}O$ values of all GTVF and BPVF deposits sampled in this study with values ranging from 5.880 to 6.520 ‰. Olivine from PC exhibit the lowest $\delta^{18}O$ values of all olivine phenocrysts analyzed in the GTVF and BPVF, ranging from 5.554 to 5.643 ‰. Two PC samples plot within the mantle $\delta^{18}O$ field. One analysis of olivine phenocrysts obtained from QC and AC yielded values of 5.624 and 5.750 ‰, respectively.

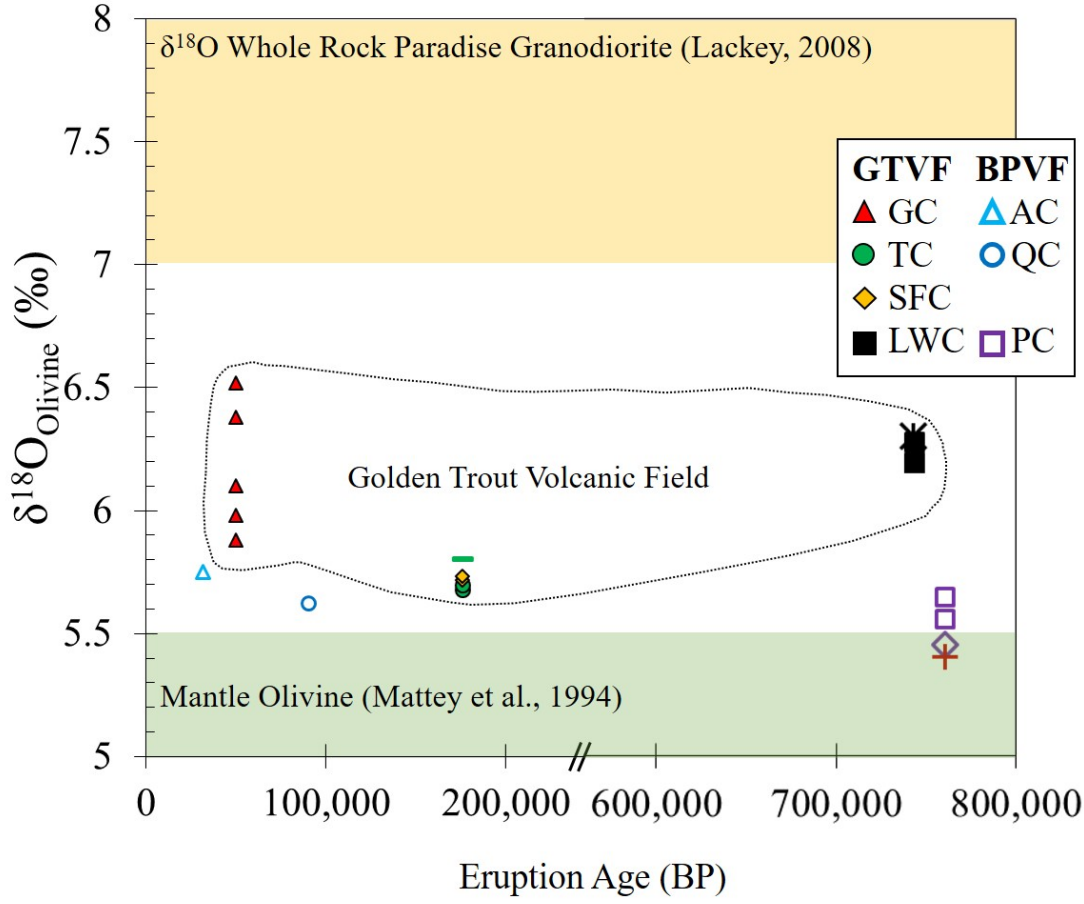

Figure 14. $\delta^{18}O$ of olivine phenocrysts from BPVF and GTVF plotted against eruption ages. GTVF values are outlined (dashed line). Fields for MORB olivine and Sierra Nevada granodiorite whole rock $\delta^{18}O$ values are shown in green and orange, respectively. GTVF samples include LWC (filled black squares), SFC (filled orange diamonds), TC (filled green circles), GC (filled red triangles), PC (empty purple squares), QC (empty dark blue circles), and AC (empty light blue triangle). Previous $\delta^{18}O$ values of olivine phenocrysts obtained by Vazquez et al. (2009) are also shown: LWC is black "x" with

vertical line, TC is green horizontal dash, PC is empty purple diamond, and BP peridotite xenolith is dark red cross.

Whole Rock Radiogenic Isotopes

Whole rock $^{87}Sr/^{86}Sr$ and $^{143}Nd/^{144}Nd$ ratios from each vent at GTVF are plotted in Figure 15 along with igneous rocks from the surrounding area. LWC ($^{87}Sr/^{86}Sr$ = 0.705420 and $^{143}Nd/^{144}Nd$ = 0.512604) and GC ($^{87}Sr/^{86}Sr$ = 0.705817 and $^{143}Nd/^{144}Nd$ = 0.512578) have the most primitive source compositions while SFC ($^{87}Sr/^{86}Sr$ = 0.706026 and $^{143}Nd/^{144}Nd$ = 0.512492) and TC ($^{87}Sr/^{86}Sr$ = 0.705865 and $^{143}Nd/^{144}Nd$ = 0.512533) are more evolved.

Similar to the other datasets collected in this study, the GTVF and BPVF are overlapping in $^{87}Sr/^{86}Sr$ and $^{143}Nd/^{144}Nd$ compositions. Vents from other regional volcanic fields are not so similar (Putirka et al., 2012a). CVF and Southern Cascade values are more primitive than both the GTVF and BPVF. The GTVF $^{143}Nd/^{144}Nd$ values overlap with Tahoe basalts, but Tahoe has lower $^{87}Sr/^{86}Sr$ ratios. Compared to the GTVF, high-K_2O Pliocene lavas of the southern Sierra are markedly lower in $^{143}Nd/^{144}Nd$, though they mostly overlap with $^{87}Sr/^{86}Sr$. Death Valley basalts overlap with the GTVF and BPVF, but the ranges for $^{87}Sr/^{86}Sr$ and $^{143}Nd/^{144}Nd$ ratios exceed both fields.

The $^{87}Sr/^{86}Sr$ and $^{143}Nd/^{144}Nd$ ratios at the GTVF do not reflect the field evolution trend exhibited by the whole-rock compositions. While LWC represents the most primitive mantle source, as reflected by whole-rock compositions, TC and SFC have the

most evolved source compositions, rather than intermediate. Likewise, GC has higher $^{143}Nd/^{144}Nd$ ratios than SFC and TC indicating a slightly more primitive mantle source. This again is in contrast to the most evolved whole-rock compositions of GC.

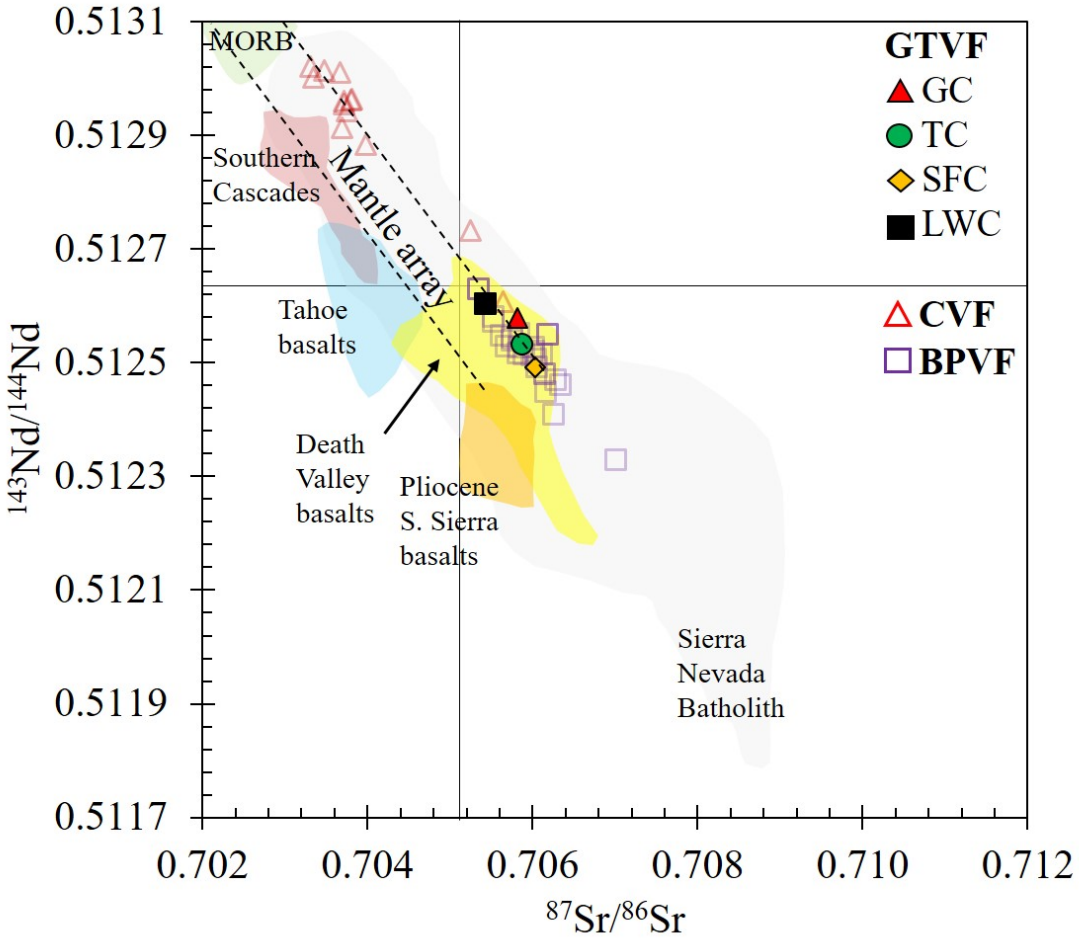

Figure 15. $^{87}Sr/^{86}Sr$ vs $^{143}Nd/^{144}Nd$ for GTVF, BPVF, and other surrounding volcanic fields and Sierran rocks (from Putirka et al., 2012a). LWC (black filled squares), SFC (orange filled diamonds), TC (green filled circles), GC (red filled triangles), BPVF (purple empty squares), Coso Volcanic Field (red empty triangles). All other fields are

denoted by colors and the appropriate labels. BPVF data are from Blondes et al. (2008). CVF data are from Bacon et al. (1984) and Groves (1996).

DISCUSSION

I interpret data from (1) major and trace element compositional analyses of olivine phenocrysts of the GTVF and BPVF, (2) oxygen isotope ratios of olivine phenocrysts from the GTVF and BPVF, and (3) whole-rock Nd and Sr isotope ratios of volcanic rocks from the GTVF. These interpretations allow me to assess my two hypotheses described in the introduction and ultimately advance our understanding of magma petrogenesis and differentiation history of the GTVF compared to the BPVF and CVF.

Olivine Major and Trace Elements

Major and trace element compositions of olivine phenocryst cores from both the GTVF and BPVF range widely, but several key observations can be used to constrain their formation and significance in the origin and differentiation history of basaltic magmas. First, all volcanic rocks sampled in this study contain some olivine with compositions consistent with a mantle origin (e.g., Takahashi, 1987; McDonough and Sun, 1995; Deer et al., 1997; Palme and O'Neill, 2003; De Hoog et al., 2010). Second, volcanic rocks that were erupted early in the evolution of the BPVF and GTVF contain olivine that is both the most homogeneous and the most mantle-like, such as Papoose

Cone (Fo85 – Fo88) in the BPVF and Little Whitney Cone (Fo84 – Fo88) in the GTVF. Third, olivine in younger volcanic rocks from GTVF and to a lesser extent BPVF are characterized by compositions that progressively deviate from mantle-like olivine, where olivine in the youngest GTVF vent – Groundhog Cone – show the greatest deviation (Fo67 – Fo88) from mantle-like olivine compositions. And fourth, olivine in all volcanic rocks erupted from both volcanic fields show a range in composition, which requires nucleation and growth from slightly different melt compositions at different pressures and temperatures.

These key observations described above are consistent with a model of magma formation involving (1) partial melting of mantle to form basaltic magmas, (2) buoyant rise of basalt with entrained mantle-olivine crystals, and (3) ascent and storage of basaltic magmas through the continental lithosphere, where olivine phenocrysts nucleate and grow from variably differentiated and crustal contaminated melt compositions before finally erupting at the surface.

GC in particular requires a unique ascent and storage process to explain both the range of olivine compositions and to account for the overlapping compositions of deposits emplaced via different mechanisms. The spatter agglutinate (GCPS0703) that overlaps compositionally with lava flows both near the vent (17GT8) and at the flow terminus (GCPS0710) suggests a relatively uniform magma chamber leading to eruption. However, the presence of an additional spatter agglutinate sample (17GT10), which correlates well with a different near vent lava flow (GCPS0701) of a different flow lobe

than 17GT8, indicates complex magma storage leading up to the eruption and a range of magma compositions being erupted during the event.

In the GTVF and BPVF, major and trace element compositions of olivine, specifically NiO and MgO, suggest that both volcanic fields initially erupted the least differentiated magmas (PC, LCW) before transitioning (e.g., SFC, TC) to more differentiated compositions over time (GC). Whole-rock compositions of GTVF volcanic rocks (Figure 12) and the increasing occurrence of xenocrystic plagioclase and granitic xenoliths in volcanic rocks over time (Browne et al., 2017a) agree with this model. Interestingly, BPVF olivine does not appear to record as steady a differentiation trend with time compared to olivine from the GTVF, although many vents from the BPVF were not investigated in this study. That said, data presented here show that olivine in the oldest (PC) and youngest (AC) vents are the least differentiated compared to olivine from Quarry Cone, which is intermediate in age. This suggests that magma formation and ascent in the BPVF is more variable, which agrees with findings from other researchers who employed different datasets (e.g., Blondes et al., 2008).

Olivine Oxygen Isotopes

Observations of stable oxygen isotope compositions of olivine in volcanic rocks erupted from the GTVF and BPVF can be used to constrain their origin and crystallization history. The caveat of this data, however, is that $\delta^{18}O$ values presented here define aggregate compositions of multiple olivine crystals that were analyzed

together (see Methods section). One key observation is that $\delta^{18}O$ values in olivine from both fields negatively correlate with Fo content, where the least differentiated olivine are characterized by the lowest $\delta^{18}O$ values. Another key observation is that most olivine from the GTVF ($\delta^{18}O$ = 5.68 to 6.52 ‰) and BPVF ($\delta^{18}O$ = 5.55 to 5.75 ‰) are intermediate in composition between established mantle olivine $\delta^{18}O$ values of 4.8 to 5.5 ‰ (Mattey et al., 1994) and $\delta^{18}O$ values of the Paradise Granodiorite, which is typical of Sierra Nevada Batholith crust (Lackey, 2008) (Figure 14). Only volcanic rocks erupted from Papoose Cone contain olivine with stable oxygen isotope compositions that are consistent with mantle-olivine. Finally, olivine in volcanic rocks erupted from vents in the GTVF generally have higher $\delta^{18}O$ values and a larger range in $\delta^{18}O$ values.

These observations are consistent with a model of crystallization that requires nucleation and growth of olivine from mantle-derived melt compositions that have been variably contaminated by partially melted continental crust (Eiler et al., 2001). Olivine in the GTVF show the largest range in $\delta^{18}O$ values, which suggests that crustal contamination is more extensive in the formation of magmas erupted from GTVF compared to those erupted from the BPVF. Moreover, the range of $\delta^{18}O$ values in olivine from GC, which is the most differentiated in terms of whole-rock compositions (Browne et al., 2017a) and major and trace elemental olivine compositions, requires olivine crystallization over a range of temperatures and pressures as well as melt compositions. However, the extent of crustal contamination in the GTVF fluctuates over time. Whereas olivine from the oldest and youngest vents in the GTVF (LWC and GC) record crystallization from crustal contaminated melts based on their higher $\delta^{18}O$ values (6.195

to 6.280 ‰ and 5.880 to 6.520 ‰, respectively), olivine from vents that are intermediate in age record $\delta^{18}O$ values consistent with crystallization from less contaminated melts. The decrease in $\delta^{18}O$ values in olivine from LWC to olivine in TC and SFC appears to conflict with whole-rock and major and trace element compositions of olivine, which suggest that the melt in SFC and TC lavas from which olivine crystallized was more differentiated than LWC.

Whole Rock Radiogenic Isotopes

Whole-rock radiogenic isotope compositions of volcanic rocks erupted from the GTVF can be used to constrain their mantle source and serve as a valuable comparison to neighboring volcanic fields where the mantle source and tectonic processes are better understood. One key observation of $^{87}Sr/^{86}Sr$ and $^{143}Nd/^{144}Nd$ ratios of basaltic volcanic rocks from GTVF is that they overlap with those from the BPVF and some volcanic rocks erupted from the Death Valley Volcanic Field (DVVF) (Figure 15), requiring a similar mantle source for the GTVF, BPVF, and DVVF. This is an intriguing result because unlike the GTVF, the BPVF and DVVF are known to be controlled by magma production resulting from regional extensional promoting adiabatic melting of asthenospheric mantle and partial melting and metasomatism of the overlying lithospheric mantle (e.g., Manely et al. 2000; Gazel et al., 2012; Putirka et al., 2012a). Manley et al. (2000) described significant extension in Death Valley ca. 7 or 6 Ma, which propagated westward to the Sierra Nevada range front and coincided with the Pliocene

pulse of high-K_2O magmatism in the San Joaquin and Kings volcanic fields. Data from this study support the possibility that this extensional regime continued to affect the southeastern Sierra Nevada and contributed to the generation of magma beneath the GTVF. Alternatively, partial melting of asthenospheric and lithospheric mantle may occur beneath volcanic fields with or without the aid of tectonic processes like faulting. The GTVF is significantly less productive than the BPVF or DVVF, thus, it seems that the absence of faults at the surface does not inhibit magma production at depth, but rather plays an important role in providing pathways for magmas to reach the surface and erupt.

The results of this study indicate that hypothesis #1 is invalid. Whole-rock $^{87}Sr/^{86}Sr$ and $^{143}Nd/^{144}Nd$ ratios at the GTVF overlap with BPVF ratios and, therefore, both were sourced from similar mantle compositions. This result raises questions about magma production and ascent differences between the two fields. Is the rate of magma production lower beneath the GTVF, or does unfaulted, overlying crust prevent much of it from erupting? The answer to this question may reveal if the role of tectonics has a bigger role in magma genesis or magma ascent and requires further investigation.

Hypothesis #2 is valid with important exceptions. Whole-rock compositions at the GTVF show more evolved compositions compared to the BPVF and display increased differentiation through time. Major and trace element compositions of olivine from the GTVF share this trend with time, although they are more similar to BPVF in terms of whole-rock compositions. The variable olivine compositions at GC require prolonged differentiation over time. The $\delta^{18}O$ values at GTVF and BPVF suggest crustal

contamination at the GTVF has been more significant, although not constant through time.

CONCLUSIONS

Quaternary mafic volcanism in the western Basin and Range and in the southeastern Sierra Nevada is largely controlled by extensional stresses which allow for decompression melting and magma generation from both the lithospheric and asthenospheric mantle. The Golden Trout Volcanic Field is one example of this volcanic activity. Whole-rock compositions from previous work and the major and trace element compositions of olivine phenocrysts, stable oxygen isotopes of olivine phenocrysts, and whole-rock radiogenic isotopes presented in this study indicate that, despite its location in a separate physiographic province, the GTVF has a similar mechanism for magma production at depth to other Basin and Range volcanic fields such as the BPVF or DVVF. The $\delta^{18}O$ values at GTVF indicate that its crustal setting has resulted in more crustal contamination and differentiation over time compared to the BPVF. Radiogenic isotopes indicate the GTFV and BPVF have similar mantle sources. These results suggest that magma production at the GTVF is comparatively lower than other Basin and Range volcanic fields because magmas at the GTVF travel through unfaulted crust.

REFERENCES

Auer, S., Bindeman, I., Wallace, P., Ponomareva, V. & Portnyagin, M., 2009, The origin of hydrous, high-$\delta^{18}O$ voluminous volcanism: diverse oxygen isotope values and high magmatic water contents within the volcanic record of Klyuchevskoy volcano, Kamchatka, Russia: Contributions to Mineralogy & Petrology, vol. 157, p. 209.

Bacon, C. R. & Duffield, W. A., 1981, Late Cenozoic rhyolites from the Kern Plateau, southern Sierra Nevada, California: American Journal of Science, vol. 281, p. 1–34.

Bacon, C.R., 1982. Time-predictable bimodal volcanism in the Coso Range, California: Geology vol. 10, p. 65-69.

Bacon, C.R., Kurasawa, H., Delevaux, M., Kistler, R.W., & Doe, B.R., 1984, Lead and strontium isotopic evidence for crustal interaction and compositional zonation in the source regions of Pleistocene basaltic and rhyolitic magmas of the Coso volcanic field, California: Contributions to Mineralogy and Petrology, v. 85, p. 366–375.

Bateman, P. C., 1992, Plutonism in the central part of the Sierra Nevada Batholith, California: USGS Professional Paper, no. 1483.

Beard, B.L., Glazner, A.F., 1995, Trace element and Sr and Nd isotopic composition of mantle xenoliths from the Big Pine Volcanic Field, California: Journal of Geophysical Research vol. 100, p. 4169-4179.

Bierman, P., Gillespie, K.W., Clark, D., 1991. Quaternary geomorphic and geochronology of the Owens Valley, California: Geological Society of America Field Trip.

Bindeman, I., 2008a, Oxygen Isotopes in Mantle and Crustal Magmas as Revealed by Single Crystal Analysis: Reviews in Mineralogy and Geochemistry vol. 69, p. 445–478.

Bindeman, I., Gurenko, A., Sigmarsson, O. & Chaussidon, M., 2008, Oxygen isotope heterogeneity and disequilibria of olivine crystals in large volume Holocene basalts from Iceland: Evidence for magmatic digestion and erosion of Pleistocene hyaloclastites: Geochimica et Cosmochimica Acta, vol. 72, p. 4397–4420.

Blondes, M.S., Reiners, P.W., Ducea, M.N., Singer, B.S., Chesley, J., 2008, Temporal–compositional trends over short and long time-scales in basalts of the Big Pine Volcanic Field, California: Earth and Planetary Science Letters vol. 269, p. 140-154.

Brossy, C.C., Kelson, K.I., Amos, C.B., Baldwin, J.N., Kozlowicz, B., Simpson, D., Ticci, M.G., Lutz, A.T., Kozaci, O., Streig, A., Turner, R., Rose, R., 2012. Map of the late Quaternary active Kern Canyon and Breckenridge faults, southern Sierra Nevada, California. Geosphere 8, 581–591.

Browne, B., Becerra, R., Campbell, C., Saleen, P., Wille, F.R., 2017a, Eruptive Styles and Petrological Insights into Quaternary Basalt in the Golden Trout Volcanic Field, southern Sierra Nevada: Journal of Volcanology and Geothermal Research.

Browne, B.L., Sion, B.D., Phillips, F., Nicholson, R., 2017b, Eruption styles and late Pleistocene ages from 36Cl dating of Groundhog Cone, the most recent and unglaciated basaltic volcano in the Golden Trout Volcanic Field, Kern Plateau, Sierra Nevada. Geological Society of America Abstracts with Programs. Vol. 49, No. 6 doi: 10.1130/abs/2017AM-295298

Chen, J.H., and Moore, J.G., 1982, Uranium-lead isotopic ages from the Sierra Nevada batholith, California: Journal of Geophysical Research. B, vol. 87, p. 4761-4784.

Coleman, D. S., Gray, W., Glazner, A. F., 2004, Rethinking the emplacement and evolution of zoned plutons: Geochronologic evidence for incremental assembly of the Tuolumne Intrusive Suite, California: Geology vol. 32**,** no. 5, p. 433–436.

Deer, W.A., Howie, R.A., Zussman, J. 1997. Rock forming minerals: Orthosilicates. 2 ed., Geological Society of London.

De Hoog, J. C. M., Gall, L. & Cornell, D. H., 2010, Trace-element geochemistry of mantle olivine and application to mantle petrogenesis and geothermobarometry: Chemical Geology vol. 270, p. 196–215.

DePaolo, D. J. & Wasserburg, G. J., 1979, Petrogenetic mixing models and Nd-Sr isotopic patterns: Geochimica et Cosmochimica Acta vol. 43, p. 615–627.

Dixon, T.H., Miller, M., Farina, F., Wang, H, and Johnson, D., 2000, Present-day motion of the Sierra Nevada block and some tectonic implications for the Basin and Range province, North America: Tectonics vol. 19, p. 1-14.

du Bray, E.A., Dellinger, D.A., 1981, Geologic map of the Golden Trout Wilderness, southern Sierra Nevada, California: U.S. Geological Survey Miscellaneous Field Studies Map MF-1231-A, scale 1:48,000.

Ducea, M. & Saleeby, J., 1998, A Case for Delamination of the Deep Batholithic Crust beneath the Sierra Nevada, California: International Geology Review, vol. 40, p. 78–93.

Duffield, W. A., Bacon, C. R. & Dalrymple, G. B., 1980, Late Cenozoic volcanism, geochronology, and structure of the Coso Range, Inyo County, California: Journal of Geophysical Research, vol. 85, p. 2381–2404.

Eaton, G. P., 1982, The Basin and Range Province: Origin and Tectonic Significance: Annual Review of Earth and Planetary Sciences vol. 10, p. 409–440.

Eiler, J. M., Farley, K. A., Valley, J. W., Hauri, E., Craig, H., Hart, S. R., Stolper, E. M., 1997, Oxygen isotope variations in ocean island basalt phenocrysts: Geochimica et Cosmochimica Acta vol. 61**,** no. 11, p. 2281–2293.

Eiler, J. M., 2001, Oxygen isotope variations of basaltic lavas and upper mantle rocks: Reviews in mineralogy and geochemistry vol. 43, p. 319–364.

Farmer, G. L., Glazner, A. F. & Manley, C. R., 2002, Did lithospheric delamination trigger late Cenozoic potassic volcanism in the southern Sierra Nevada, California?: GSA Bulletin, vol. 114, p. 754–768.

Gazel, E., Plank, T., Forsyth, D. W., Bendersky, C., Lee, C. A., Hauri, E. H., 2012, Lithosphere versus asthenosphere mantle sources at the Big Pine Volcanic Field, California: Geochemistry, Geophysics, Geosystems vol. 13, no. 1, p. 1–25.

Groves, K.R., 1996, Geochemical and isotopic analysis of Pleistocene basalts from the southern Coso volcanic field, California [Ph.D. thesis]: Chapel Hill, University of North Carolina, 84 p.

Kirby, E., Anandakrishnan, S., Phillips, F. & Marrero, 2008, S. Late Pleistocene slip rate along the Owens Valley fault, eastern California: Geophysical Research Letters, vol. 35**,** L01304.

Kistler, R. W., Evernden, J. F., 1971, Sierra Nevada Plutonic Cycle: Part I, Origin of Composite Granitic Batholiths: GSA Bulletin vol. 82, p. 853–868.

Knopf, A., 1918, A geologic reconnaissance of the Inyo Range and the eastern slope of the Sierra Nevada, California: US Geological Survey Professional Paper 110, p. 130.

Lawson, A.C., 1904, The geomorphogeny of the upper Kern Basin: Univ. Calif. Pub., Dept. Geology Bulletin 4, p. 291-376.

Luedke, R.G., Smith, R.L., 1981. Map showing distribution, composition, and age of late Cenozoic volcanic centers in California and Nevada: U.S. Geol. Survey Map, I-1091-C.

Manley, C. R., Glazner, A. F. & Farmer, G. L., 2000, Timing of volcanism in the Sierra Nevada of California: Evidence for Pliocene delamination of the batholithic root?: Geology vol. 28, p. 811–814.

McClusky, S. C., Bjornstad, S.C., Hager, B. H., King, R. W., Meade, B. J., Miller, M. M., Monastero, F. C., Souter, B. J., 2001, Present day kinematics of the Eastern California Shear Zone from a geodetically constrained block model: Geophysical Research Letters, vol. 28, p. 3369–3372.

McDonough, W. F. & Sun, S., 1995, The composition of the Earth: Chemical Geology vol. 120, iss. 3-4, p. 223–253.

Moore, J. G. & Dodge, F. C. W., 1980, Late Cenozoic Volcanic Rocks of the Southern Sierra Nevada, California: I. Geology and Petrology: GSA Bulletin vol. 91, p. 1995–2038.

Moore, J. G. & Lamphere, M., 1983, Age of the Golden Trout Creek volcanic field, Sierra Nevada, CA: Eos vol. 64, p. 895–897.

Moore, J. G. & Sisson, T. W., 1985, Geologic Map of the Kern Peak Quadrangle, Tulare County, California: US Geological Survey.

Mordick, B.E. Glazner, A.F., 2006, Clinopyroxene thermobarometry of basalts from the Coso and Big Pine Volcanic Fields, California: Contributions to Mineralogy and Petrology vol. 152, p. 111-124.

Nadin, E. S. & Saleeby, J. B., 2008, Disruption of regional primary structure of the Sierra Nevada batholith by the Kern Canyon fault system, California: Geological Society of America Special Paper 438: Ophiolites, Arcs, and Batholiths: A Tribute to Cliff Hopson vol. 438, p. 429–454.

Nadin, E. S. & Saleeby, J. B., 2010, Quaternary reactivation of the Kern Canyon fault system, southern Sierra Nevada, California: GSA Bulletin no. 122, p. 1671–1685.

Ormerod, D.S., Rogers, N.W., and Hawkesworth, C.J., 1991, Melting in the lithospheric mantle: Inverse modelling of alkali-olivine basalts form the Big Pine Volcanic Field, California: Contributions to Mineralogy and Petrology, v. 108, p. 305–317, doi: 10.1007/BF00285939.

Palme, H. & O'Neill, H. S. C., 2003, Cosmochemical Estimates of Mantle Composition: Treatise on Geochemistry, vol. 2, p. 568.

Paterson, S. R., Okaya, D., Memeti, V., Economos, R., Miller, R. B., 2011, Magma addition and flux calculations of incrementally constructed magma chambers in continental margin arcs: Combined field, geochronologic, and thermal modeling studies: Geosphere vol. 7, no. 6, p. 1439–1468.

Phillips, F.M., Majkowski, L., 2011, The role of low-angle normal faulting in active tectonics of the northern Owens Valley, California: Lithosphere vol. 3, p. 22–36.

Putirka, K. & Busby, C. J., 2007, The tectonic significance of high-K2O volcanism in the Sierra Nevada, California: Geology vol. 35, p. 923–926 (2007).

Putirka, K., Jean, M., Cousens, B., Sharma, R., Torrez, G., Carlson, C., 2012a, Cenozoic volcanism in the Sierra Nevada and Walker Lane, California, and a new model for lithosphere degradation: Geosphere vol. 8, p. 265–291.

Putirka, K., & Platt, B., 2012b, Basin and Range volcanism as a passive response to extensional tectonics: Geosphere, vol. 8, no. 6, p. 1274-1285.

Rollinson, H., 1993, Using Geochemical Data: Evolution, Presentation, Interpretation. Longman Scientific and Technical Press 26.

Saleeby, J. B., Sams, D. B., Kistler, R. W., 1987, U/PB zircon, strontium, and oxygen isotopic and geochronological study of the southernmost Sierra Nevada Batholith, California: Journal of Geophysical Research, vol. 92, iss. B10, p. 10443-10466.

Slemmons, D.B., Vitori, E., Jayko, A.S., Carver, G.A., Bacon, S.N., 2008, Quaternary fault and linement map of Owens Valley, Inyo County, eastern California: Geological Society of America, Map and Chart Series MCH096.

Stewart, J. H., 1971, Basin and Range Structure: A System of Horsts and Grabens Produced by Deep-Seated Extension: GSA Bulletin no. 82, p. 1019–1044.

Takahashi, E., 1985, Origin of basaltic magma-Implications from peridotite melting experiments and an olivine fractionation model: Bulletin Volcanology Society of Japan vol. 30, S17–S40.

Turrin, B., Gillespie, A., 1986, K/Ar ages of basaltic volcanism of the Big Pine volcanic field, California: Implications for glacial stratigraphy and neotectonics of the Sierra Nevada: Geological Society of America Abstracts with Programs 18.

Unruh, J., Humphrey, J. & Barron, A., 2003, Transtensional model for the Sierra Nevada frontal fault system, eastern California: Geology vol. 31, p. 327–330.

Valentine, G. A. & Perry, F. V., 2007, Tectonically controlled, time-predictable basaltic volcanism from a lithospheric mantle source (central Basin and Range Province, USA): Earth and Planetary Science Letters vol. 261, p. 201–216.

Kooten, V., K., G., 1980, Mineralogy, Petrology, and Geochemistry of an Ultrapotassic Basaltic Suite, Central Sierra Nevada, California, U.S.A: Journal of Petrology vol. 21, iss. 4, p. 651–684.

Kooten, G. K. V., 1981, Pb and Sr systematics of ultrapotassic and basaltic rocks from the central Sierra Nevada, California: Contributions to Mineralogy and Petrology, vol. 76, p. 378–385.

Vazquez, J.A., Bindeman, I.N., Browne, B.L., 2009. Oxygen-isotope composition of Quaternary rhyolitic and basaltic lavas in the southern Owens Valley and Kern Plateau, CA: In AGU Fall Meeting Abstracts 1, 1657.

Vazquez, J. A., and J. M. Woolford, 2015, Late Pleistocene ages for the most recent volcanism and glacial-pluvial deposits at Big Pine volcanic field, California, USA, from cosmogenic ^{36}Cl dating: Geochemistry, Geophysics, Geosystems, vol. 16, p. 2812–2828.

Webb, R.W., 1950, Volcanic geology of Toowa Valley, southern Sierra Nevada, California: Geological Society of America Bulletin vol. 61, p. 349-357.

White, W. M., 2013, Geochemistry: Wiley.

Wilshire, H. G., Bedford, D. R. & Coleman, T., 2002, Digital Version of‘ Open-file Report 92-183’: Geologic Map of the Granite Spring Quadrangle, San Bernardino County, California: US Department of the Interior, US Geological Survey.

Woolford, J.M., 2009, Distribution and stratigraphy of basalts in the Southwest (Aberdeen) Portion of the Big Pine Volcanic Field, Owens Valley, California. MS Thesis, California State University, Northridge.

APPENDIX A: RAW OLIVINE PHENOCRYST CORE COMPOSITIONS VIA EMPA

Comment	17GT6 ol1	17GT6 ol1	17GT6 ol2	17GT6 ol2
Vent	Little Whitney Cone	Little Whitney Cone	Little Whitney Cone	Little Whitney Cone
Latitude	N 36.36795	N 36.36795	N 36.36795	N 36.36795
Longitude	W 118.28320	W 118.28320	W 118.28320	W 118.28320
Lithology	East Lava	East Lava	East Lava	East Lava
Image #	092917_17GT6_ol1	092917_17GT6_ol1	092917_17GT6_ol2	092917_17GT6_ol2
Data	CORE	CORE	CORE	CORE
DataSet/Point	1 / 1 .	1 / 2 .	2 / 1 .	2 / 2 .
SiO_2	40.78	40.35	40.54	40.02
Al_2O_3	0.03	0.03	0.03	0.03
Cr_2O_3	0.06	0.05	0.06	0.04
FeO	11.15	11.02	11.04	11.14
MnO	0.17	0.15	0.17	0.16
MgO	47.30	47.41	47.57	47.62
CaO	0.14	0.14	0.13	0.13
Total	100.08	99.57	99.98	99.57
Si	4.045	4.015	4.019	3.980
Al	0.003	0.004	0.004	0.003
Cr	0.004	0.004	0.005	0.003
Fe	0.925	0.917	0.915	0.893
Mn	0.014	0.012	0.014	0.014
Mg	6.994	7.034	7.030	7.060
Ca	0.015	0.015	0.014	0.014
Total	12.000	12.000	12.000	11.966
Fo	**88.00**	**88.17**	**88.17**	**88.09**

17GT6 ol3 Little Whitney Cone N 36.36795 W 118.28320 East Lava 092917_17GT6_ol3 CORE 3 / 1 .	17GT6 ol3 Little Whitney Cone N 36.36795 W 118.28320 East Lava 092917_17GT6_ol3 CORE 3 / 2 .	17GT6 ol4 Little Whitney Cone N 36.36795 W 118.28320 East Lava 092917_17GT6_ol4 CORE 4 / 1 .	17GT6 ol4 Little Whitney Cone N 36.36795 W 118.28320 East Lava 092917_17GT6_ol4 CORE 4 / 2 .	17GT6 ol5 Little Whitney Cone N 36.36795 W 118.28320 East Lava 092917_17GT6_ol5 CORE 5 / 1 .
39.71	39.34	40.17	39.63	39.41
0.02	0.01	0.03	0.02	0.03
0.03	0.02	0.04	0.05	0.00
13.34	13.35	11.92	11.90	13.70
0.18	0.22	0.17	0.14	0.20
45.83	45.85	46.57	46.73	45.21
0.17	0.17	0.15	0.14	0.19
99.53	99.18	99.41	98.97	98.96
3.986	3.958	4.020	3.977	3.985
0.003	0.002	0.003	0.003	0.003
0.003	0.002	0.003	0.004	0.000
1.096	1.044	0.997	0.959	1.133
0.015	0.018	0.015	0.012	0.017
6.856	6.877	6.946	6.990	6.815
0.018	0.019	0.016	0.015	0.020
11.977	11.920	12.000	11.960	11.975
85.61	**85.56**	**87.11**	**87.20**	**85.07**

17GT6 ol5 Little Whitney Cone N 36.36795 W 118.28320 East Lava 092917_17GT6_ol5 CORE 5 / 2 .	17GT6 ol6 Little Whitney Cone N 36.36795 W 118.28320 East Lava 092917_17GT6_ol6 CORE 6 / 1 .	17GT6 ol6 Little Whitney Cone N 36.36795 W 118.28320 East Lava 092917_17GT6_ol6 CORE 6 / 2 .	17GT6 ol7 Little Whitney Cone N 36.36795 W 118.28320 East Lava 092917_17GT6_ol7 CORE 7 / 1 .	17GT6 ol7 Little Whitney Cone N 36.36795 W 118.28320 East Lava 092917_17GT6_ol7 CORE 7 / 2 .
39.31	39.63	39.10	39.54	39.69
0.03	0.03	0.02	0.02	0.03
0.02	0.04	0.03	0.04	0.05
13.75	12.03	13.47	12.51	12.43
0.21	0.19	0.21	0.17	0.18
45.30	46.36	45.64	46.57	46.65
0.18	0.15	0.17	0.16	0.16
99.04	98.79	98.88	99.32	99.49
3.972	3.990	3.950	3.961	3.968
0.003	0.003	0.002	0.002	0.004
0.001	0.003	0.003	0.003	0.004
1.111	0.999	1.042	0.975	0.983
0.018	0.016	0.018	0.014	0.015
6.823	6.959	6.872	6.955	6.952
0.020	0.017	0.018	0.017	0.018
11.949	11.986	11.904	11.927	11.943
85.05	**86.94**	**85.41**	**86.56**	**86.64**

17GT6 ol8 Little Whitney Cone N 36.36795 W 118.28320 East Lava 092917_17GT6_ol8 CORE 8 / 1 .	17GT6 ol8 Little Whitney Cone N 36.36795 W 118.28320 East Lava 092917_17GT6_ol8 CORE 8 / 2 .	17GT6 ol9 Little Whitney Cone N 36.36795 W 118.28320 East Lava 092917_17GT6_ol9 CORE 9 / 1 .	17GT6 ol9 Little Whitney Cone N 36.36795 W 118.28320 East Lava 092917_17GT6_ol9 CORE 9 / 2 .	17GT6 ol10 Little Whitney Cone N 36.36795 W 118.28320 East Lava 092917_17GT6_ol10 CORE 10 / 1 .	17GT6 ol10 Little Whitney Cone N 36.36795 W 118.28320 East Lava 092917_17GT6_ol10 CORE 10 / 2 .
39.52	39.96	39.66	39.87	40.09	39.93
0.03	0.03	0.03	0.03	0.04	0.03
0.05	0.04	0.04	0.05	0.04	0.05
10.64	10.47	11.19	11.27	10.99	10.92
0.15	0.18	0.17	0.16	0.12	0.15
47.89	47.90	47.56	47.66	47.96	47.64
0.13	0.12	0.13	0.13	0.13	0.14
98.92	99.18	99.24	99.63	99.86	99.28
3.947	3.980	3.957	3.964	3.973	3.979
0.003	0.004	0.004	0.003	0.004	0.003
0.004	0.004	0.003	0.004	0.003	0.004
0.791	0.839	0.854	0.873	0.864	0.874
0.012	0.015	0.014	0.013	0.010	0.013
7.130	7.113	7.074	7.064	7.084	7.077
0.013	0.013	0.014	0.014	0.014	0.015
11.902	11.967	11.921	11.936	11.953	11.965
88.63	**88.77**	**88.03**	**87.98**	**88.34**	**88.31**

17GT8 ol1 Groundhog Cone N 36.36534 W 118.32214 Lava 092917_17GT8_ol1 CORE 21 / 1 .	17GT8 ol1 Groundhog Cone N 36.36534 W 118.32214 Lava 092917_17GT8_ol1 CORE 21 / 2 .	17GT8 ol2 Groundhog Cone N 36.36534 W 118.32214 Lava 092917_17GT8_ol2 CORE 22 / 1 .	17GT8 ol2 Groundhog Cone N 36.36534 W 118.32214 Lava 092917_17GT8_ol2 CORE 22 / 2 .	17GT8 ol3 Groundhog Cone N 36.36534 W 118.32214 Lava 092917_17GT8_ol3 CORE 23 / 1 .
37.78	37.97	38.40	37.36	38.00
0.02	0.03	0.02	0.01	0.02
0.00	0.00	0.01	0.00	0.01
20.61	20.85	20.04	22.00	19.51
0.29	0.32	0.27	0.35	0.30
39.64	39.36	40.69	38.70	41.05
0.12	0.13	0.14	0.14	0.13
98.70	98.85	99.81	98.72	99.20
3.960	3.978	3.965	3.936	3.933
0.002	0.003	0.002	0.001	0.002
0.000	0.000	0.001	0.000	0.000
1.728	1.788	1.663	1.811	1.557
0.025	0.028	0.023	0.031	0.026
6.192	6.149	6.263	6.078	6.335
0.014	0.014	0.015	0.016	0.015
11.922	11.960	11.933	11.873	11.869
77.04	**76.68**	**77.98**	**75.38**	**78.55**

17GT8 ol3 Groundhog Cone N 36.36534 W 118.32214 Lava 092917_17GT8_ol3 CORE 23 / 2 .	17GT8 ol4 Groundhog Cone N 36.36534 W 118.32214 Lava 092917_17GT8_ol4 CORE 24 / 1 .	17GT8 ol4 Groundhog Cone N 36.36534 W 118.32214 Lava 092917_17GT8_ol4 CORE 24 / 2 .	17GT8 ol5 Groundhog Cone N 36.36534 W 118.32214 Lava 092917_17GT8_ol5 CORE 25 / 1 .	17GT8 ol5 Groundhog Cone N 36.36534 W 118.32214 Lava 092917_17GT8_ol5 CORE 25 / 2 .
38.00	36.43	36.39	36.47	36.62
0.02	0.02	0.02	0.02	0.02
0.01	0.00	0.00	0.00	0.00
19.75	25.53	25.74	26.58	26.98
0.32	0.40	0.42	0.41	0.40
40.73	35.66	35.90	34.89	34.59
0.13	0.14	0.16	0.19	0.17
99.12	98.63	99.18	98.71	99.03
3.942	3.922	3.900	3.932	3.949
0.003	0.003	0.002	0.002	0.003
0.001	0.000	0.000	0.000	0.000
1.600	2.146	2.109	2.264	2.333
0.028	0.036	0.038	0.038	0.037
6.299	5.724	5.735	5.608	5.560
0.015	0.016	0.018	0.022	0.019
11.887	11.847	11.803	11.867	11.900
78.21	**70.88**	**70.82**	**69.53**	**69.08**

17GT8 ol6 Groundhog Cone N 36.36534 W 118.32214 Lava 092917_17GT8_ol6 CORE 26 / 1 .	17GT8 ol6 Groundhog Cone N 36.36534 W 118.32214 Lava 092917_17GT8_ol6 CORE 26 / 2 .	17GT8 ol7 Groundhog Cone N 36.36534 W 118.32214 Lava 092917_17GT8_ol7 CORE 27 / 1 .	17GT8 ol7 Groundhog Cone N 36.36534 W 118.32214 Lava 092917_17GT8_ol7 CORE 27 / 2 .	17GT8 ol8 Groundhog Cone N 36.36534 W 118.32214 Lava 092917_17GT8_ol8 CORE 28 / 1 .
37.77	37.37	38.10	37.44	35.72
0.02	0.03	0.02	0.01	0.71
0.01	0.00	0.01	0.01	0.01
22.68	25.19	21.87	23.79	26.77
0.36	0.41	0.32	0.38	0.47
38.70	36.26	39.39	37.62	32.75
0.17	0.16	0.14	0.15	0.21
99.91	99.62	99.97	99.56	97.03
3.943	3.967	3.957	3.944	3.954
0.003	0.004	0.002	0.001	0.092
0.001	0.000	0.001	0.001	0.001
1.870	2.174	1.816	1.986	2.478
0.032	0.037	0.028	0.034	0.044
6.023	5.738	6.097	5.908	5.405
0.019	0.018	0.016	0.017	0.025
11.890	11.937	11.917	11.890	12.000
74.79	**71.46**	**75.84**	**73.35**	**67.97**

17GT8 ol8 Groundhog Cone N 36.36534 W 118.32214 Lava 092917_17GT8_ol8 CORE 28 / 2 .	17GT8 ol9 Groundhog Cone N 36.36534 W 118.32214 Lava 092917_17GT8_ol9 CORE 29 / 1 .	17GT8 ol9 Groundhog Cone N 36.36534 W 118.32214 Lava 092917_17GT8_ol9 CORE 29 / 2 .	17GT8 ol10 Groundhog Cone N 36.36534 W 118.32214 Lava 092917_17GT8_ol10 CORE 30 / 1 .	17GT8 ol10 Groundhog Cone N 36.36534 W 118.32214 Lava 092917_17GT8_ol10 CORE 30 / 2 .
36.38	36.40	37.04	37.50	37.36
0.01	0.03	0.02	0.02	0.02
0.01	0.01	0.00	0.01	0.01
28.06	26.32	26.24	22.10	23.63
0.49	0.42	0.38	0.34	0.37
33.73	35.02	35.33	38.36	37.52
0.19	0.15	0.17	0.14	0.13
99.05	98.57	99.53	98.78	99.31
3.941	3.929	3.962	3.960	3.949
0.001	0.004	0.003	0.003	0.002
0.001	0.001	0.000	0.001	0.001
2.426	2.238	2.275	1.876	1.988
0.045	0.038	0.034	0.030	0.033
5.448	5.635	5.633	6.038	5.912
0.022	0.018	0.020	0.016	0.015
11.884	11.863	11.927	11.924	11.900
67.61	**69.86**	**70.12**	**75.14**	**73.45**

17GT10 ol1 Groundhog Cone N 36.35870 W 118.31567 Agglutinate 093017_17GT10_ol1 CORE 7 / 1 .	17GT10 ol1 Groundhog Cone N 36.35870 W 118.31567 Agglutinate 093017_17GT10_ol1 CORE 7 / 2 .	17GT10 ol2 Groundhog Cone N 36.35870 W 118.31567 Agglutinate 093017_17GT10_ol2 CORE 8 / 1 .	17GT10 ol2 Groundhog Cone N 36.35870 W 118.31567 Agglutinate 093017_17GT10_ol2 CORE 8 / 2 .	17GT10 ol3 Groundhog Cone N 36.35870 W 118.31567 Agglutinate 093017_17GT10_ol3 CORE 9 / 1 .
39.55	39.47	39.56	39.93	38.76
0.04	0.05	0.06	0.04	0.02
0.04	0.02	0.02	0.01	0.02
14.60	14.66	14.63	14.18	19.37
0.23	0.24	0.22	0.21	0.38
44.77	44.78	44.87	45.07	41.65
0.20	0.21	0.23	0.14	0.18
99.66	99.70	99.85	99.81	100.72
3.989	3.980	3.982	4.015	3.955
0.004	0.006	0.007	0.005	0.002
0.003	0.002	0.001	0.001	0.002
1.217	1.204	1.206	1.193	1.567
0.019	0.020	0.018	0.018	0.033
6.732	6.732	6.733	6.755	6.335
0.021	0.023	0.025	0.015	0.020
11.985	11.968	11.974	12.000	11.915
84.10	**84.03**	**84.08**	**84.65**	**78.79**

17GT10 ol3 Groundhog Cone N 36.35870 W 118.31567 Agglutinate 093017_17GT10_ol3 CORE 9 / 2 .	17GT10 ol4 Groundhog Cone N 36.35870 W 118.31567 Agglutinate 093017_17GT10_ol4 CORE 10 / 1 .	17GT10 ol4 Groundhog Cone N 36.35870 W 118.31567 Agglutinate 093017_17GT10_ol4 CORE 10 / 2 .	17GT10 ol5 Groundhog Cone N 36.35870 W 118.31567 Agglutinate 093017_17GT10_ol5 CORE 11 / 1 .	17GT10 ol5 Groundhog Cone N 36.35870 W 118.31567 Agglutinate 093017_17GT10_ol5 CORE 11 / 2 .
37.31	39.61	39.24	40.07	39.85
0.10	0.03	0.03	0.03	0.04
0.01	0.00	0.03	0.03	0.02
18.54	13.94	13.76	14.73	14.53
0.34	0.19	0.22	0.26	0.22
39.71	45.37	45.57	45.29	45.09
0.20	0.20	0.17	0.19	0.20
96.38	99.62	99.46	100.90	100.21
3.975	3.984	3.954	3.994	3.995
0.013	0.004	0.004	0.003	0.005
0.000	0.000	0.002	0.002	0.001
1.614	1.144	1.073	1.222	1.216
0.031	0.016	0.019	0.022	0.019
6.307	6.801	6.844	6.730	6.740
0.023	0.022	0.018	0.021	0.021
11.963	11.972	11.913	11.994	11.997
78.72	**84.89**	**85.12**	**84.12**	**84.27**

17GT10 ol6 Groundhog Cone N 36.35870 W 118.31567 Agglutinate 093017_17GT10_ol6 CORE 12 / 1 .	17GT10 ol6 Groundhog Cone N 36.35870 W 118.31567 Agglutinate 093017_17GT10_ol6 CORE 12 / 2 .	17GT10 ol7 Groundhog Cone N 36.35870 W 118.31567 Agglutinate 093017_17GT10_ol7 CORE 13 / 1 .	17GT10 ol7 Groundhog Cone N 36.35870 W 118.31567 Agglutinate 093017_17GT10_ol7 CORE 13 / 2 .	17GT10 ol8 Groundhog Cone N 36.35870 W 118.31567 Agglutinate 093017_17GT10_ol8 CORE 14 / 1 .
39.46	39.27	39.93	39.72	41.04
0.05	0.02	0.05	0.03	0.02
0.03	0.01	0.02	0.03	0.02
15.93	16.89	11.67	11.72	11.52
0.24	0.23	0.14	0.17	0.15
44.30	43.57	47.39	47.51	47.74
0.20	0.18	0.19	0.20	0.16
100.45	100.36	99.66	99.67	100.92
3.969	3.968	3.968	3.947	4.031
0.006	0.002	0.006	0.004	0.003
0.002	0.001	0.001	0.002	0.002
1.285	1.367	0.914	0.874	0.946
0.020	0.020	0.012	0.014	0.013
6.642	6.562	7.022	7.038	6.989
0.021	0.019	0.021	0.021	0.017
11.946	11.940	11.944	11.900	12.000
82.78	**81.74**	**87.50**	**87.46**	**87.75**

17GT10 ol8 Groundhog Cone N 36.35870 W 118.31567 Agglutinate 093017_17GT10_ol8 CORE 14 / 2 .	17GT10 ol9 Groundhog Cone N 36.35870 W 118.31567 Agglutinate 093017_17GT10_ol9 CORE 15 / 1 .	17GT10 ol9 Groundhog Cone N 36.35870 W 118.31567 Agglutinate 093017_17GT10_ol9 CORE 15 / 2 .	17GT10 ol10 Groundhog Cone N 36.35870 W 118.31567 Agglutinate 093017_17GT10_ol10 CORE 16 / 1 .	17GT10 ol10 Groundhog Cone N 36.35870 W 118.31567 Agglutinate 093017_17GT10_ol10 CORE 16 / 2 .
40.04	39.92	39.92	39.71	39.85
0.03	0.02	0.02	0.05	0.04
0.02	0.03	0.03	0.03	0.02
11.40	12.17	12.13	13.37	13.23
0.17	0.20	0.18	0.17	0.20
47.36	47.33	47.18	46.42	46.20
0.19	0.20	0.19	0.17	0.17
99.46	100.14	99.92	100.13	99.88
3.985	3.956	3.966	3.954	3.978
0.004	0.003	0.003	0.006	0.004
0.002	0.002	0.002	0.002	0.002
0.924	0.926	0.944	1.030	1.067
0.014	0.017	0.015	0.014	0.017
7.026	6.992	6.987	6.891	6.876
0.021	0.021	0.020	0.018	0.018
11.975	11.917	11.936	11.916	11.962
87.72	**86.98**	**87.01**	**85.73**	**85.78**

17GT2 ol1 Tunnel Cone N 36.36636 W 118.28241 Agglutinate 093017_17GT2_ol1 CORE 1 / 1 .	17GT2 ol1 Tunnel Cone N 36.36636 W 118.28241 Agglutinate 093017_17GT2_ol1 CORE 1 / 2 .	17GT2 ol2 Tunnel Cone N 36.36636 W 118.28241 Agglutinate 093017_17GT2_ol2 CORE 2 / 1 .	17GT2 ol2 Tunnel Cone N 36.36636 W 118.28241 Agglutinate 093017_17GT2_ol2 CORE 2 / 2 .	17GT2 ol3 Tunnel Cone N 36.36636 W 118.28241 Agglutinate 093017_17GT2_ol3 CORE 3 / 1 .
39.10	39.07	38.50	38.37	39.50
0.09	0.04	0.02	0.03	0.03
0.05	0.05	0.01	0.02	0.04
12.92	14.19	16.98	17.27	11.79
0.19	0.21	0.28	0.29	0.16
45.79	44.90	42.71	42.32	46.76
0.19	0.18	0.19	0.19	0.17
98.59	98.88	98.82	98.69	98.71
3.954	3.962	3.954	3.956	3.968
0.010	0.005	0.003	0.004	0.004
0.004	0.004	0.001	0.001	0.003
1.015	1.136	1.369	1.406	0.933
0.016	0.018	0.025	0.025	0.013
6.903	6.788	6.539	6.504	7.003
0.020	0.020	0.021	0.021	0.019
11.923	11.932	11.911	11.917	11.943
85.95	**84.54**	**81.30**	**80.90**	**87.26**

17GT2 ol3 Tunnel Cone N 36.36636 W 118.28241 Agglutinate 093017_17GT2_ol3 CORE 3 / 2 .	17GT2 ol4 Tunnel Cone N 36.36636 W 118.28241 Agglutinate 093017_17GT2_ol4 CORE 4 / 1 .	17GT2 ol4 Tunnel Cone N 36.36636 W 118.28241 Agglutinate 093017_17GT2_ol4 CORE 4 / 2 .	17GT2 ol5 Tunnel Cone N 36.36636 W 118.28241 Agglutinate 093017_17GT2_ol5 CORE 5 / 1 .	17GT2 ol5 Tunnel Cone N 36.36636 W 118.28241 Agglutinate 093017_17GT2_ol5 CORE 5 / 2 .
39.35	39.58	39.32	39.22	39.28
0.04	0.04	0.04	0.04	0.04
0.03	0.04	0.07	0.08	0.07
12.10	11.43	11.59	12.63	12.29
0.17	0.19	0.17	0.19	0.20
46.40	47.10	46.87	46.10	46.01
0.19	0.18	0.19	0.18	0.18
98.50	98.80	98.48	98.68	98.39
3.966	3.965	3.954	3.956	3.974
0.005	0.005	0.005	0.004	0.005
0.003	0.003	0.006	0.007	0.005
0.960	0.896	0.894	0.987	0.998
0.015	0.016	0.014	0.016	0.017
6.972	7.034	7.026	6.932	6.939
0.020	0.019	0.020	0.020	0.020
11.940	11.938	11.919	11.922	11.958
86.86	**87.63**	**87.44**	**86.29**	**86.57**

17GT2 ol6 Tunnel Cone N 36.36636 W 118.28241 Agglutinate 093017_17GT2_ol6 CORE 6 / 1 .	17GT2 ol6 Tunnel Cone N 36.36636 W 118.28241 Agglutinate 093017_17GT2_ol6 CORE 6 / 2 .	17GT2 ol7 Tunnel Cone N 36.36636 W 118.28241 Agglutinate 093017_17GT2_ol7 CORE 7 / 1 .	17GT2 ol7 Tunnel Cone N 36.36636 W 118.28241 Agglutinate 093017_17GT2_ol7 CORE 7 / 2 .	17GT2 ol8 Tunnel Cone N 36.36636 W 118.28241 Agglutinate 093017_17GT2_ol8 CORE 8 / 1 .
39.14	38.08	38.38	38.78	39.10
0.04	0.04	0.04	0.03	0.04
0.02	0.02	0.01	0.03	0.05
16.00	16.35	17.03	16.69	13.37
0.25	0.24	0.30	0.27	0.19
43.66	43.02	42.57	42.47	45.18
0.18	0.17	0.19	0.19	0.17
99.55	98.08	98.68	98.64	98.32
3.978	3.928	3.950	3.993	3.974
0.005	0.004	0.005	0.004	0.005
0.002	0.002	0.001	0.003	0.004
1.323	1.273	1.371	1.430	1.092
0.021	0.021	0.026	0.024	0.016
6.615	6.616	6.532	6.518	6.846
0.020	0.018	0.021	0.021	0.019
11.963	11.863	11.905	11.992	11.956
82.53	**82.02**	**81.20**	**81.47**	**85.38**

17GT2 ol8 Tunnel Cone N 36.36636 W 118.28241 Agglutinate 093017_17GT2_ol8 CORE 8 / 2 .	17GT2 ol9 Tunnel Cone N 36.36636 W 118.28241 Agglutinate 093017_17GT2_ol9 CORE 9 / 1 .	17GT2 ol9 Tunnel Cone N 36.36636 W 118.28241 Agglutinate 093017_17GT2_ol9 CORE 9 / 2 .	17GT2 ol10 Tunnel Cone N 36.36636 W 118.28241 Agglutinate 093017_17GT2_ol10 CORE 10 / 1 .	17GT2 ol10 Tunnel Cone N 36.36636 W 118.28241 Agglutinate 093017_17GT2_ol10 CORE 10 / 2 .
38.92	39.51	39.66	38.80	38.98
0.05	0.06	0.06	0.04	0.05
0.03	0.04	0.05	0.05	0.07
14.57	10.69	10.72	14.24	14.60
0.21	0.15	0.17	0.21	0.19
44.61	47.38	47.55	44.71	44.85
0.20	0.17	0.18	0.18	0.18
98.87	98.31	98.71	98.53	99.27
3.955	3.968	3.968	3.951	3.947
0.006	0.007	0.007	0.005	0.005
0.003	0.003	0.004	0.004	0.005
1.158	0.844	0.843	1.125	1.141
0.018	0.013	0.014	0.018	0.016
6.758	7.093	7.092	6.789	6.771
0.021	0.018	0.019	0.020	0.019
11.919	11.946	11.946	11.912	11.905
84.10	**88.43**	**88.41**	**84.44**	**84.19**

17GT3 ol1 South Fork Cone N 36.36198 W 118.28104 Lava 093017_17GT3_ol1 CORE 11 / 1 .	17GT3 ol1 South Fork Cone N 36.36198 W 118.28104 Lava 093017_17GT3_ol1 CORE 11 / 2 .	17GT3 ol2 South Fork Cone N 36.36198 W 118.28104 Lava 093017_17GT3_ol2 CORE 12 / 1 .	17GT3 ol2 South Fork Cone N 36.36198 W 118.28104 Lava 093017_17GT3_ol2 CORE 12 / 2 .	17GT3 ol3 South Fork Cone N 36.36198 W 118.28104 Lava 093017_17GT3_ol3 CORE 13 / 1 .
38.58	37.84	38.91	38.73	38.71
0.03	0.37	0.03	0.03	0.03
0.04	0.46	0.01	0.02	0.04
18.29	21.05	17.73	18.07	18.73
0.31	0.35	0.27	0.30	0.31
41.93	38.83	42.45	42.17	42.17
0.19	0.17	0.23	0.21	0.19
99.61	99.24	99.89	99.68	100.38
3.959	3.962	3.972	3.965	3.944
0.004	0.046	0.003	0.004	0.004
0.003	0.038	0.001	0.002	0.003
1.495	1.843	1.463	1.482	1.492
0.027	0.031	0.024	0.026	0.026
6.416	6.060	6.461	6.434	6.406
0.021	0.020	0.025	0.023	0.020
11.925	12.000	11.949	11.935	11.895
79.87	**76.19**	**80.52**	**80.14**	**79.59**

17GT3 ol3 South Fork Cone N 36.36198 W 118.28104 Lava 093017_17GT3_ol3 CORE 13 / 2 .	17GT3 ol4 South Fork Cone N 36.36198 W 118.28104 Lava 093017_17GT3_ol4 CORE 14 / 1 .	17GT3 ol4 South Fork Cone N 36.36198 W 118.28104 Lava 093017_17GT3_ol4 CORE 14 / 2 .	17GT3 ol5 South Fork Cone N 36.36198 W 118.28104 Lava 093017_17GT3_ol5 CORE 15 / 1 .	17GT3 ol5 South Fork Cone N 36.36198 W 118.28104 Lava 093017_17GT3_ol5 CORE 15 / 2 .
38.87	39.44	39.20	39.49	39.28
0.05	0.04	0.08	0.04	0.04
0.05	0.04	0.03	0.03	0.06
17.72	15.54	14.75	12.71	14.52
0.27	0.24	0.21	0.20	0.21
42.40	44.02	44.46	46.15	45.08
0.21	0.19	0.20	0.19	0.20
99.86	99.77	99.20	99.04	99.62
3.971	3.992	3.975	3.970	3.957
0.006	0.005	0.010	0.005	0.005
0.004	0.003	0.002	0.002	0.005
1.466	1.309	1.213	1.016	1.147
0.023	0.020	0.018	0.017	0.018
6.459	6.643	6.722	6.916	6.770
0.023	0.020	0.022	0.021	0.022
11.952	11.993	11.962	11.948	11.924
80.54	**83.04**	**83.89**	**86.20**	**84.28**

17GT3 ol6 South Fork Cone N 36.36198 W 118.28104 Lava 093017_17GT3_ol6 CORE 16 / 1 .	17GT3 ol6 South Fork Cone N 36.36198 W 118.28104 Lava 093017_17GT3_ol6 CORE 16 / 2 .	17GT3 ol7 South Fork Cone N 36.36198 W 118.28104 Lava 093017_17GT3_ol7 CORE 17 / 1 .	17GT3 ol7 South Fork Cone N 36.36198 W 118.28104 Lava 093017_17GT3_ol7 CORE 17 / 2 .	17GT3 ol8 South Fork Cone N 36.36198 W 118.28104 Lava 093017_17GT3_ol8 CORE 18 / 1 .
39.86	39.02	39.16	38.64	39.02
0.04	0.03	0.02	0.03	0.04
0.05	0.04	0.02	0.02	0.05
14.58	16.67	16.42	17.19	17.26
0.23	0.26	0.27	0.29	0.28
45.38	43.32	43.78	42.68	42.84
0.20	0.19	0.20	0.18	0.19
100.56	99.75	100.03	99.24	99.93
3.980	3.967	3.960	3.959	3.974
0.005	0.004	0.003	0.003	0.004
0.004	0.003	0.001	0.002	0.004
1.185	1.358	1.314	1.395	1.425
0.019	0.022	0.023	0.025	0.024
6.754	6.566	6.602	6.518	6.504
0.021	0.021	0.021	0.020	0.020
11.968	11.941	11.925	11.922	11.956
84.30	**81.80**	**82.16**	**81.11**	**81.12**

17GT3 ol8 South Fork Cone N 36.36198 W 118.28104 Lava 093017_17GT3_ol8 CORE 18 / 2 .	17GT3 ol9 South Fork Cone N 36.36198 W 118.28104 Lava 093017_17GT3_ol9 CORE 19 / 1 .	17GT3 ol9 South Fork Cone N 36.36198 W 118.28104 Lava 093017_17GT3_ol9 CORE 19 / 2 .	17GT3 ol10 South Fork Cone N 36.36198 W 118.28104 Lava 093017_17GT3_ol10 CORE 20 / 1 .	17GT3 ol10 South Fork Cone N 36.36198 W 118.28104 Lava 093017_17GT3_ol10 CORE 20 / 2 .
39.23	39.90	39.93	39.25	40.09
0.04	0.05	0.03	0.05	0.03
0.01	0.04	0.04	0.06	0.05
18.73	11.64	13.26	13.65	13.05
0.29	0.17	0.20	0.24	0.23
41.61	47.28	45.97	45.62	46.35
0.18	0.20	0.20	0.18	0.19
100.27	99.51	99.86	99.27	100.26
4.009	3.971	3.993	3.952	3.990
0.004	0.005	0.004	0.006	0.004
0.001	0.003	0.003	0.005	0.004
1.601	0.920	1.102	1.064	1.075
0.025	0.014	0.017	0.021	0.019
6.339	7.015	6.853	6.848	6.876
0.020	0.021	0.021	0.020	0.020
12.000	11.951	11.993	11.915	11.988
79.39	**87.47**	**85.66**	**85.20**	**85.93**

17BP1 ol1 Armstrong Canyon N 36.96207 W 118.25827 Lava 093017_17BP1_ol1 CORE 21 / 1 .	17BP1 ol1 Armstrong Canyon N 36.96207 W 118.25827 Lava 093017_17BP1_ol1 CORE 21 / 2 .	17BP1 ol2 Armstrong Canyon N 36.96207 W 118.25827 Lava 093017_17BP1_ol2 CORE 22 / 1 .	17BP1 ol2 Armstrong Canyon N 36.96207 W 118.25827 Lava 093017_17BP1_ol2 CORE 22 / 2 .	17BP1 ol3 Armstrong Canyon N 36.96207 W 118.25827 Lava 093017_17BP1_ol3 CORE 23 / 1 .
39.72	39.66	39.75	39.73	40.08
0.15	0.03	0.04	0.03	0.05
0.02	0.01	0.05	0.04	0.08
13.58	13.35	12.33	12.42	11.36
0.20	0.20	0.22	0.19	0.16
45.57	45.76	46.82	46.61	47.31
0.28	0.26	0.24	0.24	0.20
99.75	99.54	99.75	99.51	99.54
3.984	3.981	3.963	3.970	3.989
0.018	0.004	0.005	0.004	0.006
0.001	0.001	0.004	0.003	0.006
1.125	1.088	0.962	0.984	0.935
0.017	0.017	0.019	0.016	0.014
6.812	6.847	6.957	6.944	7.018
0.030	0.028	0.025	0.026	0.022
11.987	11.967	11.934	11.946	11.990
85.18	**85.44**	**86.65**	**86.55**	**87.74**

17BP1 ol3 Armstrong Canyon N 36.96207 W 118.25827 Lava 093017_17BP1_ol3 CORE 23 / 2 .	17BP1 ol4 Armstrong Canyon N 36.96207 W 118.25827 Lava 093017_17BP1_ol4 CORE 24 / 1 .	17BP1 ol4 Armstrong Canyon N 36.96207 W 118.25827 Lava 093017_17BP1_ol4 CORE 24 / 2 .	17BP1 ol5 Armstrong Canyon N 36.96207 W 118.25827 Lava 093017_17BP1_ol5 CORE 1 / 1 .	17BP1 ol5 Armstrong Canyon N 36.96207 W 118.25827 Lava 093017_17BP1_ol5 CORE 1 / 2 .
40.20	39.50	39.71	40.18	40.05
0.04	0.04	0.04	0.04	0.06
0.04	0.02	0.04	0.04	0.06
11.82	11.61	11.84	10.99	10.91
0.19	0.21	0.16	0.17	0.18
47.10	46.95	46.82	47.35	47.30
0.22	0.22	0.21	0.20	0.20
99.93	98.84	99.10	99.30	99.12
3.994	3.961	3.976	4.005	4.000
0.004	0.004	0.004	0.005	0.007
0.003	0.002	0.003	0.003	0.004
0.978	0.902	0.950	0.916	0.911
0.016	0.018	0.014	0.014	0.015
6.977	7.018	6.989	7.036	7.041
0.024	0.023	0.023	0.021	0.022
11.996	11.929	11.959	12.000	12.000
87.23	**87.37**	**87.18**	**88.08**	**88.13**

17BP1 ol6 Armstrong Canyon N 36.96207 W 118.25827 Lava 093017_17BP1_ol6 CORE 2 / 1 .	17BP1 ol6 Armstrong Canyon N 36.96207 W 118.25827 Lava 093017_17BP1_ol6 CORE 2 / 2 .	17BP1 ol7 Armstrong Canyon N 36.96207 W 118.25827 Lava 093017_17BP1_ol7 CORE 3 / 1 .	17BP1 ol7 Armstrong Canyon N 36.96207 W 118.25827 Lava 093017_17BP1_ol7 CORE 3 / 2 .	17BP1 ol8 Armstrong Canyon N 36.96207 W 118.25827 Lava 093017_17BP1_ol8 CORE 4 / 1 .
40.27	40.16	40.62	39.99	40.11
0.05	0.04	0.05	0.06	0.05
0.05	0.04	0.04	0.05	0.04
11.49	11.27	11.29	11.57	11.40
0.17	0.18	0.18	0.20	0.22
47.35	47.34	47.51	47.46	47.20
0.20	0.20	0.22	0.22	0.21
99.89	99.57	100.20	100.02	99.55
3.997	3.996	4.017	3.968	3.994
0.006	0.005	0.006	0.007	0.005
0.004	0.003	0.003	0.004	0.003
0.954	0.938	0.933	0.906	0.946
0.014	0.015	0.015	0.017	0.018
7.005	7.021	7.003	7.021	7.007
0.022	0.022	0.023	0.023	0.022
12.000	12.000	12.000	11.946	11.997
87.62	**87.81**	**87.82**	**87.53**	**87.62**

17BP1 ol8 Armstrong Canyon N 36.96207 W 118.25827 Lava 093017_17BP1_ol8 CORE 4 / 2 .	17BP1 ol9 Armstrong Canyon N 36.96207 W 118.25827 Lava 093017_17BP1_ol9 CORE 5 / 1 .	17BP1 ol9 Armstrong Canyon N 36.96207 W 118.25827 Lava 093017_17BP1_ol9 CORE 5 / 2 .	17BP1 ol10 Armstrong Canyon N 36.96207 W 118.25827 Lava 093017_17BP1_ol10 CORE 6 / 1 .	17BP1 ol10 Armstrong Canyon N 36.96207 W 118.25827 Lava 093017_17BP1_ol10 CORE 6 / 2 .
40.09	39.64	39.82	39.89	39.62
0.05	0.07	0.05	0.05	0.05
0.05	0.06	0.04	0.03	0.04
11.22	11.31	11.31	12.32	12.07
0.18	0.14	0.18	0.17	0.19
47.60	47.55	47.64	46.59	46.77
0.20	0.20	0.20	0.21	0.19
99.71	99.35	99.54	99.52	99.25
3.979	3.949	3.957	3.986	3.965
0.006	0.008	0.006	0.006	0.006
0.004	0.004	0.003	0.002	0.003
0.900	0.854	0.862	1.009	0.951
0.015	0.012	0.015	0.014	0.016
7.043	7.062	7.058	6.940	6.978
0.021	0.022	0.021	0.022	0.021
11.968	11.912	11.923	11.980	11.940
87.91	**87.85**	**87.85**	**86.69**	**86.95**

17BP3 ol1 Papoose Canyon N 37.01527 W 118.17319 Lower Lava 092917_17BP3_ol1 CORE 11 / 1 .	17BP3 ol1 Papoose Canyon N 37.01527 W 118.17319 Lower Lava 092917_17BP3_ol1 CORE 11 / 2 .	17BP3 ol2 Papoose Canyon N 37.01527 W 118.17319 Lower Lava 092917_17BP3_ol2 CORE 12 / 1 .	17BP3 ol2 Papoose Canyon N 37.01527 W 118.17319 Lower Lava 092917_17BP3_ol2 CORE 12 / 2 .	17BP3 ol3 Papoose Canyon N 37.01527 W 118.17319 Lower Lava 092917_17BP3_ol3 CORE 13 / 1 .
39.76	39.85	39.73	39.50	39.40
0.06	0.06	0.06	0.07	0.03
0.04	0.03	0.05	0.03	0.02
11.95	12.05	11.58	11.81	11.66
0.17	0.18	0.16	0.19	0.14
46.78	46.92	47.30	47.11	47.50
0.21	0.21	0.20	0.21	0.07
99.30	99.60	99.47	99.28	99.09
3.977	3.973	3.960	3.947	3.933
0.008	0.007	0.008	0.008	0.004
0.004	0.003	0.004	0.002	0.002
0.964	0.961	0.896	0.891	0.845
0.015	0.015	0.013	0.016	0.012
6.975	6.975	7.029	7.017	7.068
0.023	0.022	0.021	0.022	0.008
11.965	11.956	11.931	11.904	11.872
87.06	**87.00**	**87.55**	**87.25**	**87.68**

17BP3 ol3 Papoose Canyon N 37.01527 W 118.17319 Lower Lava 092917_17BP3_ol3 CORE 13 / 2 .	17BP3 ol4 Papoose Canyon N 37.01527 W 118.17319 Lower Lava 092917_17BP3_ol4 CORE 14 / 1 .	17BP3 ol4 Papoose Canyon N 37.01527 W 118.17319 Lower Lava 092917_17BP3_ol4 CORE 14 / 2 .	17BP3 ol5 Papoose Canyon N 37.01527 W 118.17319 Lower Lava 092917_17BP3_ol5 CORE 15 / 1 .	17BP3 ol5 Papoose Canyon N 37.01527 W 118.17319 Lower Lava 092917_17BP3_ol5 CORE 15 / 2 .
40.14	39.68	39.62	39.64	40.07
0.03	0.03	0.04	0.04	0.05
0.00	0.07	0.05	0.03	0.03
11.60	12.05	12.39	12.31	12.12
0.16	0.17	0.20	0.21	0.18
47.46	47.14	46.60	46.63	46.63
0.07	0.21	0.22	0.22	0.22
99.74	99.58	99.35	99.36	99.77
3.986	3.951	3.964	3.966	4.000
0.003	0.004	0.005	0.005	0.006
0.000	0.006	0.004	0.002	0.003
0.939	0.916	0.974	0.969	1.012
0.014	0.014	0.017	0.018	0.016
7.026	6.999	6.950	6.955	6.940
0.008	0.022	0.023	0.024	0.023
11.975	11.912	11.937	11.939	12.000
87.70	**87.06**	**86.58**	**86.64**	**86.85**

17BP3 ol6 Papoose Canyon N 37.01527 W 118.17319 Lower Lava 092917_17BP3_ol6 CORE 16 / 1 .	17BP3 ol6 Papoose Canyon N 37.01527 W 118.17319 Lower Lava 092917_17BP3_ol6 CORE 16 / 2 .	17BP3 ol7 Papoose Canyon N 37.01527 W 118.17319 Lower Lava 092917_17BP3_ol7 CORE 17 / 1 .	17BP3 ol7 Papoose Canyon N 37.01527 W 118.17319 Lower Lava 092917_17BP3_ol7 CORE 17 / 2 .	17BP3 ol8 Papoose Canyon N 37.01527 W 118.17319 Lower Lava 092917_17BP3_ol8 CORE 18 / 1 .
39.87	39.96	39.53	39.91	39.89
0.05	0.05	0.06	0.06	0.06
0.03	0.03	0.04	0.02	0.03
11.66	11.48	11.61	12.30	12.77
0.19	0.18	0.20	0.22	0.21
47.18	47.32	47.09	46.80	46.73
0.18	0.20	0.20	0.17	0.24
99.49	99.58	99.08	99.87	100.20
3.973	3.978	3.956	3.977	3.964
0.006	0.006	0.006	0.007	0.007
0.003	0.003	0.003	0.002	0.002
0.927	0.920	0.893	0.988	0.998
0.016	0.015	0.017	0.019	0.018
7.010	7.022	7.024	6.952	6.923
0.019	0.021	0.022	0.019	0.025
11.955	11.965	11.922	11.963	11.937
87.43	**87.63**	**87.43**	**86.75**	**86.24**

17BP3 ol8 Papoose Canyon N 37.01527 W 118.17319 Lower Lava 092917_17BP3_ol8 CORE 18 / 2 .	17BP3 ol9 Papoose Canyon N 37.01527 W 118.17319 Lower Lava 092917_17BP3_ol9 CORE 19 / 1 .	17BP3 ol9 Papoose Canyon N 37.01527 W 118.17319 Lower Lava 092917_17BP3_ol9 CORE 19 / 2 .	17BP3 ol10 Papoose Canyon N 37.01527 W 118.17319 Lower Lava 092917_17BP3_ol10 CORE 20 / 1 .	17BP3 ol10 Papoose Canyon N 37.01527 W 118.17319 Lower Lava 092917_17BP3_ol10 CORE 20 / 2 .
39.16	39.77	39.89	39.08	39.79
0.05	0.05	0.05	0.05	0.05
0.04	0.03	0.04	0.08	0.03
14.03	12.79	12.40	13.37	13.56
0.23	0.21	0.23	0.24	0.21
45.33	46.73	46.70	45.91	46.09
0.25	0.24	0.23	0.24	0.25
99.36	100.08	99.82	99.20	100.21
3.949	3.956	3.975	3.932	3.966
0.006	0.006	0.006	0.006	0.006
0.004	0.002	0.003	0.006	0.002
1.090	0.984	0.993	1.001	1.071
0.020	0.018	0.019	0.020	0.018
6.813	6.928	6.938	6.885	6.850
0.026	0.026	0.025	0.026	0.027
11.907	11.920	11.960	11.876	11.941
84.71	**86.22**	**86.56**	**85.47**	**85.36**

17BP4 ol1 Quarry Cone N 37.02192 W 118.18375 Lava 092917_17BP4_ol1 CORE 31 / 1 .	17BP4 ol1 Quarry Cone N 37.02192 W 118.18375 Lava 092917_17BP4_ol1 CORE 31 / 2 .	17BP4 ol2 Quarry Cone N 37.02192 W 118.18375 Lava 092917_17BP4_ol2 CORE 32 / 1 .	17BP4 ol2 Quarry Cone N 37.02192 W 118.18375 Lava 092917_17BP4_ol2 CORE 32 / 2 .	17BP4 ol3 Quarry Cone N 37.02192 W 118.18375 Lava 092917_17BP4_ol3 CORE 33 / 1 .
39.07	39.35	38.64	38.88	38.98
0.02	0.04	0.03	0.03	0.04
0.03	0.03	0.03	0.02	0.03
14.70	14.49	15.65	15.91	14.74
0.24	0.23	0.26	0.22	0.22
44.52	44.72	43.90	43.89	44.43
0.19	0.19	0.22	0.20	0.16
98.98	99.27	98.90	99.32	98.78
3.967	3.981	3.940	3.952	3.965
0.003	0.005	0.004	0.004	0.005
0.002	0.002	0.002	0.002	0.003
1.187	1.195	1.221	1.261	1.191
0.021	0.020	0.022	0.019	0.019
6.738	6.746	6.673	6.650	6.737
0.021	0.020	0.024	0.022	0.018
11.938	11.969	11.886	11.909	11.937
83.93	**84.20**	**82.85**	**82.68**	**83.93**

17BP4 ol3 Quarry Cone N 37.02192 W 118.18375 Lava 092917_17BP4_ol3 CORE 33 / 2 .	17BP4 ol4 Quarry Cone N 37.02192 W 118.18375 Lava 092917_17BP4_ol4 CORE 34 / 1 .	17BP4 ol4 Quarry Cone N 37.02192 W 118.18375 Lava 092917_17BP4_ol4 CORE 34 / 2 .	17BP4 ol5 Quarry Cone N 37.02192 W 118.18375 Lava 092917_17BP4_ol5 CORE 35 / 1 .	17BP4 ol5 Quarry Cone N 37.02192 W 118.18375 Lava 092917_17BP4_ol5 CORE 35 / 2 .
39.13	38.18	38.34	38.77	38.88
0.04	0.03	0.13	0.03	0.04
0.02	0.00	0.04	0.03	0.03
15.67	19.97	19.56	14.78	14.68
0.24	0.31	0.33	0.25	0.23
43.82	40.50	39.80	44.48	44.63
0.18	0.20	0.35	0.19	0.19
99.29	99.35	98.71	98.76	98.86
3.979	3.958	4.005	3.945	3.949
0.005	0.003	0.016	0.004	0.004
0.002	0.000	0.004	0.002	0.003
1.296	1.650	1.709	1.155	1.151
0.021	0.027	0.029	0.022	0.020
6.643	6.258	6.199	6.748	6.757
0.020	0.022	0.039	0.021	0.021
11.963	11.919	12.000	11.897	11.905
82.88	**77.85**	**77.72**	**83.84**	**84.00**

17BP4 ol6 Quarry Cone N 37.02192 W 118.18375 Lava 092917_17BP4_ol6 CORE 36 / 1 .	17BP4 ol6 Quarry Cone N 37.02192 W 118.18375 Lava 092917_17BP4_ol6 CORE 36 / 2 .	17BP4 ol7 Quarry Cone N 37.02192 W 118.18375 Lava 092917_17BP4_ol7 CORE 37 / 1 .	17BP4 ol7 Quarry Cone N 37.02192 W 118.18375 Lava 092917_17BP4_ol7 CORE 37 / 2 .	17BP4 ol8 Quarry Cone N 37.02192 W 118.18375 Lava 092917_17BP4_ol8 CORE 38 / 1 .
39.33	39.13	39.07	39.39	39.15
0.05	0.03	0.04	0.04	0.04
0.04	0.04	0.04	0.03	0.03
13.10	13.68	13.75	13.44	15.23
0.20	0.19	0.21	0.20	0.23
45.66	45.15	45.20	45.20	43.97
0.18	0.18	0.18	0.17	0.20
98.85	98.59	98.75	98.72	99.05
3.972	3.969	3.960	3.991	3.984
0.006	0.004	0.005	0.005	0.005
0.003	0.003	0.003	0.002	0.002
1.060	1.105	1.093	1.128	1.272
0.017	0.016	0.018	0.017	0.019
6.875	6.827	6.830	6.827	6.671
0.020	0.020	0.019	0.019	0.022
11.954	11.945	11.928	11.989	11.976
85.74	**85.09**	**85.03**	**85.31**	**83.30**

17BP4 ol8 Quarry Cone N 37.02192 W 118.18375 Lava 092917_17BP4_ol8 CORE 38 / 2 .	17BP4 ol9 Quarry Cone N 37.02192 W 118.18375 Lava 092917_17BP4_ol9 CORE 39 / 1 .	17BP4 ol9 Quarry Cone N 37.02192 W 118.18375 Lava 092917_17BP4_ol9 CORE 39 / 2 .	17BP4 ol10 Quarry Cone N 37.02192 W 118.18375 Lava 092917_17BP4_ol10 CORE 40 / 1 .	17BP4 ol10 Quarry Cone N 37.02192 W 118.18375 Lava 092917_17BP4_ol10 CORE 40 / 2 .
38.81	39.00	38.90	39.10	39.56
0.04	0.03	0.04	0.04	0.04
0.02	0.02	0.03	0.06	0.02
15.09	15.99	16.25	14.12	14.34
0.26	0.23	0.27	0.20	0.23
43.97	44.04	43.03	45.19	44.66
0.19	0.19	0.20	0.18	0.19
98.60	99.69	98.88	99.13	99.28
3.965	3.950	3.984	3.952	4.003
0.005	0.004	0.005	0.004	0.004
0.001	0.002	0.003	0.004	0.002
1.225	1.259	1.369	1.106	1.213
0.022	0.020	0.024	0.017	0.020
6.696	6.649	6.570	6.809	6.737
0.021	0.021	0.022	0.020	0.021
11.936	11.905	11.977	11.913	12.000
83.40	**82.65**	**82.05**	**84.69**	**84.31**

*FeO represents all Fe calculated as FeO.

APPENDIX B: NORMALIZED OLIVINE PHENOCRYST CORE COMPOSITIONS VIA EMPA

Comment	17GT6 ol1	17GT6 ol1	17GT6 ol2	17GT6 ol2	17GT6 ol3
Vent	Little Whitney Cone	Little Whitney Cone	Little Whitney Cone	Little Whitney Cone	Little Whitney Cone
Latitude	N 36.36795	N 36.36795	N 36.36795	N 36.36795	N 36.36795
Longitude	W 118.28320	W 118.28320	W 118.28320	W 118.28320	W 118.28320
Lithology	East Lava	East Lava	East Lava	East Lava	East Lava
Image #	092917_17GT6_ol1	092917_17GT6_ol1	092917_17GT6_ol2	092917_17GT6_ol2	092917_17GT6_ol3
Data	CORE	CORE	CORE	CORE	CORE
DataSet/Point	1 / 1 .	1 / 2 .	2 / 1 .	2 / 2 .	3 / 1 .
SiO_2	40.75	40.52	40.54	40.19	39.90
Al_2O_3	0.03	0.03	0.03	0.03	0.03
Cr_2O_3	0.06	0.05	0.06	0.04	0.03
FeO*	11.14	11.06	11.04	11.19	13.40
MnO	0.17	0.15	0.17	0.16	0.18
MgO	47.26	47.62	47.58	47.82	46.04
CaO	0.14	0.14	0.13	0.13	0.17
Total	100.00	100.00	100.00	100.00	100.00

17GT6 ol3 Little Whitney Cone N 36.36795 W 118.28320 East Lava 092917_17GT6_ol3 CORE 3 / 2 .	17GT6 ol4 Little Whitney Cone N 36.36795 W 118.28320 East Lava 092917_17GT6_ol4 CORE 4 / 1 .	17GT6 ol4 Little Whitney Cone N 36.36795 W 118.28320 East Lava 092917_17GT6_ol4 CORE 4 / 2 .	17GT6 ol5 Little Whitney Cone N 36.36795 W 118.28320 East Lava 092917_17GT6_ol5 CORE 5 / 1 .	17GT6 ol5 Little Whitney Cone N 36.36795 W 118.28320 East Lava 092917_17GT6_ol5 CORE 5 / 2 .
39.67	40.41	40.04	39.83	39.69
0.01	0.03	0.02	0.03	0.03
0.02	0.04	0.05	0.00	0.02
13.47	11.99	12.03	13.84	13.89
0.22	0.17	0.14	0.20	0.21
46.23	46.85	47.22	45.68	45.74
0.18	0.15	0.14	0.19	0.18
100.00	100.00	100.00	100.00	100.00

17GT6 ol6 Little Whitney Cone N 36.36795 W 118.28320 East Lava 092917_17GT6_ol6 CORE 6 / 1 .	17GT6 ol6 Little Whitney Cone N 36.36795 W 118.28320 East Lava 092917_17GT6_ol6 CORE 6 / 2 .	17GT6 ol7 Little Whitney Cone N 36.36795 W 118.28320 East Lava 092917_17GT6_ol7 CORE 7 / 1 .	17GT6 ol7 Little Whitney Cone N 36.36795 W 118.28320 East Lava 092917_17GT6_ol7 CORE 7 / 2 .	17GT6 ol8 Little Whitney Cone N 36.36795 W 118.28320 East Lava 092917_17GT6_ol8 CORE 8 / 1 .
40.11	39.54	39.81	39.89	39.96
0.03	0.02	0.02	0.03	0.03
0.04	0.03	0.04	0.05	0.05
12.18	13.62	12.60	12.49	10.76
0.19	0.21	0.17	0.18	0.15
46.93	46.15	46.89	46.89	48.41
0.16	0.17	0.16	0.16	0.13
100.00	100.00	100.00	100.00	100.00

17GT6 ol8 Little Whitney Cone N 36.36795 W 118.28320 East Lava 092917_17GT6_ol8 CORE 8 / 2 .	17GT6 ol9 Little Whitney Cone N 36.36795 W 118.28320 East Lava 092917_17GT6_ol9 CORE 9 / 1 .	17GT6 ol9 Little Whitney Cone N 36.36795 W 118.28320 East Lava 092917_17GT6_ol9 CORE 9 / 2 .	17GT6 ol10 Little Whitney Cone N 36.36795 W 118.28320 East Lava 092917_17GT6_ol10 CORE 10 / 1 .	17GT6 ol10 Little Whitney Cone N 36.36795 W 118.28320 East Lava 092917_17GT6_ol10 CORE 10 / 2 .
40.29	39.96	40.02	40.15	40.22
0.03	0.03	0.03	0.04	0.03
0.04	0.04	0.05	0.04	0.05
10.55	11.27	11.31	11.01	11.00
0.18	0.17	0.16	0.12	0.15
48.30	47.93	47.84	48.03	47.99
0.12	0.13	0.13	0.13	0.14
100.00	100.00	100.00	100.00	100.00

17GT8 ol1 Groundhog Cone N 36.36534 W 118.32214 Lava 092917_17GT8_ol1 CORE 21 / 1 .	17GT8 ol1 Groundhog Cone N 36.36534 W 118.32214 Lava 092917_17GT8_ol1 CORE 21 / 2 .	17GT8 ol2 Groundhog Cone N 36.36534 W 118.32214 Lava 092917_17GT8_ol2 CORE 22 / 1 .	17GT8 ol2 Groundhog Cone N 36.36534 W 118.32214 Lava 092917_17GT8_ol2 CORE 22 / 2 .	17GT8 ol3 Groundhog Cone N 36.36534 W 118.32214 Lava 092917_17GT8_ol3 CORE 23 / 1 .
38.28	38.41	38.47	37.85	38.30
0.02	0.03	0.02	0.01	0.02
0.00	0.00	0.01	0.00	0.01
20.88	21.10	20.07	22.29	19.67
0.29	0.32	0.27	0.35	0.30
40.16	39.82	40.77	39.21	41.38
0.13	0.13	0.14	0.14	0.14
100.00	100.00	100.00	100.00	100.00

17GT8 ol3 Groundhog Cone N 36.36534 W 118.32214 Lava 092917_17GT8_ol3 CORE 23 / 2 .	17GT8 ol4 Groundhog Cone N 36.36534 W 118.32214 Lava 092917_17GT8_ol4 CORE 24 / 1 .	17GT8 ol4 Groundhog Cone N 36.36534 W 118.32214 Lava 092917_17GT8_ol4 CORE 24 / 2 .	17GT8 ol5 Groundhog Cone N 36.36534 W 118.32214 Lava 092917_17GT8_ol5 CORE 25 / 1 .	17GT8 ol5 Groundhog Cone N 36.36534 W 118.32214 Lava 092917_17GT8_ol5 CORE 25 / 2 .
38.34	36.94	36.69	36.95	36.98
0.02	0.02	0.02	0.02	0.02
0.01	0.00	0.00	0.00	0.00
19.92	25.89	25.95	26.93	27.24
0.32	0.40	0.42	0.42	0.41
41.10	36.16	36.19	35.34	34.92
0.13	0.14	0.16	0.20	0.17
100.00	100.00	100.00	100.00	100.00

17GT8 ol6 Groundhog Cone N 36.36534 W 118.32214 Lava 092917_17GT8_ol6 CORE 26 / 1 .	17GT8 ol6 Groundhog Cone N 36.36534 W 118.32214 Lava 092917_17GT8_ol6 CORE 26 / 2 .	17GT8 ol7 Groundhog Cone N 36.36534 W 118.32214 Lava 092917_17GT8_ol7 CORE 27 / 1 .	17GT8 ol7 Groundhog Cone N 36.36534 W 118.32214 Lava 092917_17GT8_ol7 CORE 27 / 2 .	17GT8 ol8 Groundhog Cone N 36.36534 W 118.32214 Lava 092917_17GT8_ol8 CORE 28 / 1 .
37.81	37.51	38.12	37.61	36.81
0.02	0.03	0.02	0.01	0.73
0.01	0.00	0.01	0.01	0.01
22.70	25.29	21.87	23.89	27.59
0.36	0.41	0.32	0.38	0.48
38.73	36.40	39.40	37.79	33.75
0.17	0.16	0.14	0.15	0.22
100.00	100.00	100.00	100.00	100.00

17GT8 ol8 Groundhog Cone N 36.36534 W 118.32214 Lava 092917_17GT8_ol8 CORE 28 / 2 .	17GT8 ol9 Groundhog Cone N 36.36534 W 118.32214 Lava 092917_17GT8_ol9 CORE 29 / 1 .	17GT8 ol9 Groundhog Cone N 36.36534 W 118.32214 Lava 092917_17GT8_ol9 CORE 29 / 2 .	17GT8 ol10 Groundhog Cone N 36.36534 W 118.32214 Lava 092917_17GT8_ol10 CORE 30 / 1 .	17GT8 ol10 Groundhog Cone N 36.36534 W 118.32214 Lava 092917_17GT8_ol10 CORE 30 / 2 .
36.73	36.93	37.22	37.97	37.62
0.01	0.03	0.02	0.02	0.02
0.01	0.01	0.00	0.01	0.01
28.33	26.70	26.37	22.37	23.79
0.49	0.42	0.38	0.34	0.37
34.05	35.53	35.50	38.83	37.79
0.19	0.16	0.17	0.14	0.13
100.00	100.00	100.00	100.00	100.00

17GT10 ol1 Groundhog Cone N 36.35870 W 118.31567 Agglutinate 093017_17GT10_ol1 CORE 7 / 1 .	17GT10 ol1 Groundhog Cone N 36.35870 W 118.31567 Agglutinate 093017_17GT10_ol1 CORE 7 / 2 .	17GT10 ol2 Groundhog Cone N 36.35870 W 118.31567 Agglutinate 093017_17GT10_ol2 CORE 8 / 1 .	17GT10 ol2 Groundhog Cone N 36.35870 W 118.31567 Agglutinate 093017_17GT10_ol2 CORE 8 / 2 .	17GT10 ol3 Groundhog Cone N 36.35870 W 118.31567 Agglutinate 093017_17GT10_ol3 CORE 9 / 1 .
39.68	39.59	39.62	40.01	38.49
0.04	0.05	0.06	0.04	0.02
0.04	0.02	0.02	0.01	0.02
14.65	14.71	14.66	14.21	19.23
0.23	0.24	0.22	0.21	0.37
44.92	44.92	44.94	45.16	41.35
0.20	0.21	0.23	0.14	0.18
100.00	100.00	100.00	100.00	100.00

17GT10 ol3 Groundhog Cone N 36.35870 W 118.31567 Agglutinate 093017_17GT10_ol3 CORE 9 / 2 .	17GT10 ol4 Groundhog Cone N 36.35870 W 118.31567 Agglutinate 093017_17GT10_ol4 CORE 10 / 1 .	17GT10 ol4 Groundhog Cone N 36.35870 W 118.31567 Agglutinate 093017_17GT10_ol4 CORE 10 / 2 .	17GT10 ol5 Groundhog Cone N 36.35870 W 118.31567 Agglutinate 093017_17GT10_ol5 CORE 11 / 1 .	17GT10 ol5 Groundhog Cone N 36.35870 W 118.31567 Agglutinate 093017_17GT10_ol5 CORE 11 / 2 .
38.71	39.76	39.46	39.72	39.76
0.10	0.03	0.03	0.03	0.04
0.01	0.00	0.03	0.03	0.02
19.23	13.99	13.84	14.60	14.50
0.35	0.19	0.22	0.26	0.22
41.20	45.54	45.82	44.89	44.99
0.21	0.21	0.17	0.19	0.20
100.00	100.00	100.00	100.00	100.00

17GT10 ol6 Groundhog Cone N 36.35870 W 118.31567 Agglutinate 093017_17GT10_ol6 CORE 12 / 1 .	17GT10 ol6 Groundhog Cone N 36.35870 W 118.31567 Agglutinate 093017_17GT10_ol6 CORE 12 / 2 .	17GT10 ol7 Groundhog Cone N 36.35870 W 118.31567 Agglutinate 093017_17GT10_ol7 CORE 13 / 1 .	17GT10 ol7 Groundhog Cone N 36.35870 W 118.31567 Agglutinate 093017_17GT10_ol7 CORE 13 / 2 .	17GT10 ol8 Groundhog Cone N 36.35870 W 118.31567 Agglutinate 093017_17GT10_ol8 CORE 14 / 1 .
39.28	39.13	40.07	39.85	40.67
0.05	0.02	0.05	0.03	0.02
0.03	0.01	0.02	0.03	0.02
15.86	16.83	11.71	11.76	11.41
0.23	0.23	0.14	0.17	0.15
44.10	43.41	47.56	47.67	47.30
0.20	0.18	0.20	0.20	0.16
100.00	100.00	100.00	100.00	100.00

17GT10 ol8 Groundhog Cone N 36.35870 W 118.31567 Agglutinate 093017_17GT10_ol8 CORE 14 / 2 .	17GT10 ol9 Groundhog Cone N 36.35870 W 118.31567 Agglutinate 093017_17GT10_ol9 CORE 15 / 1 .	17GT10 ol9 Groundhog Cone N 36.35870 W 118.31567 Agglutinate 093017_17GT10_ol9 CORE 15 / 2 .	17GT10 ol10 Groundhog Cone N 36.35870 W 118.31567 Agglutinate 093017_17GT10_ol10 CORE 16 / 1 .	17GT10 ol10 Groundhog Cone N 36.35870 W 118.31567 Agglutinate 093017_17GT10_ol10 CORE 16 / 2 .
40.26	39.87	39.95	39.65	39.89
0.03	0.02	0.02	0.05	0.04
0.02	0.03	0.03	0.03	0.02
11.46	12.15	12.14	13.36	13.25
0.17	0.20	0.18	0.17	0.20
47.61	47.27	47.21	46.36	46.25
0.19	0.20	0.19	0.17	0.17
100.00	100.00	100.00	100.00	100.00

17GT2 ol1 Tunnel Cone N 36.36636 W 118.28241 Agglutinate 093017_17GT2_ol1 CORE 1 / 1 .	17GT2 ol1 Tunnel Cone N 36.36636 W 118.28241 Agglutinate 093017_17GT2_ol1 CORE 1 / 2 .	17GT2 ol2 Tunnel Cone N 36.36636 W 118.28241 Agglutinate 093017_17GT2_ol2 CORE 2 / 1 .	17GT2 ol2 Tunnel Cone N 36.36636 W 118.28241 Agglutinate 093017_17GT2_ol2 CORE 2 / 2 .	17GT2 ol3 Tunnel Cone N 36.36636 W 118.28241 Agglutinate 093017_17GT2_ol3 CORE 3 / 1 .
39.66	39.51	38.96	38.88	40.02
0.09	0.04	0.02	0.03	0.03
0.05	0.05	0.01	0.02	0.04
13.10	14.35	17.18	17.50	11.94
0.19	0.21	0.29	0.29	0.16
46.44	45.41	43.22	42.88	47.37
0.19	0.18	0.19	0.19	0.17
100.00	100.00	100.00	100.00	100.00

17GT2 ol3 Tunnel Cone N 36.36636 W 118.28241 Agglutinate 093017_17GT2_ol3 CORE 3 / 2 .	17GT2 ol4 Tunnel Cone N 36.36636 W 118.28241 Agglutinate 093017_17GT2_ol4 CORE 4 / 1 .	17GT2 ol4 Tunnel Cone N 36.36636 W 118.28241 Agglutinate 093017_17GT2_ol4 CORE 4 / 2 .	17GT2 ol5 Tunnel Cone N 36.36636 W 118.28241 Agglutinate 093017_17GT2_ol5 CORE 5 / 1 .	17GT2 ol5 Tunnel Cone N 36.36636 W 118.28241 Agglutinate 093017_17GT2_ol5 CORE 5 / 2 .
39.95	40.06	39.93	39.74	39.92
0.04	0.04	0.04	0.04	0.04
0.03	0.04	0.07	0.08	0.07
12.28	11.57	11.77	12.80	12.49
0.17	0.19	0.17	0.19	0.20
47.11	47.67	47.59	46.72	46.76
0.19	0.18	0.19	0.19	0.19
100.00	100.00	100.00	100.00	100.00

17GT2 ol6 Tunnel Cone N 36.36636 W 118.28241 Agglutinate 093017_17GT2_ol6 CORE 6 / 1 .	17GT2 ol6 Tunnel Cone N 36.36636 W 118.28241 Agglutinate 093017_17GT2_ol6 CORE 6 / 2 .	17GT2 ol7 Tunnel Cone N 36.36636 W 118.28241 Agglutinate 093017_17GT2_ol7 CORE 7 / 1 .	17GT2 ol7 Tunnel Cone N 36.36636 W 118.28241 Agglutinate 093017_17GT2_ol7 CORE 7 / 2 .	17GT2 ol8 Tunnel Cone N 36.36636 W 118.28241 Agglutinate 093017_17GT2_ol8 CORE 8 / 1 .
39.32	38.82	38.89	39.31	39.76
0.04	0.04	0.04	0.03	0.04
0.02	0.02	0.01	0.03	0.05
16.07	16.67	17.26	16.92	13.60
0.25	0.24	0.31	0.28	0.19
43.86	43.86	43.14	43.05	45.96
0.18	0.17	0.19	0.19	0.18
100.00	100.00	100.00	100.00	100.00

17GT2 ol8 Tunnel Cone N 36.36636 W 118.28241 Agglutinate 093017_17GT2_ol8 CORE 8 / 2 .	17GT2 ol9 Tunnel Cone N 36.36636 W 118.28241 Agglutinate 093017_17GT2_ol9 CORE 9 / 1 .	17GT2 ol9 Tunnel Cone N 36.36636 W 118.28241 Agglutinate 093017_17GT2_ol9 CORE 9 / 2 .	17GT2 ol10 Tunnel Cone N 36.36636 W 118.28241 Agglutinate 093017_17GT2_ol10 CORE 10 / 1 .	17GT2 ol10 Tunnel Cone N 36.36636 W 118.28241 Agglutinate 093017_17GT2_ol10 CORE 10 / 2 .
39.37	40.19	40.18	39.38	39.27
0.05	0.06	0.06	0.04	0.05
0.03	0.04	0.05	0.05	0.07
14.74	10.87	10.86	14.45	14.71
0.22	0.15	0.17	0.21	0.19
45.12	48.20	48.17	45.38	45.18
0.20	0.17	0.18	0.19	0.18
100.00	100.00	100.00	100.00	100.00

17GT3 ol1 South Fork Cone N 36.36198 W 118.28104 Lava 093017_17GT3_ol1 CORE 11 / 1 .	17GT3 ol1 South Fork Cone N 36.36198 W 118.28104 Lava 093017_17GT3_ol1 CORE 11 / 2 .	17GT3 ol2 South Fork Cone N 36.36198 W 118.28104 Lava 093017_17GT3_ol2 CORE 12 / 1 .	17GT3 ol2 South Fork Cone N 36.36198 W 118.28104 Lava 093017_17GT3_ol2 CORE 12 / 2 .	17GT3 ol3 South Fork Cone N 36.36198 W 118.28104 Lava 093017_17GT3_ol3 CORE 13 / 1 .
38.73	38.13	38.96	38.86	38.56
0.03	0.38	0.03	0.03	0.03
0.04	0.46	0.01	0.02	0.04
18.36	21.21	17.75	18.13	18.66
0.31	0.35	0.28	0.30	0.30
42.10	39.12	42.50	42.30	42.01
0.19	0.18	0.23	0.21	0.18
100.00	100.00	100.00	100.00	100.00

17GT3 ol3 South Fork Cone N 36.36198 W 118.28104 Lava 093017_17GT3_ol3 CORE 13 / 2 .	17GT3 ol4 South Fork Cone N 36.36198 W 118.28104 Lava 093017_17GT3_ol4 CORE 14 / 1 .	17GT3 ol4 South Fork Cone N 36.36198 W 118.28104 Lava 093017_17GT3_ol4 CORE 14 / 2 .	17GT3 ol5 South Fork Cone N 36.36198 W 118.28104 Lava 093017_17GT3_ol5 CORE 15 / 1 .	17GT3 ol5 South Fork Cone N 36.36198 W 118.28104 Lava 093017_17GT3_ol5 CORE 15 / 2 .
38.92	39.53	39.52	39.88	39.43
0.05	0.04	0.08	0.04	0.04
0.05	0.04	0.03	0.03	0.06
17.74	15.58	14.87	12.83	14.57
0.27	0.24	0.21	0.20	0.21
42.46	44.12	44.82	46.59	45.25
0.21	0.19	0.20	0.20	0.20
100.00	100.00	100.00	100.00	100.00

17GT3 ol6 South Fork Cone N 36.36198 W 118.28104 Lava 093017_17GT3_ol6 CORE 16 / 1 .	17GT3 ol6 South Fork Cone N 36.36198 W 118.28104 Lava 093017_17GT3_ol6 CORE 16 / 2 .	17GT3 ol7 South Fork Cone N 36.36198 W 118.28104 Lava 093017_17GT3_ol7 CORE 17 / 1 .	17GT3 ol7 South Fork Cone N 36.36198 W 118.28104 Lava 093017_17GT3_ol7 CORE 17 / 2 .	17GT3 ol8 South Fork Cone N 36.36198 W 118.28104 Lava 093017_17GT3_ol8 CORE 18 / 1 .
39.64	39.12	39.14	38.94	39.04
0.04	0.03	0.02	0.03	0.04
0.05	0.04	0.02	0.02	0.05
14.50	16.71	16.41	17.32	17.27
0.22	0.26	0.27	0.29	0.28
45.13	43.43	43.77	43.01	42.87
0.20	0.19	0.20	0.19	0.19
100.00	100.00	100.00	100.00	100.00

17GT3 ol8 South Fork Cone N 36.36198 W 118.28104 Lava 093017_17GT3_ol8 CORE 18 / 2 .	17GT3 ol9 South Fork Cone N 36.36198 W 118.28104 Lava 093017_17GT3_ol9 CORE 19 / 1 .	17GT3 ol9 South Fork Cone N 36.36198 W 118.28104 Lava 093017_17GT3_ol9 CORE 19 / 2 .	17GT3 ol10 South Fork Cone N 36.36198 W 118.28104 Lava 093017_17GT3_ol10 CORE 20 / 1 .	17GT3 ol10 South Fork Cone N 36.36198 W 118.28104 Lava 093017_17GT3_ol10 CORE 20 / 2 .
39.12	40.09	39.98	39.54	39.99
0.04	0.05	0.03	0.05	0.03
0.01	0.04	0.04	0.06	0.05
18.68	11.70	13.28	13.75	13.02
0.29	0.17	0.20	0.24	0.23
41.49	47.51	46.03	45.95	46.22
0.18	0.20	0.20	0.19	0.19
100.00	100.00	100.00	100.00	100.00

17BP1 ol1 Armstrong Canyon N 36.96207 W 118.25827 Lava 093017_17BP1_ol1 CORE 21 / 1 .	17BP1 ol1 Armstrong Canyon N 36.96207 W 118.25827 Lava 093017_17BP1_ol1 CORE 21 / 2 .	17BP1 ol2 Armstrong Canyon N 36.96207 W 118.25827 Lava 093017_17BP1_ol2 CORE 22 / 1 .	17BP1 ol2 Armstrong Canyon N 36.96207 W 118.25827 Lava 093017_17BP1_ol2 CORE 22 / 2 .	17BP1 ol3 Armstrong Canyon N 36.96207 W 118.25827 Lava 093017_17BP1_ol3 CORE 23 / 1 .
39.82	39.84	39.86	39.92	40.27
0.15	0.03	0.04	0.03	0.05
0.02	0.01	0.05	0.04	0.08
13.61	13.42	12.36	12.48	11.41
0.20	0.20	0.22	0.19	0.16
45.68	45.97	46.94	46.84	47.53
0.28	0.27	0.24	0.24	0.20
100.00	100.00	100.00	100.00	100.00

17BP1 ol3 Armstrong Canyon N 36.96207 W 118.25827 Lava 093017_17BP1_ol3 CORE 23 / 2 .	17BP1 ol4 Armstrong Canyon N 36.96207 W 118.25827 Lava 093017_17BP1_ol4 CORE 24 / 1 .	17BP1 ol4 Armstrong Canyon N 36.96207 W 118.25827 Lava 093017_17BP1_ol4 CORE 24 / 2 .	17BP1 ol5 Armstrong Canyon N 36.96207 W 118.25827 Lava 093017_17BP1_ol5 CORE 1 / 1 .	17BP1 ol5 Armstrong Canyon N 36.96207 W 118.25827 Lava 093017_17BP1_ol5 CORE 1 / 2 .
40.23	39.97	40.07	40.46	40.41
0.04	0.04	0.04	0.04	0.06
0.04	0.02	0.04	0.04	0.06
11.83	11.75	11.94	11.07	11.01
0.19	0.21	0.17	0.17	0.18
47.13	47.50	47.25	47.68	47.72
0.22	0.22	0.21	0.20	0.21
100.00	100.00	100.00	100.00	100.00

17BP1 ol6 Armstrong Canyon N 36.96207 W 118.25827 Lava 093017_17BP1_ol6 CORE 2 / 1 .	17BP1 ol6 Armstrong Canyon N 36.96207 W 118.25827 Lava 093017_17BP1_ol6 CORE 2 / 2 .	17BP1 ol7 Armstrong Canyon N 36.96207 W 118.25827 Lava 093017_17BP1_ol7 CORE 3 / 1 .	17BP1 ol7 Armstrong Canyon N 36.96207 W 118.25827 Lava 093017_17BP1_ol7 CORE 3 / 2 .	17BP1 ol8 Armstrong Canyon N 36.96207 W 118.25827 Lava 093017_17BP1_ol8 CORE 4 / 1 .
40.32	40.33	40.54	39.98	40.29
0.05	0.04	0.05	0.06	0.05
0.05	0.04	0.04	0.05	0.04
11.51	11.32	11.26	11.57	11.45
0.17	0.18	0.18	0.20	0.22
47.40	47.54	47.41	47.45	47.42
0.20	0.20	0.21	0.22	0.21
100.00	100.00	100.00	100.00	100.00

17BP1 ol8 Armstrong Canyon N 36.96207 W 118.25827 Lava 093017_17BP1_ol8 CORE 4 / 2 .	17BP1 ol9 Armstrong Canyon N 36.96207 W 118.25827 Lava 093017_17BP1_ol9 CORE 5 / 1 .	17BP1 ol9 Armstrong Canyon N 36.96207 W 118.25827 Lava 093017_17BP1_ol9 CORE 5 / 2 .	17BP1 ol10 Armstrong Canyon N 36.96207 W 118.25827 Lava 093017_17BP1_ol10 CORE 6 / 1 .	17BP1 ol10 Armstrong Canyon N 36.96207 W 118.25827 Lava 093017_17BP1_ol10 CORE 6 / 2 .
40.20	39.90	40.00	40.08	39.92
0.05	0.07	0.05	0.05	0.05
0.05	0.06	0.04	0.03	0.04
11.26	11.39	11.36	12.38	12.16
0.18	0.14	0.18	0.17	0.19
47.74	47.86	47.86	46.81	47.12
0.20	0.20	0.20	0.21	0.20
100.00	100.00	100.00	100.00	100.00

17BP3 ol1 Papoose Canyon N 37.01527 W 118.17319 Lower Lava 092917_17BP3_ol1 CORE 11 / 1 .	17BP3 ol1 Papoose Canyon N 37.01527 W 118.17319 Lower Lava 092917_17BP3_ol1 CORE 11 / 2 .	17BP3 ol2 Papoose Canyon N 37.01527 W 118.17319 Lower Lava 092917_17BP3_ol2 CORE 12 / 1 .	17BP3 ol2 Papoose Canyon N 37.01527 W 118.17319 Lower Lava 092917_17BP3_ol2 CORE 12 / 2 .	17BP3 ol3 Papoose Canyon N 37.01527 W 118.17319 Lower Lava 092917_17BP3_ol3 CORE 13 / 1 .
40.04	40.01	39.94	39.79	39.76
0.07	0.06	0.06	0.07	0.03
0.04	0.03	0.05	0.03	0.02
12.03	12.10	11.64	11.90	11.76
0.18	0.18	0.16	0.20	0.15
47.11	47.11	47.56	47.45	47.94
0.21	0.21	0.20	0.21	0.07
100.00	100.00	100.00	100.00	100.00

17BP3 ol3 Papoose Canyon N 37.01527 W 118.17319 Lower Lava 092917_17BP3_ol3 CORE 13 / 2 .	17BP3 ol4 Papoose Canyon N 37.01527 W 118.17319 Lower Lava 092917_17BP3_ol4 CORE 14 / 1 .	17BP3 ol4 Papoose Canyon N 37.01527 W 118.17319 Lower Lava 092917_17BP3_ol4 CORE 14 / 2 .	17BP3 ol5 Papoose Canyon N 37.01527 W 118.17319 Lower Lava 092917_17BP3_ol5 CORE 15 / 1 .	17BP3 ol5 Papoose Canyon N 37.01527 W 118.17319 Lower Lava 092917_17BP3_ol5 CORE 15 / 2 .
40.24	39.84	39.88	39.89	40.16
0.03	0.03	0.04	0.04	0.05
0.00	0.07	0.05	0.03	0.03
11.63	12.10	12.48	12.39	12.15
0.16	0.17	0.20	0.21	0.18
47.58	47.34	46.90	46.93	46.74
0.07	0.21	0.22	0.23	0.22
100.00	100.00	100.00	100.00	100.00

17BP3 ol6 Papoose Canyon N 37.01527 W 118.17319 Lower Lava 092917_17BP3_ol6 CORE 16 / 1 .	17BP3 ol6 Papoose Canyon N 37.01527 W 118.17319 Lower Lava 092917_17BP3_ol6 CORE 16 / 2 .	17BP3 ol7 Papoose Canyon N 37.01527 W 118.17319 Lower Lava 092917_17BP3_ol7 CORE 17 / 1 .	17BP3 ol7 Papoose Canyon N 37.01527 W 118.17319 Lower Lava 092917_17BP3_ol7 CORE 17 / 2 .	17BP3 ol8 Papoose Canyon N 37.01527 W 118.17319 Lower Lava 092917_17BP3_ol8 CORE 18 / 1 .
40.07	40.13	39.90	39.97	39.81
0.05	0.05	0.06	0.06	0.06
0.03	0.03	0.04	0.02	0.03
11.72	11.52	11.72	12.31	12.74
0.20	0.18	0.20	0.22	0.21
47.43	47.52	47.53	46.86	46.64
0.18	0.20	0.21	0.17	0.24
100.00	100.00	100.00	100.00	100.00

17BP3 ol8 Papoose Canyon N 37.01527 W 118.17319 Lower Lava 092917_17BP3_ol8 CORE 18 / 2 .	17BP3 ol9 Papoose Canyon N 37.01527 W 118.17319 Lower Lava 092917_17BP3_ol9 CORE 19 / 1 .	17BP3 ol9 Papoose Canyon N 37.01527 W 118.17319 Lower Lava 092917_17BP3_ol9 CORE 19 / 2 .	17BP3 ol10 Papoose Canyon N 37.01527 W 118.17319 Lower Lava 092917_17BP3_ol10 CORE 20 / 1 .	17BP3 ol10 Papoose Canyon N 37.01527 W 118.17319 Lower Lava 092917_17BP3_ol10 CORE 20 / 2 .
39.42	39.74	39.96	39.40	39.70
0.05	0.05	0.05	0.05	0.05
0.04	0.03	0.04	0.08	0.03
14.12	12.78	12.42	13.47	13.53
0.24	0.21	0.23	0.24	0.21
45.62	46.69	46.78	46.28	46.00
0.25	0.24	0.23	0.24	0.25
100.00	100.00	100.00	100.00	100.00

17BP4 ol1 Quarry Cone N 37.02192 W 118.18375 Lava 092917_17BP4_ol1 CORE 31 / 1 .	17BP4 ol1 Quarry Cone N 37.02192 W 118.18375 Lava 092917_17BP4_ol1 CORE 31 / 2 .	17BP4 ol2 Quarry Cone N 37.02192 W 118.18375 Lava 092917_17BP4_ol2 CORE 32 / 1 .	17BP4 ol2 Quarry Cone N 37.02192 W 118.18375 Lava 092917_17BP4_ol2 CORE 32 / 2 .	17BP4 ol3 Quarry Cone N 37.02192 W 118.18375 Lava 092917_17BP4_ol3 CORE 33 / 1 .
39.47	39.64	39.07	39.14	39.46
0.02	0.04	0.03	0.03	0.04
0.03	0.03	0.03	0.02	0.03
14.86	14.59	15.83	16.02	14.92
0.24	0.24	0.26	0.22	0.22
44.98	45.05	44.39	44.19	44.98
0.19	0.19	0.22	0.20	0.17
100.00	100.00	100.00	100.00	100.00

17BP4 ol3 Quarry Cone N 37.02192 W 118.18375 Lava 092917_17BP4_ol3 CORE 33 / 2 .	17BP4 ol4 Quarry Cone N 37.02192 W 118.18375 Lava 092917_17BP4_ol4 CORE 34 / 1 .	17BP4 ol4 Quarry Cone N 37.02192 W 118.18375 Lava 092917_17BP4_ol4 CORE 34 / 2 .	17BP4 ol5 Quarry Cone N 37.02192 W 118.18375 Lava 092917_17BP4_ol5 CORE 35 / 1 .	17BP4 ol5 Quarry Cone N 37.02192 W 118.18375 Lava 092917_17BP4_ol5 CORE 35 / 2 .
39.41	38.43	38.84	39.26	39.33
0.04	0.03	0.13	0.03	0.04
0.02	0.00	0.04	0.03	0.03
15.78	20.10	19.82	14.96	14.84
0.24	0.31	0.33	0.25	0.23
44.14	40.77	40.32	45.04	45.14
0.18	0.20	0.35	0.20	0.19
100.00	100.00	100.00	100.00	100.00

17BP4 ol6 Quarry Cone N 37.02192 W 118.18375 Lava 092917_17BP4_ol6 CORE 36 / 1 .	17BP4 ol6 Quarry Cone N 37.02192 W 118.18375 Lava 092917_17BP4_ol6 CORE 36 / 2 .	17BP4 ol7 Quarry Cone N 37.02192 W 118.18375 Lava 092917_17BP4_ol7 CORE 37 / 1 .	17BP4 ol7 Quarry Cone N 37.02192 W 118.18375 Lava 092917_17BP4_ol7 CORE 37 / 2 .	17BP4 ol8 Quarry Cone N 37.02192 W 118.18375 Lava 092917_17BP4_ol8 CORE 38 / 1 .
39.78	39.68	39.56	39.90	39.52
0.05	0.03	0.04	0.04	0.04
0.04	0.04	0.04	0.03	0.03
13.25	13.88	13.92	13.62	15.37
0.20	0.19	0.21	0.20	0.23
46.19	45.79	45.77	45.79	44.39
0.18	0.19	0.18	0.18	0.21
100.00	100.00	100.00	100.00	100.00

17BP4 ol8 Quarry Cone N 37.02192 W 118.18375 Lava 092917_17BP4_ol8 CORE 38 / 2 .	17BP4 ol9 Quarry Cone N 37.02192 W 118.18375 Lava 092917_17BP4_ol9 CORE 39 / 1 .	17BP4 ol9 Quarry Cone N 37.02192 W 118.18375 Lava 092917_17BP4_ol9 CORE 39 / 2 .	17BP4 ol10 Quarry Cone N 37.02192 W 118.18375 Lava 092917_17BP4_ol10 CORE 40 / 1 .	17BP4 ol10 Quarry Cone N 37.02192 W 118.18375 Lava 092917_17BP4_ol10 CORE 40 / 2 .
39.36	39.12	39.34	39.45	39.84
0.05	0.03	0.04	0.04	0.04
0.02	0.02	0.03	0.06	0.02
15.30	16.04	16.43	14.24	14.44
0.26	0.23	0.28	0.20	0.23
44.59	44.18	43.52	45.59	44.98
0.20	0.20	0.20	0.19	0.19
100.00	100.00	100.00	100.00	100.00

FeO* represents all Fe calculated as FeO.

APPENDIX C: BSE IMAGES AND EMP ANALYSIS LOCATIONS

Images in this section are shown with sample names and olivine numbers (ten per sample) in the upper left hand corner. The numbered points refer to the location of EMP analyses for each olivine. The values determined by these analyses can be found in Appendices A and B.

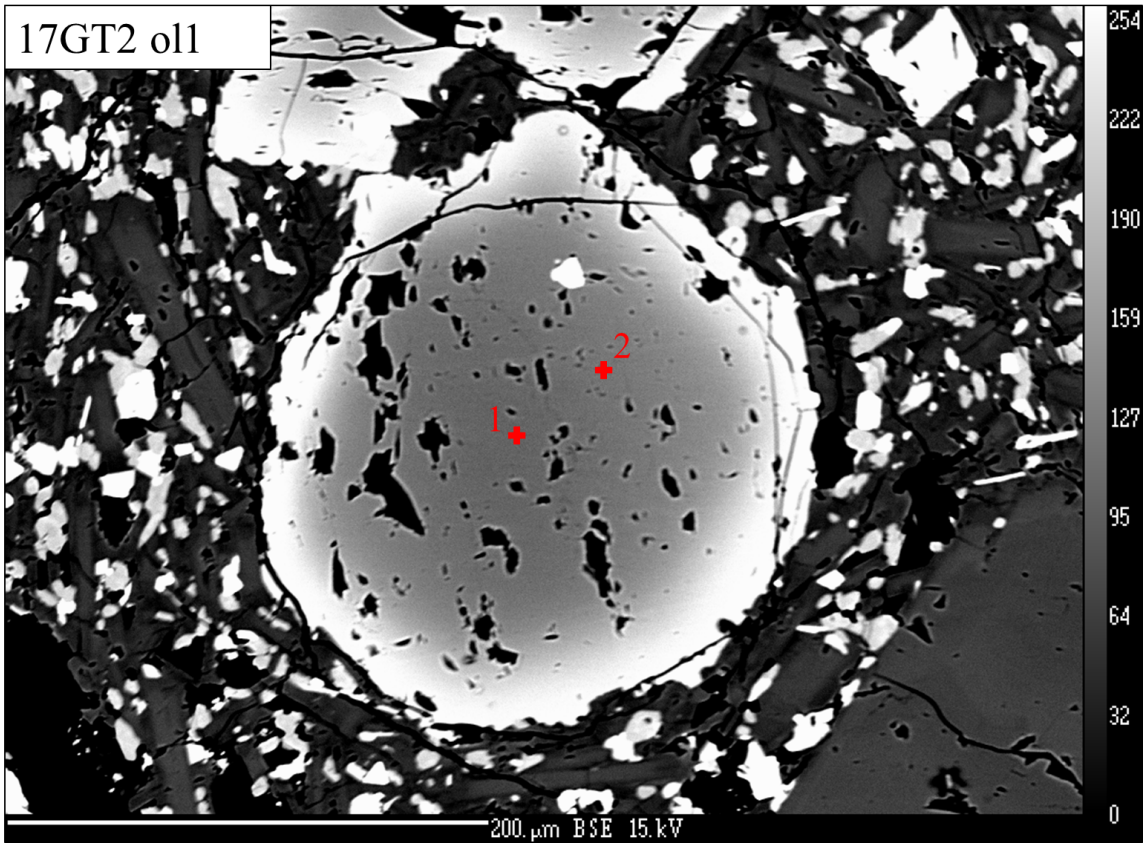

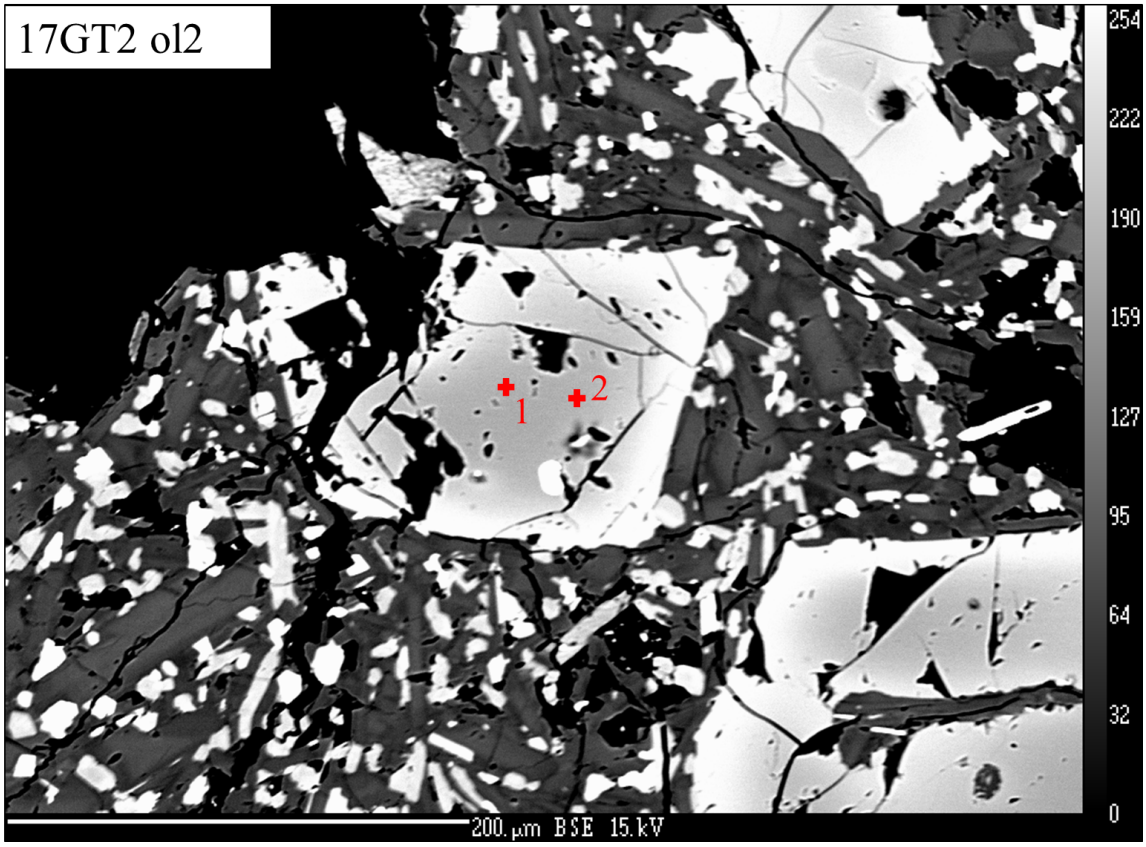
17GT2 ol2
1
2
254
222
190
159
127
95
64
32
0
200.µm BSE 15.kV

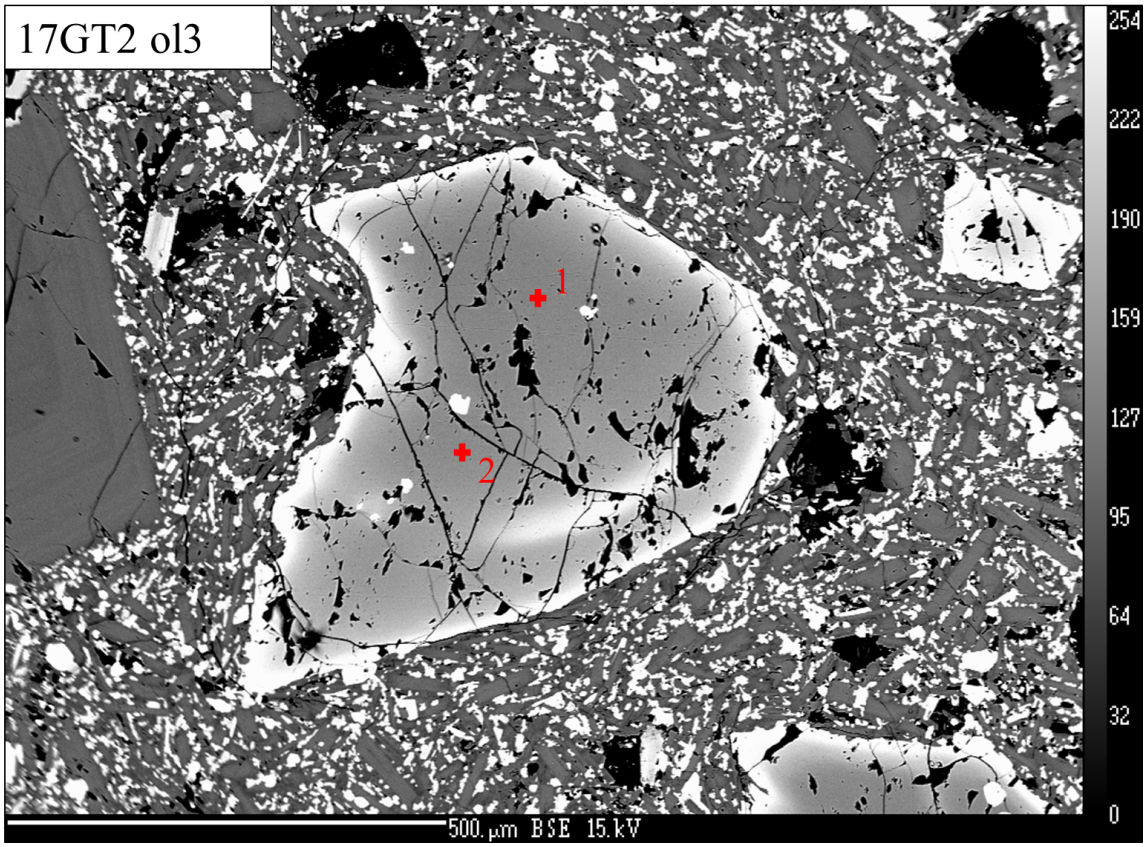
17GT2 ol3
1
2
500.µm BSE 15.kV
254
222
190
159
127
95
64
32
0

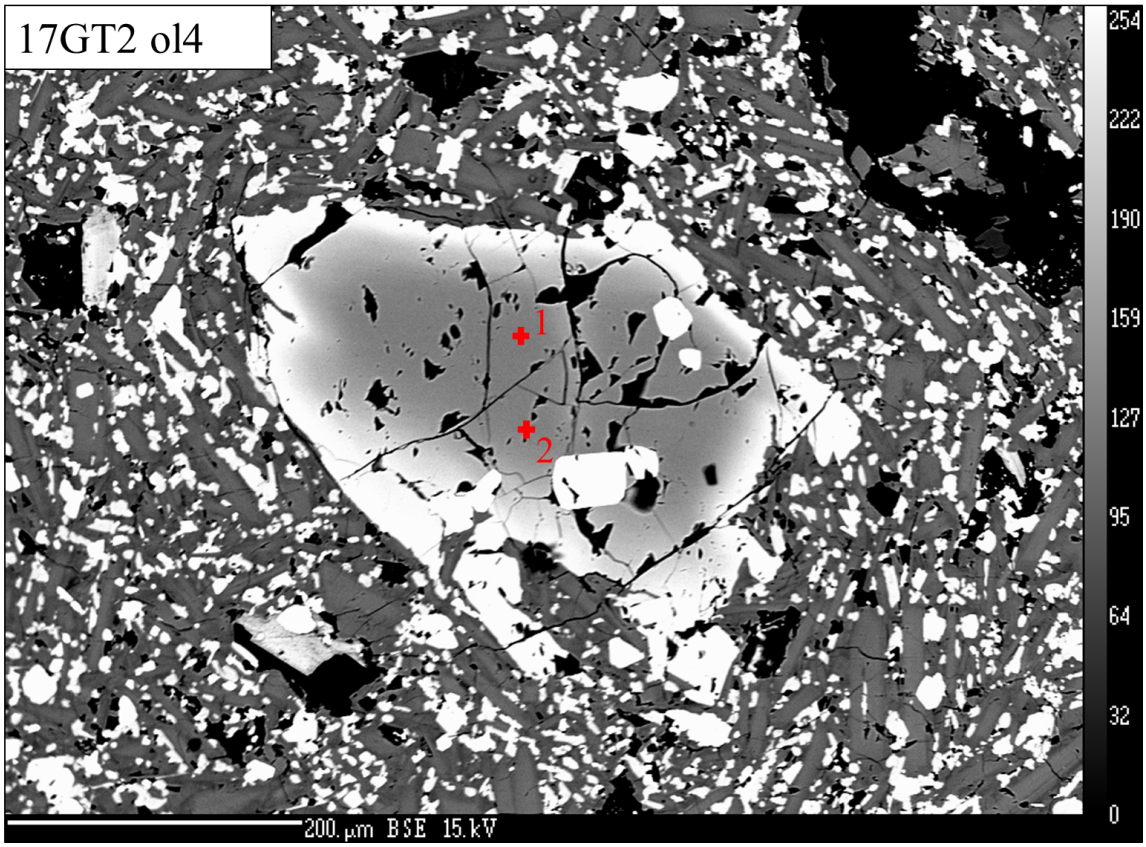
17GT2 ol4
1
2
254
222
190
159
127
95
64
32
0
200.μm BSE 15.kV

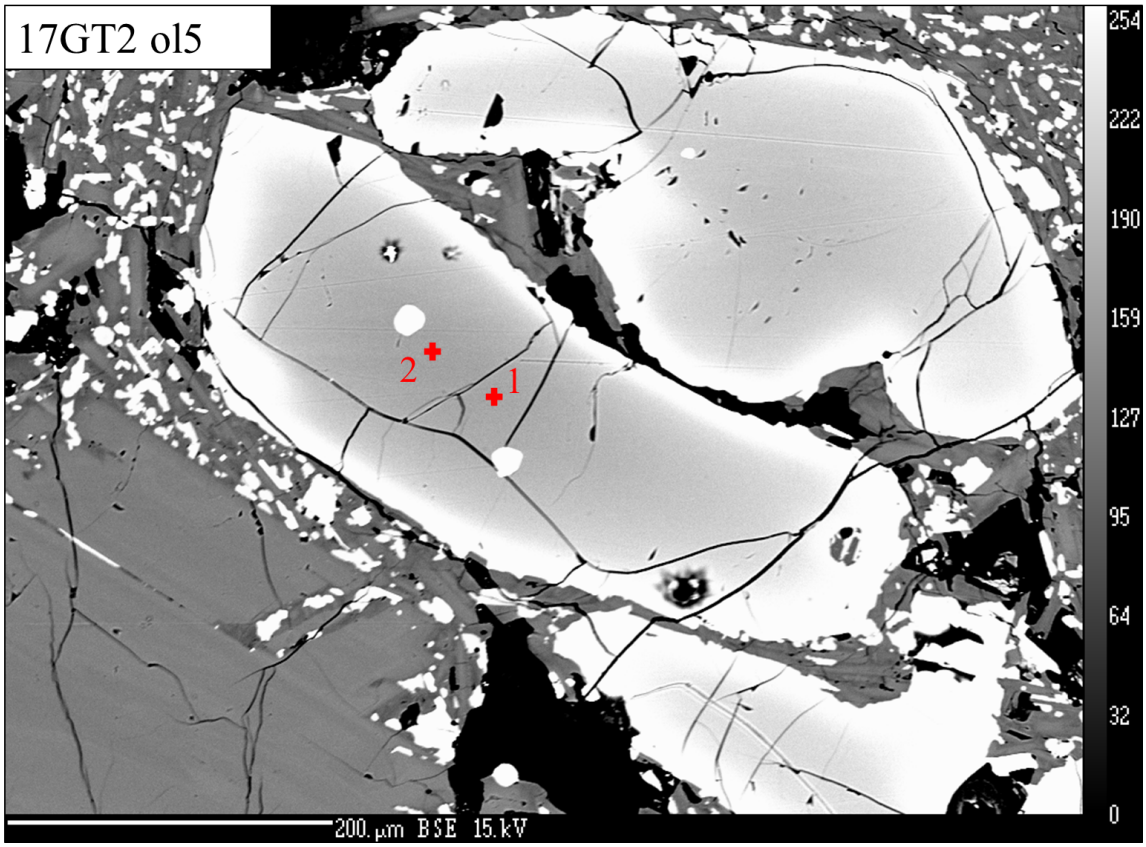
17GT2 ol5
2
1
254
222
190
159
127
95
64
32
0
200.μm BSE 15.kV

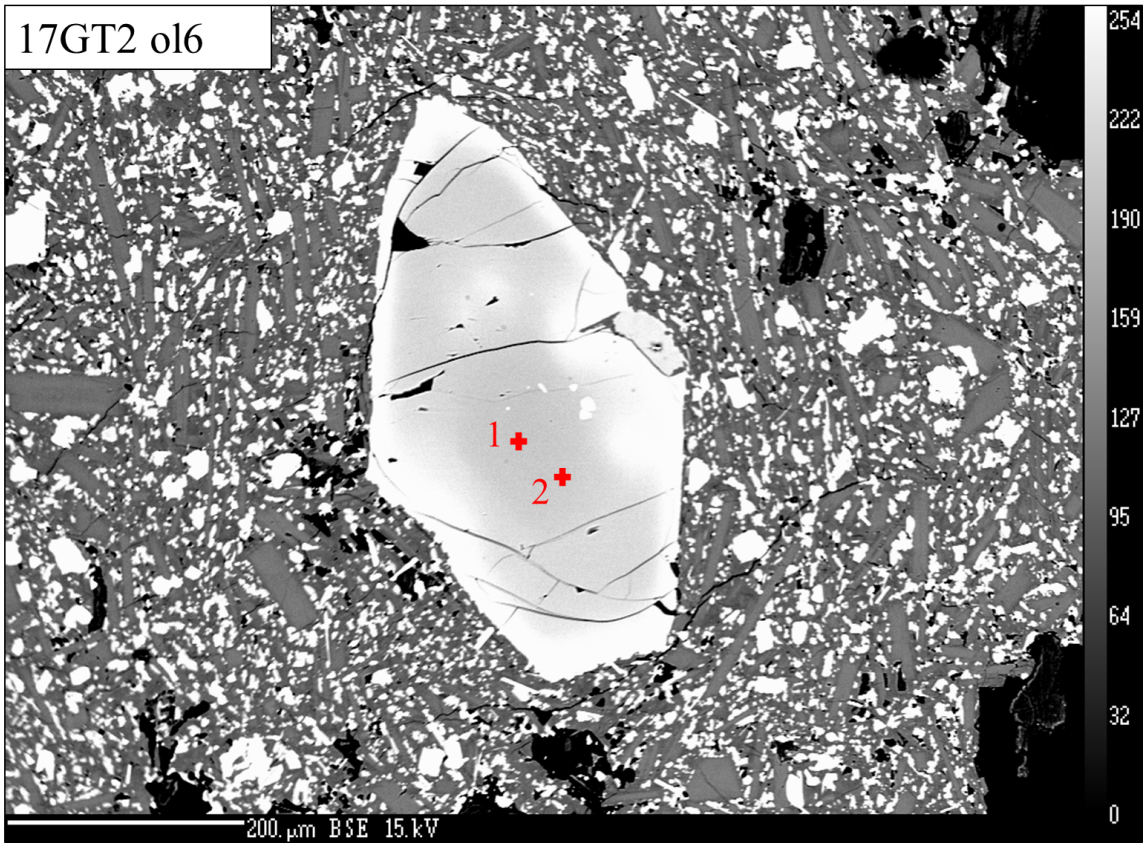
17GT2 ol6
1
2
200.μm BSE 15.kV
254
222
190
159
127
95
64
32
0

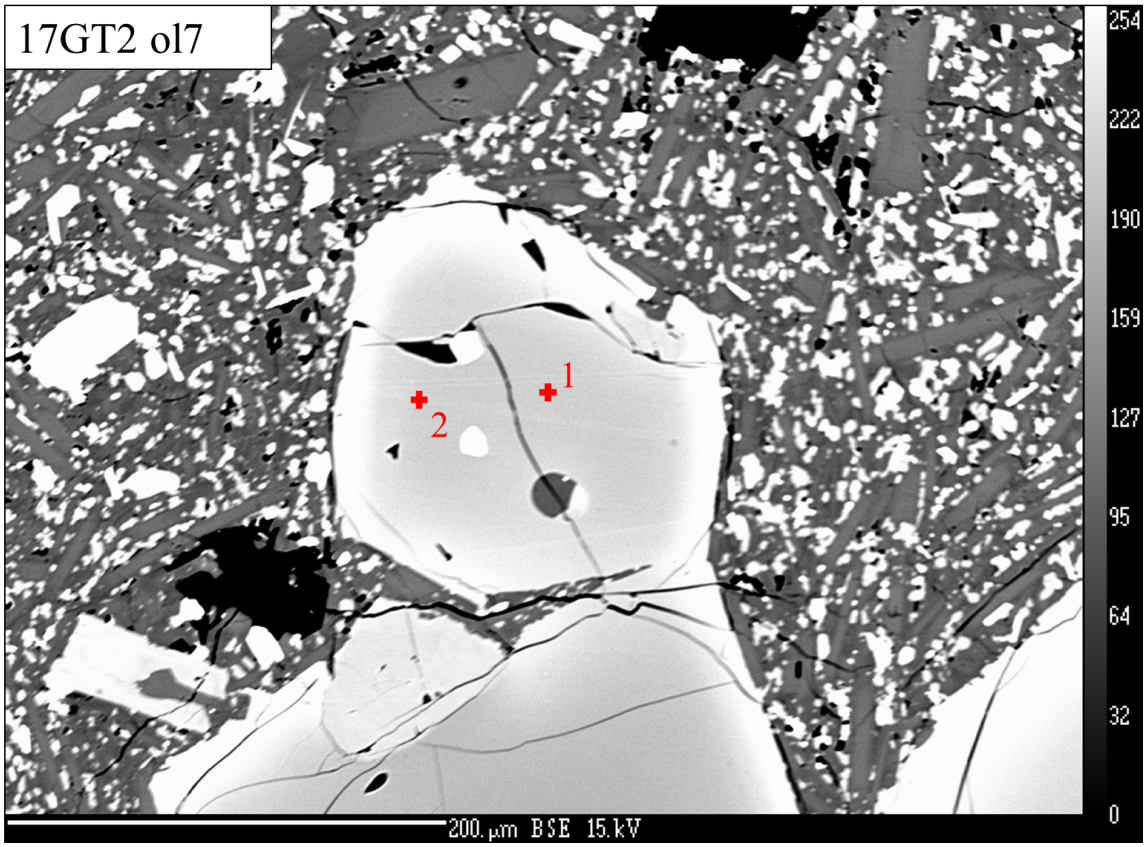
17GT2 ol7
1
2
254
222
190
159
127
95
64
32
0
200.µm BSE 15.kV

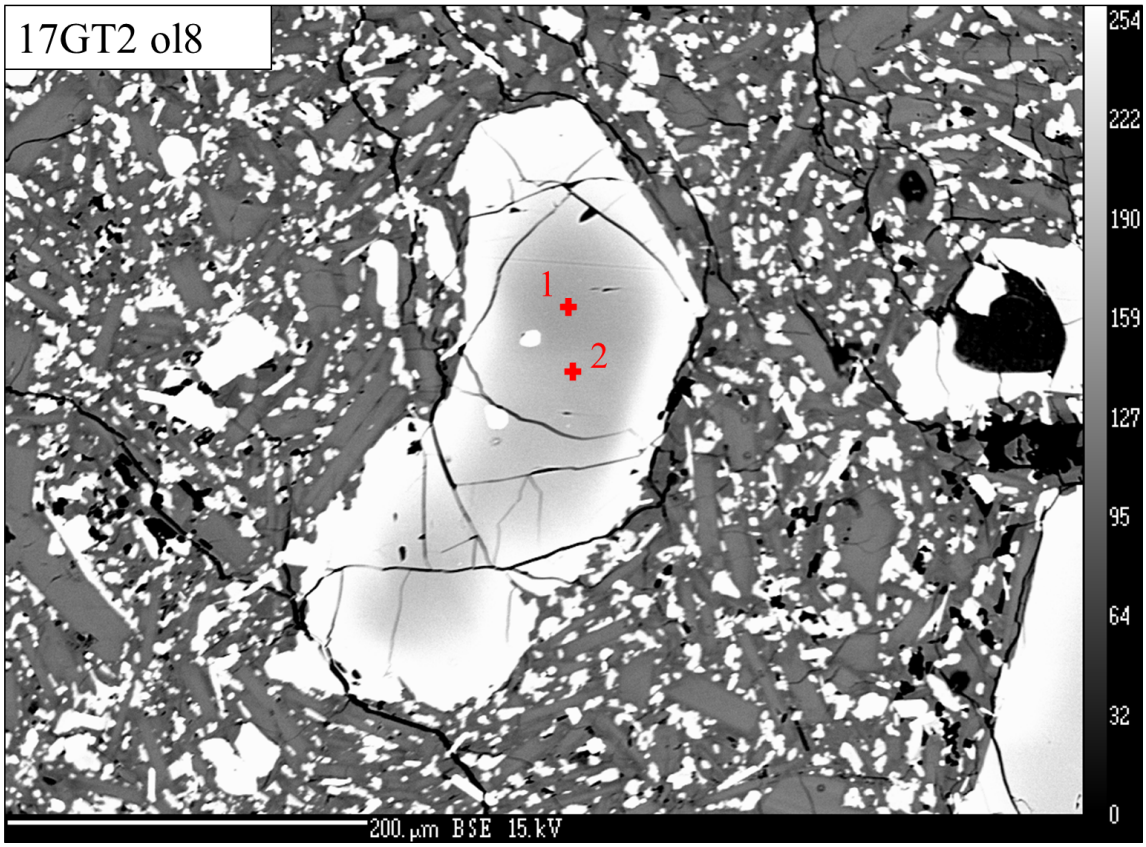
17GT2 ol8
1
2
254
222
190
159
127
95
64
32
0
200 µm BSE 15 kV

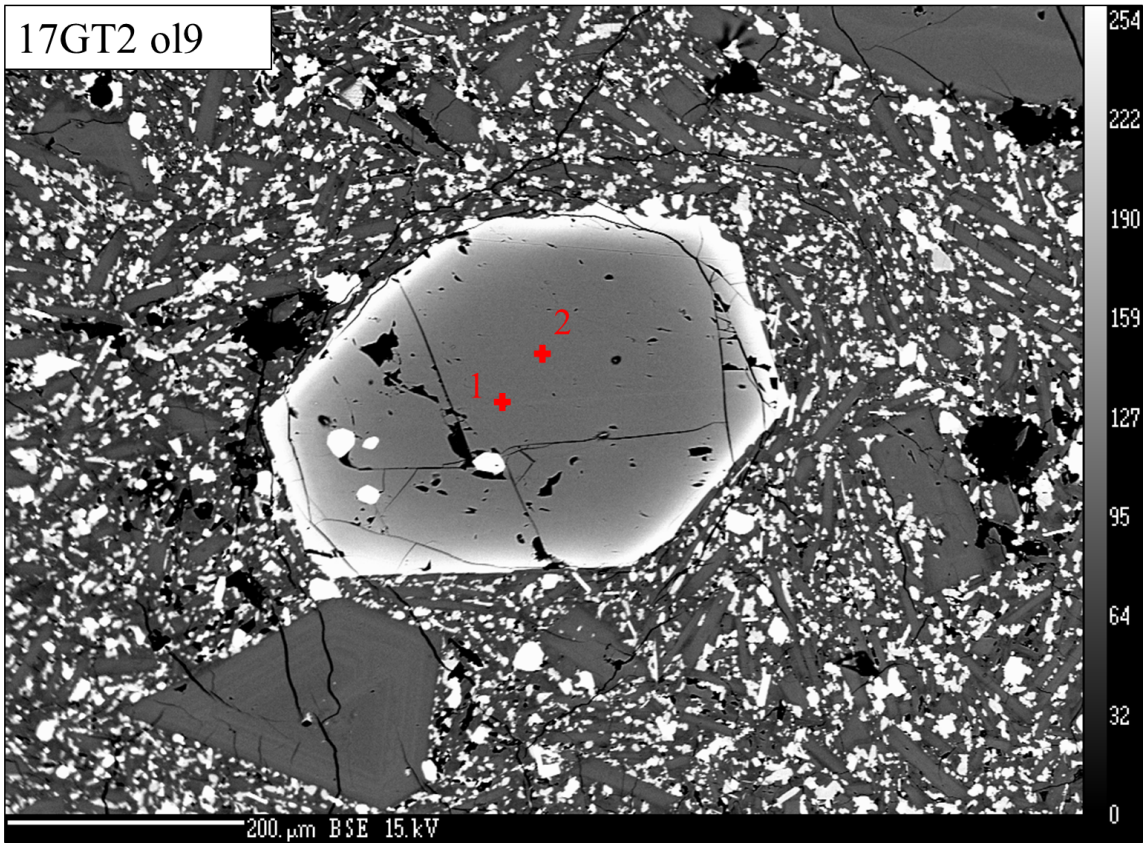
17GT2 ol9
1
2
200.μm BSE 15.kV
254
222
190
159
127
95
64
32
0

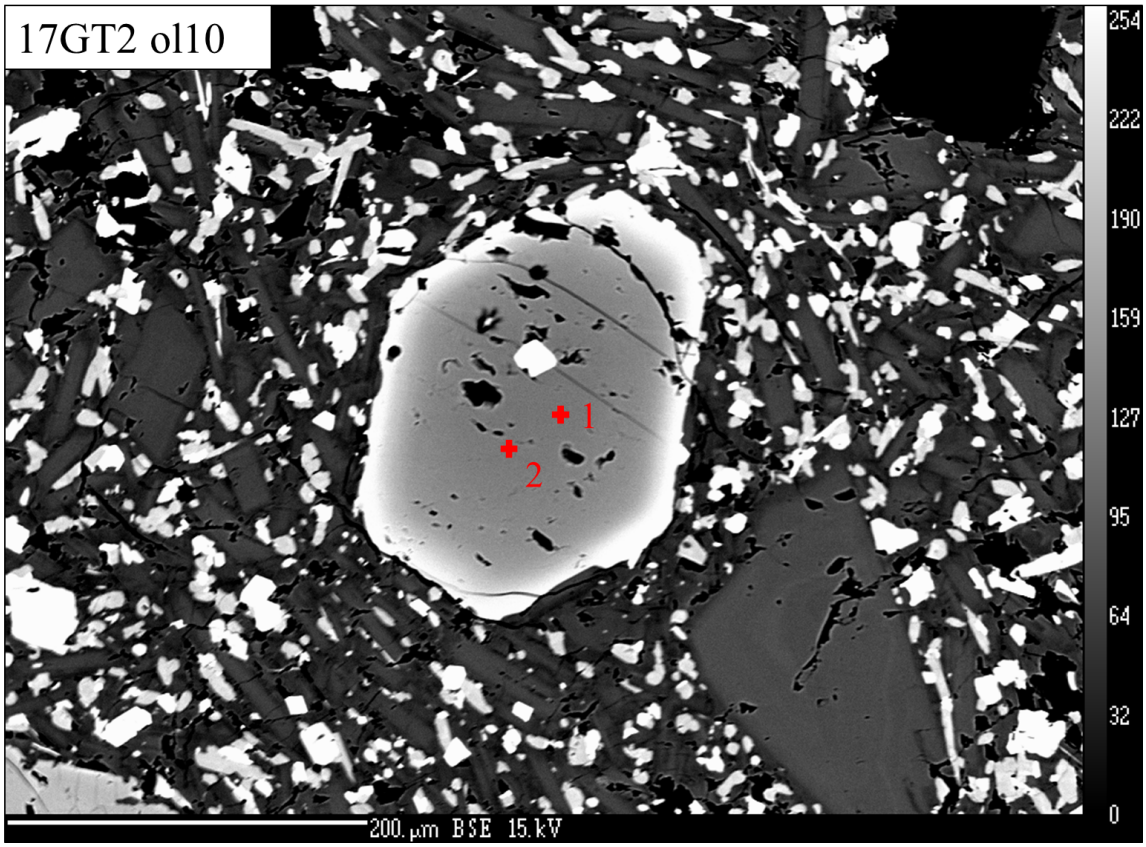
17GT2 ol10
1
2
254
222
190
159
127
95
64
32
0
200 μm BSE 15 kV

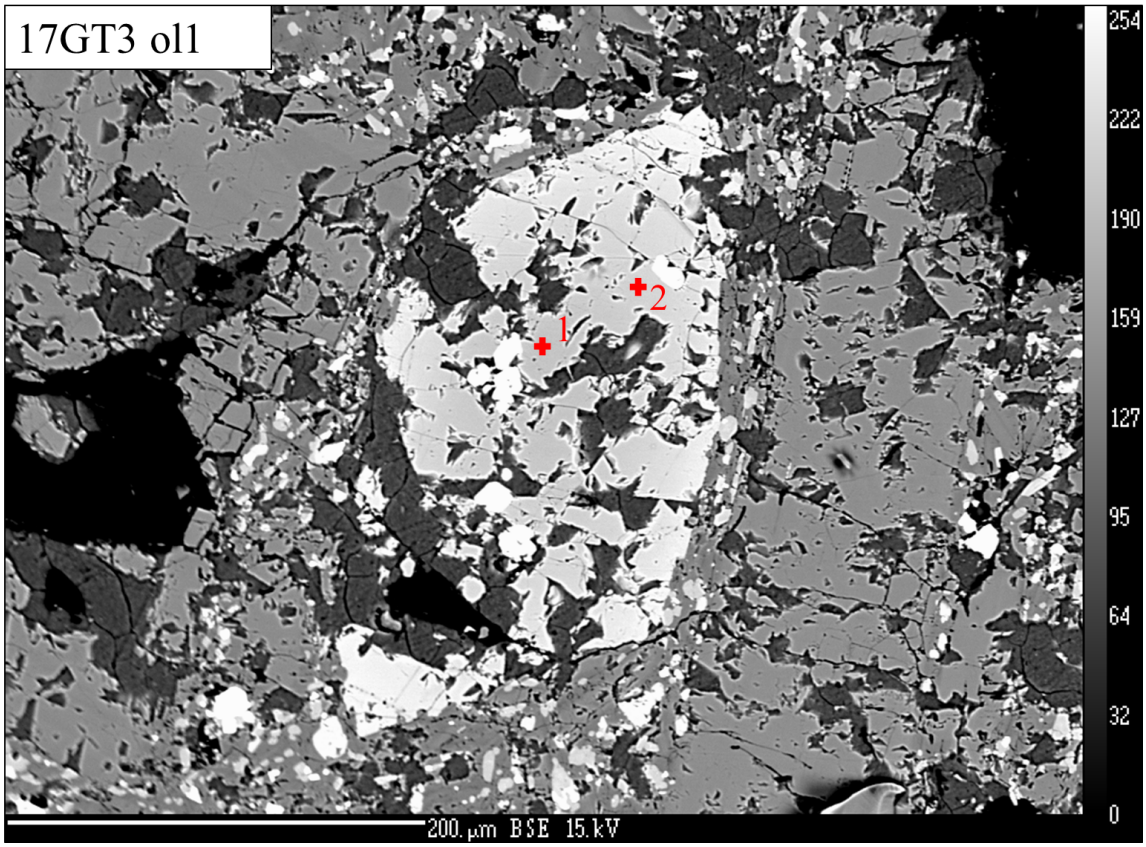
17GT3 ol1
1
2
254
222
190
159
127
95
64
32
0
200.µm BSE 15.kV

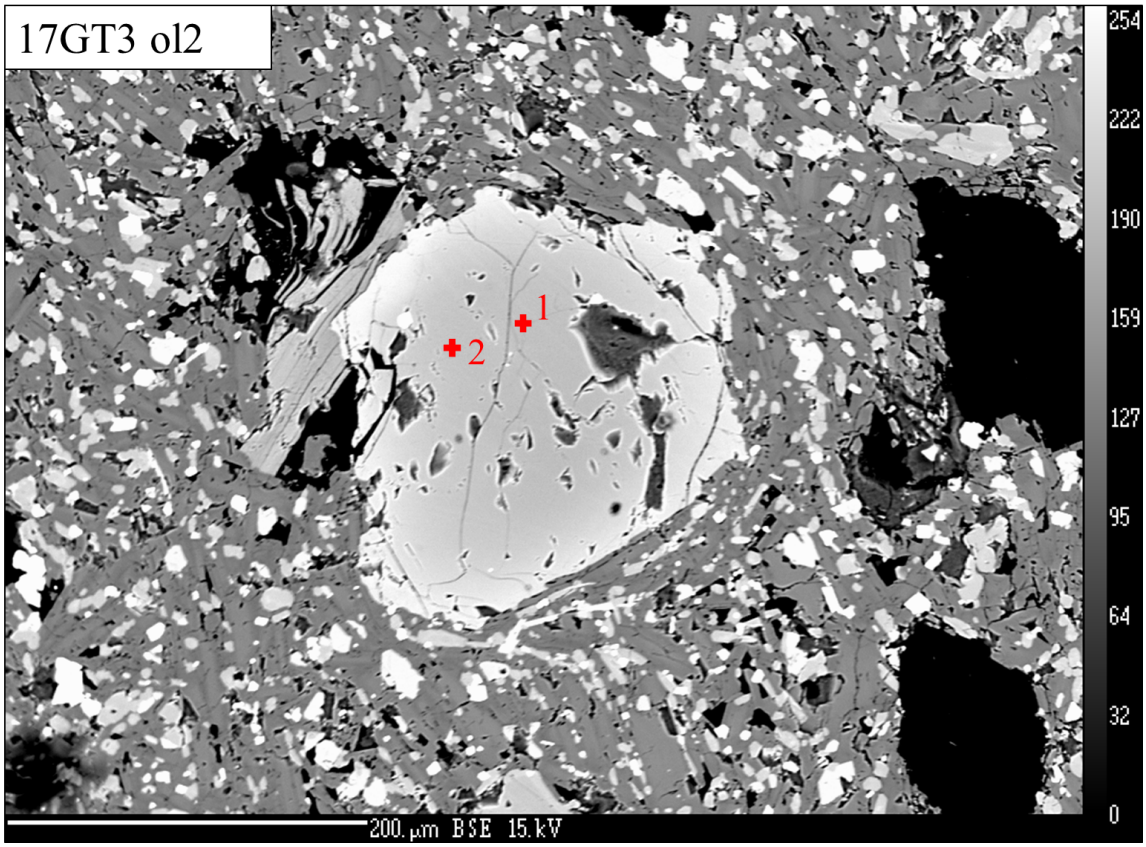
17GT3 ol2
1
2
254
222
190
159
127
95
64
32
0
200 µm BSE 15 kV

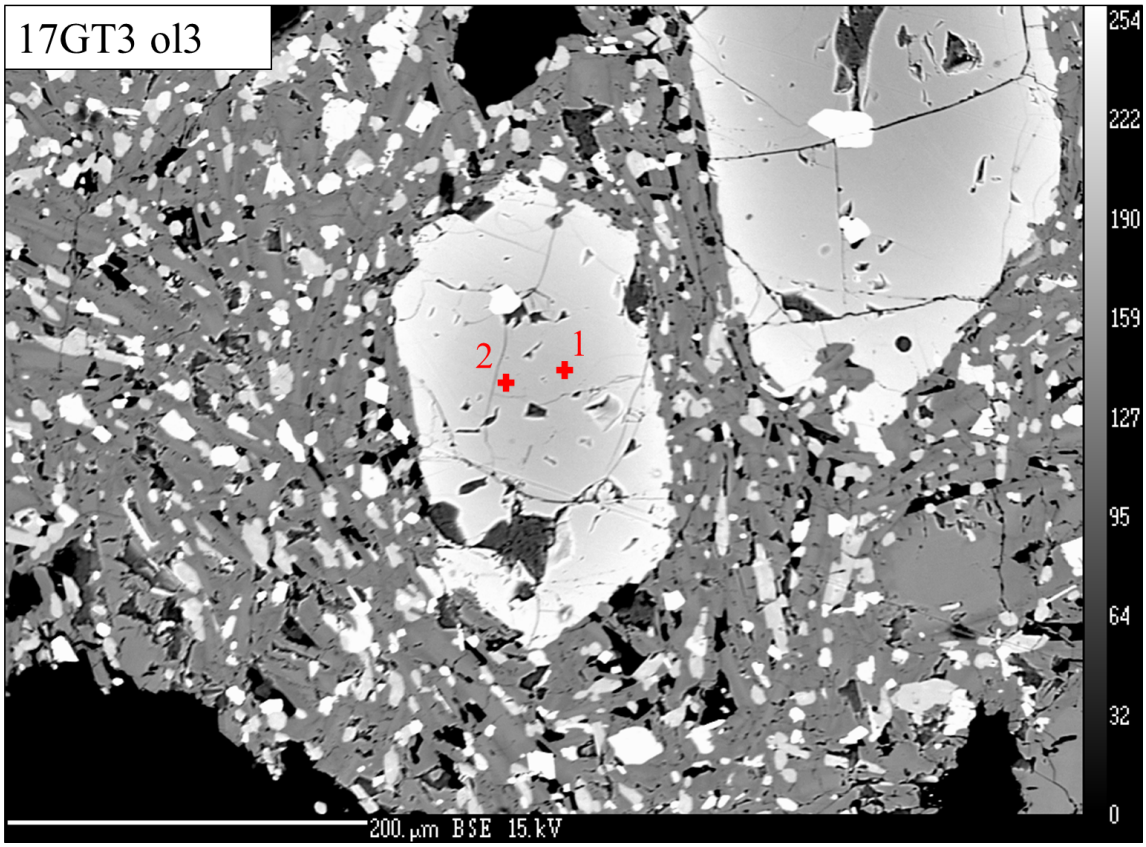
17GT3 ol3
2
1
254
222
190
159
127
95
64
32
0
200 µm BSE 15 kV

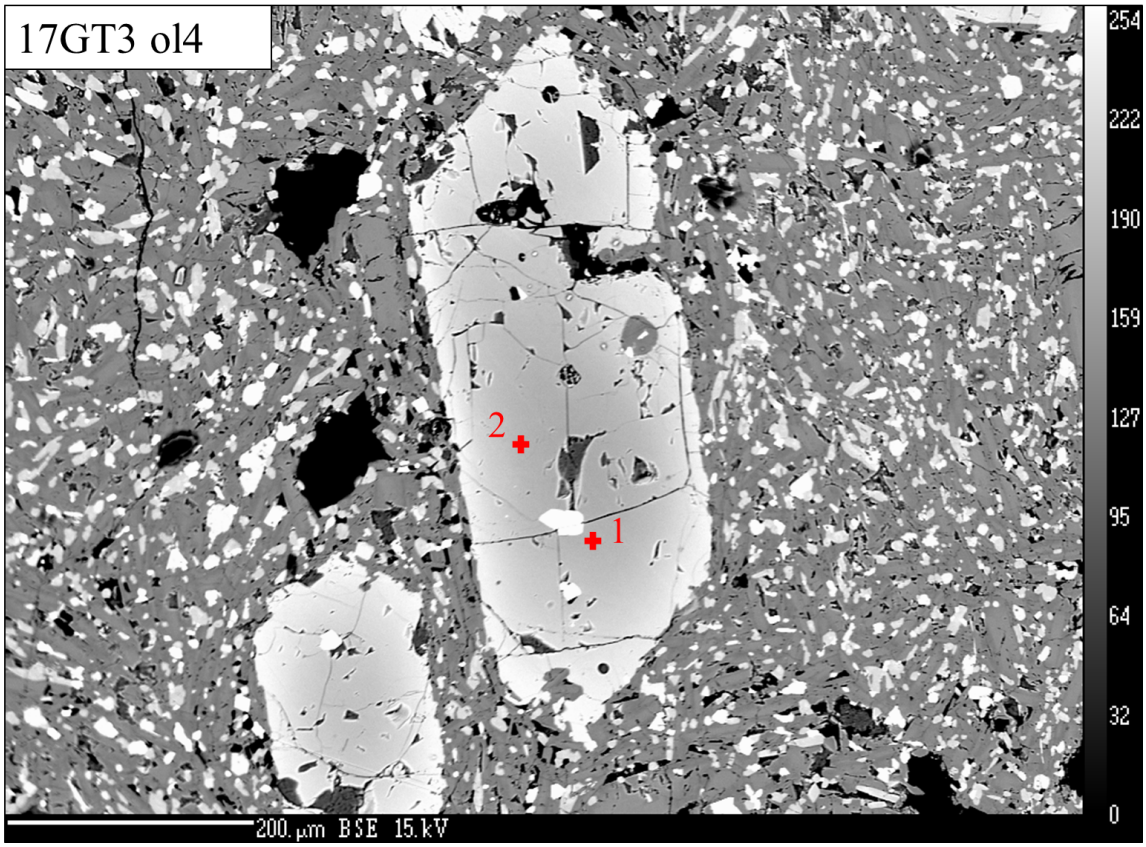
17GT3 ol4
2
1
200.µm BSE 15.kV
254
222
190
159
127
95
64
32
0

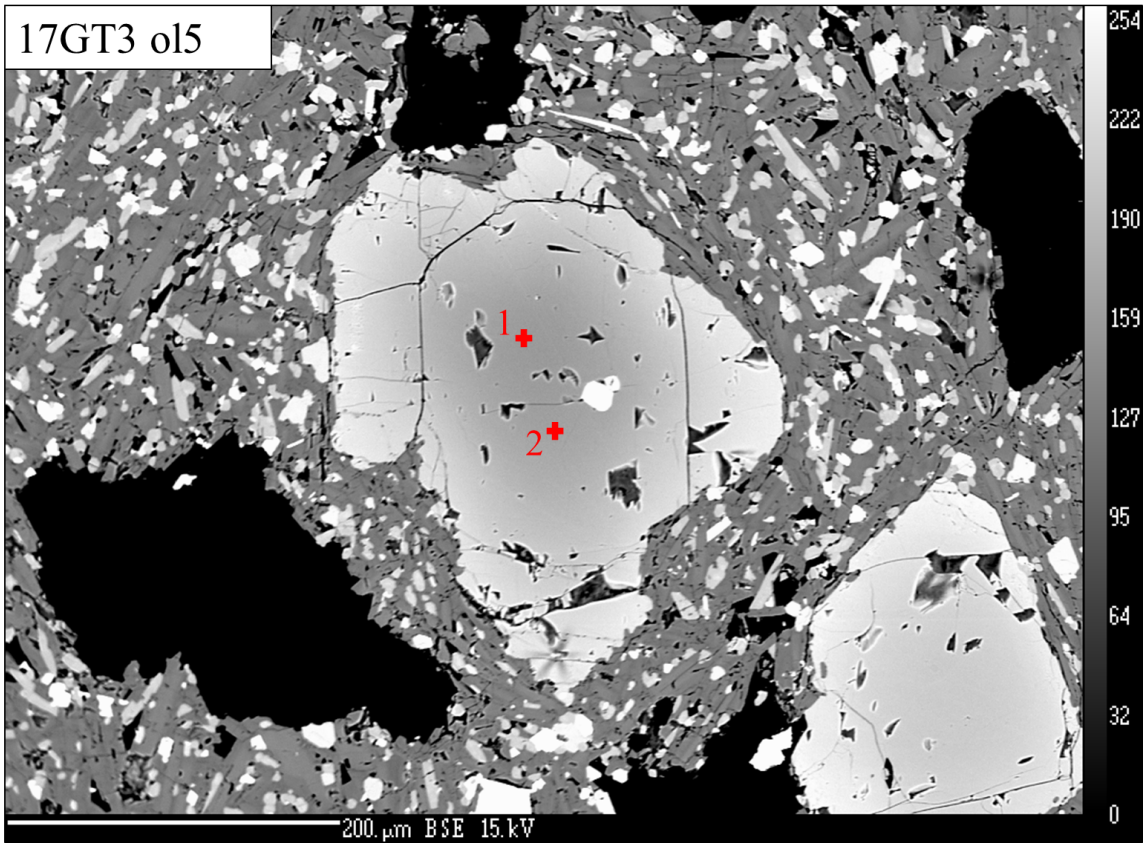
17GT3 ol5
1
2
254
222
190
159
127
95
64
32
0
200 µm BSE 15 kV

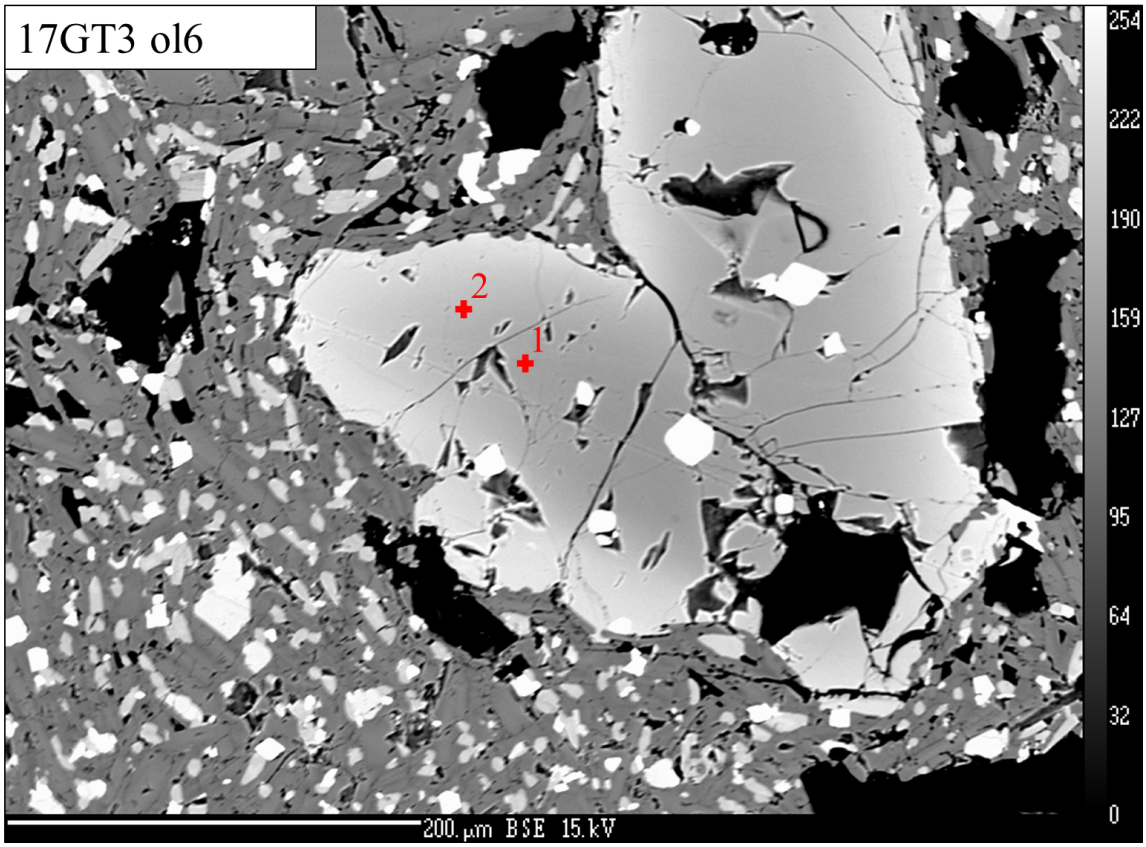
17GT3 ol6
2
1
254
222
190
159
127
95
64
32
0
200.µm BSE 15.kV

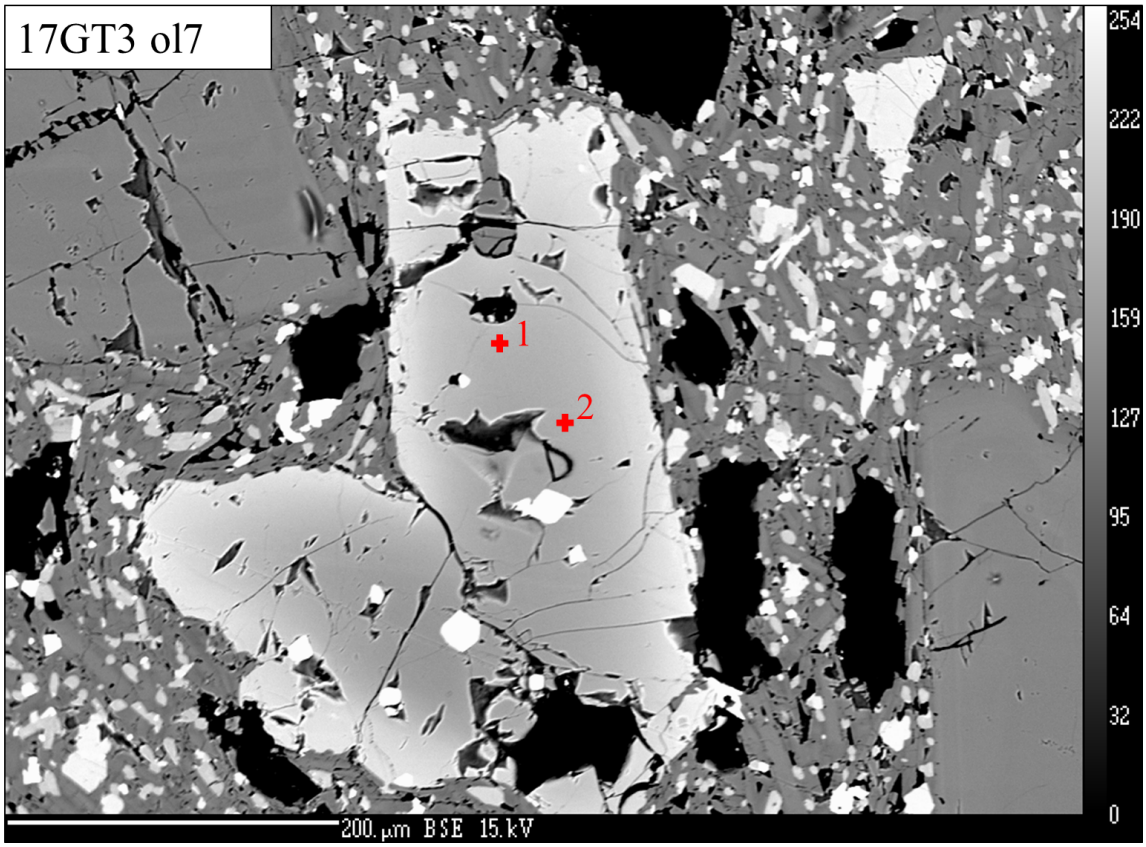
17GT3 ol7
1
2
254
222
190
159
127
95
64
32
0
200 µm BSE 15 kV

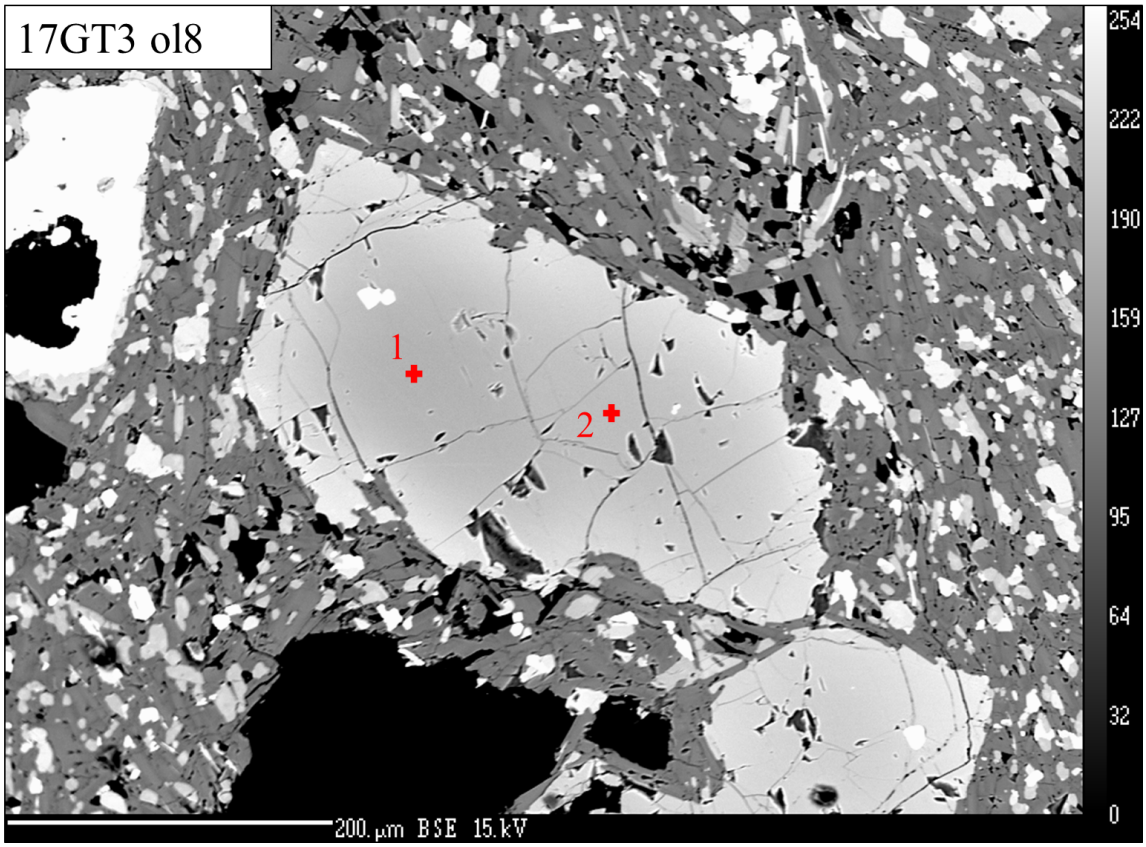
17GT3 ol8
1
2
254
222
190
159
127
95
64
32
0
200.μm BSE 15.kV

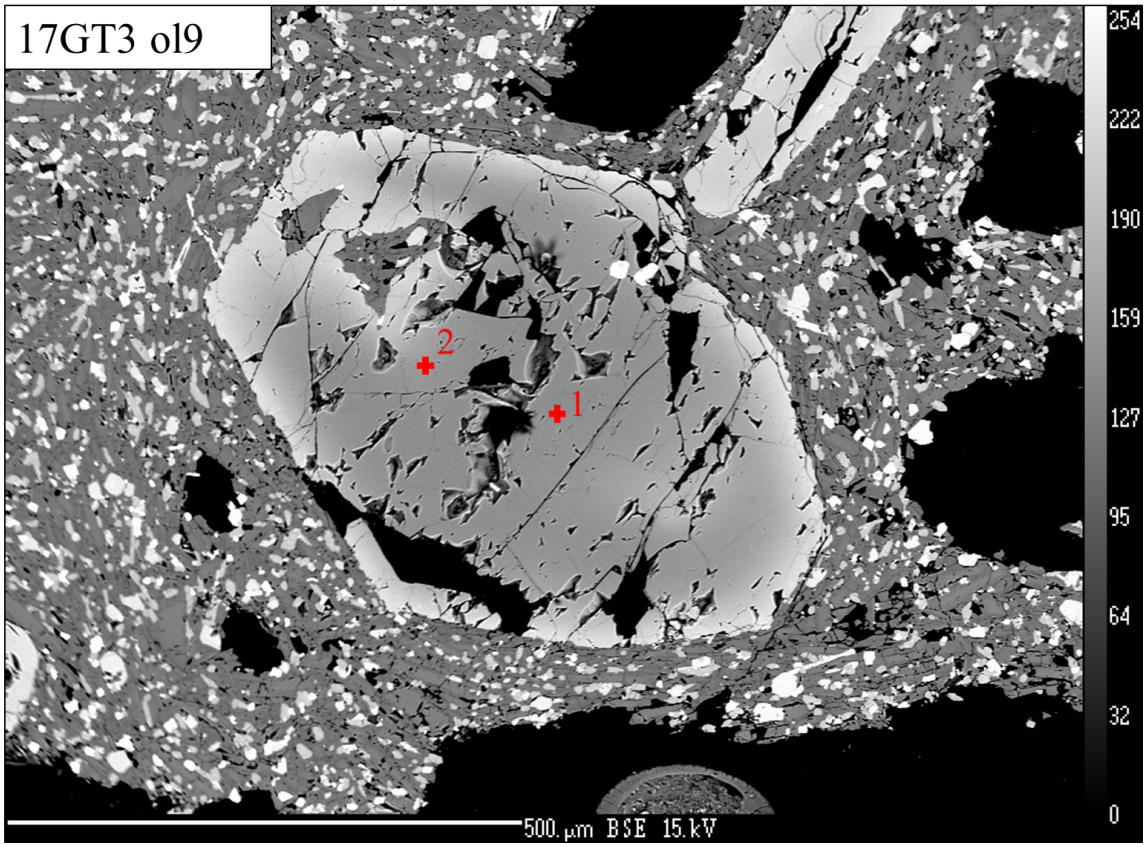
17GT3 ol9
2
1
254
222
190
159
127
95
64
32
0
500.μm BSE 15.kV

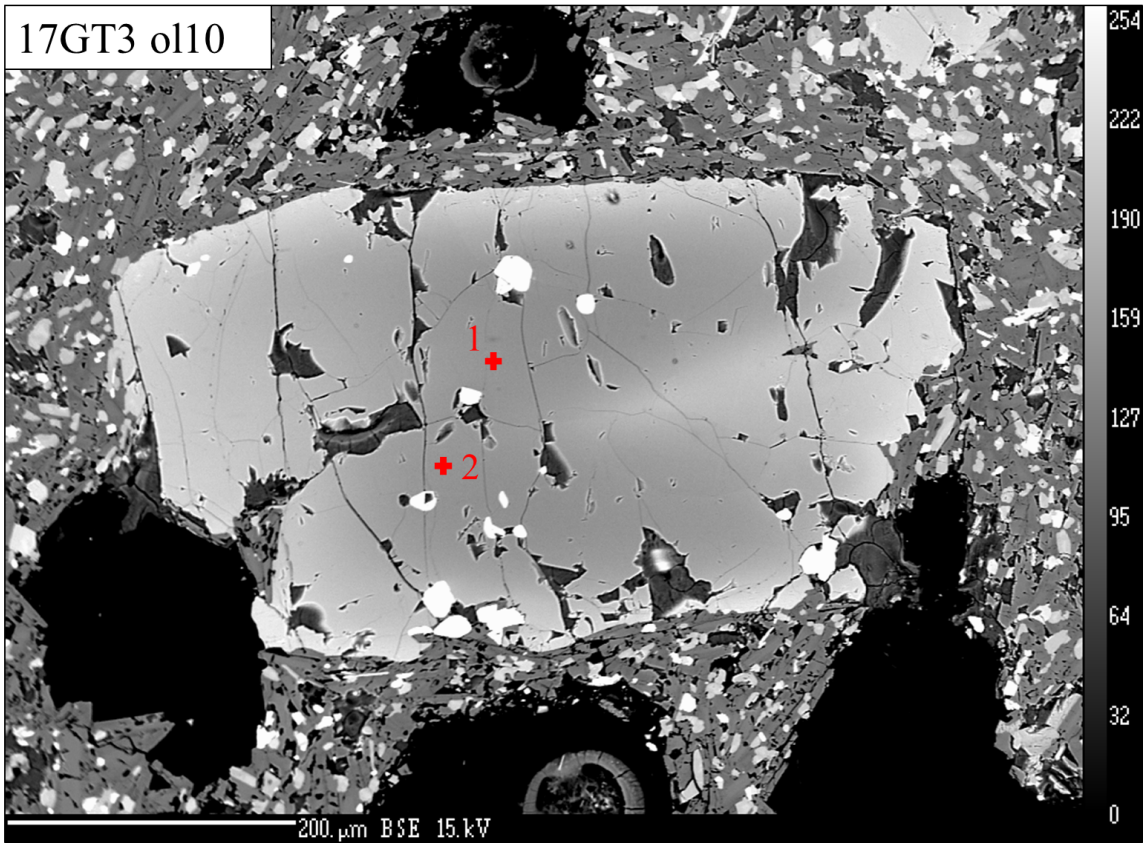
17GT3 ol10
1
2
254
222
190
159
127
95
64
32
0
200.μm BSE 15.kV

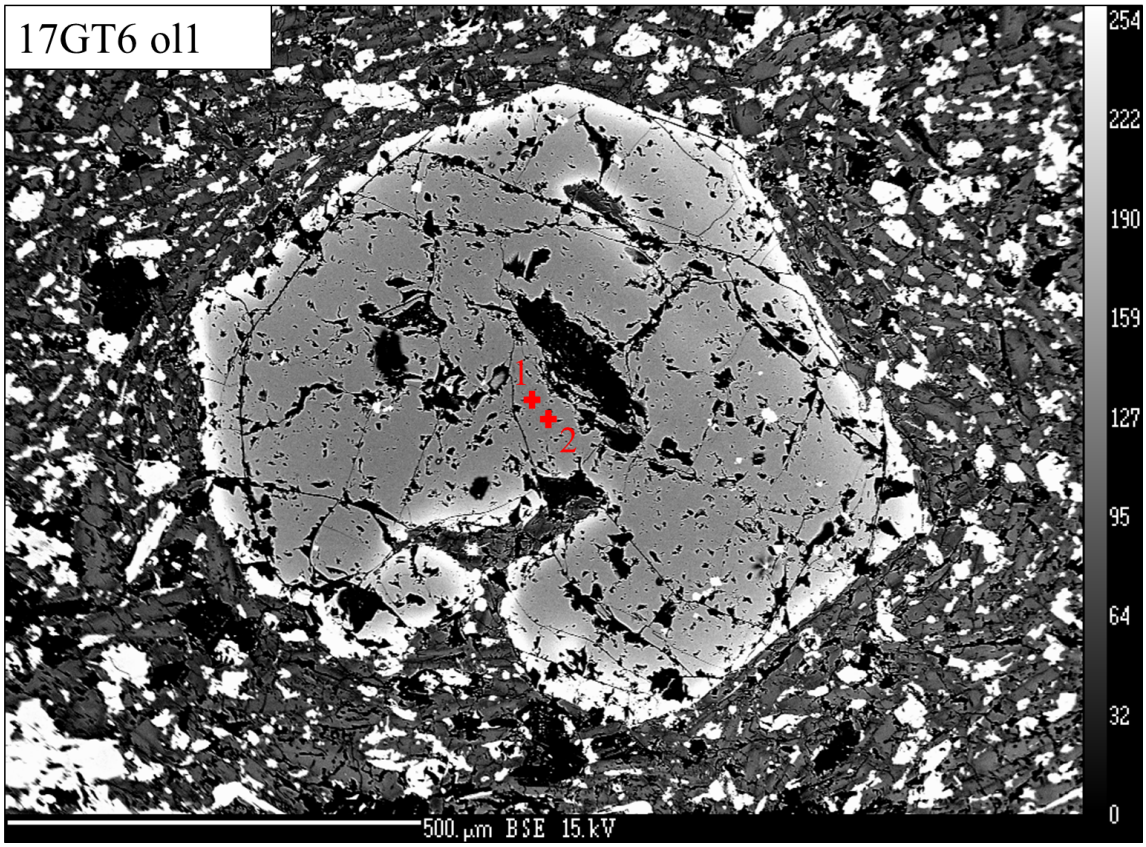
17GT6 ol1
1
2
254
222
190
159
127
95
64
32
0
500.µm BSE 15.kV

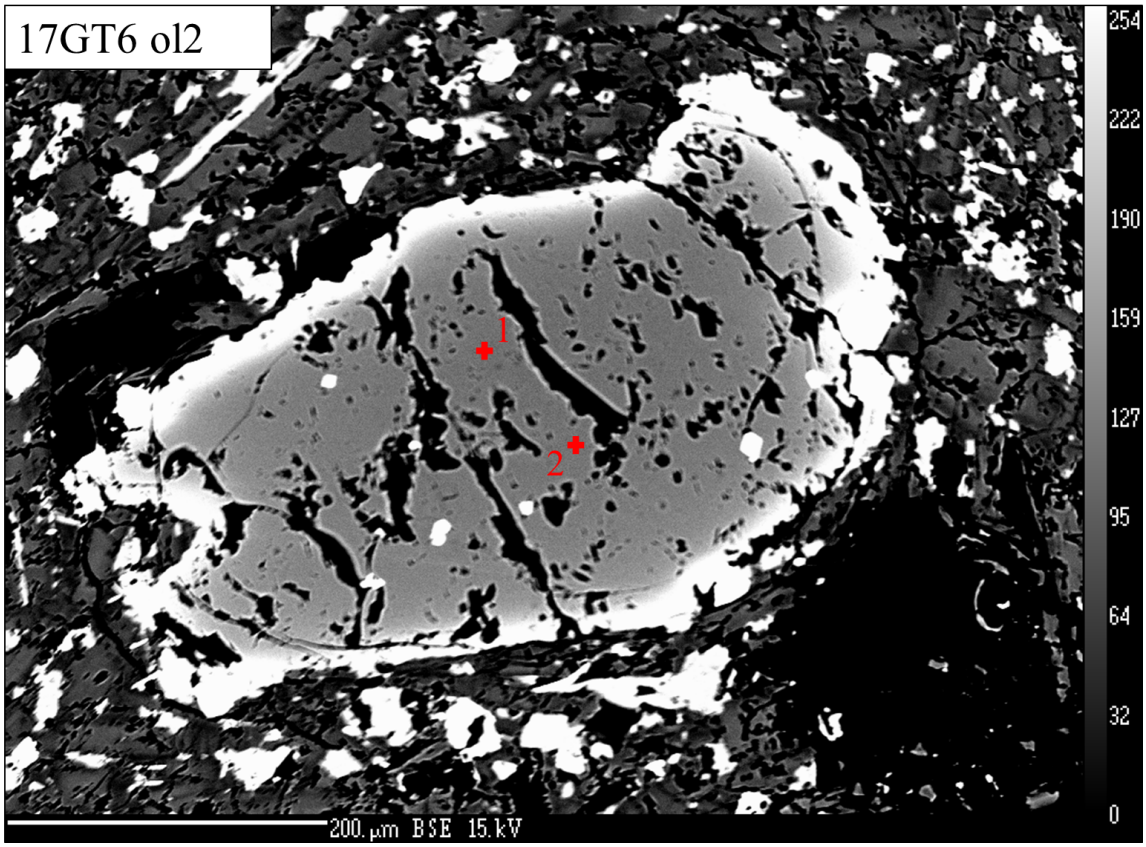
17GT6 ol2
1
2
254
222
190
159
127
95
64
32
0
200 µm BSE 15 kV

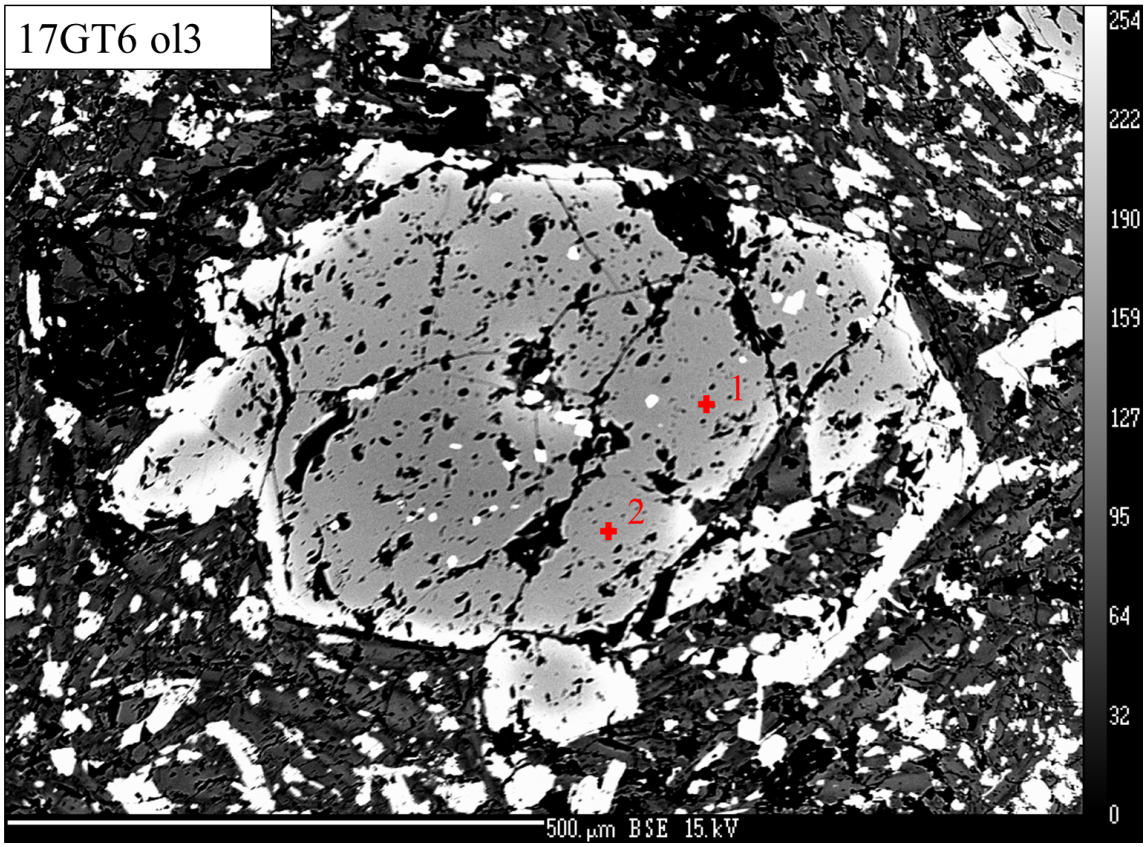
17GT6 ol3
1
2
254
222
190
159
127
95
64
32
0
500.µm BSE 15.kV

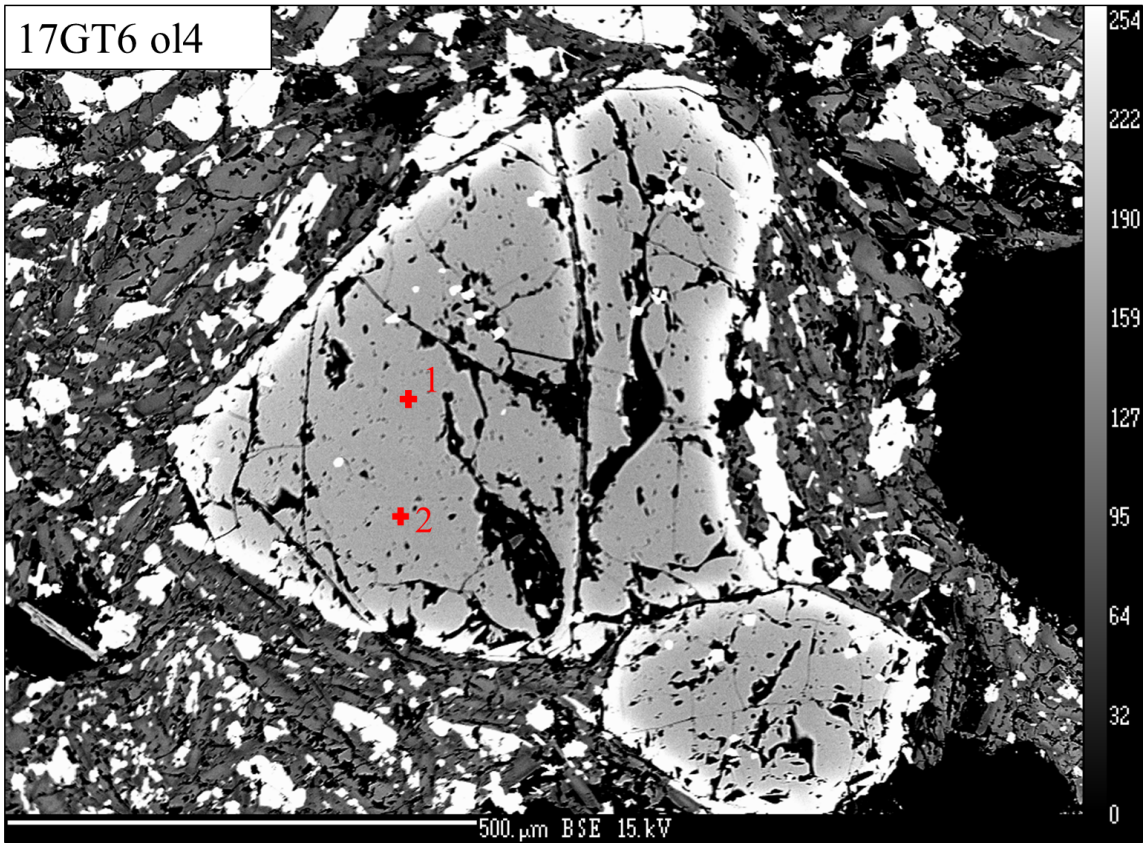
17GT6 ol4
1
2
254
222
190
159
127
95
64
32
0
500.µm BSE 15.kV

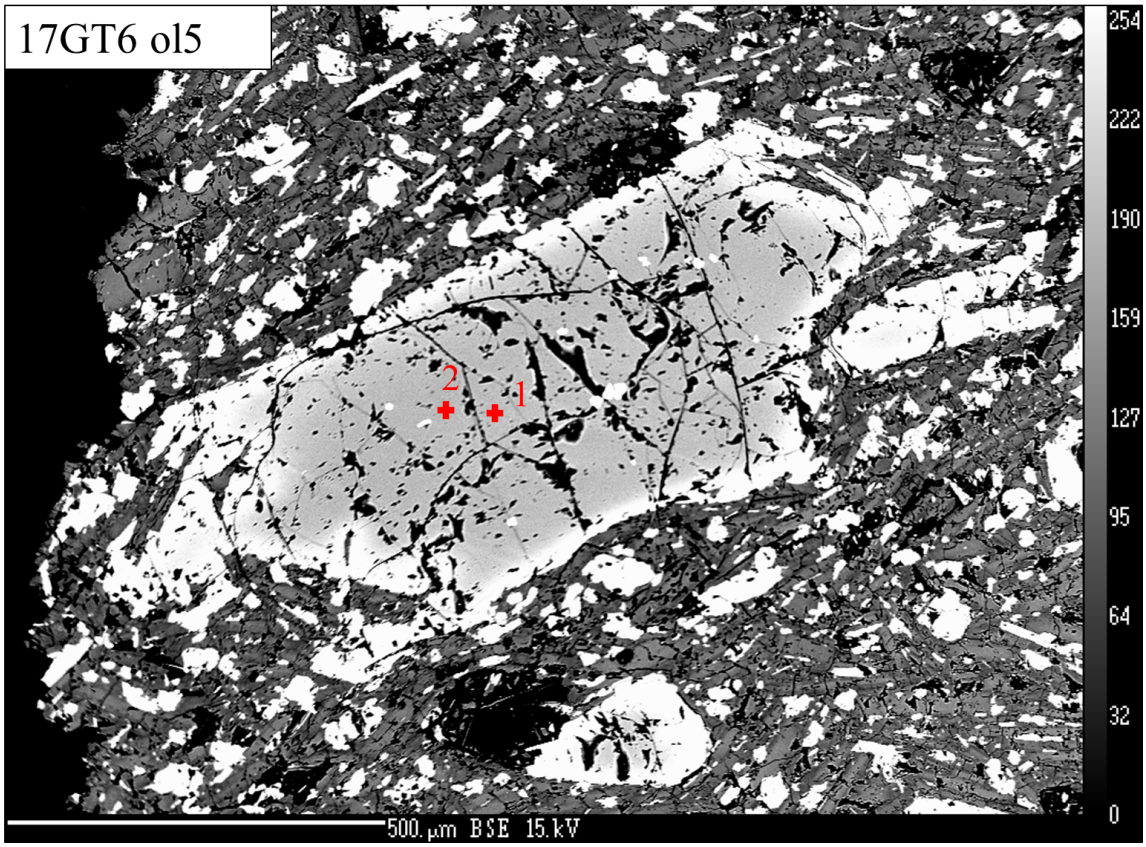
17GT6 ol5
2
1
254
222
190
159
127
95
64
32
0
500.µm BSE 15.kV

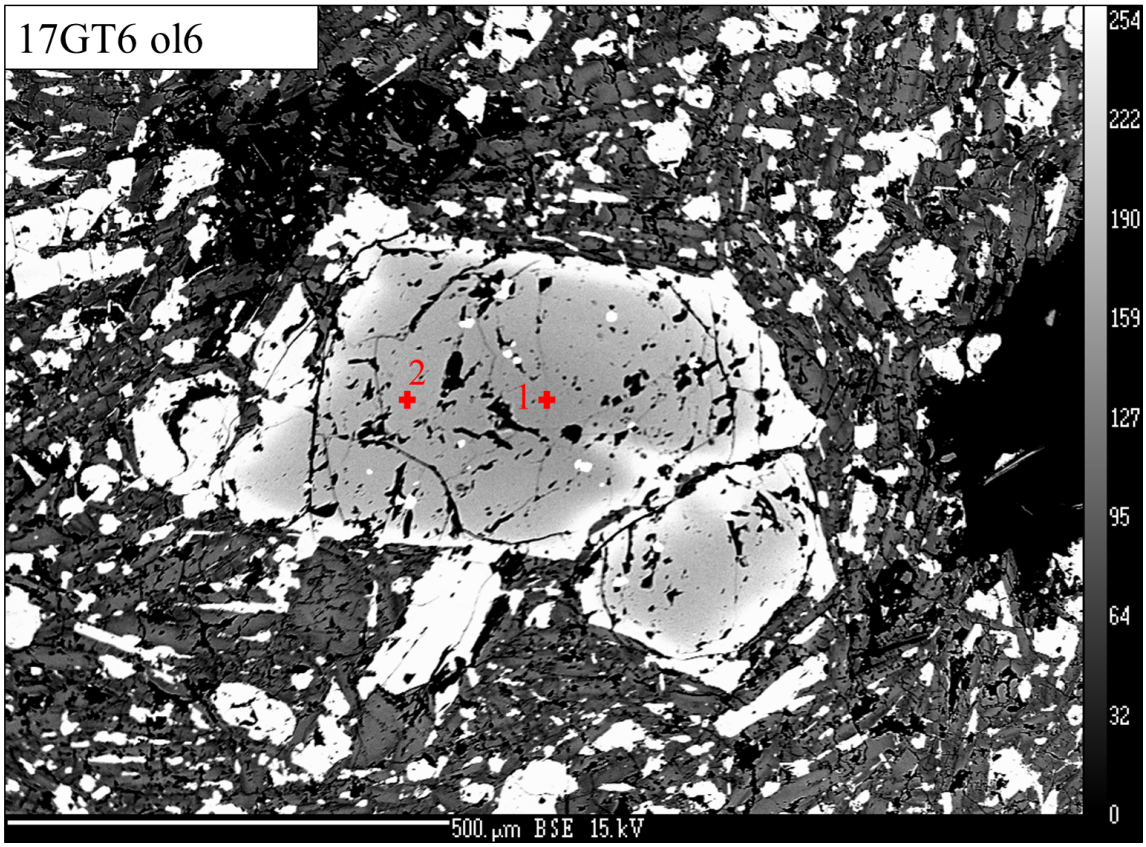
17GT6 ol6
2
1
254
222
190
159
127
95
64
32
0
500.µm BSE 15.kV

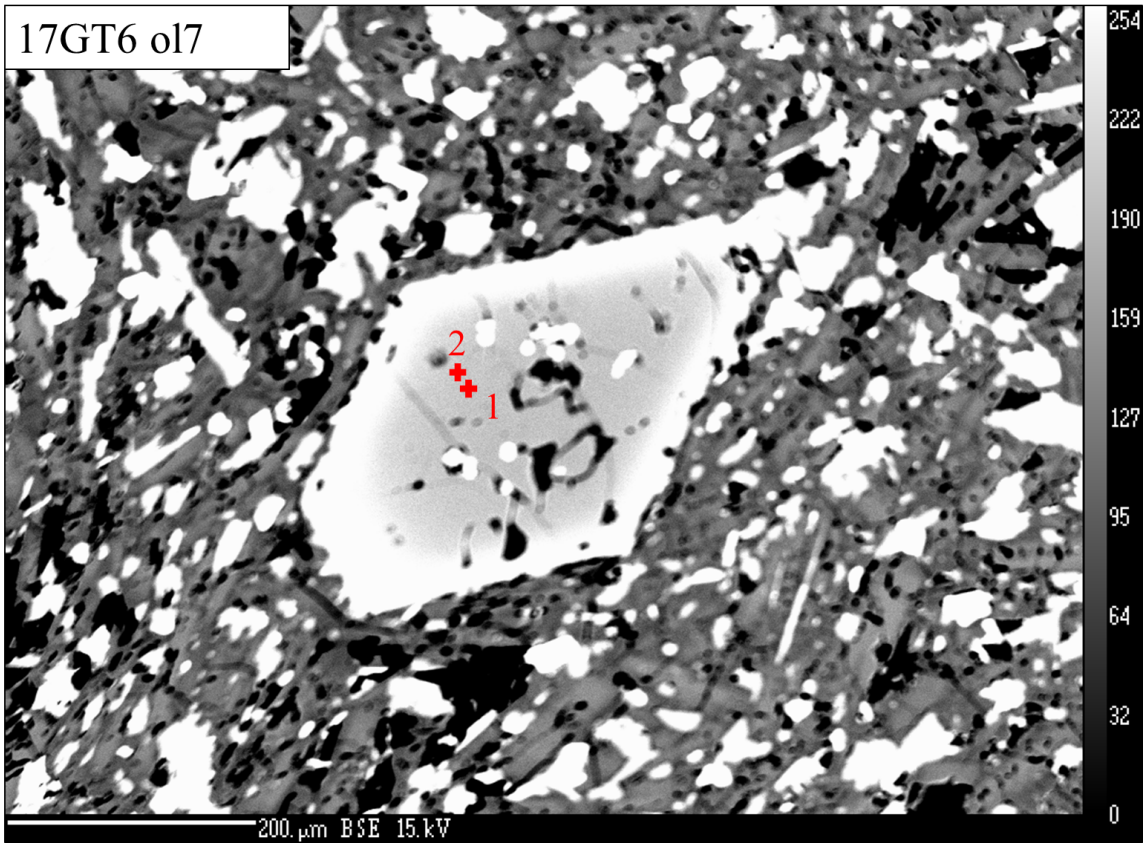
17GT6 ol7
2
1
200 µm BSE 15 kV
254
222
190
159
127
95
64
32
0

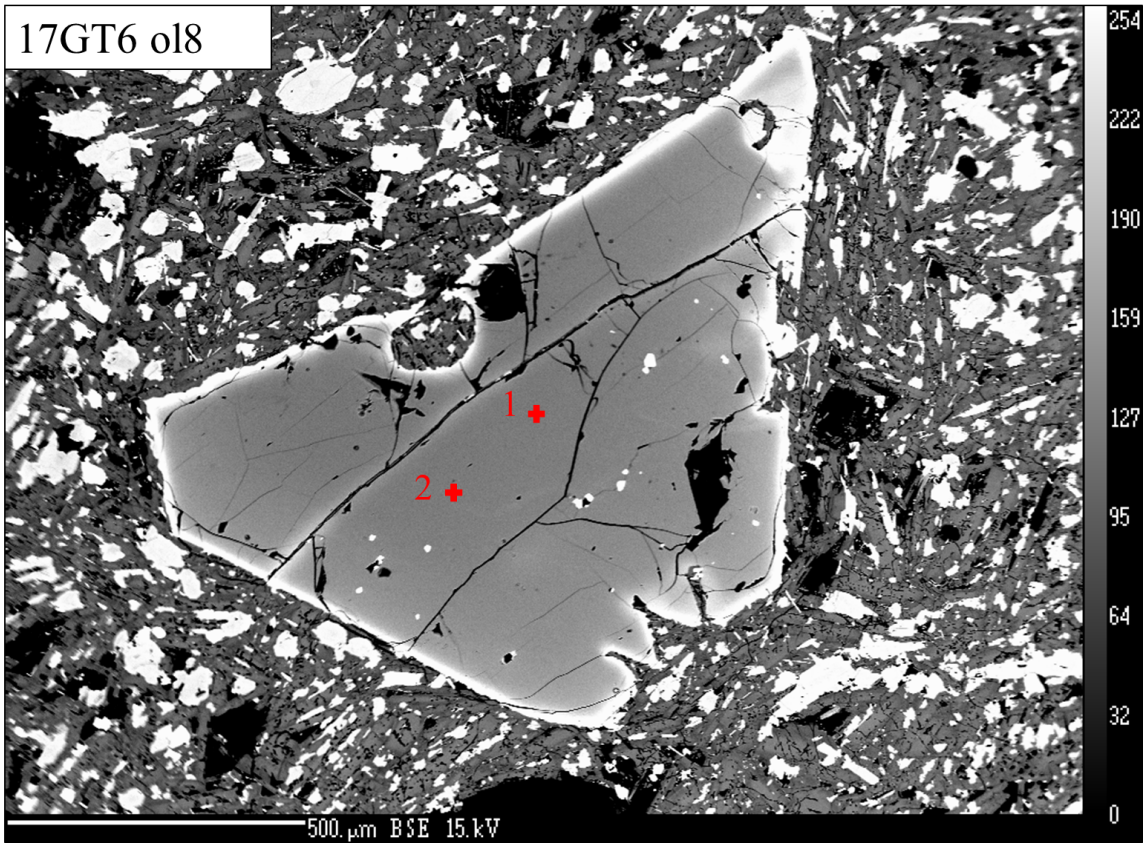
17GT6 ol8
1
2
500.µm BSE 15.kV
254
222
190
159
127
95
64
32
0

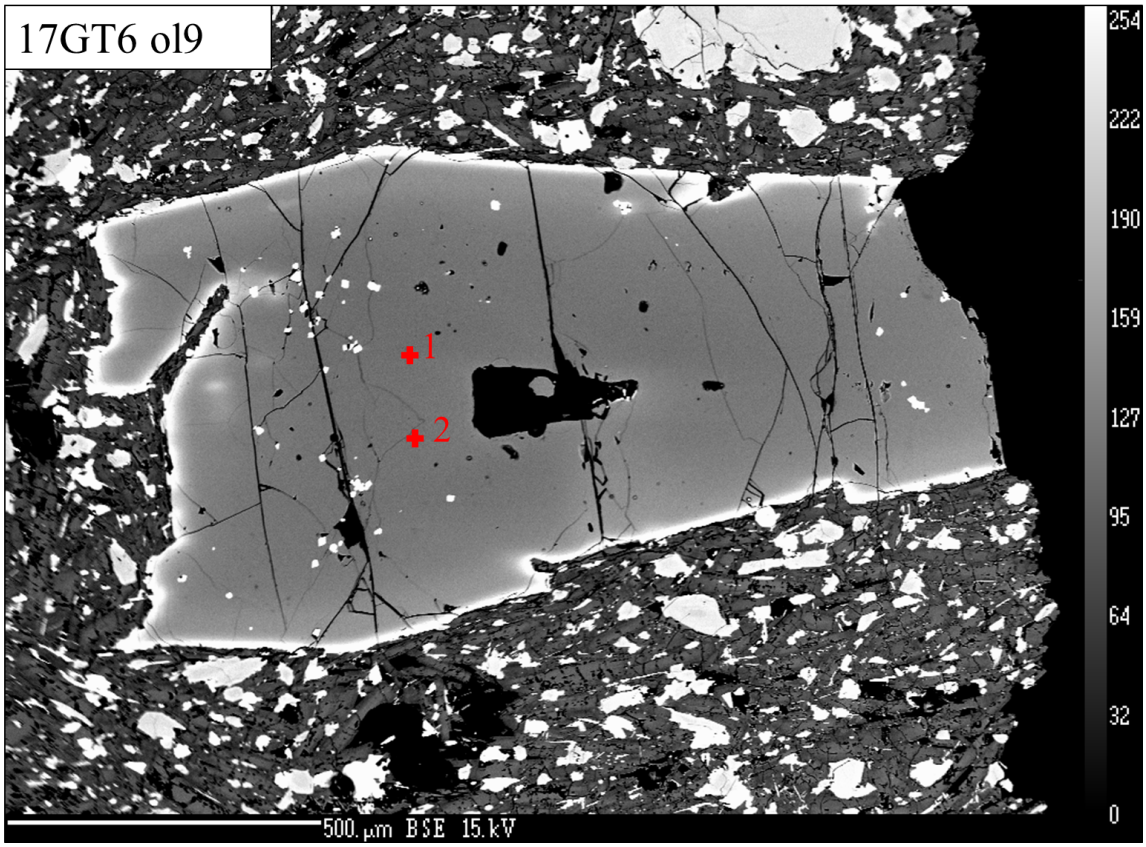
17GT6 ol9
1
2
500.µm BSE 15.kV
254
222
190
159
127
95
64
32
0

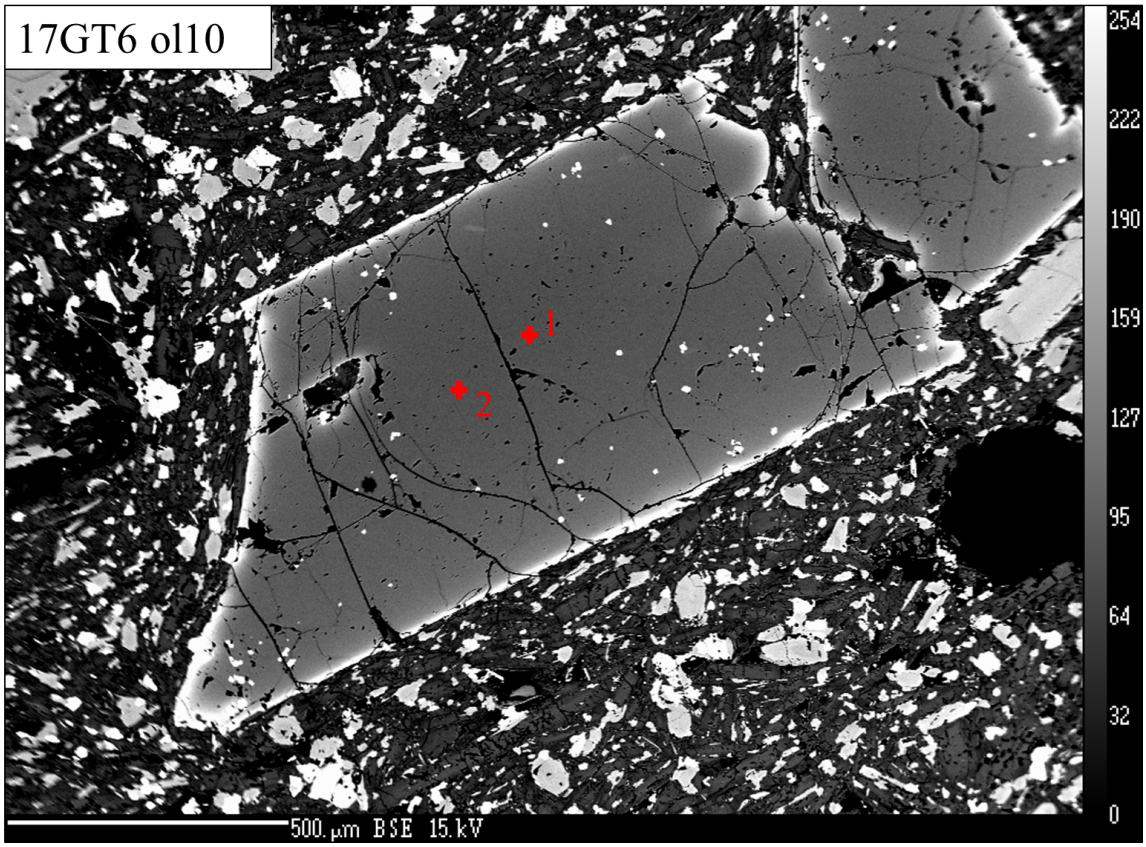
17GT6 ol10
1
2
254
222
190
159
127
95
64
32
0
500.µm BSE 15.kV

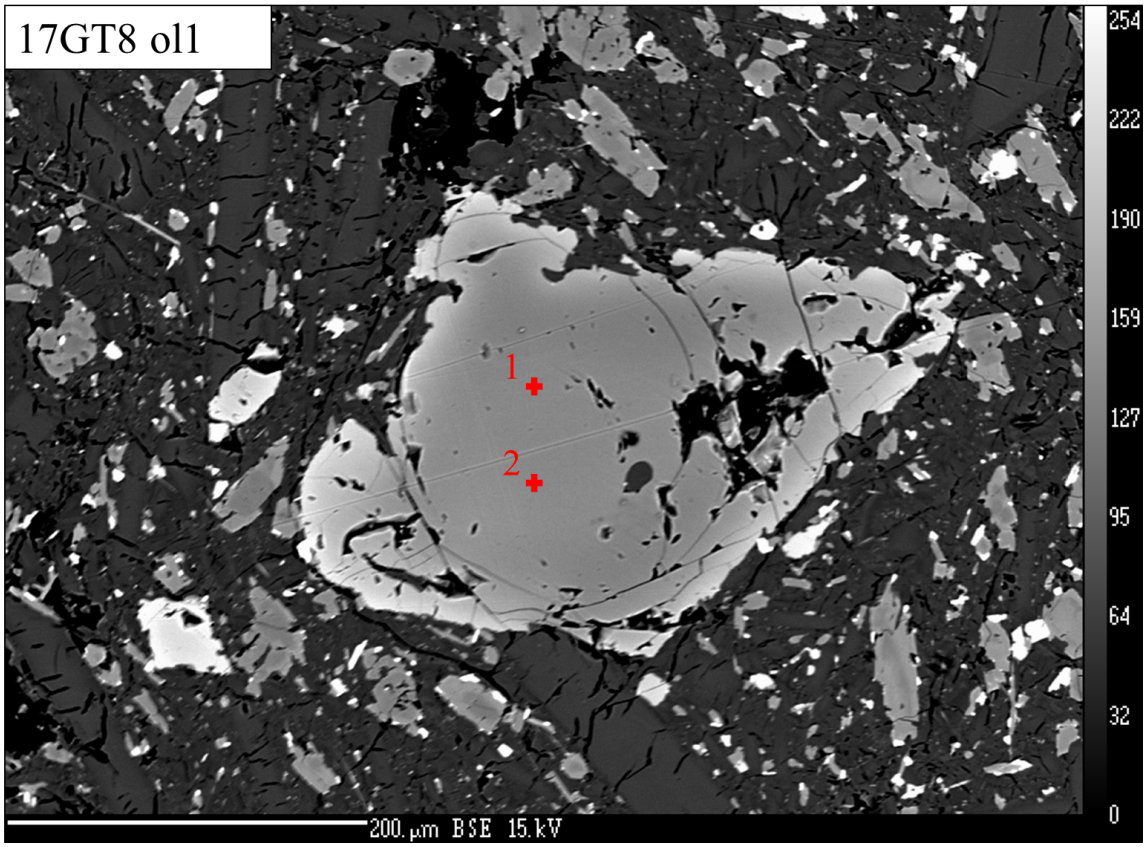
17GT8 ol1
1
2
254
222
190
159
127
95
64
32
0
200 µm BSE 15 kV

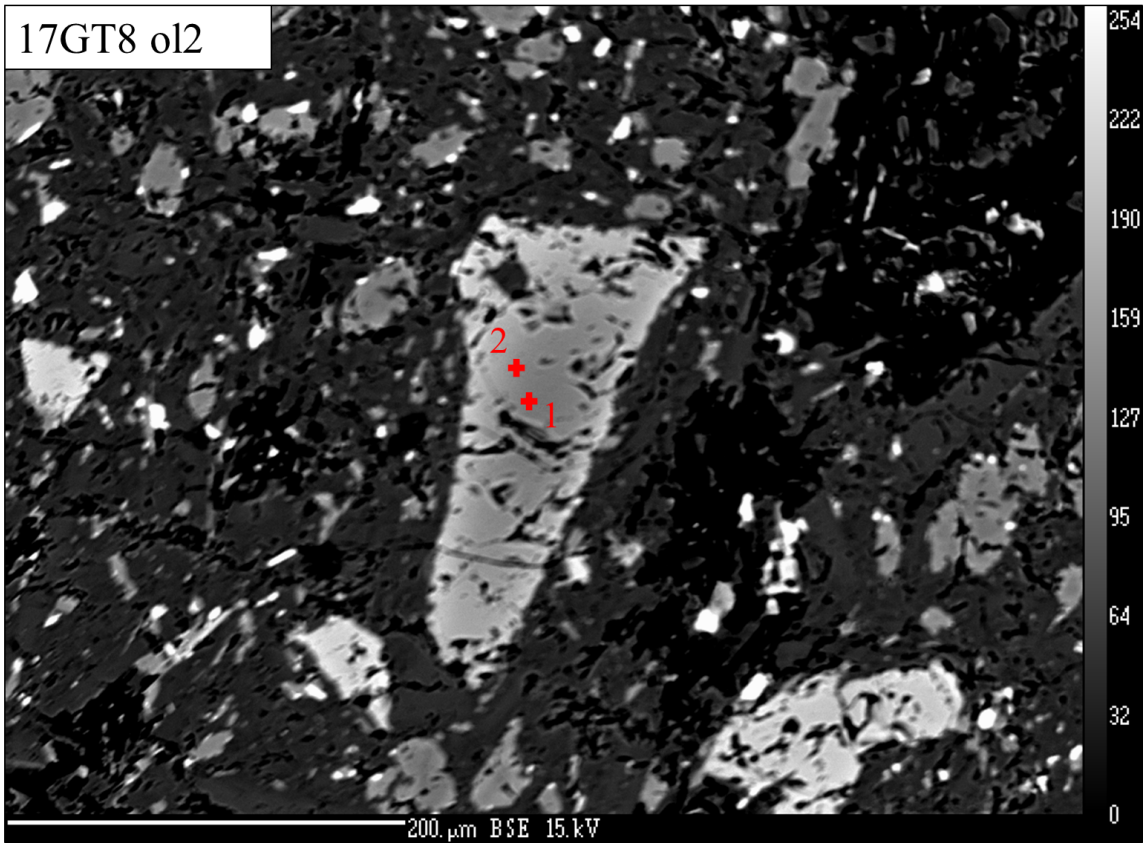
17GT8 ol2
2
1
254
222
190
159
127
95
64
32
0
200.µm BSE 15.kV

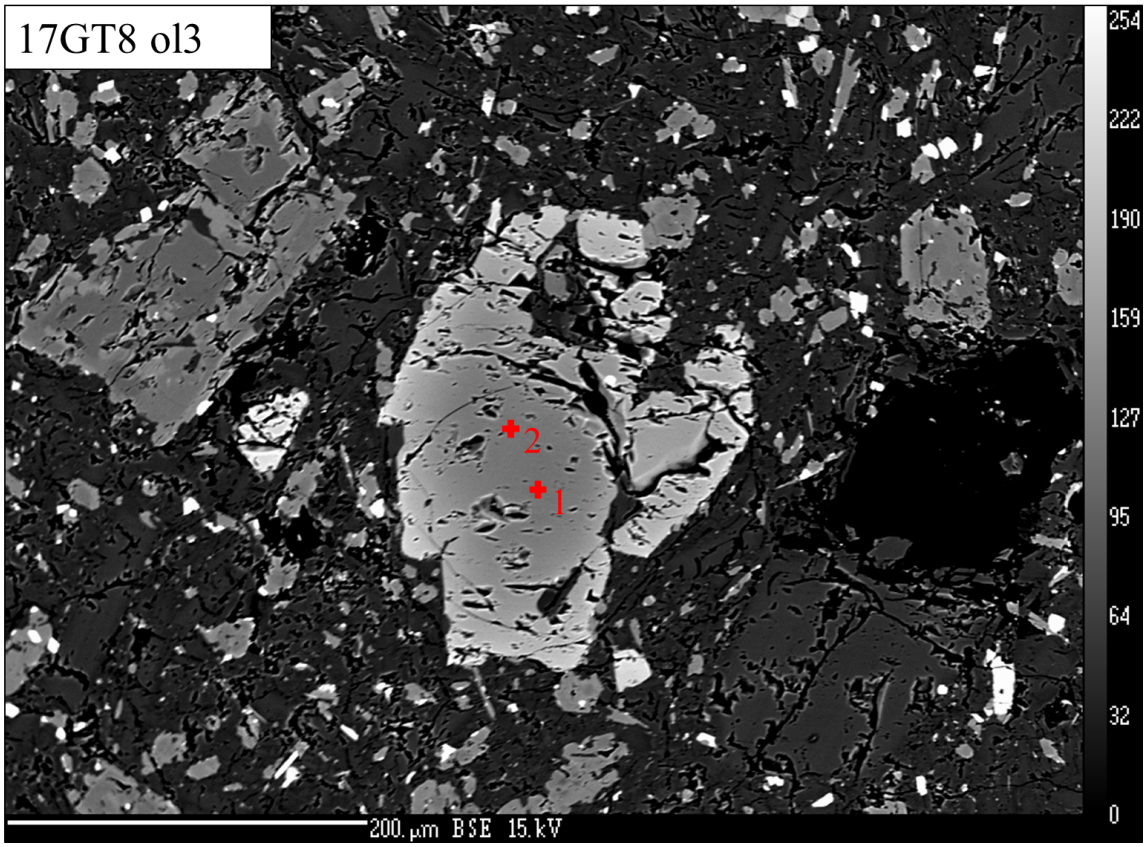
17GT8 ol3
2
1
200 µm BSE 15 kV
254
222
190
159
127
95
64
32
0

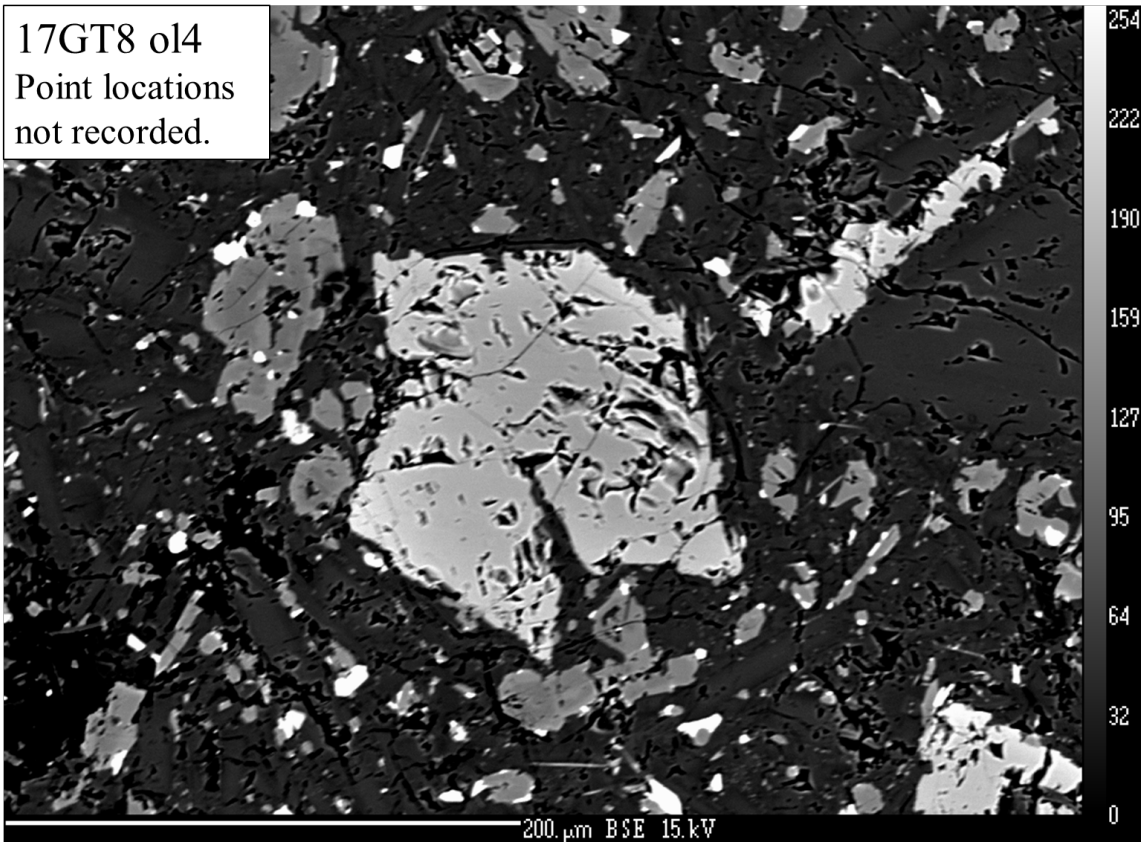
17GT8 ol4
Point locations
not recorded.
254
222
190
159
127
95
64
32
0
200 µm BSE 15 kV

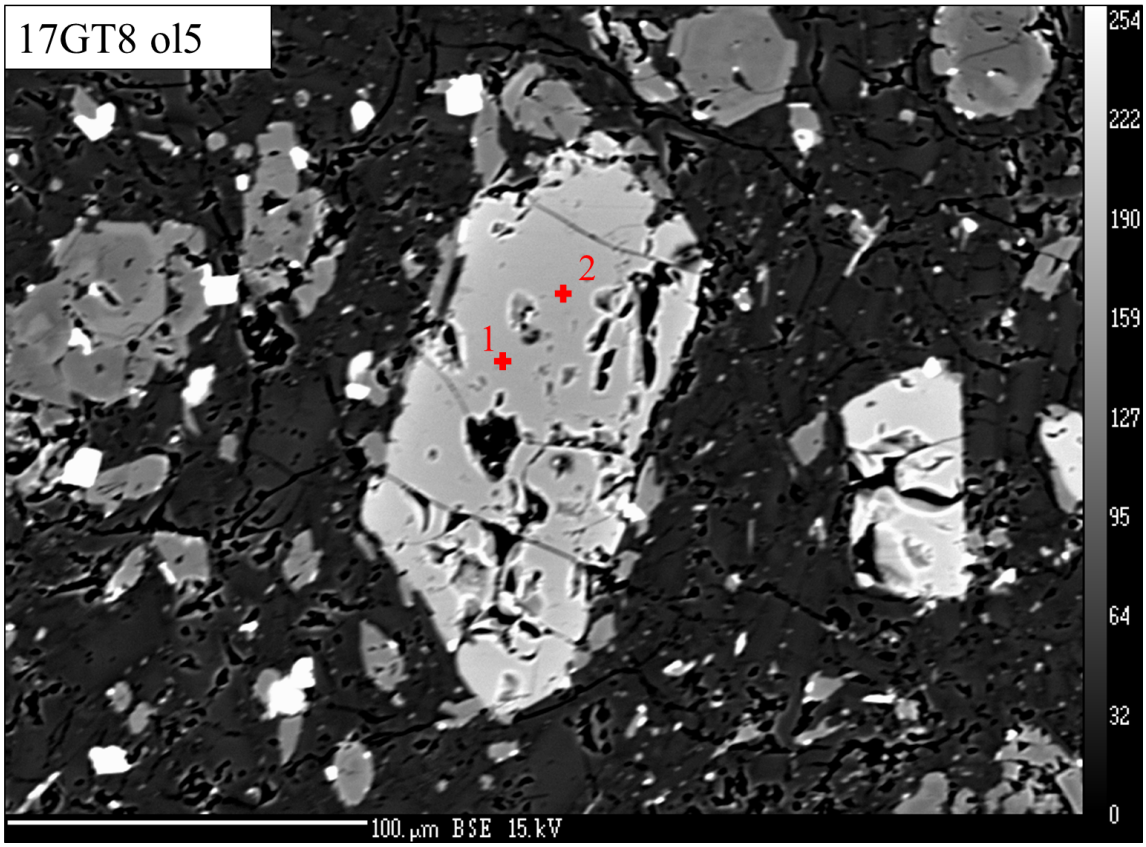
17GT8 ol5
1
2
100 µm BSE 15 kV
254
222
190
159
127
95
64
32
0

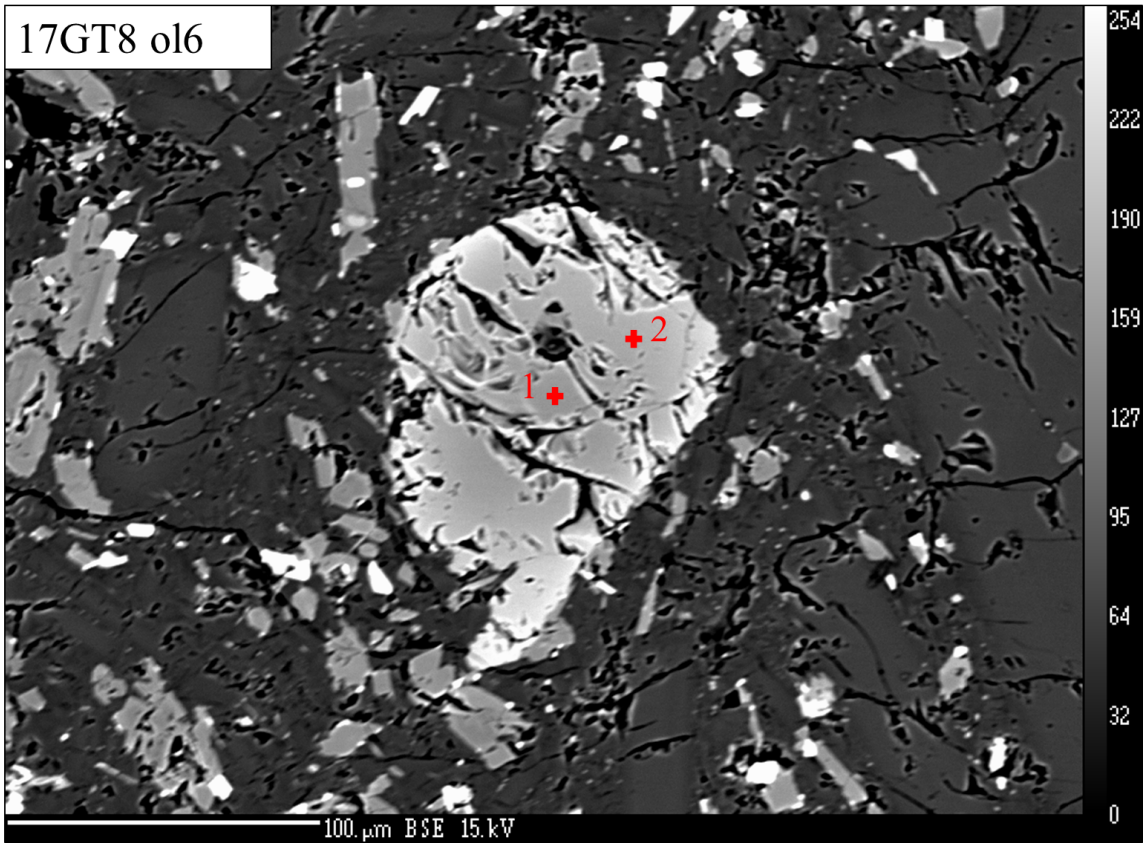
17GT8 ol6
1
2
254
222
190
159
127
95
64
32
0
100.µm BSE 15.kV

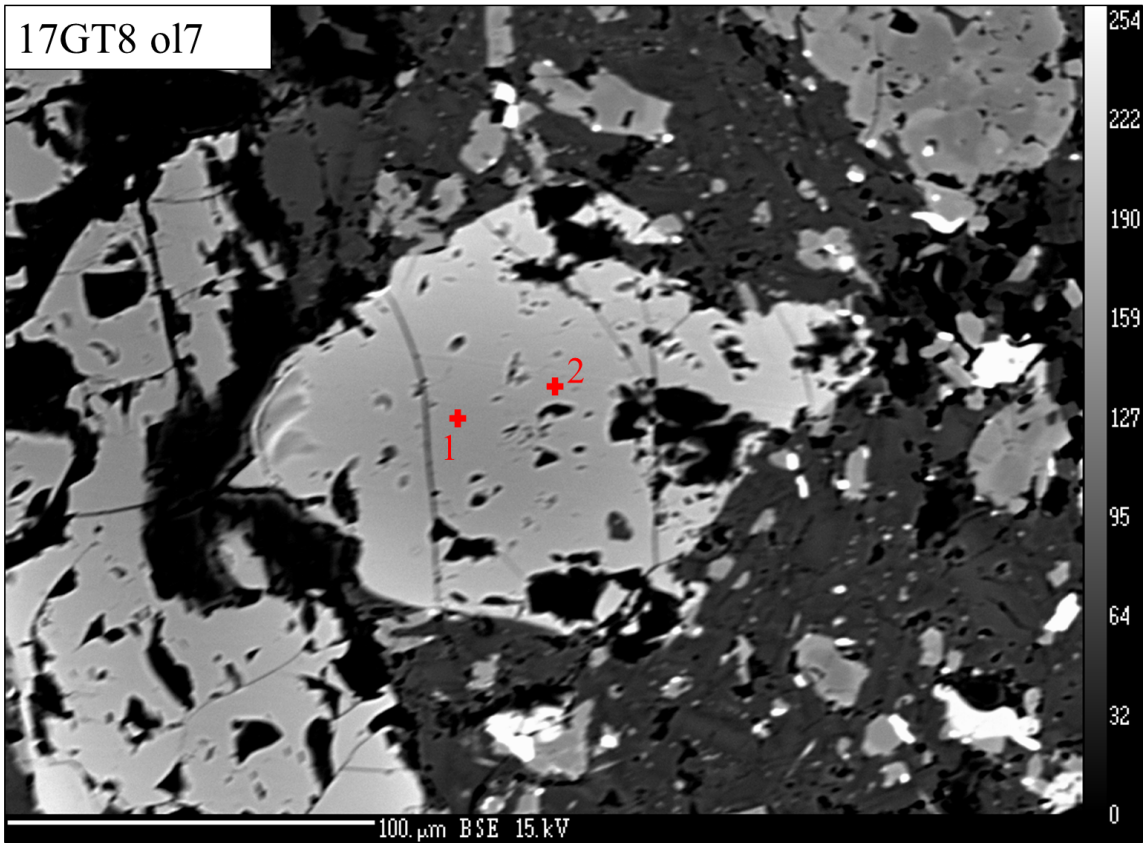
17GT8 ol7
1
2
100.μm BSE 15.kV
254
222
190
159
127
95
64
32
0

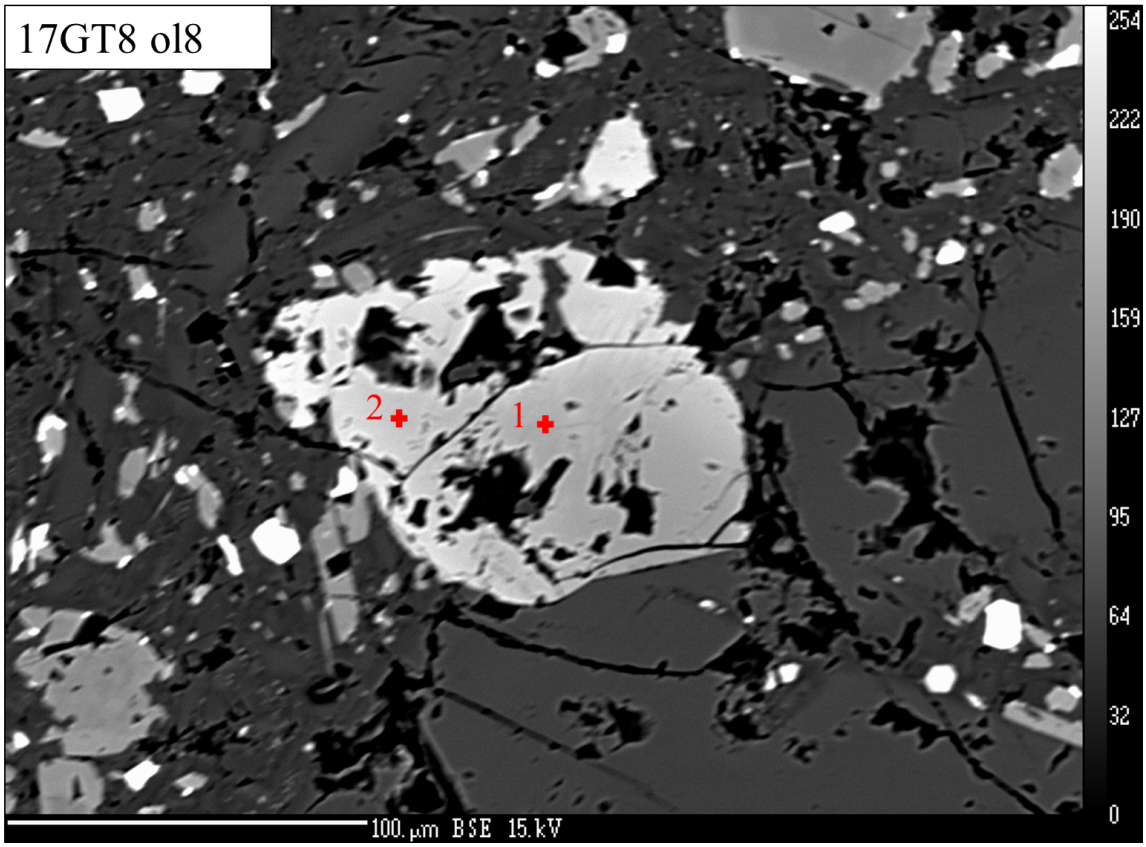
17GT8 ol8
2
1
100 µm BSE 15 kV
254
222
190
159
127
95
64
32
0

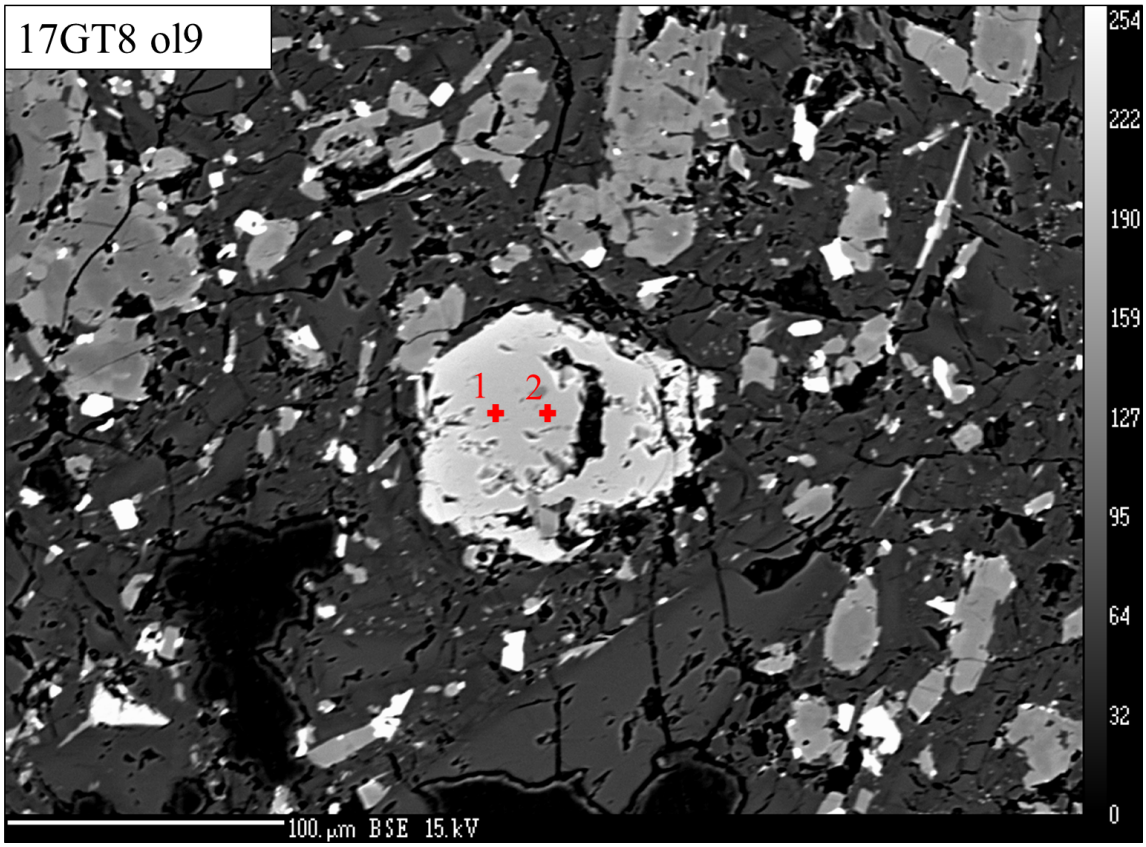
17GT8 ol9
1
2
100 µm BSE 15 kV
254
222
190
159
127
95
64
32
0

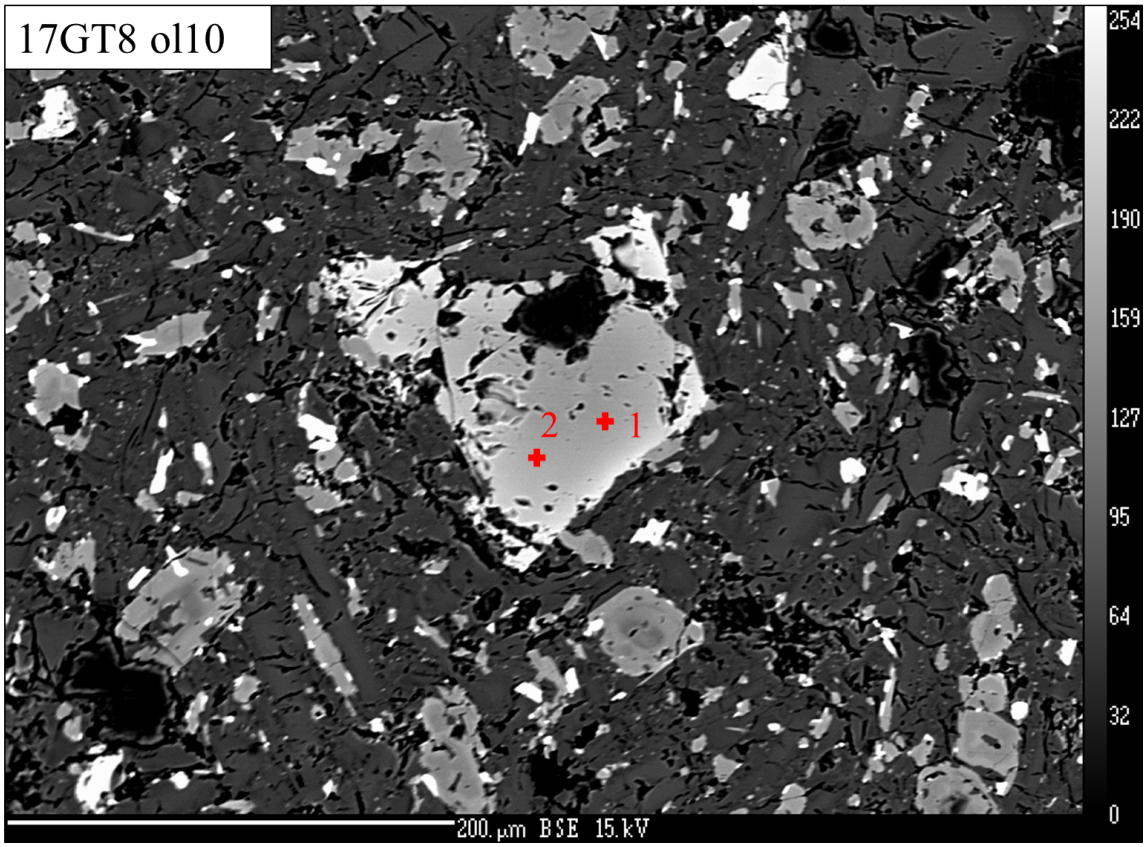
17GT8 ol10
2
1
254
222
190
159
127
95
64
32
0
200.µm BSE 15.kV

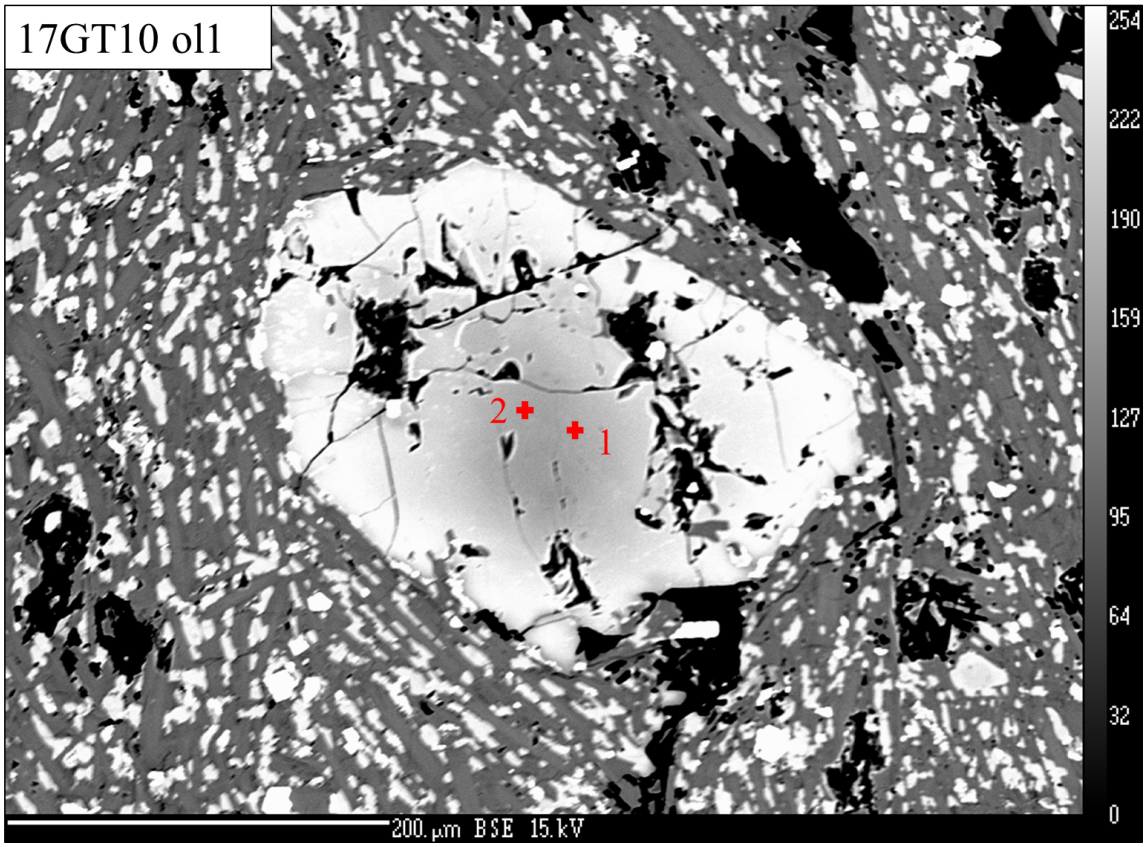
17GT10 ol1
2
1
254
222
190
159
127
95
64
32
0
200.µm BSE 15.kV

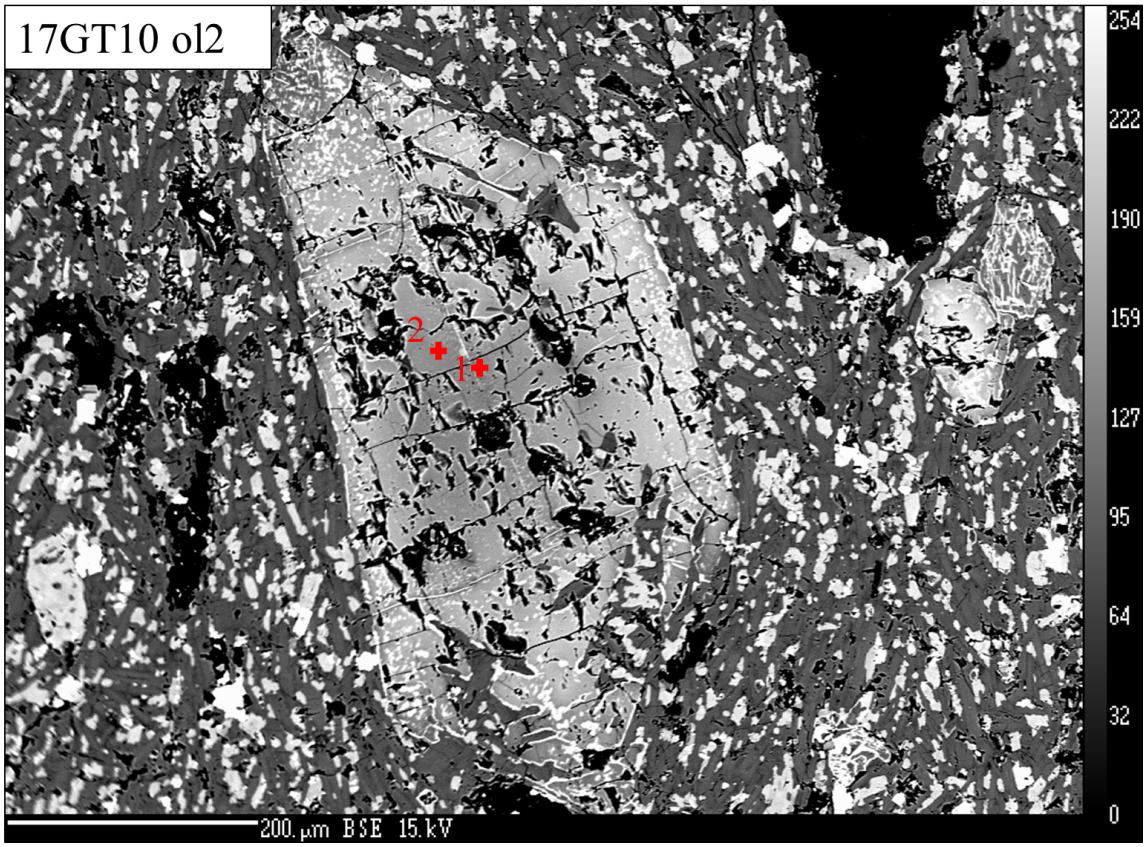
17GT10 ol2
2
1
254
222
190
159
127
95
64
32
0
200.µm BSE 15.kV

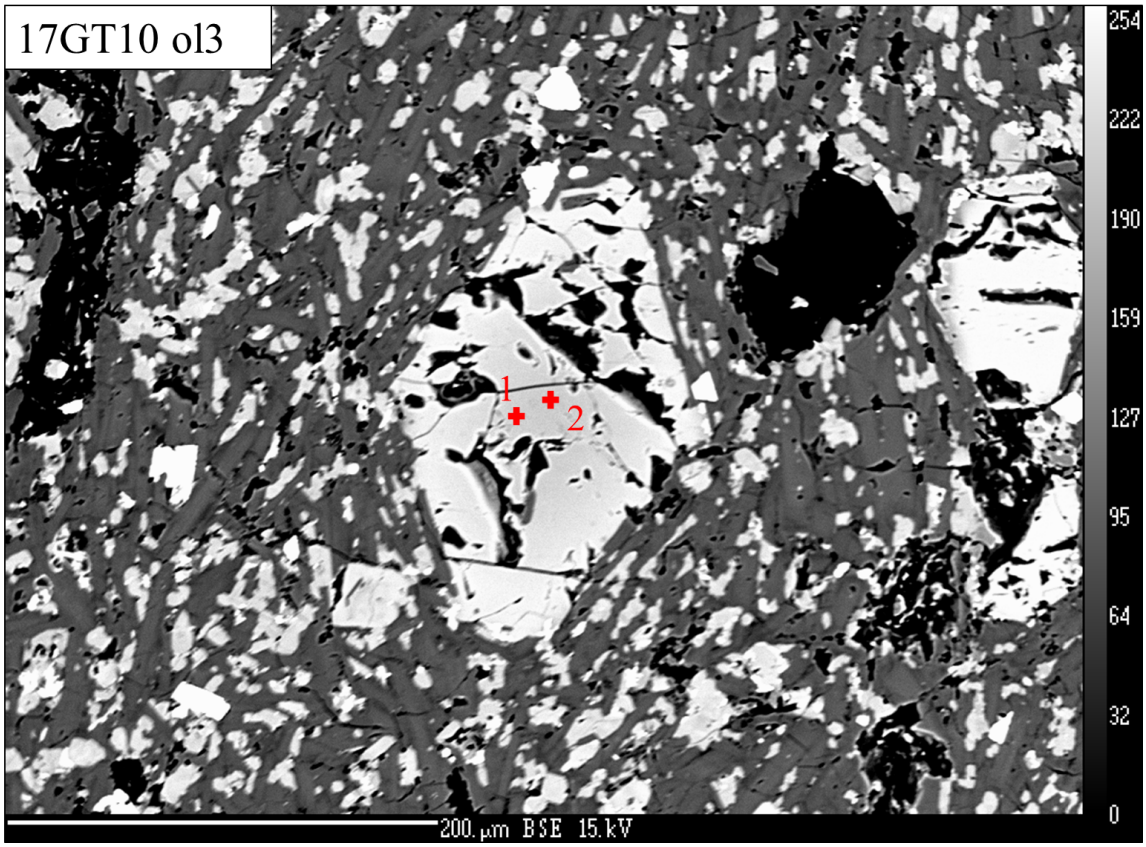
17GT10 ol3
1
2
254
222
190
159
127
95
64
32
0
200 µm BSE 15 kV

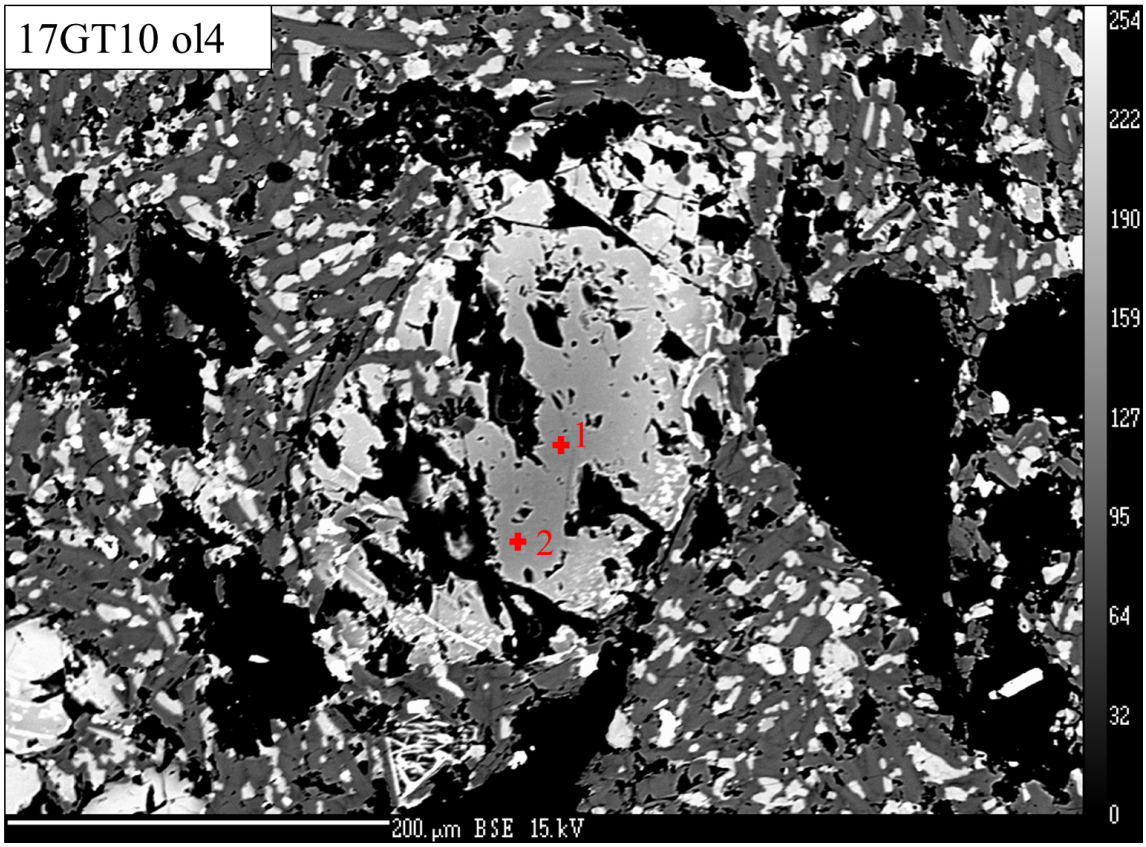
17GT10 ol4
1
2
254
222
190
159
127
95
64
32
0
200.µm BSE 15.kV

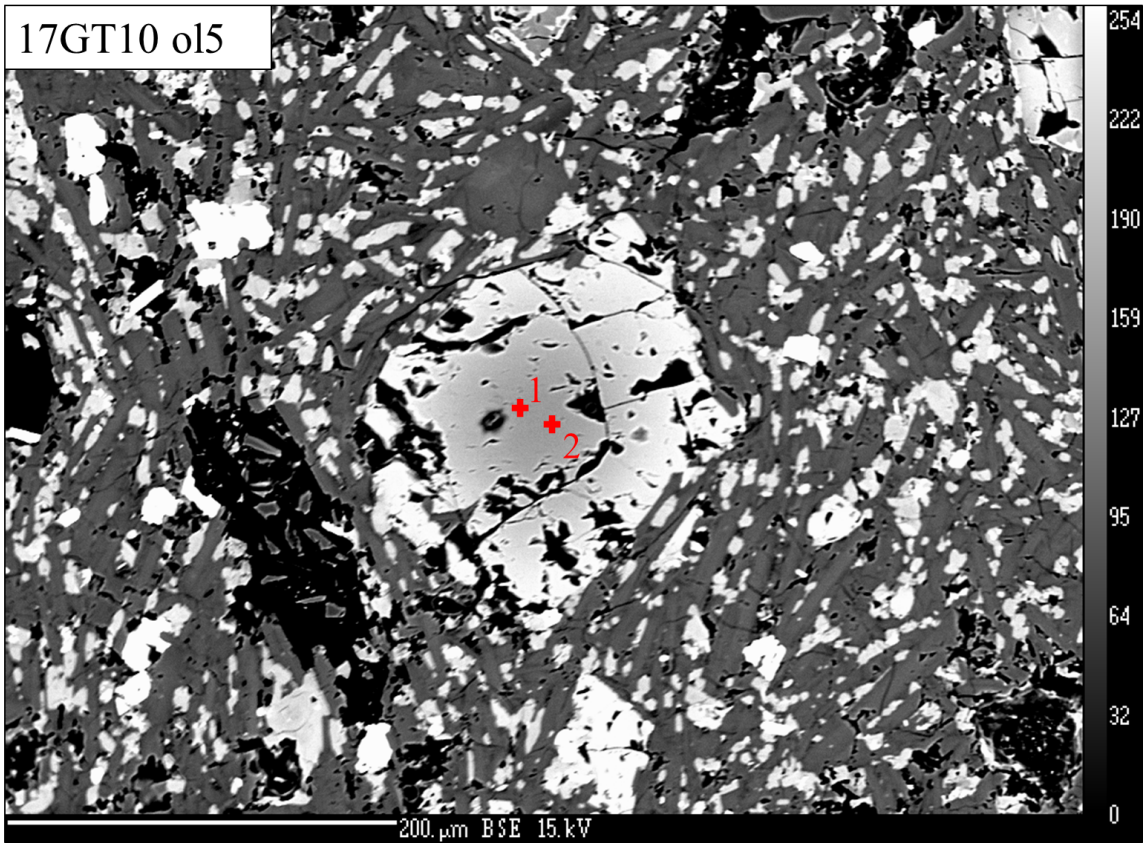
17GT10 ol5
1
2
200.µm BSE 15.kV
254
222
190
159
127
95
64
32
0

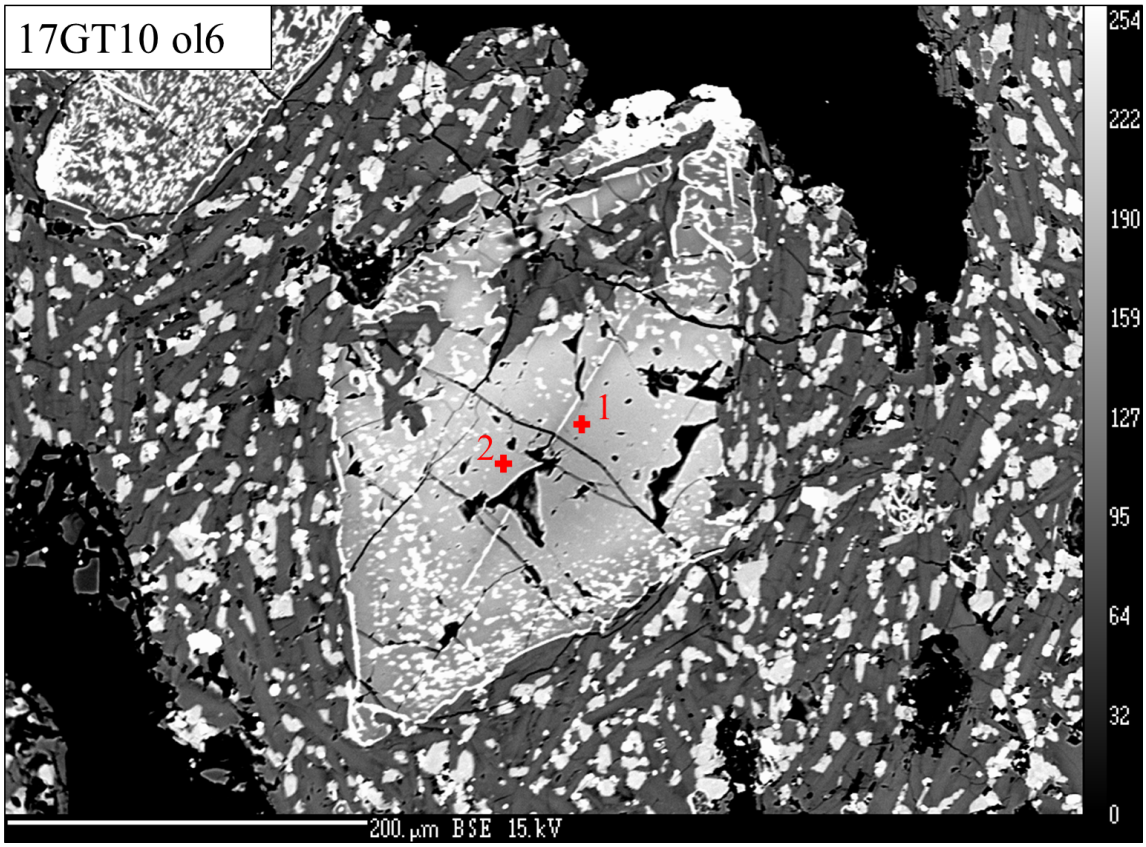
17GT10 ol6
1
2
254
222
190
159
127
95
64
32
0
200 µm BSE 15 kV

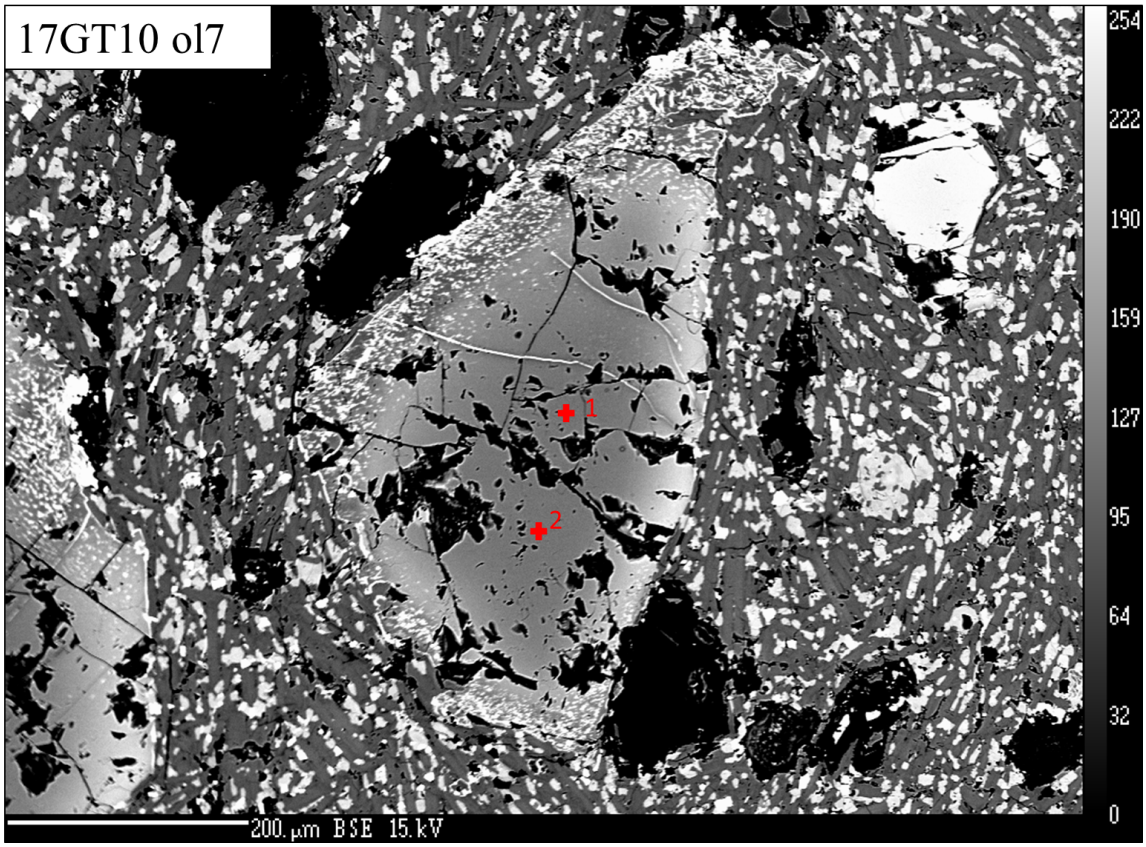
17GT10 ol7
1
2
200.µm BSE 15.kV
254
222
190
159
127
95
64
32
0

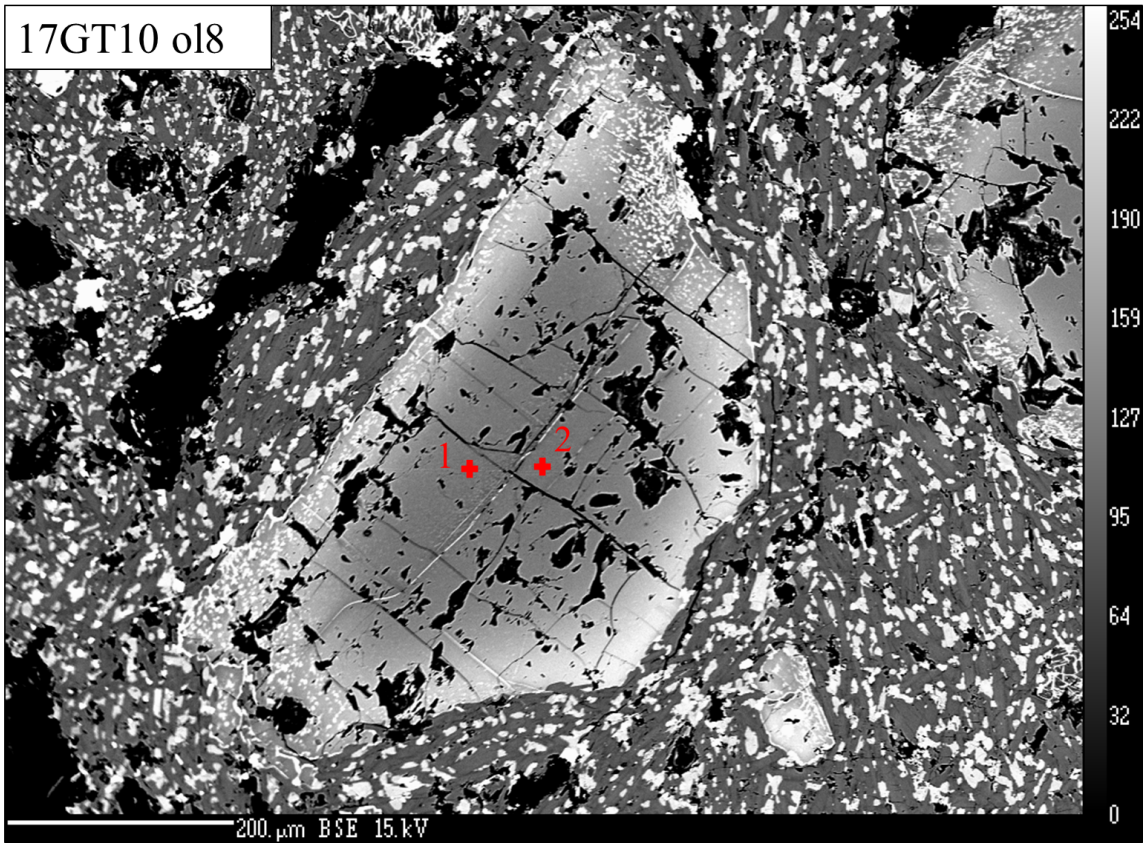
17GT10 ol8
1
2
254
222
190
159
127
95
64
32
0
200.µm BSE 15.kV

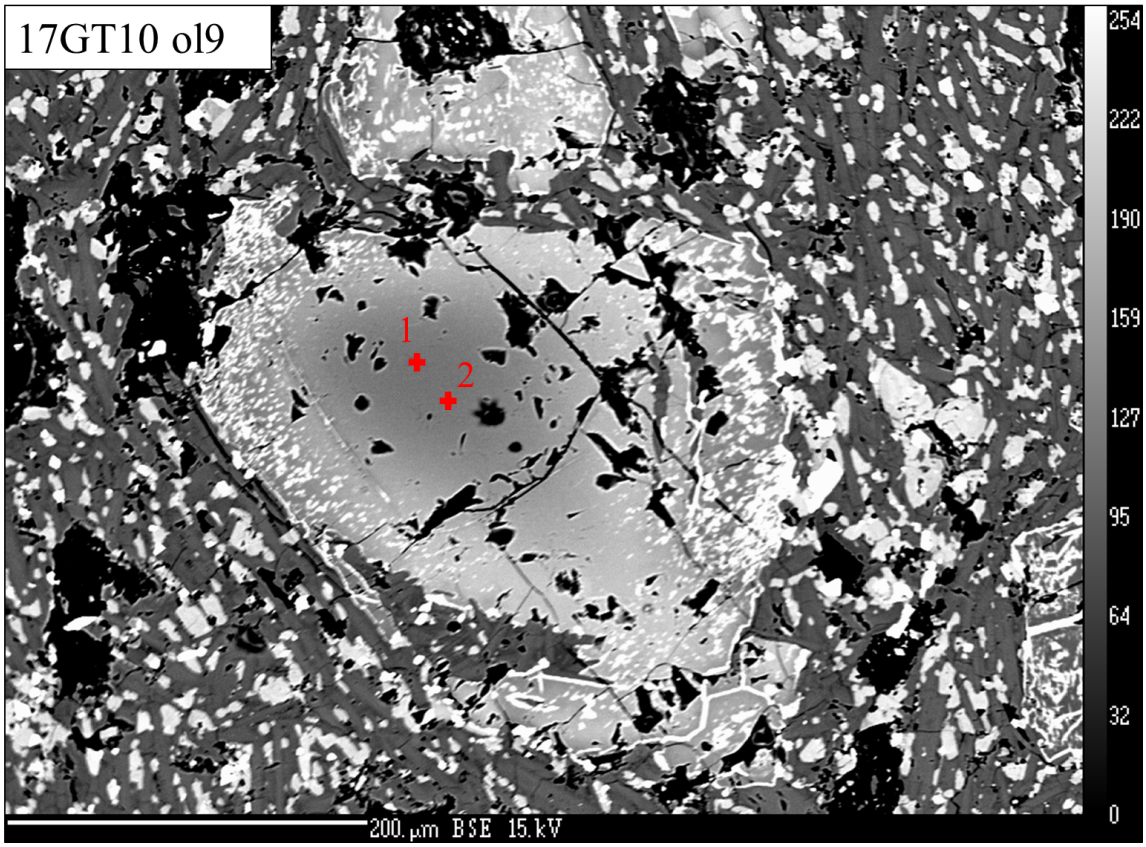
17GT10 ol9
1
2
254
222
190
159
127
95
64
32
0
200 µm BSE 15 kV

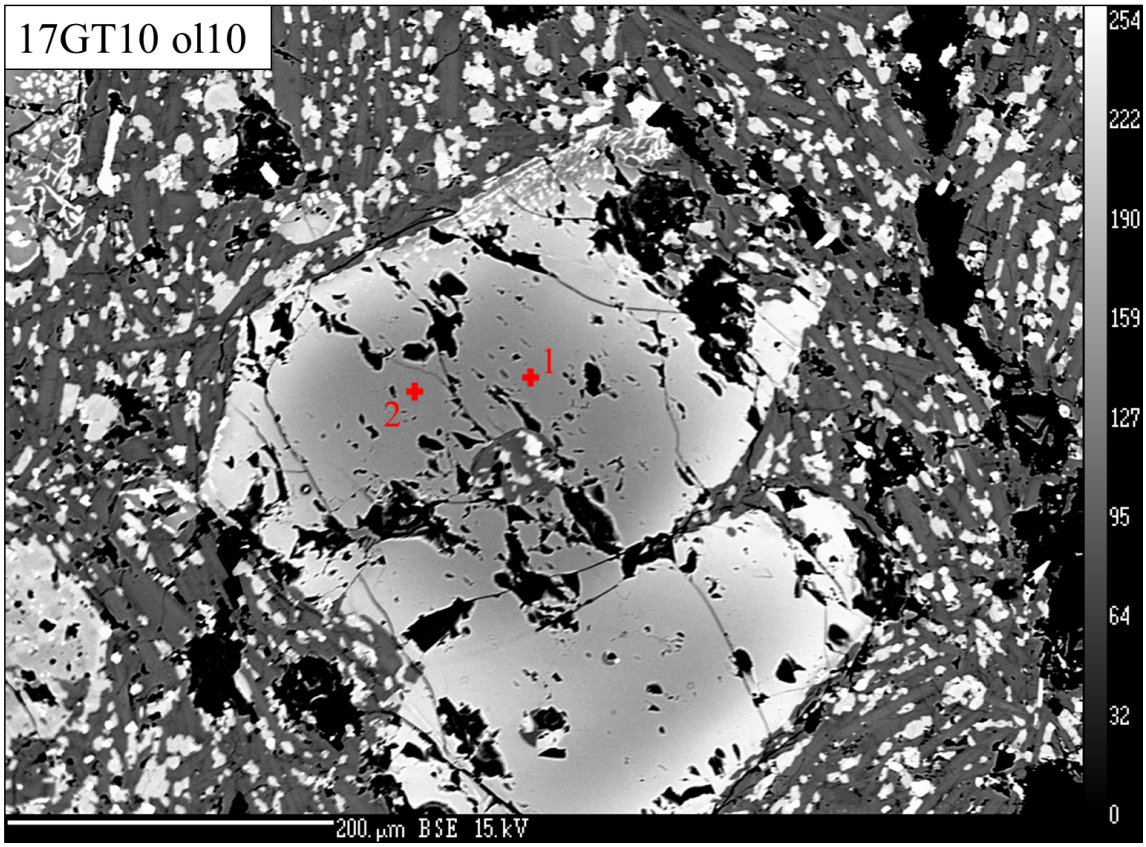
17GT10 ol10
1
2
254
222
190
159
127
95
64
32
0
200.µm BSE 15.kV

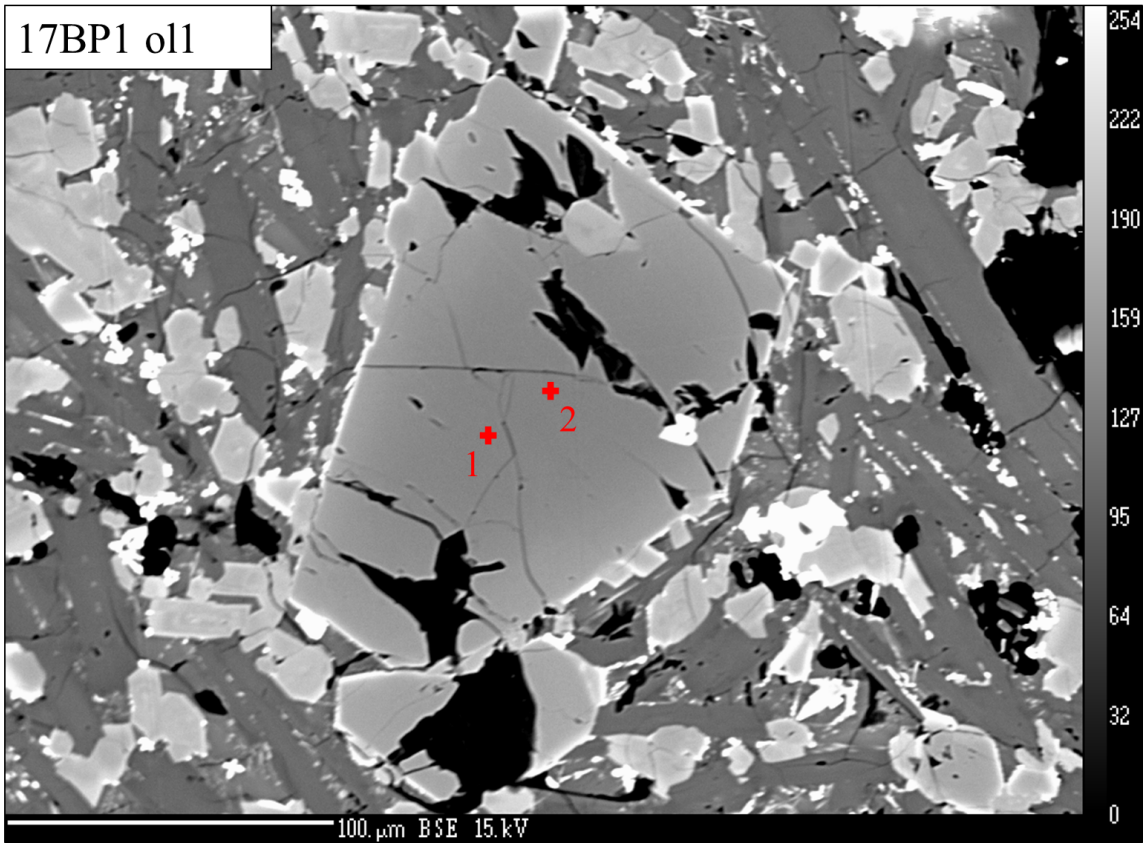
17BP1 ol1
1
2
100.μm BSE 15.kV
254
222
190
159
127
95
64
32
0

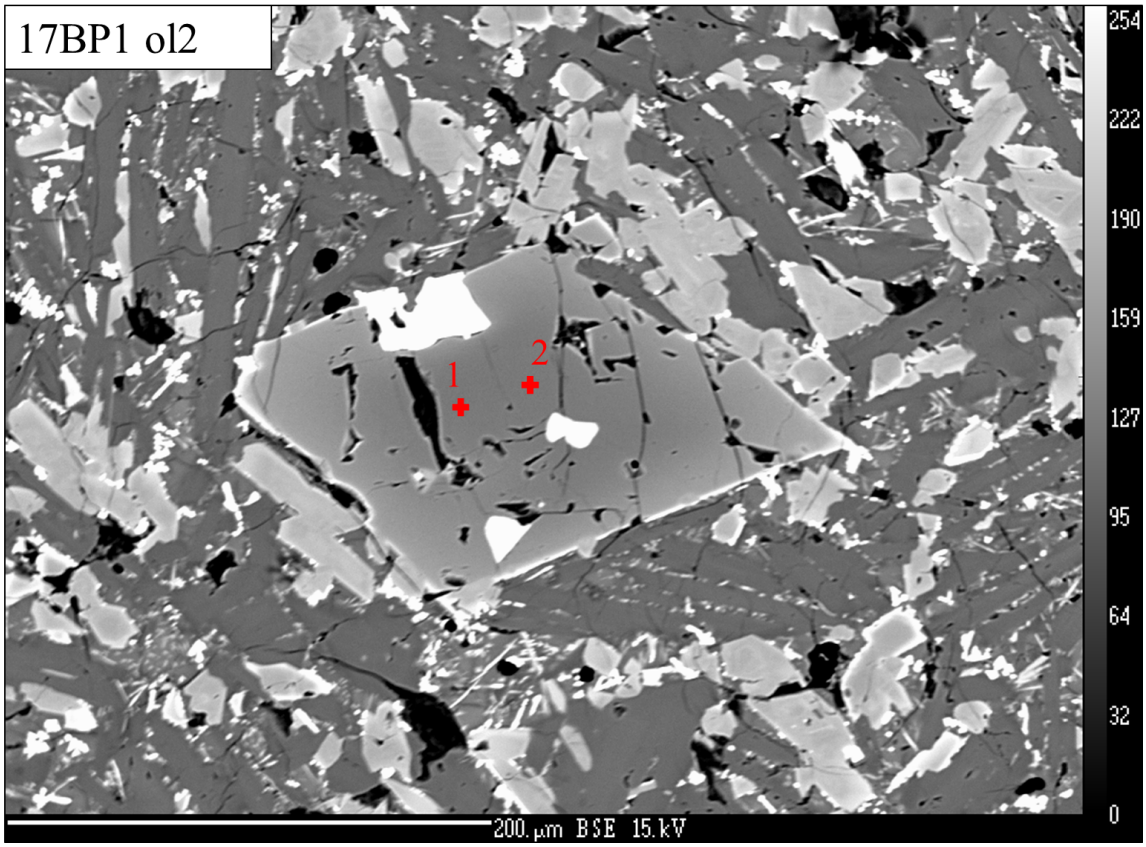
17BP1 ol2
1
2
254
222
190
159
127
95
64
32
0
200.µm BSE 15.kV

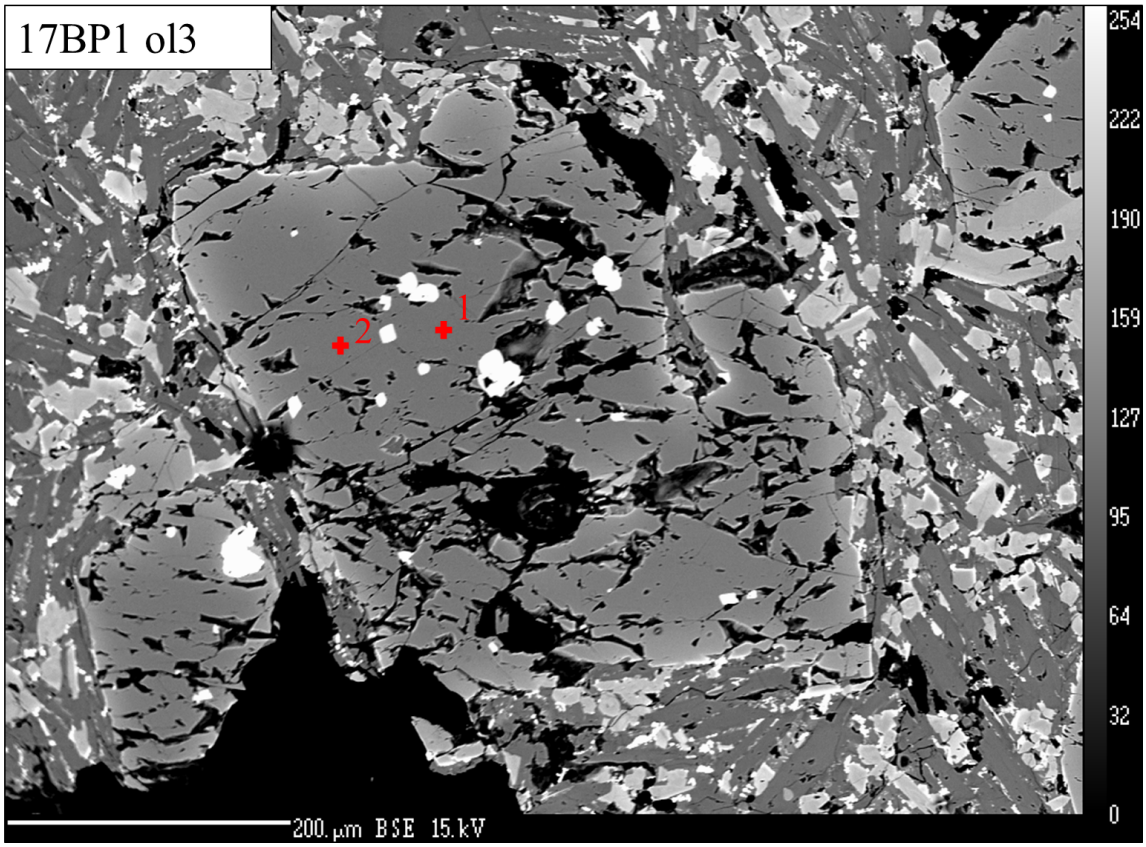
17BP1 ol3
1
2
254
222
190
159
127
95
64
32
0
200.μm BSE 15.kV

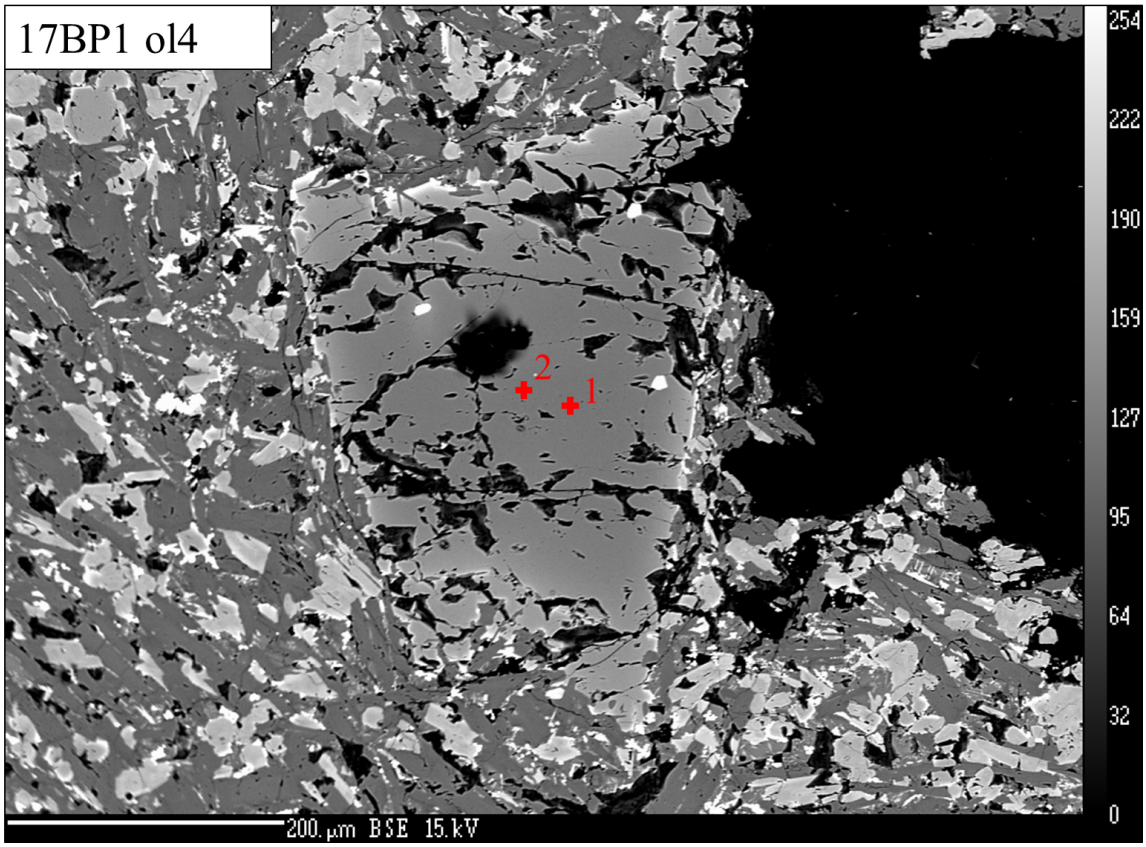
17BP1 ol4
2
1
254
222
190
159
127
95
64
32
0
200 µm BSE 15 kV

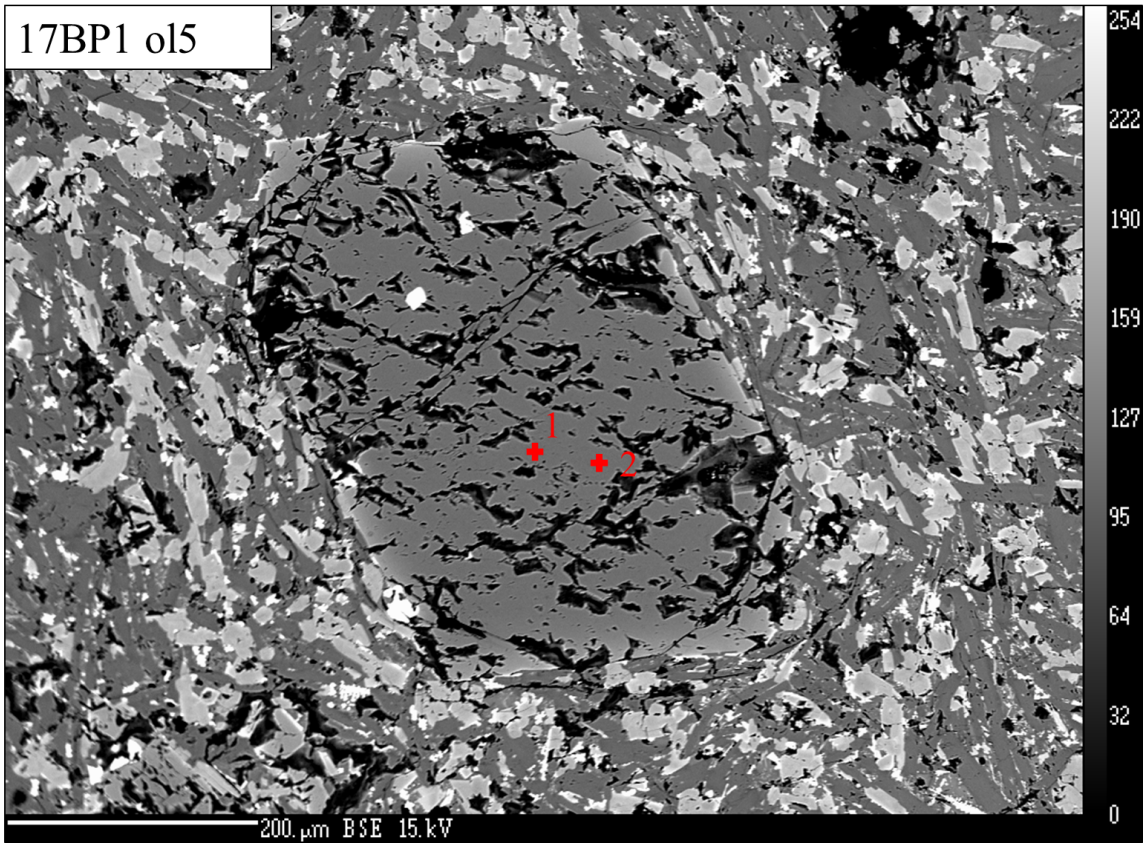
17BP1 ol5
1
2
200.µm BSE 15.kV
254
222
190
159
127
95
64
32
0

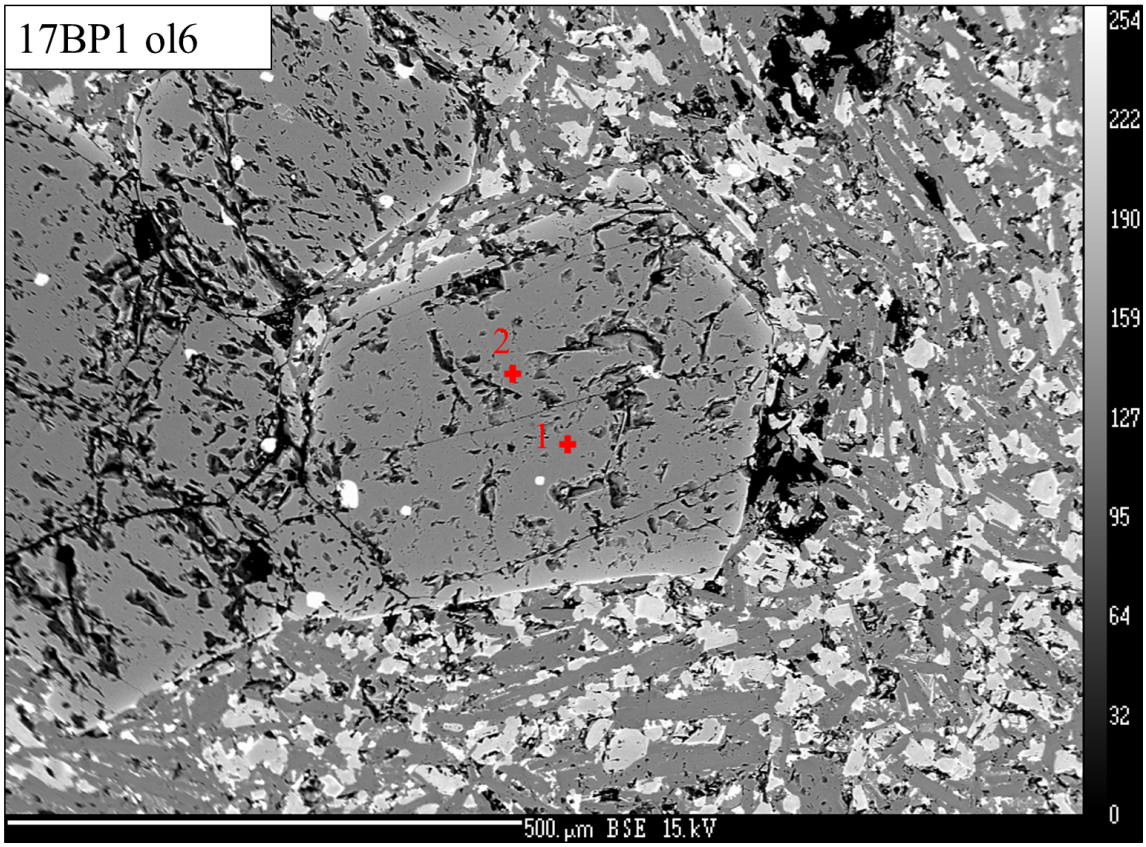
17BP1 ol6
2
1
500 µm BSE 15 kV
254
222
190
159
127
95
64
32
0

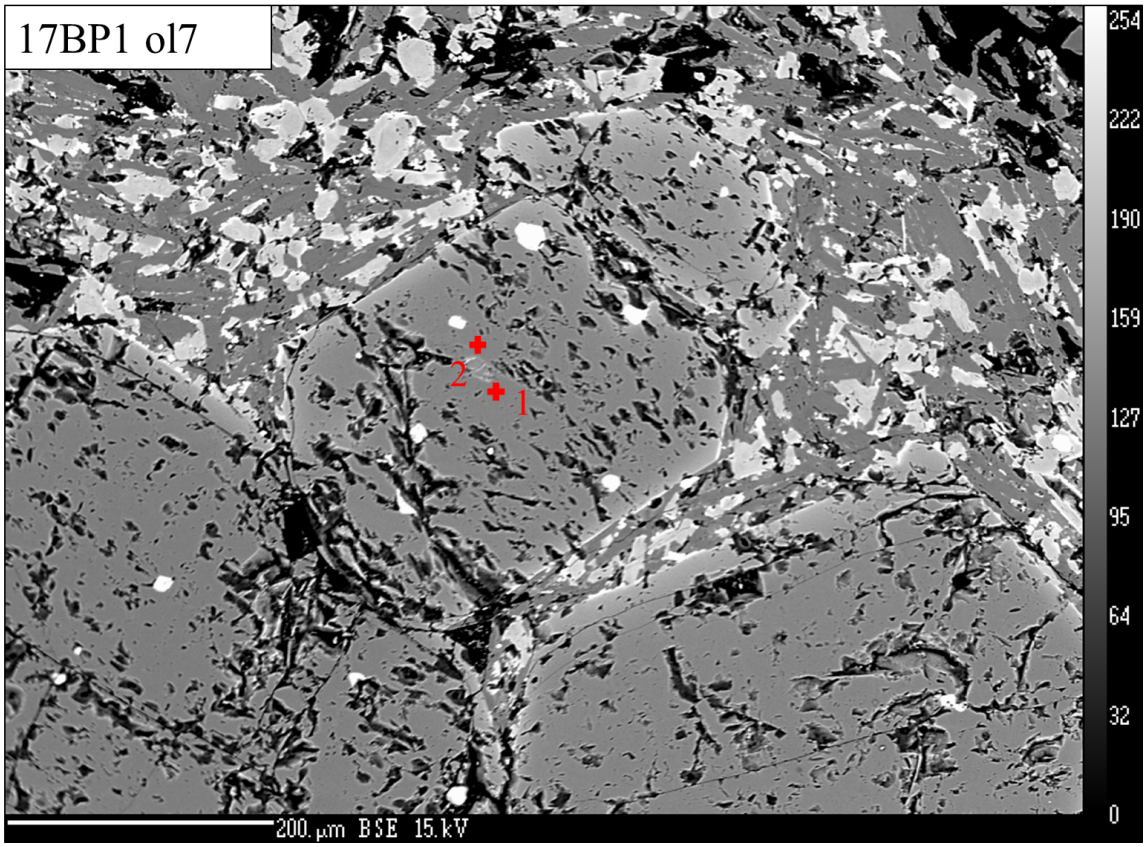
17BP1 ol7
2
1
200.μm BSE 15.kV
254
222
190
159
127
95
64
32
0

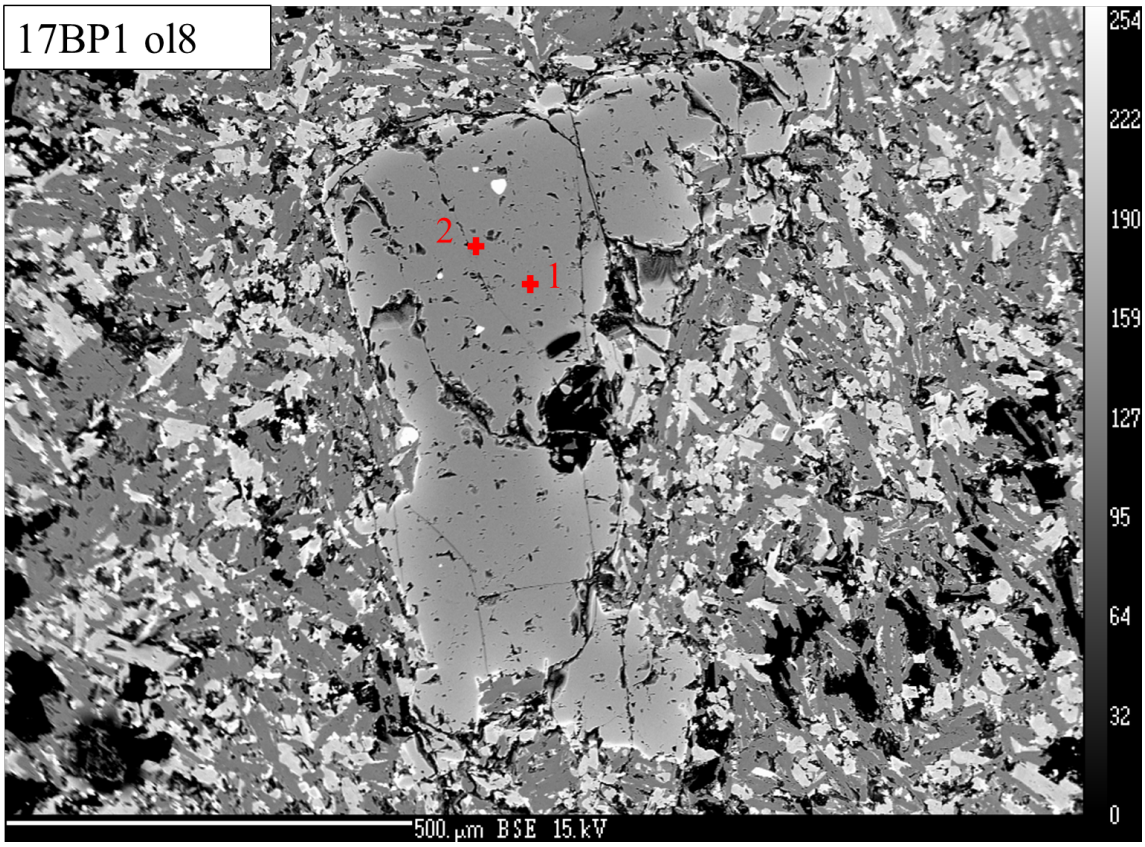
17BP1 ol8
2
1
254
222
190
159
127
95
64
32
0
500.μm BSE 15.kV

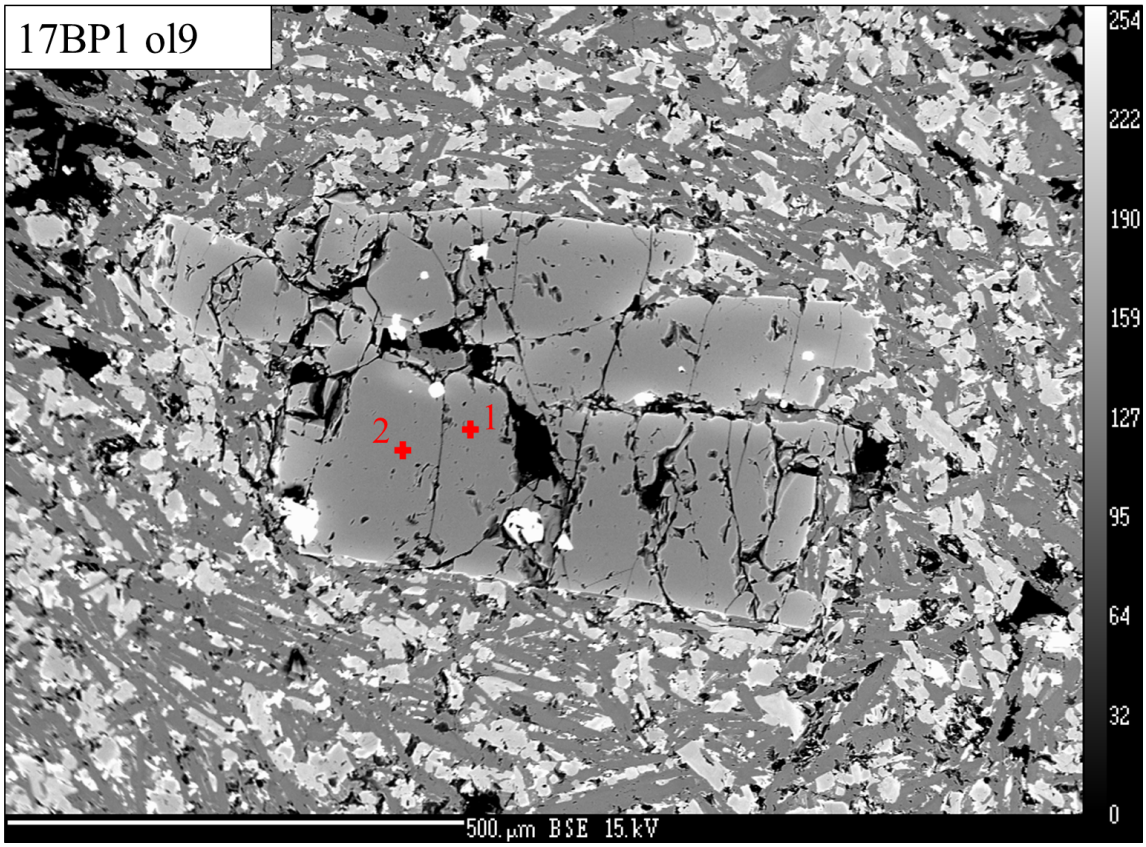
17BP1 ol9
2
1
500.µm BSE 15.kV
254
222
190
159
127
95
64
32
0

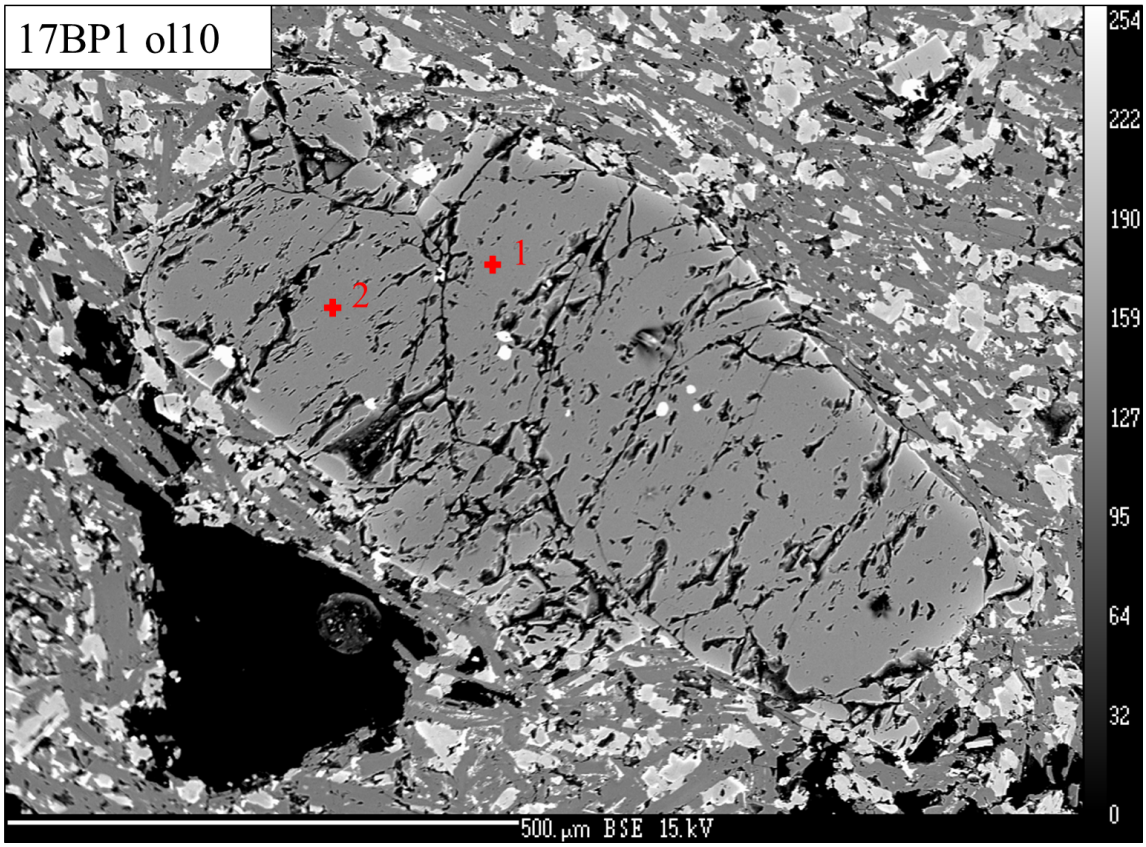
17BP1 ol10
1
2
254
222
190
159
127
95
64
32
0
500.µm BSE 15.kV

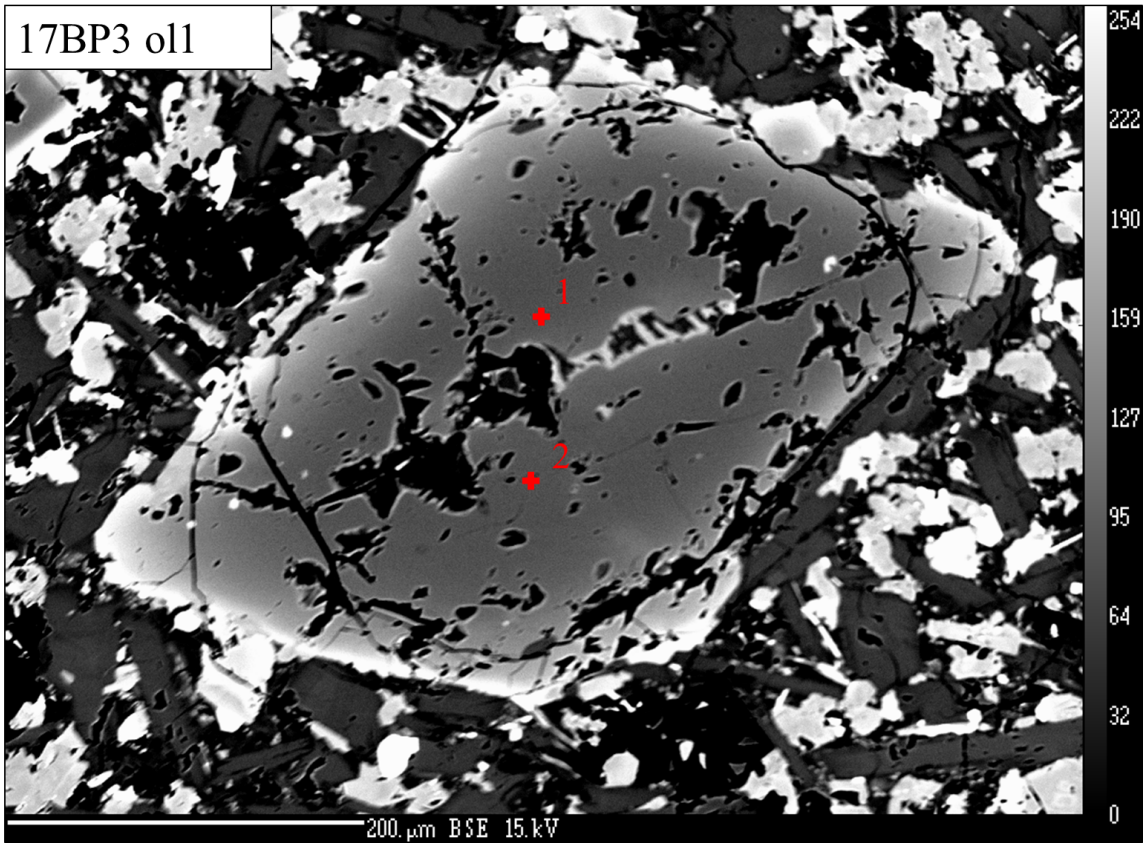
17BP3 ol1
1
2
200.µm BSE 15.kV
254
222
190
159
127
95
64
32
0

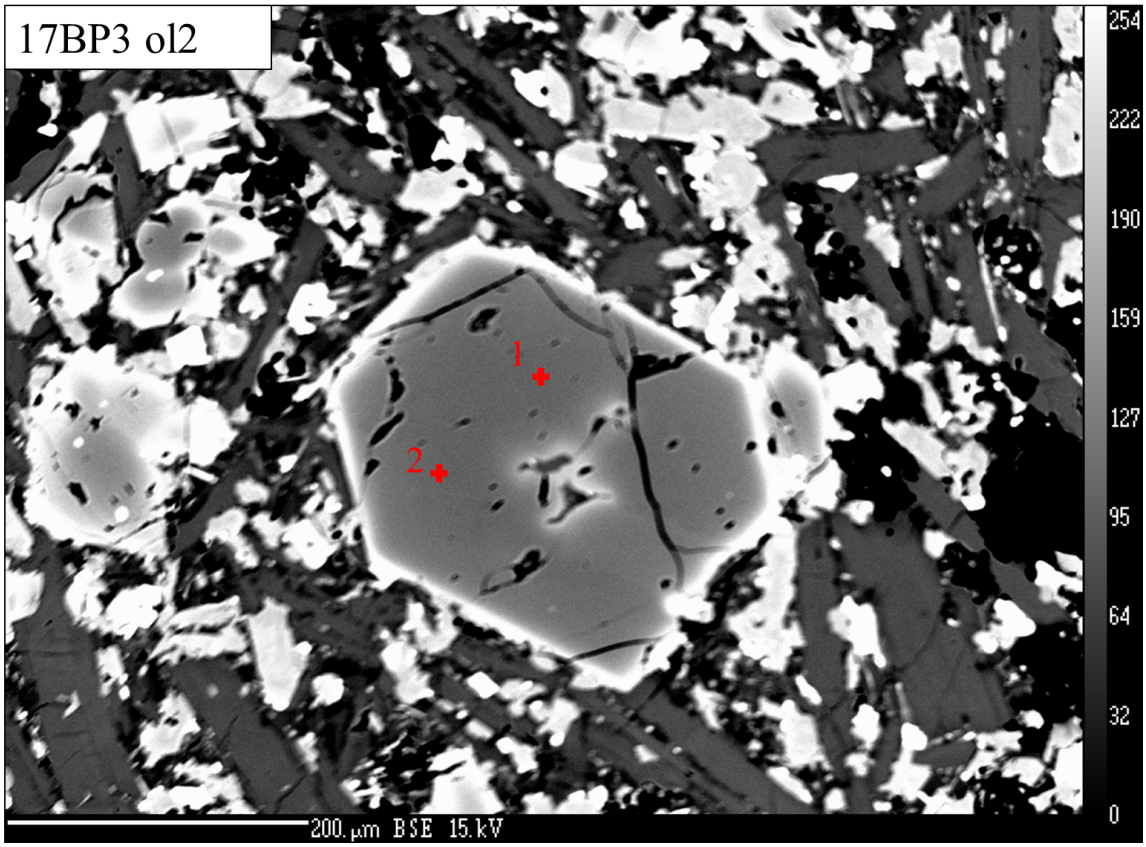
17BP3 ol2
1
2
254
222
190
159
127
95
64
32
0
200.µm BSE 15.kV

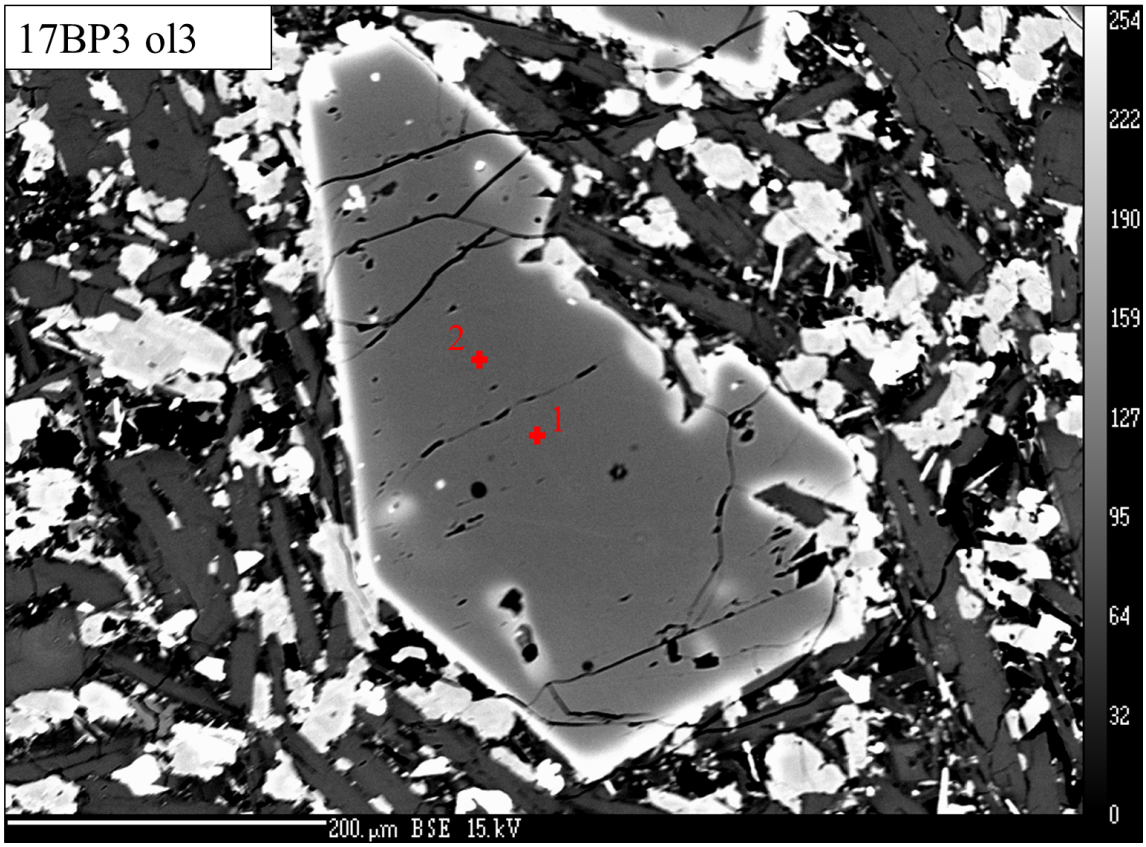
17BP3 ol3
2
1
254
222
190
159
127
95
64
32
0
200.μm BSE 15.kV

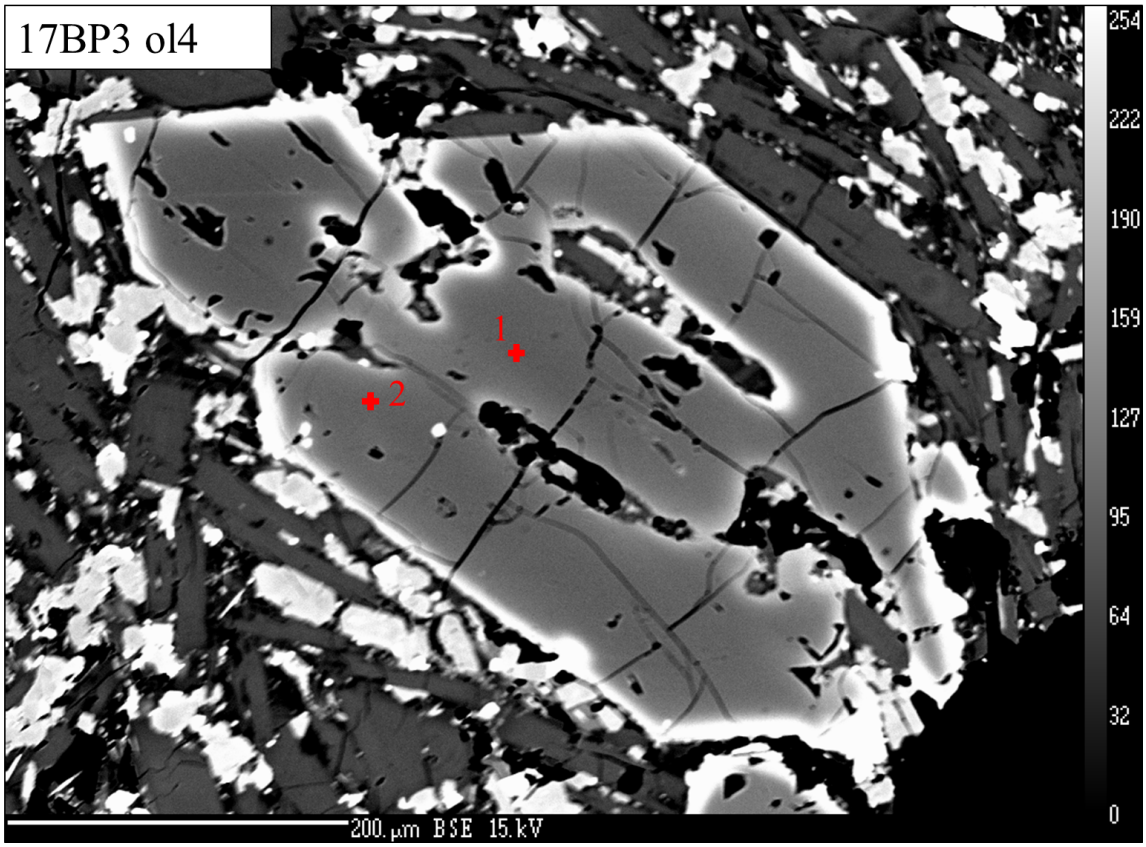
17BP3 ol4
1
2
254
222
190
159
127
95
64
32
0
200.μm BSE 15.kV

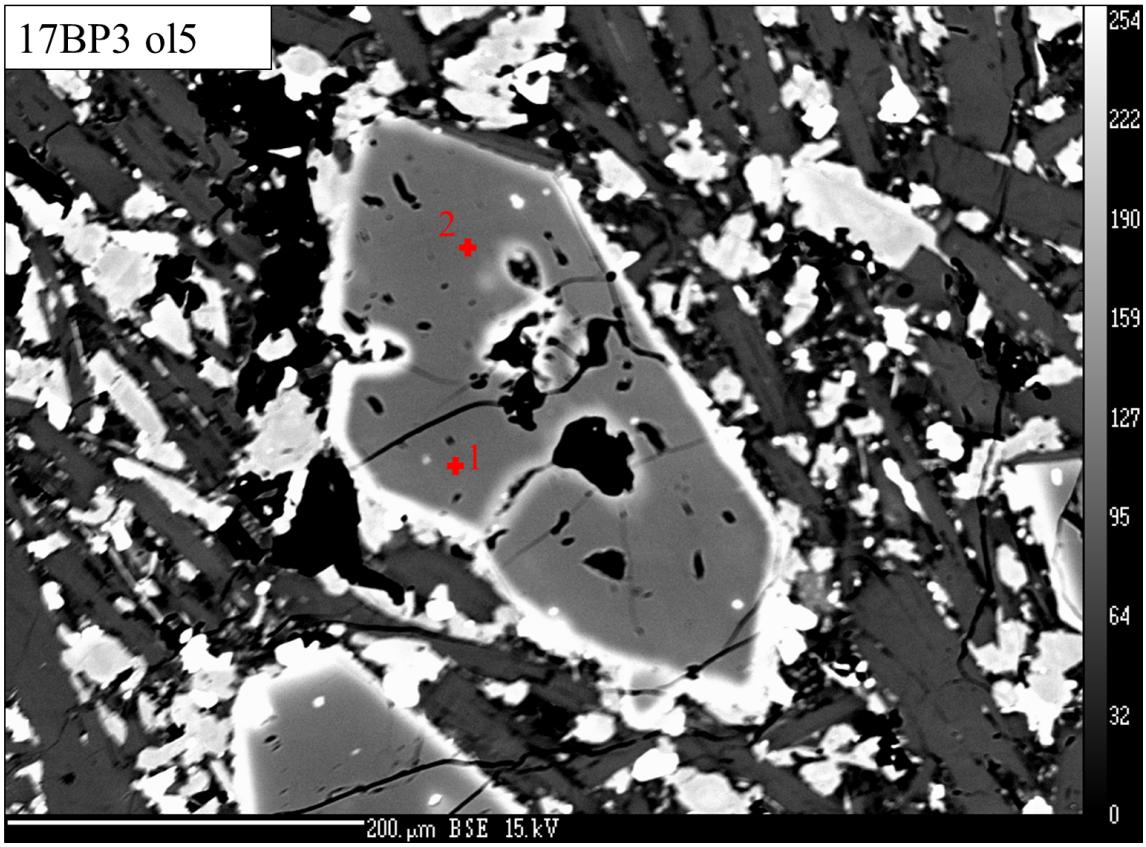
17BP3 ol5
2
1
254
222
190
159
127
95
64
32
0
200.µm BSE 15.kV

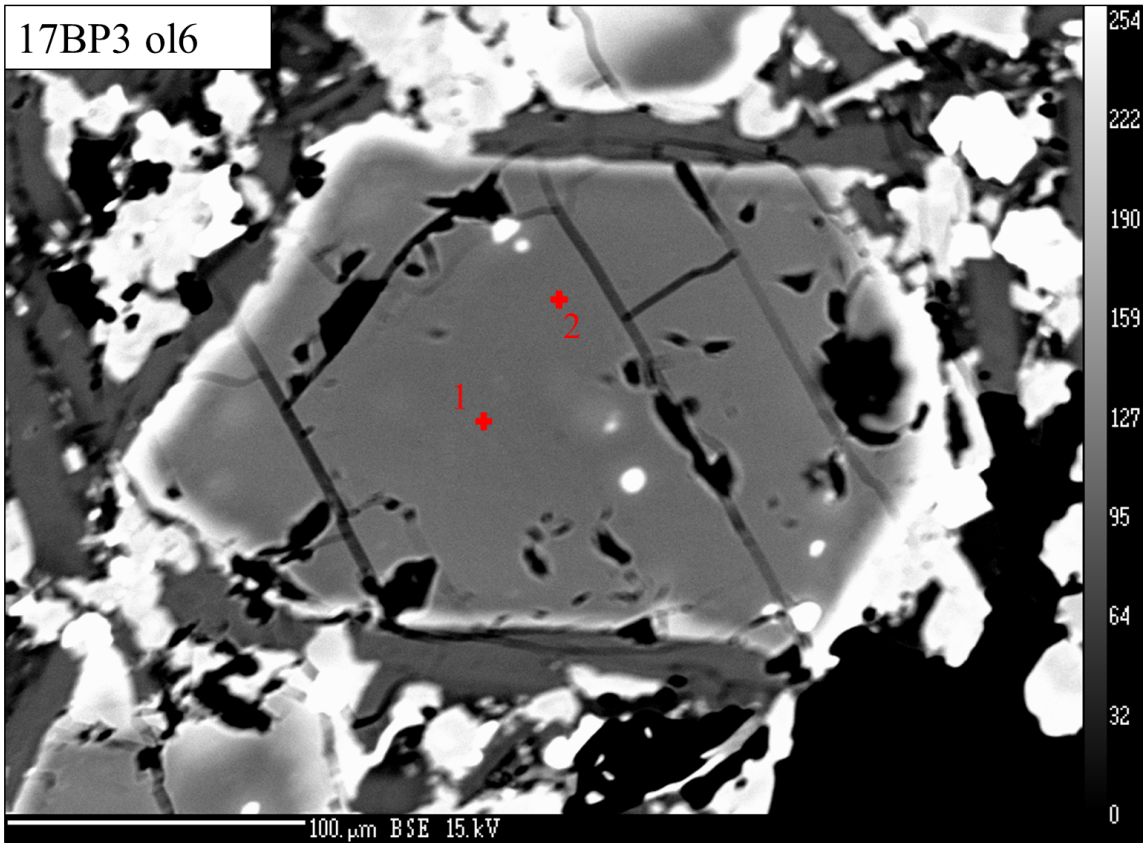
17BP3 ol6
254
222
190
159
127
95
64
32
0
2
1
100.μm BSE 15.kV

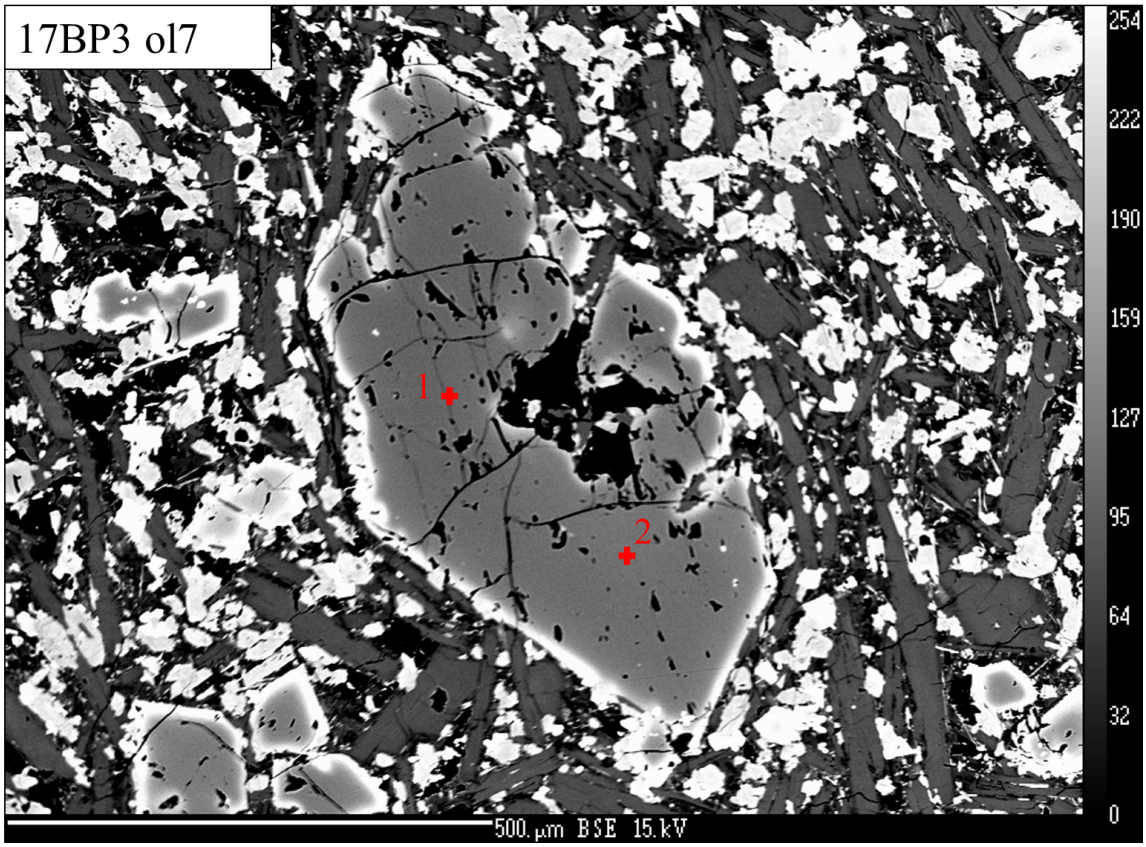
17BP3 ol7
1
2
500.µm BSE 15.kV
254
222
190
159
127
95
64
32
0

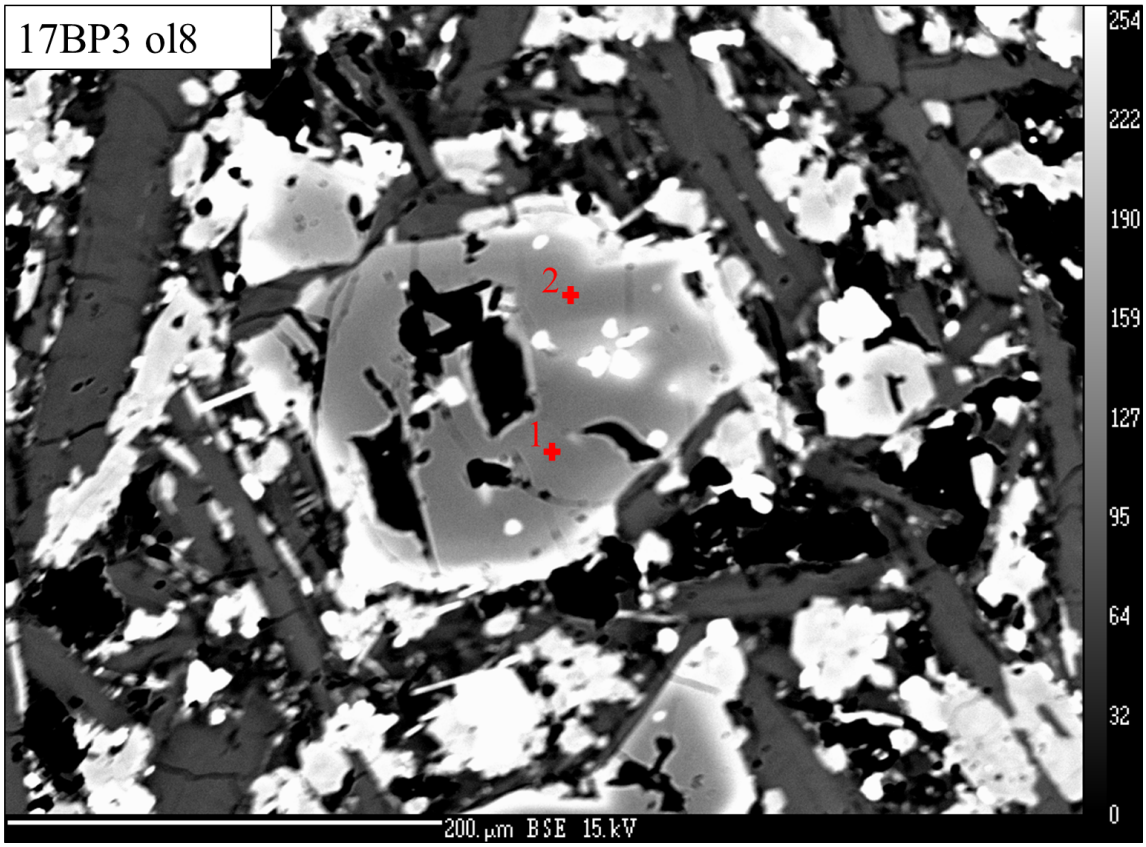
17BP3 ol8
2
1
254
222
190
159
127
95
64
32
0
200.μm BSE 15.kV

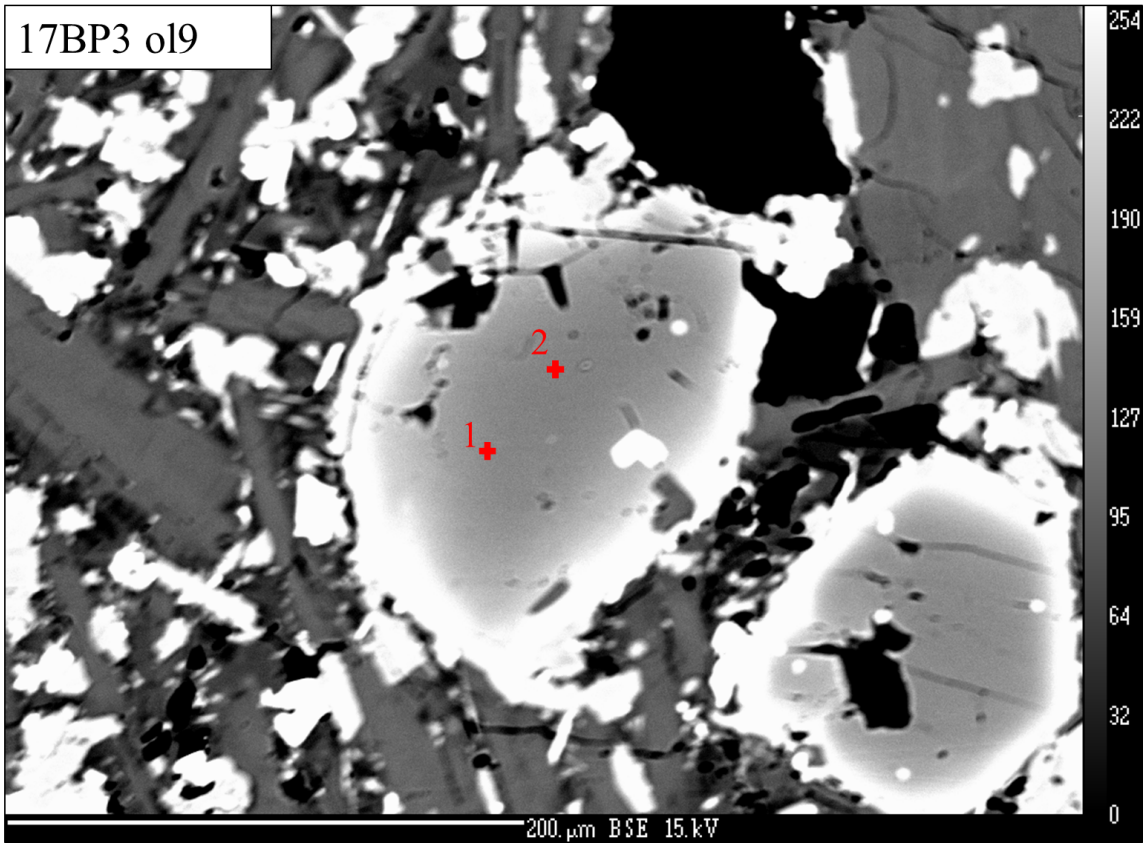
17BP3 ol9
2
1
254
222
190
159
127
95
64
32
0
200.μm BSE 15.kV

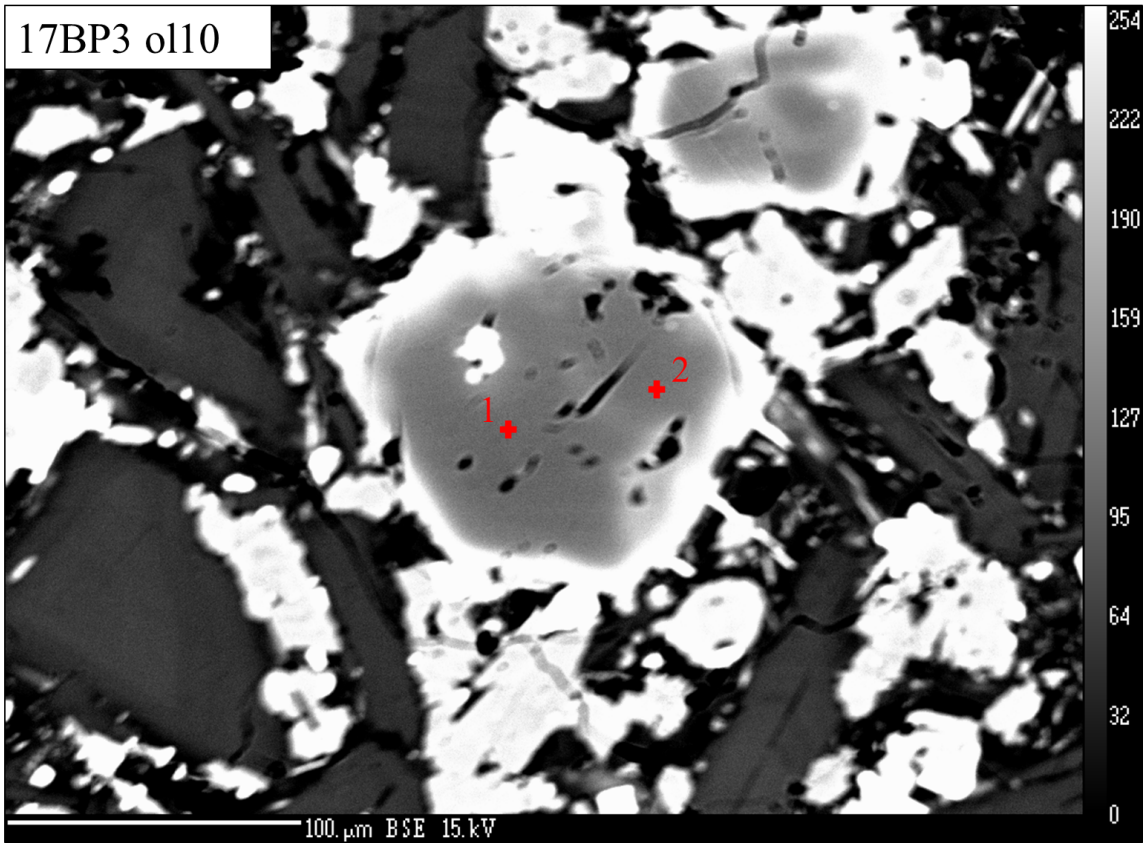
17BP3 ol10
1
2
254
222
190
159
127
95
64
32
0
100.μm BSE 15.kV

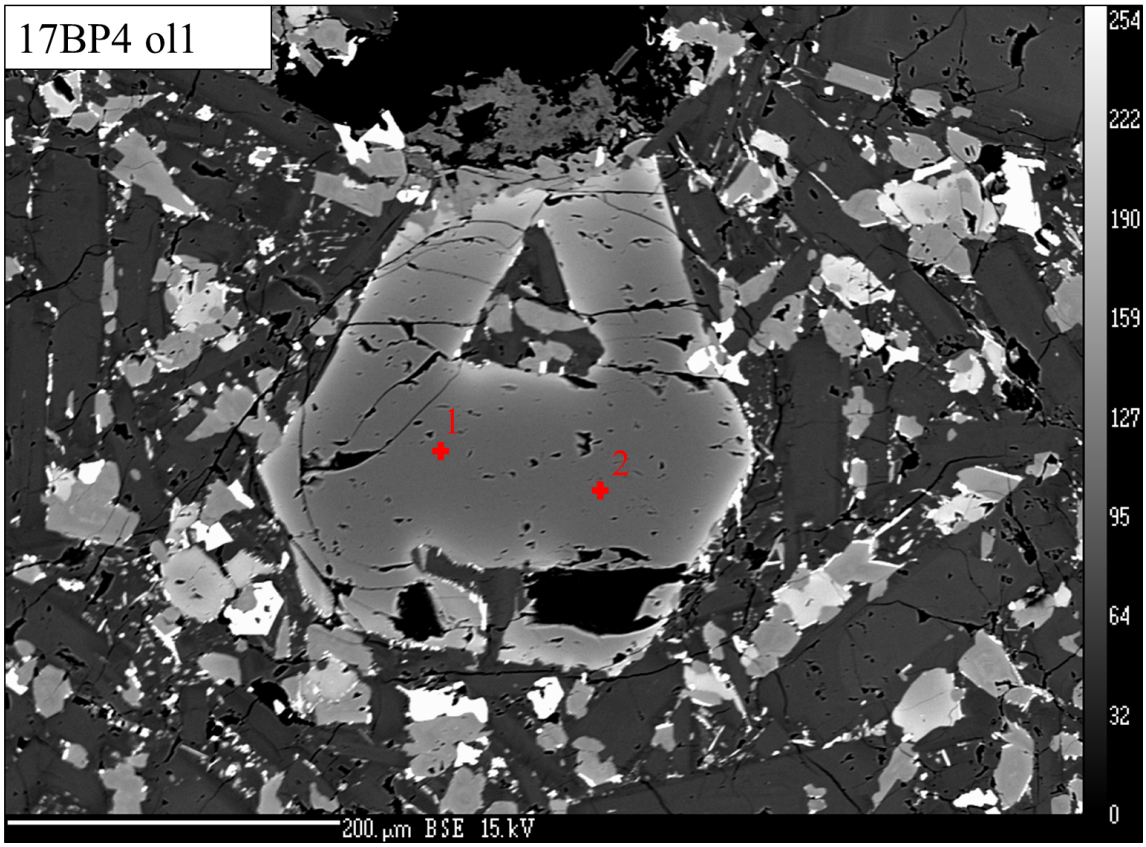
17BP4 ol1
1
2
200.μm BSE 15.kV
254
222
190
159
127
95
64
32
0

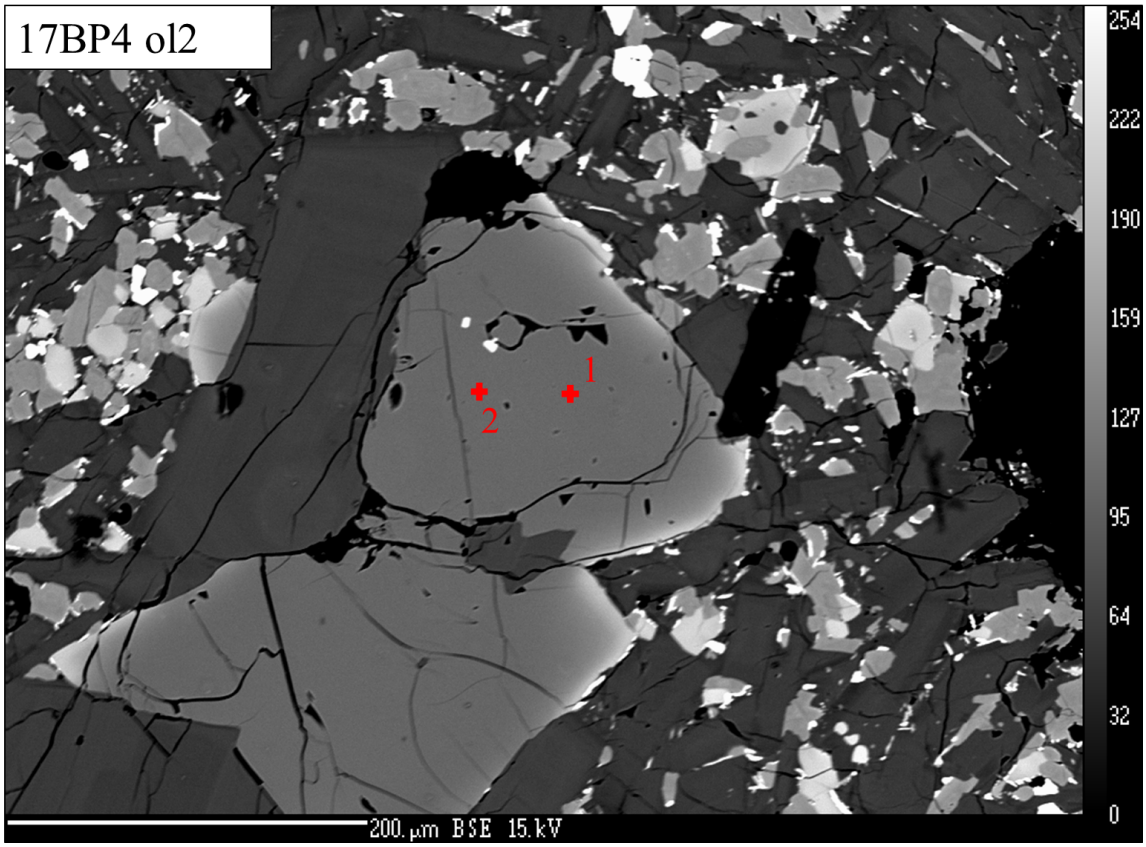
17BP4 ol2
1
2
200.μm BSE 15.kV
254
222
190
159
127
95
64
32
0

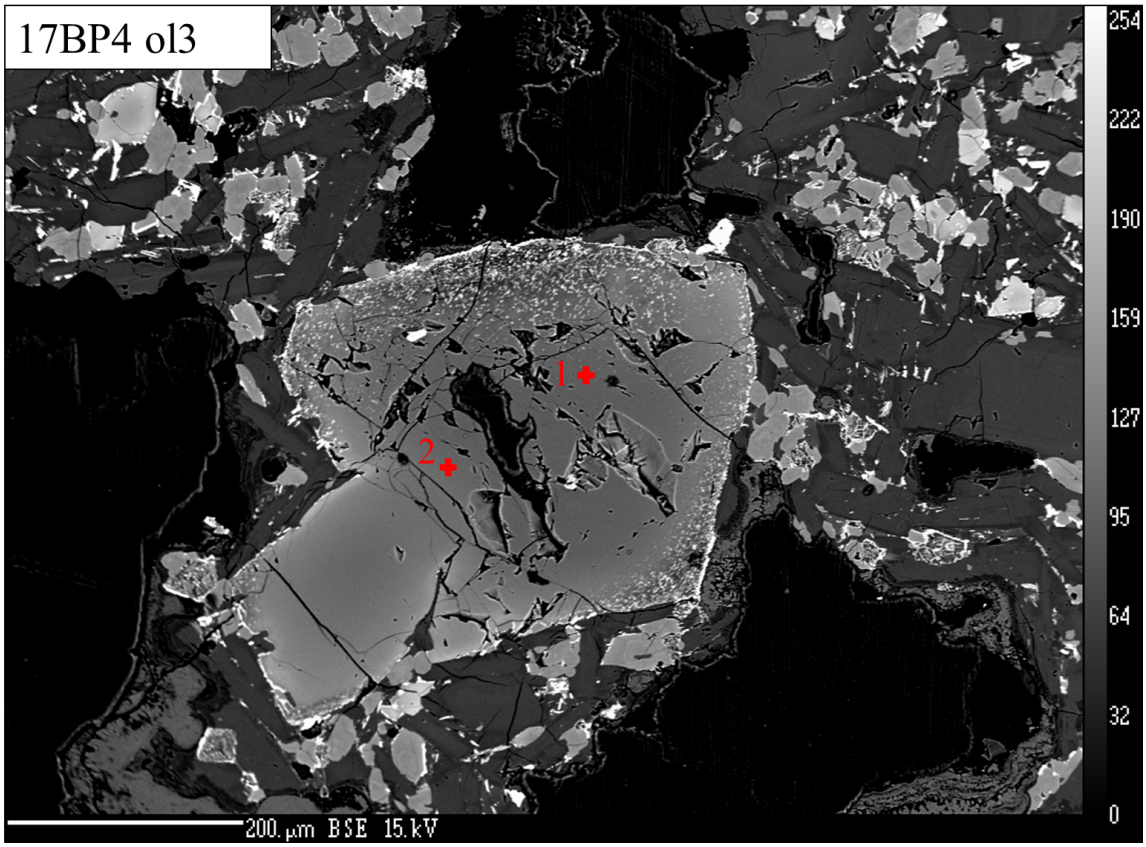
17BP4 ol3
1
2
200.µm BSE 15.kV
254
222
190
159
127
95
64
32
0

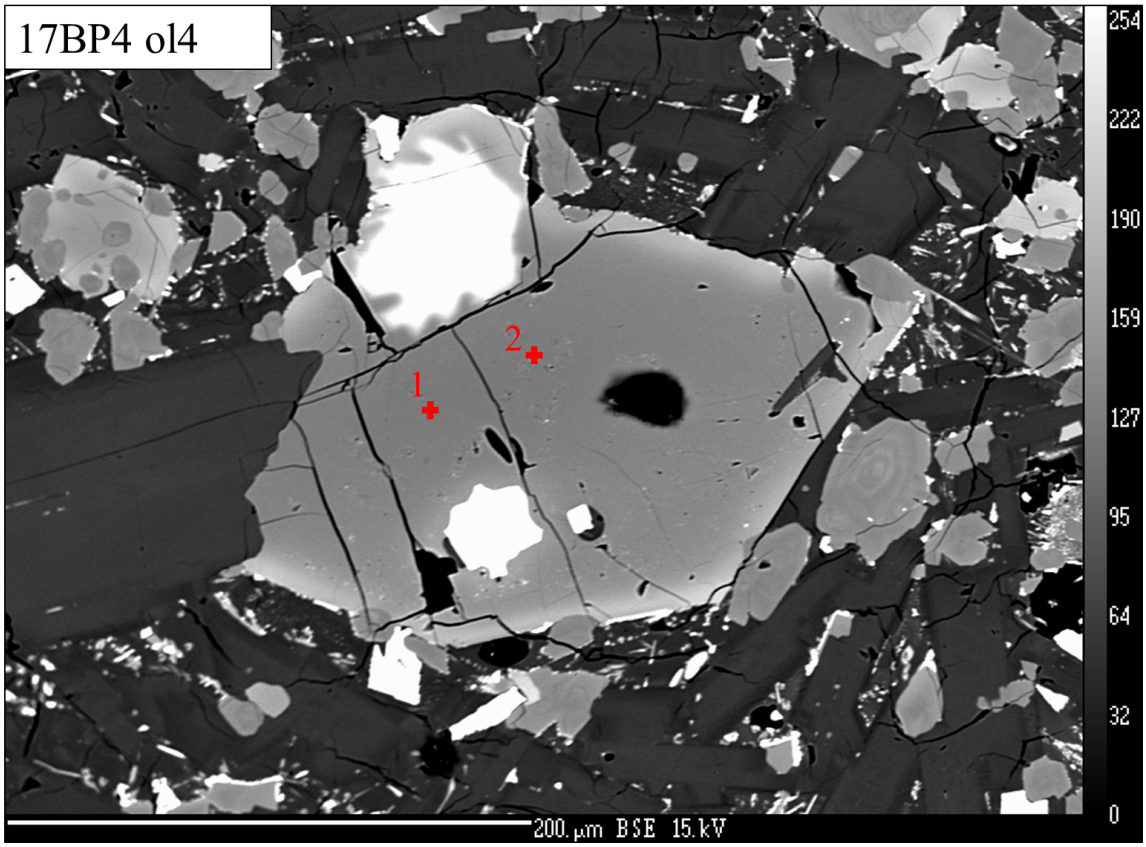
17BP4 ol4
1
2
254
222
190
159
127
95
64
32
0
200.µm BSE 15.kV

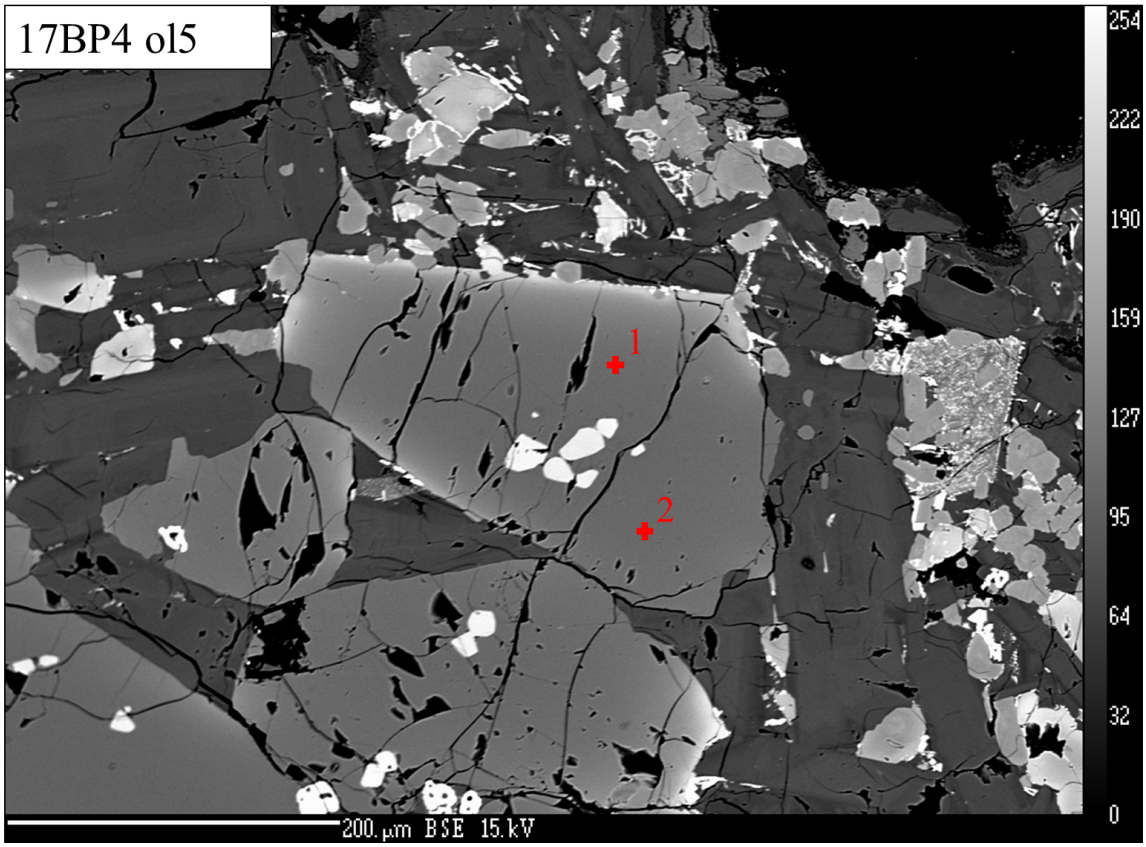
17BP4 ol5
1
2
200.μm BSE 15.kV
254
222
190
159
127
95
64
32
0

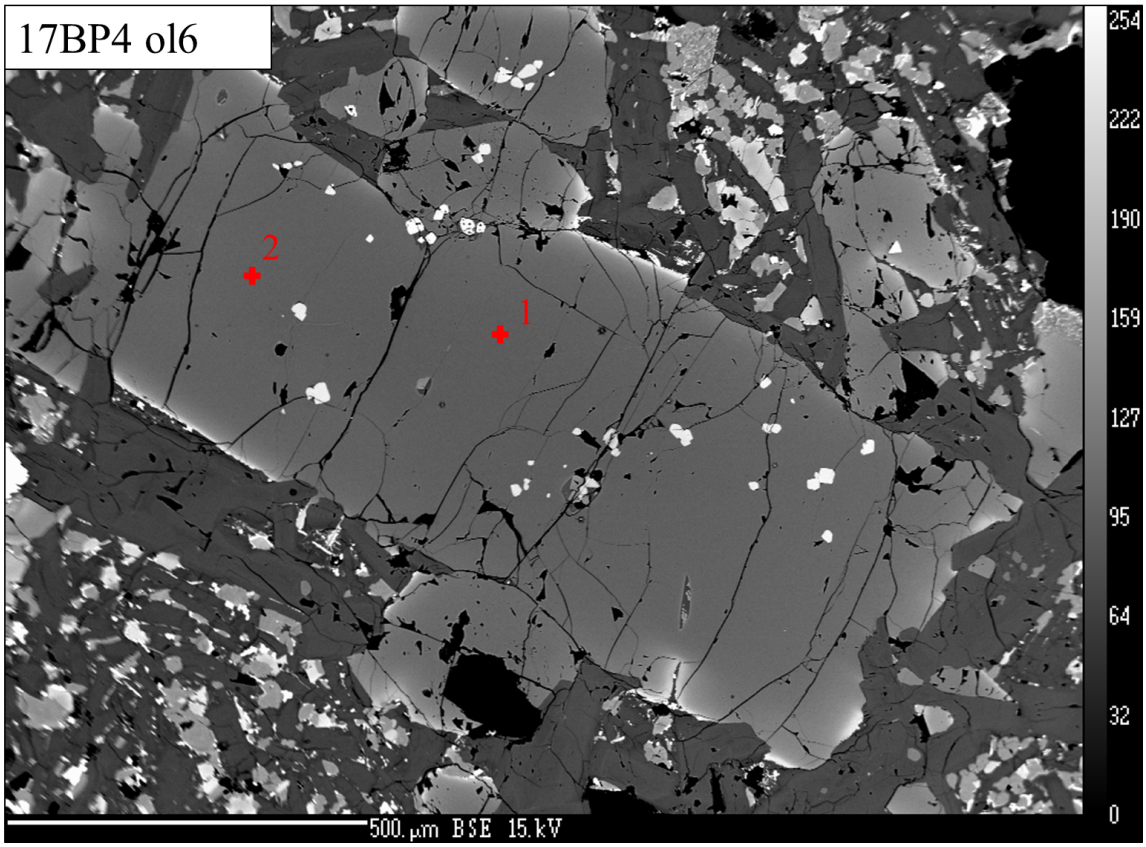
17BP4 ol6
2
1
500.μm BSE 15.kV
254
222
190
159
127
95
64
32
0

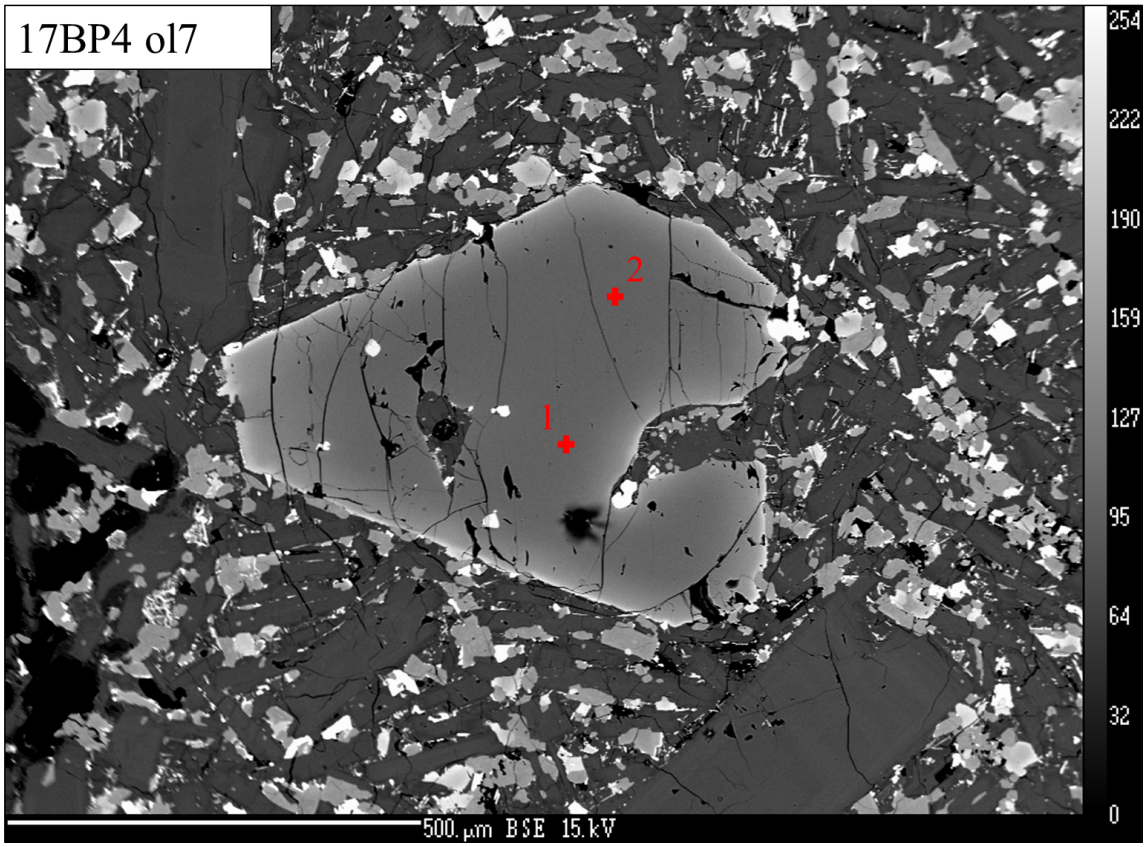
17BP4 ol7
1
2
254
222
190
159
127
95
64
32
0
500.µm BSE 15.kV

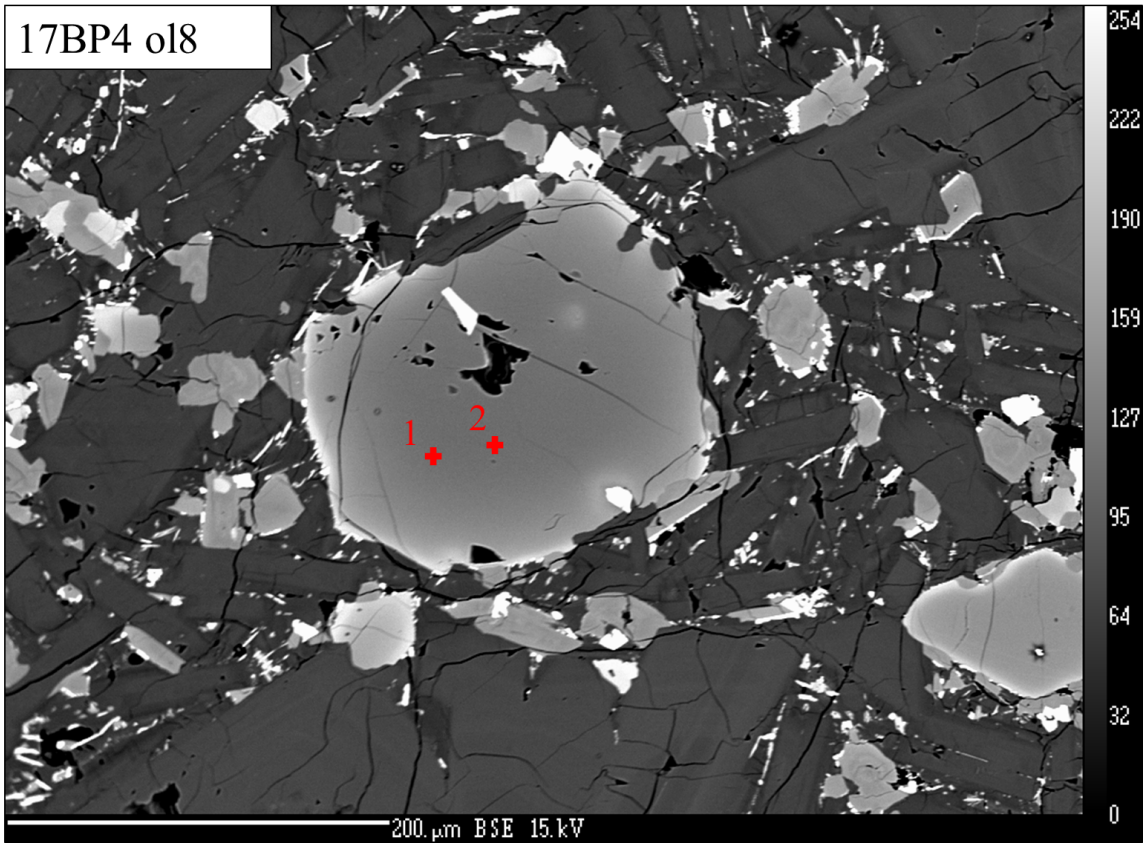
17BP4 ol8
1
2
200.μm BSE 15.kV
254
222
190
159
127
95
64
32
0

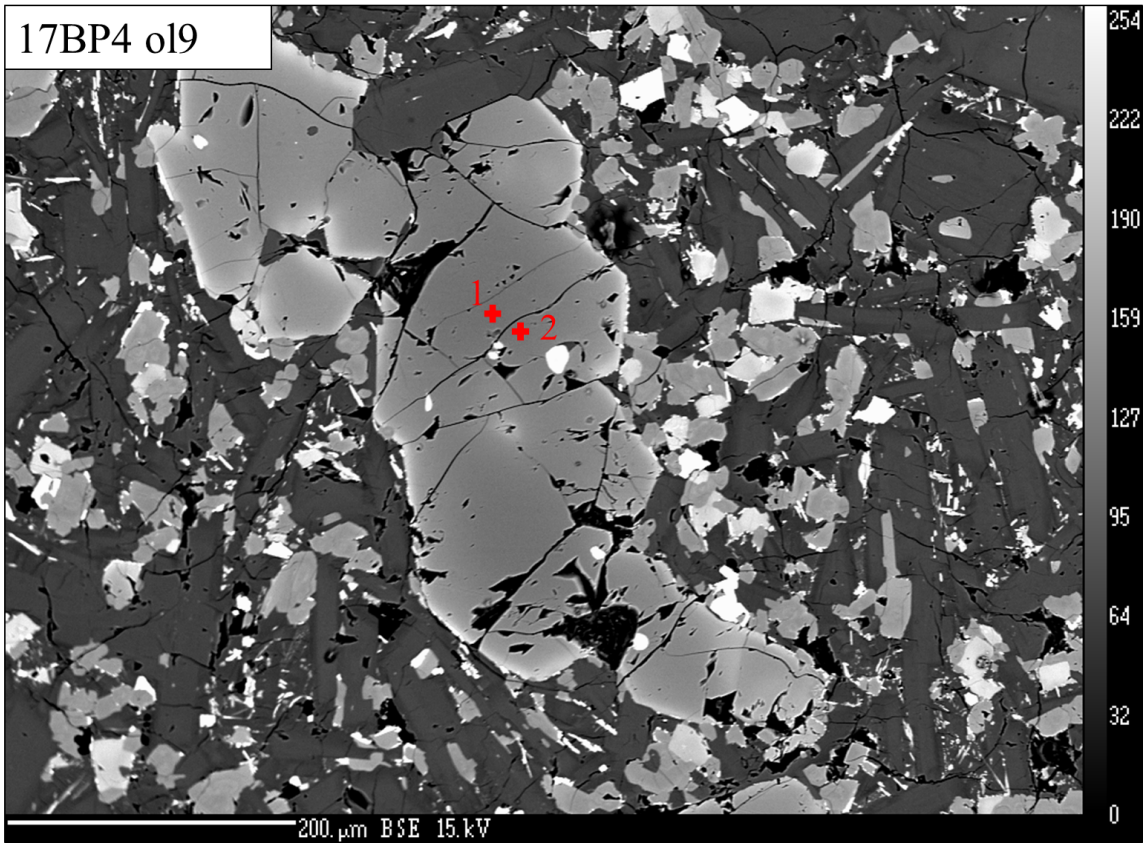
17BP4 ol9
1
2
254
222
190
159
127
95
64
32
0
200.µm BSE 15.kV

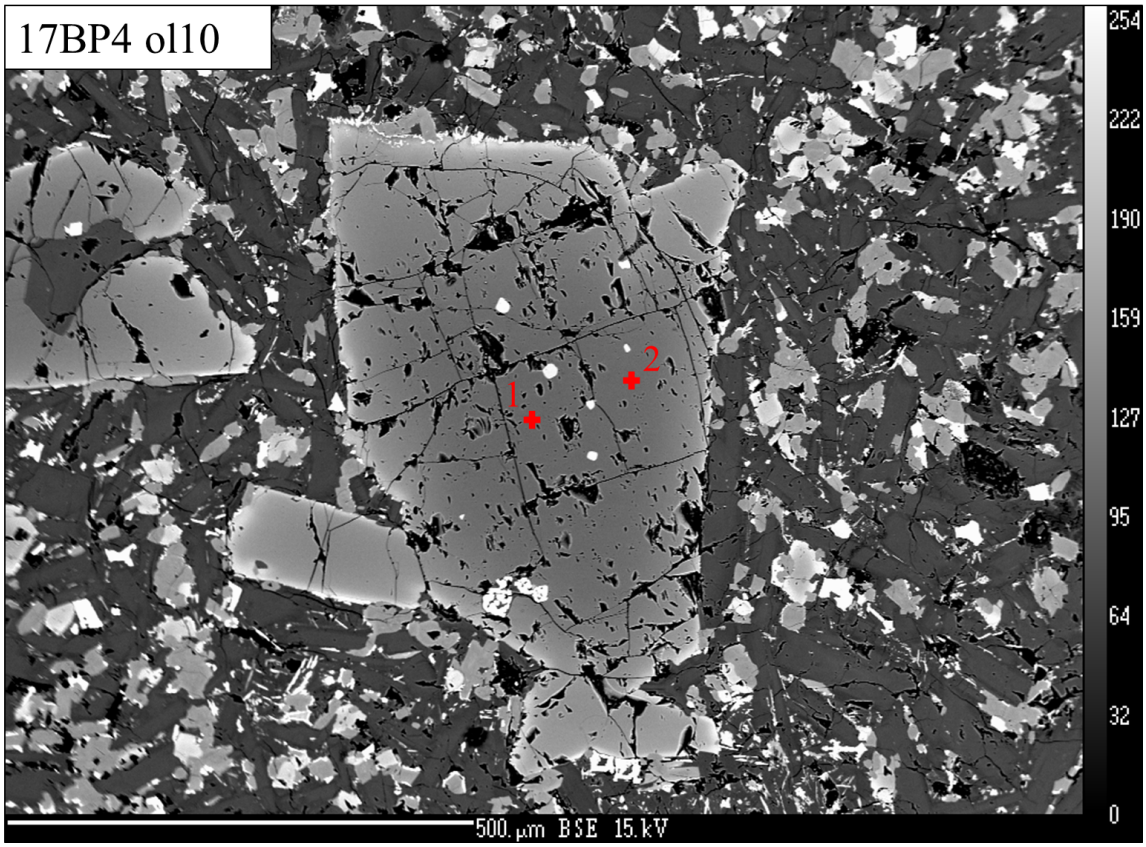
17BP4 ol10
1
2
500.μm BSE 15.kV
254
222
190
159
127
95
64
32
0